# RADAR SCATTERING FROM THE SUMMER POLAR MESOSPHERE: THEORY AND OBSERVATIONS

A Dissertation
Presented to the Faculty of the Graduate School
of Cornell University
in Partial Fulfillment of the Requirements for the Degree of
Doctor of Philosophy

by
John Yungdo Nagamichi Cho
May 1993

# RADAR SCATTERING FROM THE SUMMER POLAR MESOSPHERE: THEORY AND OBSERVATIONS

John Yungdo Nagamichi Cho, Ph.D.

Cornell University, 1993

The anomalously large radar reflectivities observed in the summer polar mesosphere have eluded satisfactory explanation until now. We propose that the following chain of causality is responsible for the so-called polar mesosphere summer echoes (PMSE): The uniquely low temperatures in the summer mesopause produce ice aerosols. Because the aerosols exist in a plasma, they become electrically charged. The ambient electrons become coupled to the aerosols through electric fields and their effective diffusivity is retarded due to the large size of the aerosols. The reduction in diffusivity allows electron density inhomogeneities to be maintained at the radar Bragg scales. The radar waves are then scattered by the inhomogeneities.

We support the above concept by developing a quantitative theory of ambipolar diffusion in the mesosphere. We then apply the results to isotropic turbulence and Fresnel radar scatter to show that the observed radar reflectivities can be explained by the theory. We show that the presence of realistic charged aerosols are sufficient to explain PMSE. We also show that dressed aerosol radar scatter, proposed by others as a generation mechanism for PMSE, can only apply to echoes detected by UHF radars. We present data taken with the Sondrestrom 1.29-GHz radar, which we believe to be the first PMSE event observed above one gigahertz, and attribute it to dressed aerosol scatter.

In the summer of 1991, we used the Cornell University portable radar interferometer (CUPRI) to observe the mesosphere while rockets carrying in situ sensors were flown through two PMSE occurrences and a noctilucent cloud/PMSE event. We present a selection of first results from this campaign (NLC-91). The first simultaneous height comparison between noctilucent clouds and PMSE show that the radar scattering region was near or slightly above the visible cloud layer. We also infer from aspect sensitivity measurements and Doppler spectrograms that there were two distinct types of PMSE: enhanced turbulent scatter and partial (Fresnel)

reflection from steep edges in the electron density. Both mechanisms require an anomalously low electron diffusion coefficient.

## Biographical Sketch

*Official version*: John attended Stanford University. He received a B.S. in 1985 and an M.S. in 1986, both in electrical engineering. Since 1988 he had been a doctoral candidate with the Space Plasma Physics Group at Cornell University.

*Unauthorized version*: The day after Jack Kennedy died, JYNC was born as a South Korean national in Tokyo, Japan. He began reading numbers at age one and could sing harmony at age three.

He attended an international school which was taught in English. He skipped third grade, but received a "D" in penmanship. He taught himself to read Japanese with the novels of Kita Morio.

In 1975 he emigrated to the United States and attended public schools in Tacoma, Washington. During his senior year, his high school was set on fire by a fellow student. A bond issue to build a new school was turned down by the local residents.

The college years began in 1981. He spent most of his time consuming the four basic food groups: love, literature, music, and angst. During the summers he held various stimulating jobs such as forklift operator at the Disneyland warehouse, handyman at a Best Western motel, delivery man for a florist, and assembly language programmer in Mönchengladbach, Germany. Somehow he managed to graduate in 1985 and went on to work with L. R. Owen Storey for his M.S. degree in 1986.

In 1983 he had become a U.S. citizen. This was the first time since he was born that he was a citizen of the country in which he lived.

From 1986 to 1988 he was a Peace Corps volunteer in Sierra Leone. In the first year he taught physics and mathematics at St. Francis Secondary School in Makeni. During the second year he was a lecturer in the Electrical Engineering Department at Fourah Bay College. Like the locals, the palms of his hands and the soles of his feet turned orange from eating palm oil every day.

From Africa JYNC applied to one graduate school—Cornell. Why? Probably because he associated it with some of his favorite writers like Nabokov and Pynchon.

He considered transferring to an M.F.A. program in English after getting there. In the end he decided to first give a try at being a professional scientist.

His current ambition is to become an accomplished djembe drummer.

**Acknowledgments**

Primary thanks go to my thesis adviser and special committee chairman, Mike Kelley, who was most instrumental in making my stay at Cornell (and travels abroad) productive and fun. He was an inexhaustible supply of ideas from which to choose and was very supportive of my work.

I had the great fortune of sharing an office with two esteemed bozonians: "Screamin' Phil" Erickson and "Jorge of the Pampas" Vago. Remarkably, they did not run out the room when I played Renaldo and the Loaf's "Songs for Swinging Larvae." Phil was especially helpful in solving my computer problems. Having said that, I must ask the current grad students to restrain themselves from asking him too many questions—give him a chance to write his thesis!

I thank Don Farley, also a special committee member, for imparting a great deal of lucid understanding concerning radars and other topics. We all look forward to the day when his book, *Zen and the Art of Incoherent Scatter Radar*, is published.

The successful CUPRI observations would have been impossible without Wes Swartz, its creator. The crew at Esrange constructed a fine site for the CUPRI and I thank Alf Wikström for coordinating it. Thanks go to Clark Miller for driving the 'Bago to Oslo by himself while I went off to Vienna and Prague.

My appreciation goes to the staff of the SRI Sondrestrom radar facility—Terri Dabbs, Annette and John Jørgenson, and Tom Lovelace—for their hospitality and flexibility. I am indebted to Craig Heinselman for creating the new radar modes and Bob Livingston for helping out with the data processing.

It is my pleasure to acknowledge the contribution of data to this thesis by the following people: Peter Stauning, Danish Meteorological Institute (Sondrestrom riometer); Urs Wälchli, University of Bern, and Georg Witt, Stockholm University (PAT and SLIPS). The dialogue with Urs through e-mail have been interesting and useful.

Discussions about PMSE with Ulf Hoppe (NDRE), Jürgen Röttger (EISCAT), and Jim Ulwick (Stewart Radiance Laboratory) have been very helpful. I would also like to acknowledge fruitful scientific collaborations with Tim Hall (NASA/GISS), Bernd Inhester (MPI-Aeronomy), Sheila Kirkwood (IRF), Franz-Josef Lübken (University of Bonn), and Alexander Zadorozhny (Novosibirsk State University).

I would like to thank Peter Gierasch for serving on my special committee and Steve Colucci for being his proxy at my thesis defense.

A special note of thanks must go to Sally Bird, Laurie Shelton, and Susie Swartz, without whom nothing would ever get done around here. Overall, the grad students of Space Plasma Physics have been very interesting company, from the ghost of "CUPLOT" Pingree to the latest tidal wave of new and returning students.

I send gratitude to my parents for letting me make all my own decisions starting at a very early age and for being supportive throughout my life.

Thanks go to Cynthia Nieb for her love and friendship (and all those free tickets at Cornell Cinema!) and to my erstwhile housemate, Diane Harris, to Djuna and Bob, the best cats in the world, and to the rest of the transient crew at 65 Middaugh Road. I wish the best of luck to Jen Zamon who has begun her PhD program: May the krill be with you. And to Tyler, who accompanied me on many hikes on the Finger Lakes Trail: May you rest in peace.

Finally, a big "Thank you" to 99.9999 % of the U.S. tax payers who have never heard of PMSE, but supported me financially for the past 4-1/2 years through a NASA Space Grant Fellowship and NSF grants. Trust me—it was really worth it.

# Contents

# List of Tables

# List of Figures

# Chapter 1

# Introduction

Look up "atmosphere" in the dictionary and one is liable to get a vague definition such as "**at • mos • phere** (at'mə̇s fir) *n.* [< Gr. *atmos*, vapor + *sphaira*, sphere] **1.** all the air surrounding the earth." Even a scientific textbook may begin with a nebulous "The atmosphere of a planet is the gaseous envelope surrounding it [*Houghton*, 1986]." This "gaseous envelope" has a different shape and size depending on whether one is concerned with the neutral or ionized particles that are trapped around the earth by its gravitational (exosphere) or magnetic field (magnetosphere), respectively. Fortunately, there is a consensus on how to divide our atmosphere into concentric shells according to the vertical temperature gradient (see Fig. 1.1, adapted from *Andrews et al.* [1987]). Sunlight that is not reflected by cloud cover mostly passes through the atmosphere and warms the earth's surface, which heats up the bottom of the atmosphere. Thus, the temperature decreases with height except for the stratosphere, in which the ozone layer intercepts a near-visible band of ultraviolet (UV), and the thermosphere, in which hard UV and X-rays are absorbed by ionization processes.

In this thesis we will be concerned with the mesosphere, which is a particularly difficult region of the atmosphere to observe. Much too high for airplanes and balloons, too low for orbital satellites to pass through, the only alternative for in situ sampling has been the launching of the occasional rocket. Active remote sensing from the ground has only been possible since the advent of the powerful MST (mesosphere-stratosphere-troposphere) radar [*Woodman and Guillén*, 1974], and more recently the lidar. General public awareness of the mere existence of

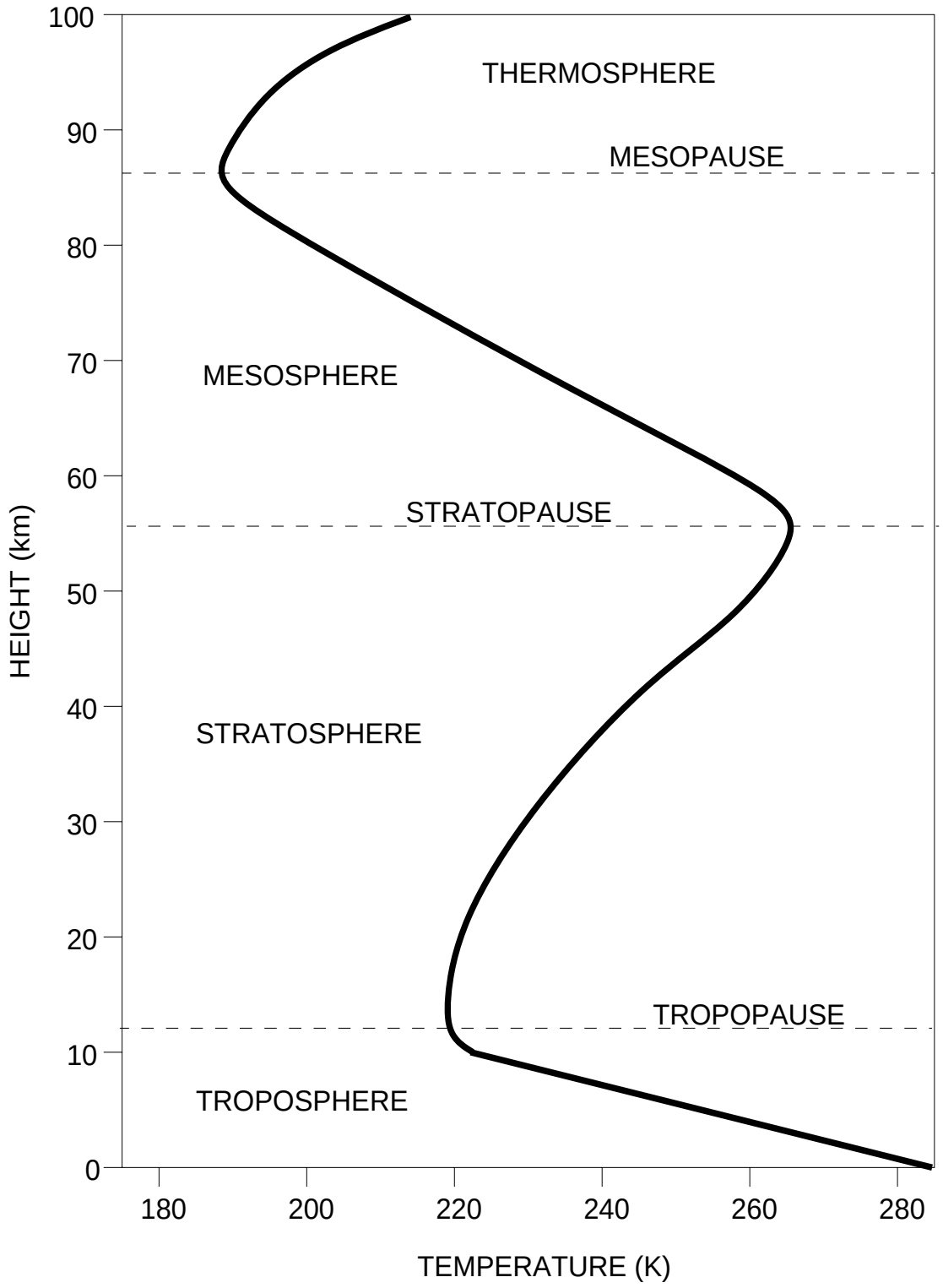


Figure 1.1: A mean, mid-latitude atmospheric temperature profile which illustrates the delineation of the different "spheres" according to the gradients. Note that the polar summer mesopause is significantly colder on the average ($\sim$ 130 K) than illustrated here.

the mesosphere is low even today, as casual conversations with the atmospherically uninitiated will attest. ("Mayzosphere? What's that—a sequel to Biosphere 2?") Even researchers in this field seem to have a hard time reaching a consensus on the pronunciation: Is it "me-zo," "me-so," "mee-zo," "mee-so," or none of the above? (We prefer "me-so" as the etymology harks back to the Greek *mesos* meaning "middle.") Because of the historical dearth of interest and information in this layer of our atmosphere, media-minded pundits have dubbed it the "ignorosphere."

The polar mesopause has always been somewhat of an exception. Ever since the summer of 1885, two years after the cataclysmic eruption of Krakatoa, gazers of the twilight sky in the arctic have been treated to occasional summer displays of "shining night clouds" that were, from the beginning, recognized as being different from other clouds [*Backhouse*, 1885]. In 1887, photographic triangulation determined the height of the clouds to be 82 km [*Jesse*, 1887*b*] and that they were blowing towards a WSW direction [*Jesse*, 1887*a*]. All of a sudden, evidence of the atmosphere, which had previously only extended up to nacreous clouds at about 30 km, more than doubled in height. Furthermore, the so-called noctilucent cloud (NLC) revealed wave and billow structures which were presumably representative of the motions of the ambient air. Interesting dynamics were going on way up there which scientists now had a way of watching. Eyes were opened and Otto Jesse in Berlin founded the first ever research program for upper atmosphere physics in 1889.

Rocket grenades launched during the international geophysical year (IGY) of 1957-58 revealed another peculiarity of the polar mesopause: it was much colder there in the summer than in the winter [*Stroud et al.*, 1959]. This observation supported speculation that the NLC were composed of ice that formed in extremely low temperatures. Subsequent studies have confirmed that summer mesopause temperatures are the lowest found in our atmosphere (temperatures below 100 K have recently been reported by *Schmidlin* [1992]).

Nearly a century after the first sighting of NLCs, another surprise awaited students of the mesosphere. Observations with a newly installed MST radar in Poker Flat, Alaska showed that the polar summer mesosphere was incredibly adept at scattering VHF radar waves [*Ecklund and Balsley*, 1981]. The enormous radar re-

flectivities could not be explained by any existing radar scattering theories. The phenomenon was so remarkable that it has earned an acronym, PMSE, which stands for polar mesosphere summer echoes [*Röttger et al.*, 1988].

Mesospheric radar echoes from non-summer seasons and non-polar latitudes are orders of magnitude smaller than the summer polar case and can be explained by electron density inhomogeneities created by turbulence in the neutral atmosphere which in turn is generated by breaking gravity waves [*Balsley et al.*, 1983; *Røyrvik and Smith*, 1984]. The same explanation cannot be directly applied to PMSE because, at the higher altitudes at which they occur, the viscous cutoff scale of the neutral air turbulence is much larger than the radar scattering length, which means that the turbulent energy would have been dissipated by viscosity without creating significant structures at the radar scattering scales. Clearly there must be something extraordinary happening in the summer polar mesosphere that drastically enhances the radar scattering process.

So three obvious questions regarding the polar summer mesosphere are: (1) Why are clouds there? (2) Why is it so cold? (3) Why do radio waves of certain wavelengths reflect so much from there?

There is a wide consensus among researchers that the clouds form precisely because of the coldness, i.e., NLCs are composed of ice particles that have condensed out of the thin air (with the help of nucleation sites such as meteoroid dust and cluster ions). The extreme cold is necessary because the water mixing ratio is expected to be very low at those altitudes. (The atmosphere is very dry above the "cold trap" of the tropopause where water tends to freeze out and not mix into the stable stratosphere.) In fact, the lack of NLC sightings in the historical record before 1885, despite the presence of skilled observers of twilight phenomena in the arctic, suggests that they were optically too thin before that time to be visible to the naked eye. *Wegener* [1912] surmised that the eruption of Krakatoa in 1883 injected enough source of water into the stratosphere for NLCs to eventually become visible. The two-year delay is consistent with the transport of material through the stratosphere and up into the mesosphere [*Schröder*, 1985].

More recently *Thomas et al.* [1989] have proposed that the anthropogenic increase in methane gas (the oxidation of which in the stratosphere is an important

source of water in the middle atmosphere) in the industrial era was responsible for the appearance of NLCs. (This claim was noticed by none other than the Vice President, and he subsequently included it in his tome on the environment as yet another example of an "unnatural" phenomenon produced by the insidious activities of humans [*Gore*, 1992].) On the other hand, *Gadsden* [1990] has countered that a decrease in the mesopause temperature would have the same effect. Systematic observations in the last two decades that have revealed an increase in the NLC occurrence frequency bolster their claims of a changing mesosphere [*Gadsden*, 1985]. We point out that *Roble and Dickinson* [1989] have predicted a cooling of the mesopause with an increase in methane and carbon dioxide using their global upper atmosphere model. Therefore, it is very likely that anthropogenic effects on both the water mixing ratio and the temperature are working together to increase the cloudiness in the summer mesopause.

The theory of why the summer mesopause is so cold has been developed by *Lindzen* [1981] and modeled by *Holton* [1983]. The short story is that the global circulation pattern in the mesosphere is one of summer to winter meridional flow, with upward motion at the summer pole cooling adiabatically and downward flow at the winter pole warming compressionally. In effect, the summer mesosphere is being cooled by a global refrigerator which counteracts the heating of the ever-present summer sun. The refrigeration pump is the breaking of gravity waves that transfer momentum to the mean flow, spinning it up at the summer pole and spinning it down at the winter pole; continuity completes the circulation cell. The sense of flow that fixes the circuit to be a refrigerator rather than a heater is determined by the fact that the breaking waves have phase velocities that are predominantly eastward in the summer and westward in the winter; these are, in turn, determined by the seasonal stratospheric zonal winds which absorb gravity waves with matching phase velocities. (See schematic shown in Fig. 1.2.) This theory is well-accepted among researchers, but the few measurements that have been made of the mean vertical velocities in the polar mesosphere conflict with the predicted values in sign and magnitude [*Balsley and Riddle*, 1984; *Meek and Manson*, 1989]. (See, however, Section 2.1.7.)

The third question regarding the polar summer mesosphere, i.e., why are radar

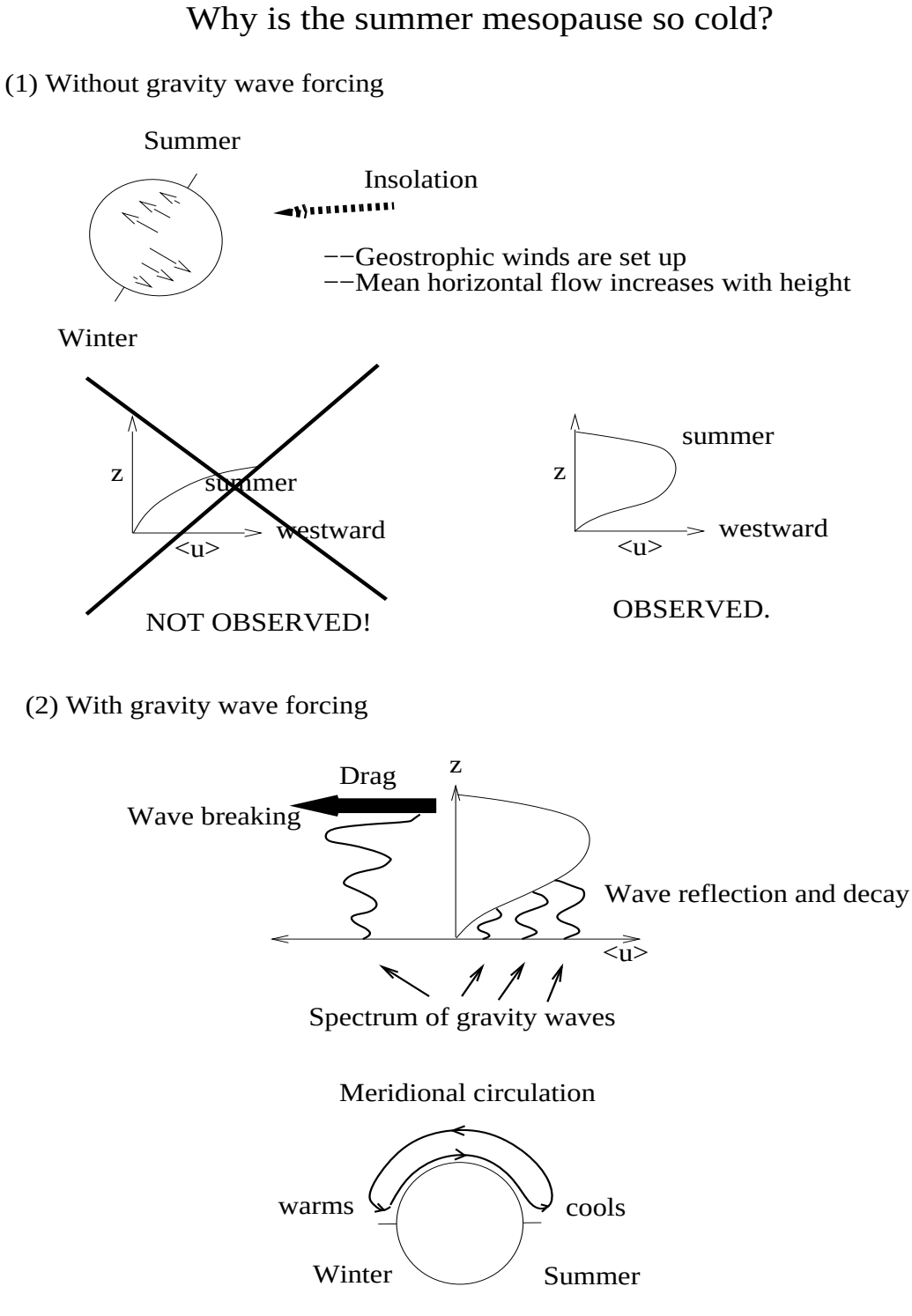


Figure 1.2: Schematic of how the summer mesopause is cooled.

waves scattered so much from there, does not have an established answer as the first two do. That is precisely the reason for writing this dissertation.

In Chapter 2 we will review the past observations and theories of PMSE, then point out that the reduced diffusivity of electrons is a key to explaining the enhancement of radar scattering in the mesosphere. Subsequently, we will develop a theory of electron diffusion in the mesosphere in Chapter 3. In Chapter 4 we will discuss our theories of PMSE genesis in which the results of Chapter 3 will figure prominently. By this time, it will be clear that the presence of charged aerosols are a crucial element in our theories, so mesospheric aerosols will be the subject of Chapter 5. In Chapters 6 and 7 we will present observational data taken with the Sondrestrom 1.29-GHz radar and the 46.9-MHz Cornell University portable radar interferometer (CUPRI). Comparisons with simultaneously taken rocket data will be included with the latter. Chapter 8 will end the thesis with a discussion of future research directions and topics.

# Chapter 2

# Review of Past Observations and Theories of PMSE

Before we can begin to present new data and ideas concerning PMSE, we need to look to the past and examine the progress that has been made in understanding this phenomenon. Fortunately, since this field is barely over a decade old, this task will take up no more than one chapter of reasonable length.

## 2.1 Observed Characteristics of PMSE

The only long-term observational data base available for PMSE is still the original Poker Flat set. It is the best source for climatological information. For higher resolution (spatially, temporally, and spectrally), data from radars that have been operated on campaign bases are available. Among those radars, a distinction should be made between VHF studies (Aberystwyth, CUPRI, European incoherent scatter (EISCAT) 224-MHz, Poker Flat, SOUSY) and UHF studies (EISCAT 933-MHz, Sondrestrom), since at the UHF frequencies PMSE are much rarer and weaker. Interferometry information is available for some of the EISCAT VHF and CUPRI data, and three-dimensional velocities (using multi-beam configurations) were measured by the Poker Flat and SOUSY radars.

### 2.1.1 Climatology

Both the long-term Poker Flat data and the shorter sets from other radars show that important features such as height of occurrence remain stable from year to year. Fig. 2.1 shows PMSE over Alaska (as marked by echoes at the higher altitudes) beginning in late May and ending in late August; the transitions at both ends are fairly abrupt (from *Ecklund and Balsley* [1981]). *Balsley et al.* [1983] showed that the transition periods correspond well to the reversal of mean zonal winds in the stratosphere and lower mesosphere. This is significant because these background horizontal motions act as a phase velocity filter on upward-propagating gravity waves and determine the heights at which they begin to break. The mesospheric seasonal circulation theory developed by *Lindzen* [1981] directly links this process to the cooling of the summer mesopause. The season of noctilucent cloud (NLC) occurrence [*Gadsden*, 1982] is also very similar to the PMSE season. We know that an extremely low temperature is one of the necessary conditions for the formation of noctilucent clouds. It seems likely that PMSE also require low temperatures.

PMSE have been observed from as far north as Tromsø, Norway (69° 35' N) [*Hoppe et al.*, 1988], and as far south as the Harz mountains of Germany (52° N) [*Reid et al.*, 1989] and Aberystwyth, Wales (52.4° N) [*Thomas et al.*, 1992]. (Echoes of the latter type are technically MSE since they are no longer in the polar region.) Radars operating further south have not observed PMSE-like phenomena. (Observations by a 2.9-MHz radar at Scott Base, Antarctica (78° S) have not exhibited the peculiar echo characteristics [*Fraser and Khan*, 1990], but neither have data from the 2.78-MHz partial reflection experiment (PRE) radar in Tromsø [*Hoppe et al.*, 1990]. As far as we know, no attempt has been made to detect PMSE in the Antarctic using a VHF radar.) Once again coldness could be the key factor since the mesopause temperature increases as one moves from the summer toward the winter pole. Noctilucent clouds also are rarely observed below about 50° in latitude [*Fogle*, 1966]. (Note that optical observation of these clouds is not possible above $\sim 70°$ latitude. This is because the clouds are so tenuous that the sun must dip at least 6° below the horizon such that the sky has darkened considerably but the clouds are still lit from below. It follows, then, that even within the latitudes of optimal observational conditions noctilucent clouds can only be seen during a

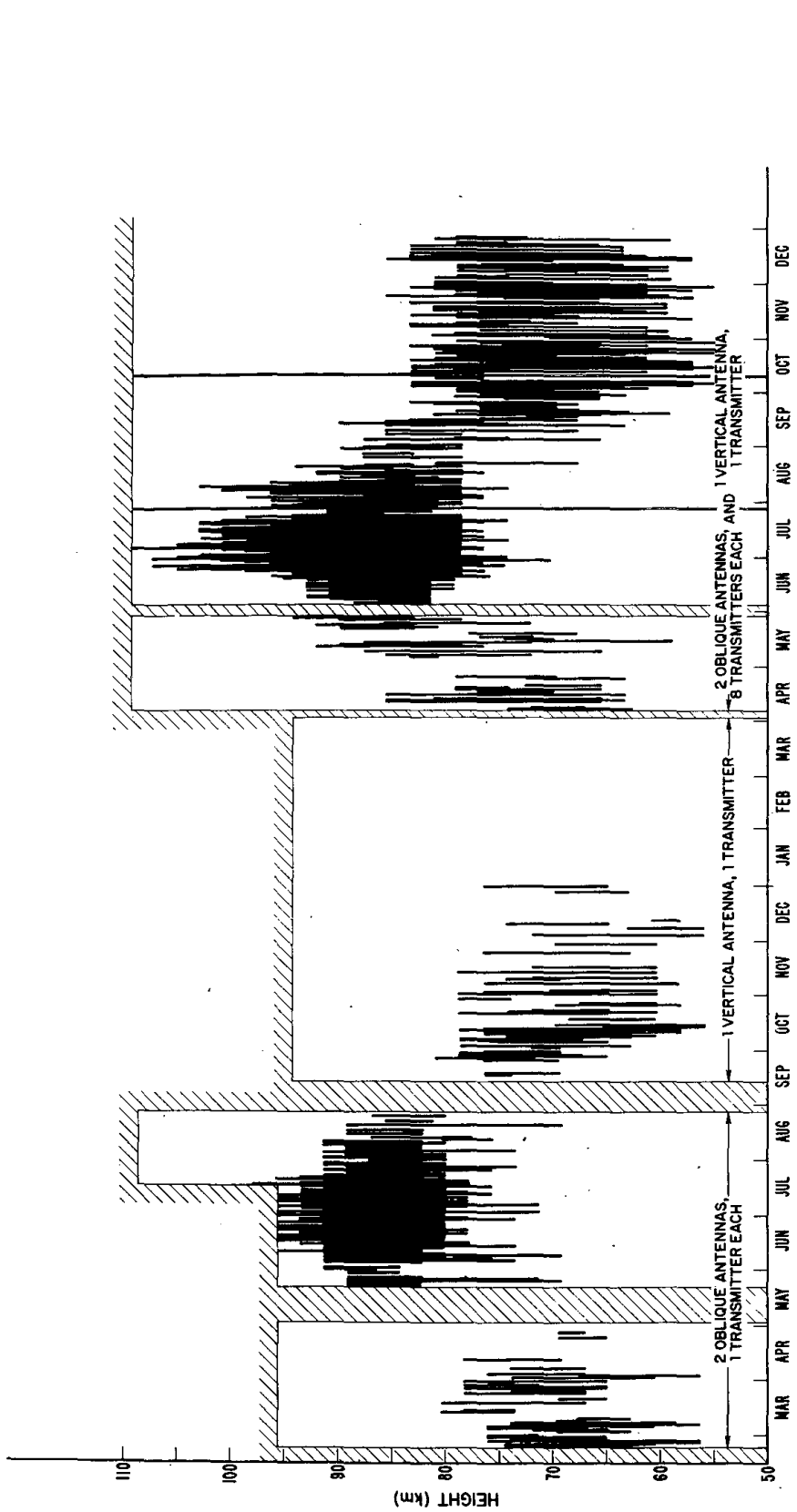


Figure 2.1: The altitude vs. season distribution of mesospheric radar echoes observed by the Poker Flat, Alaska system. Hatching indicates no datadensity data from (left) polar summer, (center) polar winter, data.

small time window during twilight.)

Since 1972 [*Donahue et al.*, 1972] satellites have been observing thin scattering layers in the polar summer mesopause. Dubbed polar mesospheric clouds (PMCs), they form patches that extend over the entire summer polar cap. Extensive measurements made by the solar mesosphere explorer (SME) satellite between 1982 and 1986 [*Olivero and Thomas*, 1986; *Thomas and Olivero*, 1989] have generally supported the contention that PMCs and NLCs are manifestations of the same phenomenon. Some differences do exist, however. A comparison of arctic PMCs and NLCs showed that the southern border of the latter was typically located about 10° below the southern border of the former [*Gadsden and Schröder*, 1989]. Also, the average cloud particle radius has been measured to be less than 0.06 $\mu$m for PMCs [*Thomas and McKay*, 1985], whereas ground-based observations of NLCs have yielded values as high as 0.3 $\mu$m [*Gadsden*, 1975]. These apparent differences suggest an interpretation of PMCs as a "nursery" of NLCs [*Gadsden and Schröder*, 1989]. NLCs may consist of large particles that occasionally develop from the embryonic PMC aerosols and are blown equatorward by the prevailing winds. Whatever the precise situation is, in this thesis we will simply refer to the clouds as NLCs in keeping with the more historical nomenclature.

Although it is tempting to postulate a link between the clouds and the radar echoes, a one-to-one correspondence is immediately ruled out since NLCs occur during only a small fraction of the time that PMSE are observed. *Taylor et al.* [1989] have even observed a case where NLC was present without PMSE, and the comparisons between the EISCAT VHF radar, CUPRI, and ground-based visual observations of NLC during the summer of 1991 showed no correlation between PMSE and NLC occurrence (S. Kirkwood, private communication). On the other hand, *Jensen et al.* [1988] have measured a weak correlation between Poker Flat PMSE and satellite UV observations, and in one instance rocket-borne instruments detected an NLC layer near the CUPRI radar volume which also registered PMSE simultaneously *Wälchli et al.* [1993] (this result will be presented and discussed in Chapter 7). To explain these ambiguous results, it may be argued that subvisible particles may be present even when clouds are not seen from the ground. Furthermore, from the ground NLCs are only observable after sunset and before

dawn, and only early and late in the summer season when the solar ionization rate is low, when fewer electrons are available for radar scattering. A theory of how aerosols influence the radar echoes will be discussed in Chapter 4.

### 2.1.2 Morphology and Temporal Variability

The Poker Flat data showed that PMSE occur in a well-defined layer between 80 and 93 km with a peak around 86 km (see Fig. 2.2) [*Ecklund and Balsley*, 1981]. These statistics are closely matched by the SOUSY 53.5-MHz radar data taken from Andøya, Norway [*Czechowsky et al.*, 1989], by the EISCAT 224-MHz radar data taken from Tromsø, Norway [*Hoppe et al.*, 1990], and by the CUPRI 46.9-MHz radar data taken also from Tromsø [*Röttger et al.*, 1990*b*]. In comparison, the average mesopause height measured in the vicinity of the SOUSY radar volume in the summer of 1987 was slightly higher at 88 km [*von Zahn and Meyer*, 1989]. The mean altitude of NLCs is 83 km [*Gadsden and Schröder*, 1989], so it appears that PMSE generally reside between the two other polar summer phenomena.

Individual scattering layers can be thinner than the height resolution of the various radars (at times even less than 100 m according to frequency-domain interferometry analysis by *Franke et al.* [1992]) and multiple layers can occur simultaneously.

Echo power fluctuations within a minute or less are usually unrelated vertically and, therefore, not caused by particle precipitation [*Röttger et al.*, 1988]. Both *Luhmann et al.* [1983] and *Czechowsky et al.* [1989] report a low correlation between PMSE power and the ambient electron density level, whereas they show that the winter echoes are highly dependent on precipitation events. The short-term variability in the summer is thought to be the result of "blobs" or "crinkled" layers being advected horizontally through the radar volume. In general, ionization enhancement due to precipitation can further "illuminate" already existing PMSE layers such that the overall signal increases. However, the baseline solar ionization level during the summer seems to provide enough electron density around the clock such that observation of PMSE is independent of extra electrons produced by precipitation events (at least for the more sensitive radars).

Semidiurnal variations in the echo power intensity were observed by *Czechowsky*

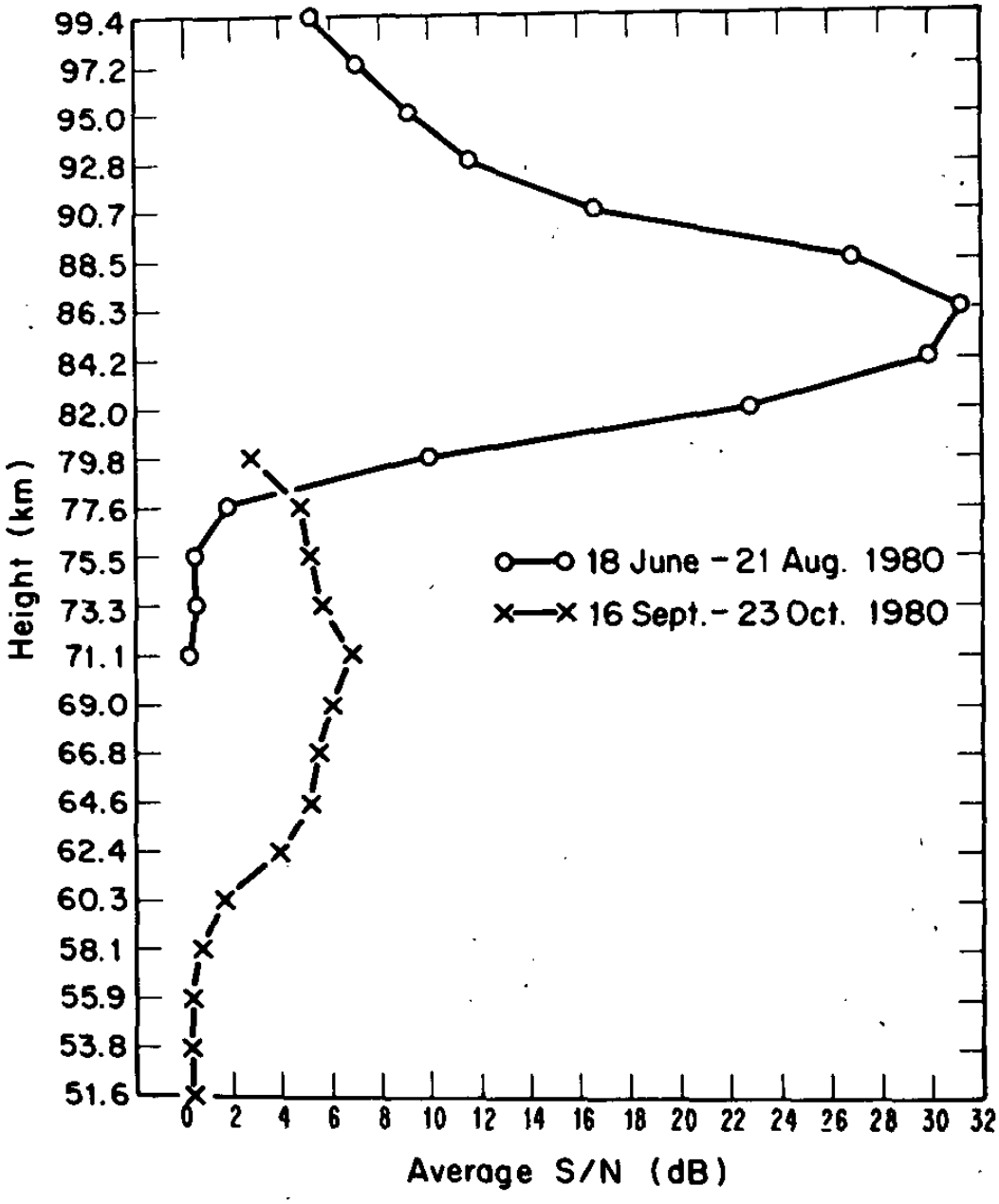


Figure 2.2: Time-averaged altitude profiles of signal-to-noise ratio for typical summer and winter periods from the Poker Flat radar.

*et al.* [1989]. Diurnal variations in the echo intensity were also observed in the long-term average of *Balsley et al.* [1983], which showed a significant dip in power around 2200 LT. *Fritts* [1988] showed a case where the regions of maximum radar backscatter matched the progression of the most unstable phase of a 7-hour wave inferred from the temperature and velocity data (see Fig. 2.3). However, *Czechowsky et al.* [1989] noted that, in their data set, regions of maximum wind shear were not always correlated with areas of largest echo return (see Fig. 2.4).

Overall, regions of strong echoes more often appear to drift downward (with velocities on the order of 1 m/s) rather than upward [*Balsley et al.*, 1983]. Since the phase velocity of gravity waves and tides have downward components, the observations suggest that the radar scattering regions correspond to a certain phase of the waves, such as maximum instability (turbulence generation) or maximum upward velocity. Correlation of the latter to echo power has been observed by *Williams et al.* [1989] during one observation period, but such a correspondence does not always hold.

Short-period gravity waves are also often observed. *Röttger et al.* [1990*a*] have noted frequent examples of steepening and tilting of Doppler velocity wave structures which imply a nonlinear transfer of energy from the fundamental wave frequency to higher harmonics. The amplitudes of gravity waves that travel up into this altitude region can become large enough to start breaking. Observations often show that the waves maintain a constant amplitude with altitude, thus supporting the idea that the waves go into a state of saturation, i.e., shedding just enough energy into turbulence to maintain a constant amplitude. (Cases have been observed, however, in which steepened waves continued to grow in amplitude through the PMSE region, thus not generating much turbulence, and only reaching saturation at higher altitudes. The height regime of saturation may be dependent on the background shear field set up by the longer period modes.) Also, there can be abrupt jumps in the Doppler spectra. *Röttger et al.* [1990*a*] attributed this phenomenon to a thin scattering layer being advected vertically by a steepened wave. This idea was further supported by a frequency-domain interferometry analysis by *Franke et al.* [1992] and a two-beam experiment by *van Eyken et al.* [1991].

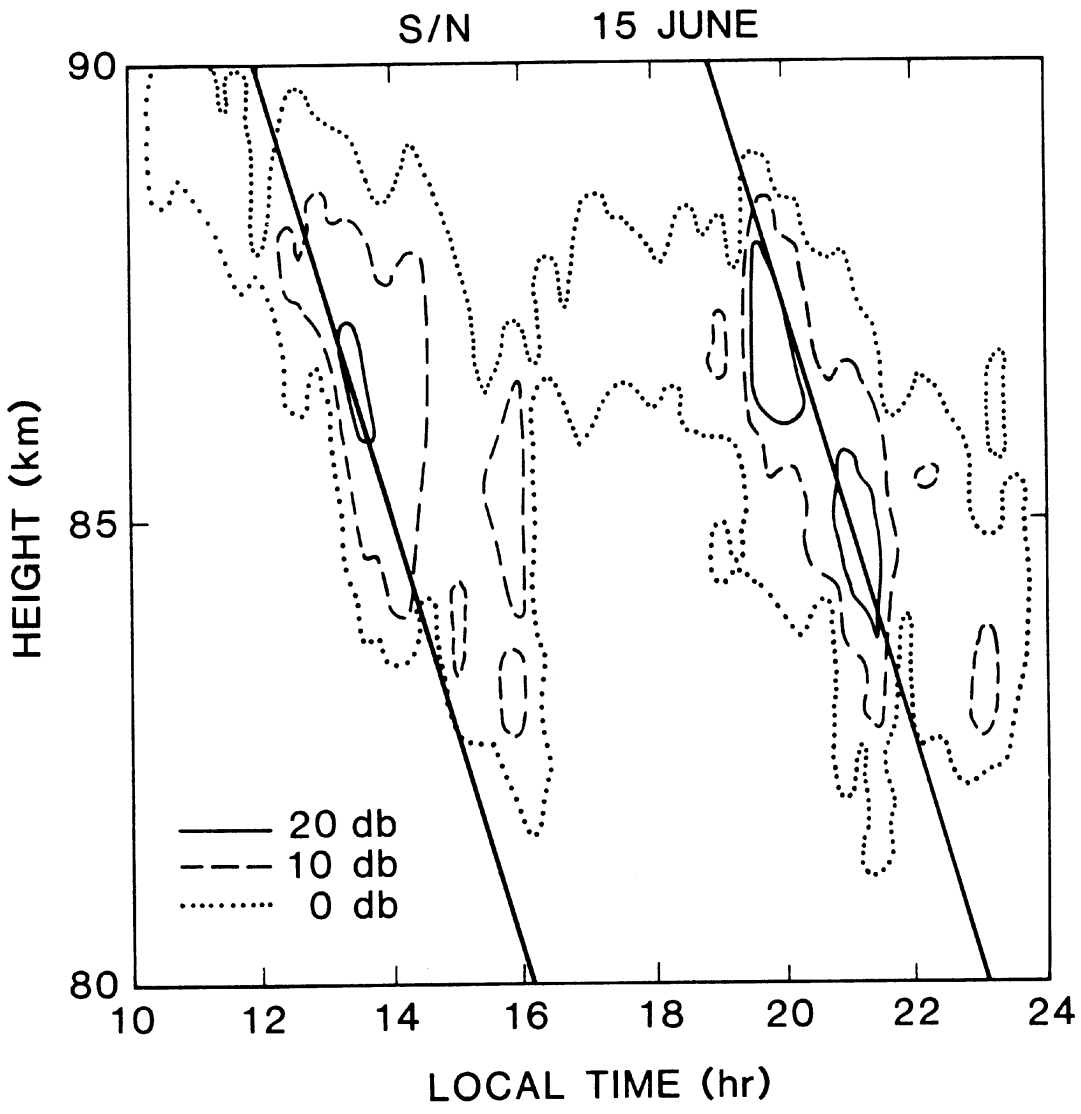


Figure 2.3: A contour plot of the Poker Flat radar signal-to-noise ratio vs. height and time from 1983. The sloped lines correspond to the most unstable phase of a 7-hour wave inferred from temperature and velocity data.

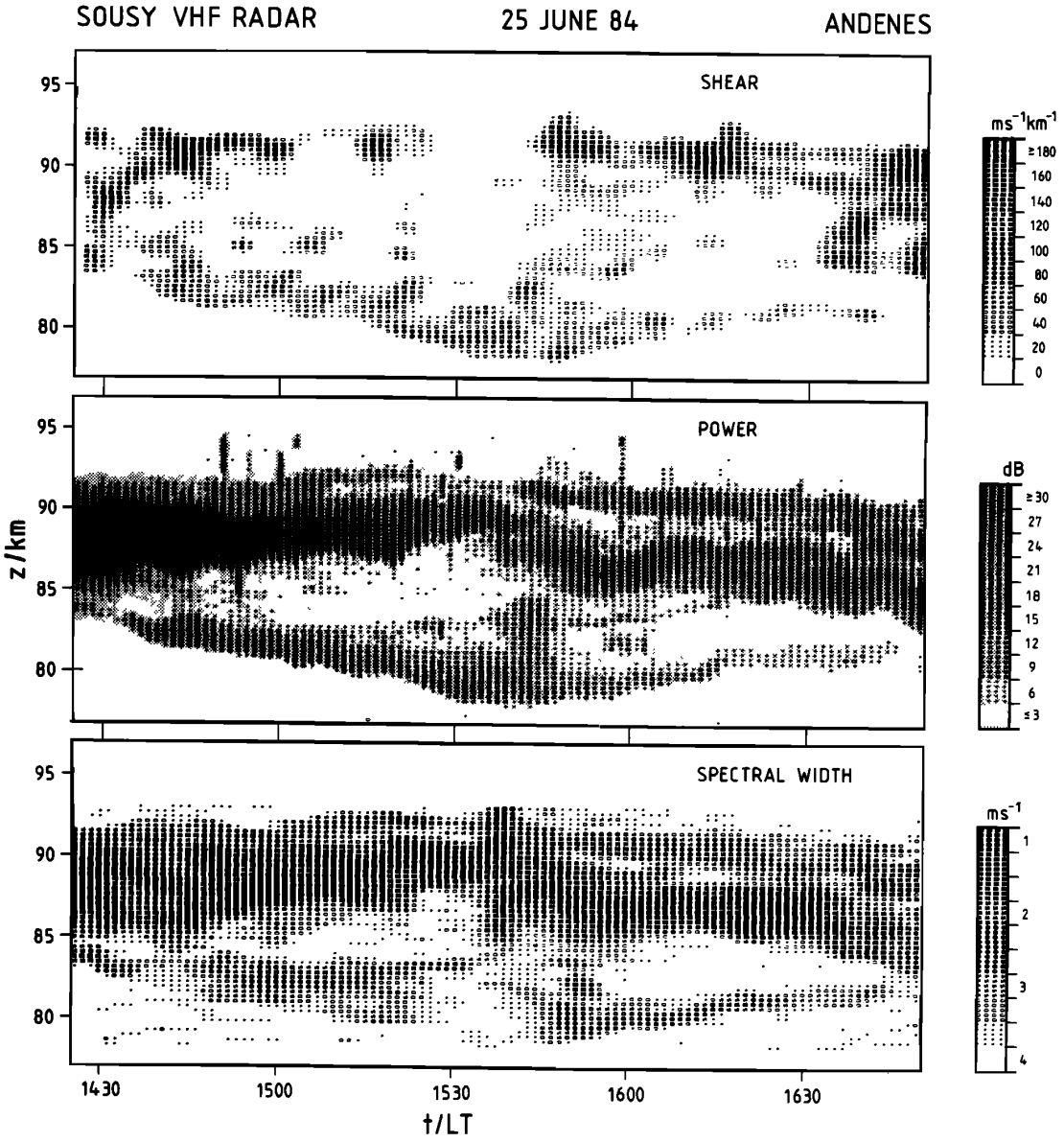


Figure 2.4: Plots of wind shear, echo power, and Doppler spectral width versus height and time as observed by the SOUSY radar.

### 2.1.3 Dependence on Radar Frequency

Because the inner scale of the neutral gas turbulence is on the order of tens of meters, it was surprising enough that a 50-MHz (3-m Bragg scatter length) radar would detect such huge echoes from the mesosphere. That the EISCAT 224-MHz radar could observe PMSE [*Hoppe et al.*, 1988] was even more astounding, even though it had been suggested by *Kelley et al.* [1987]. And then, even more improbably, an observation was made by the EISCAT 933-MHz radar [*Röttger et al.*, 1990*b*]. Observations made with the Sondrestrom 1.29-GHz radar [*Cho et al.*, 1992*b*] will be the topic of Chapter 6. Radar scattering which was thought to be highly unlikely at a Bragg scale of 3 m had now been seen at 12 cm.

Simultaneous observations by the CUPRI 46.9-MHz and the EISCAT 224-MHz radars revealed that the evolution and spatial structures of PMSE at those frequencies were very similar [*Hall*, 1991]. Thus, the same radar scattering mechanism is likely to be producing PMSE at those frequencies.

*Röttger et al.* [1990*b*] compared data taken simultaneously with the 46.9-MHz CUPRI and the 933-MHz EISCAT radar (see Fig. 2.5). At the higher frequency, the EISCAT radar is normally expected to detect only incoherent scatter with the echo power dependent almost solely on the electron density. In the period studied, at first the normal incoherent scatter dominated at 933 MHz and the EISCAT data corresponded to electron density, while the CUPRI profile showed an obvious PMSE layer. There was also a depletion in the EISCAT electron density profile at 85 km that corresponded to the peak in the CUPRI signal-to-noise ratio. Such "bite-outs" have also been measured by rocket probes (see the subsection "Comparison with Rocket Measurements" below). Then a peak in the EISCAT power profile developed in the altitude region of the CUPRI PMSE. This layer observed at UHF had a Doppler spectral width much narrower than the incoherent scatter spectra in the other range gates, indicating that the echo power enhancement was not simply due to a thin slab of extra electrons (which, in any case, would be almost impossible to explain with known electron generation mechanisms), but a manifestation of PMSE which may or may not be produced by the mechanism that causes the VHF PMSE.

It should also be noted that a simultaneous, co-located operation of the partial

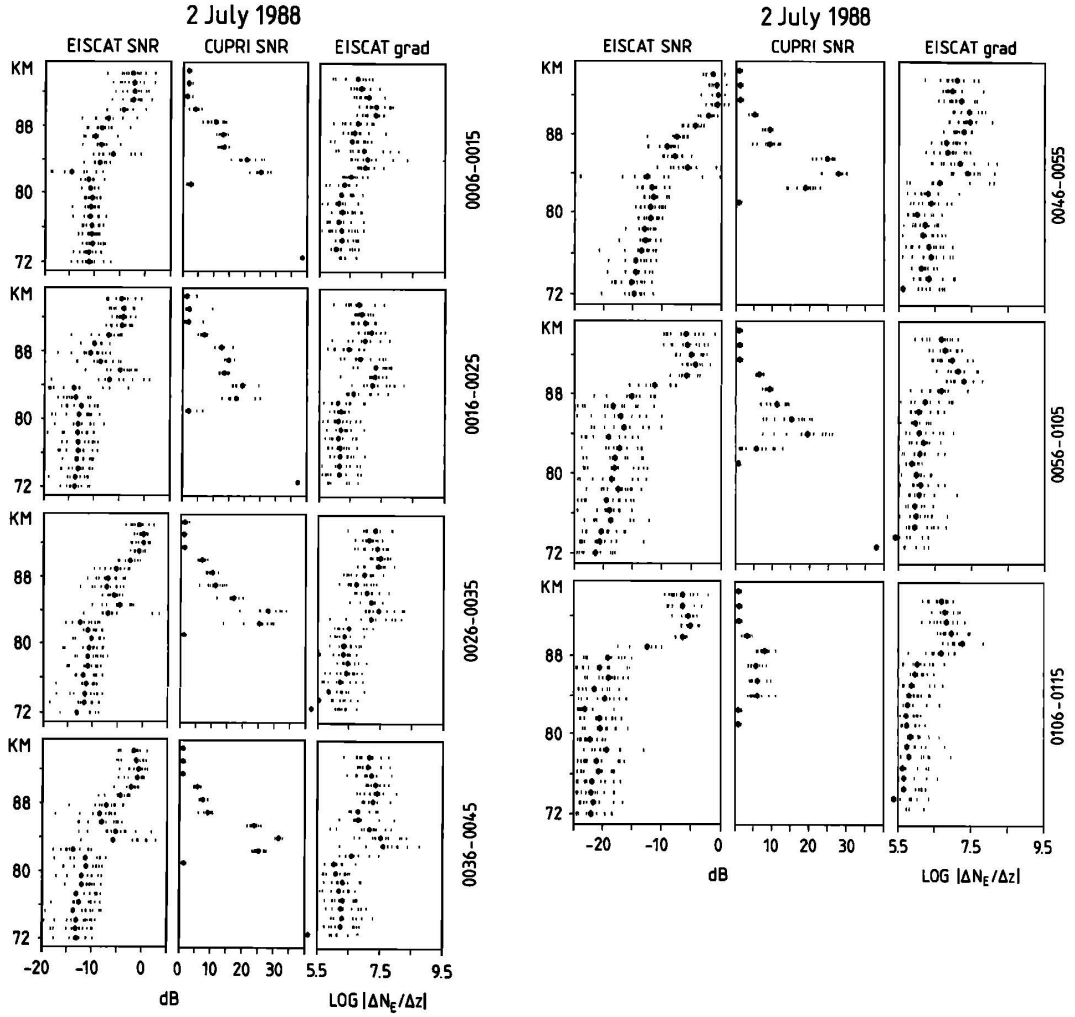


Figure 2.5: Signal-to-noise ratio versus height for the EISCAT 933-MHz radar (left columns) and the CUPRI 46.9-MHz radar (center columns), and the vertical gradient of the EISCAT-inferred electron density in units of $m^{-4}$ versus height (right columns). The small dots are averaged over 1 min, and the large dots are averaged for the indicated time per panel.

reflection experiment (PRE) 2.78-MHz (54-m Bragg scale) radar with the EISCAT VHF radar showed no correlation between the echoes observed by the two systems [*Hoppe et al.*, 1990], and a longer PRE data set from the summer did not reveal the characteristics of PMSE [*Schlegel et al.*, 1978]. On the other hand, the PRE operated in Tumanny, Russia by *Vlaskov et al.* [1992] recorded a sharp peak in the inferred electron density profile at the same time that the EISCAT VHF radar in Tromsø observed PMSE. The technique used for the PRE data in the calculation of electron density was the comparison of partially reflected O and X-mode amplitudes to the theoretical reflection coefficients developed by *Gardner and Pawsey* [1953]. It is not clear whether the electron density enhancement was real or the product of the technique which depended also on the electron-neutral collision frequency and electron gyrofrequency. It is, however, another indication that something peculiar is happening in the polar summer mesopause.

### 2.1.4 Spectral Width

One of the first things to be gleaned from the PMSE Doppler data was that the spectral widths were too narrow for classic incoherent scatter at both VHF [*Röttger et al.*, 1988] and UHF [*Röttger et al.*, 1990*b*]. Thus, PMSE were shown to be coherent echoes from this perspective as well as from echo strength considerations.

The spectral widths from coherent scatter radars can yield information regarding the scatter/reflection mechanism. In short, radar scatter from a turbulent medium corresponds to a narrow spectrum (compared with incoherent scatter) with a width which is correlated with the turbulence energy. (This is a simplified explanation since other spectral broadening factors must be taken into account before the extraction of turbulence information from the spectral width [*Hocking*, 1985].) Fresnel reflection/scatter generally produces a narrower spectrum than turbulent scatter and points to a horizontally coherent medium. Observations with the EISCAT VHF [*Röttger and La Hoz*, 1990] (see Fig. 2.6), SOUSY [*Czechowsky et al.*, 1989], and CUPRI all show little correlation between echo power and spectral width, thus implying that the echo strength of PMSE is not primarily modulated by the turbulence intensity.

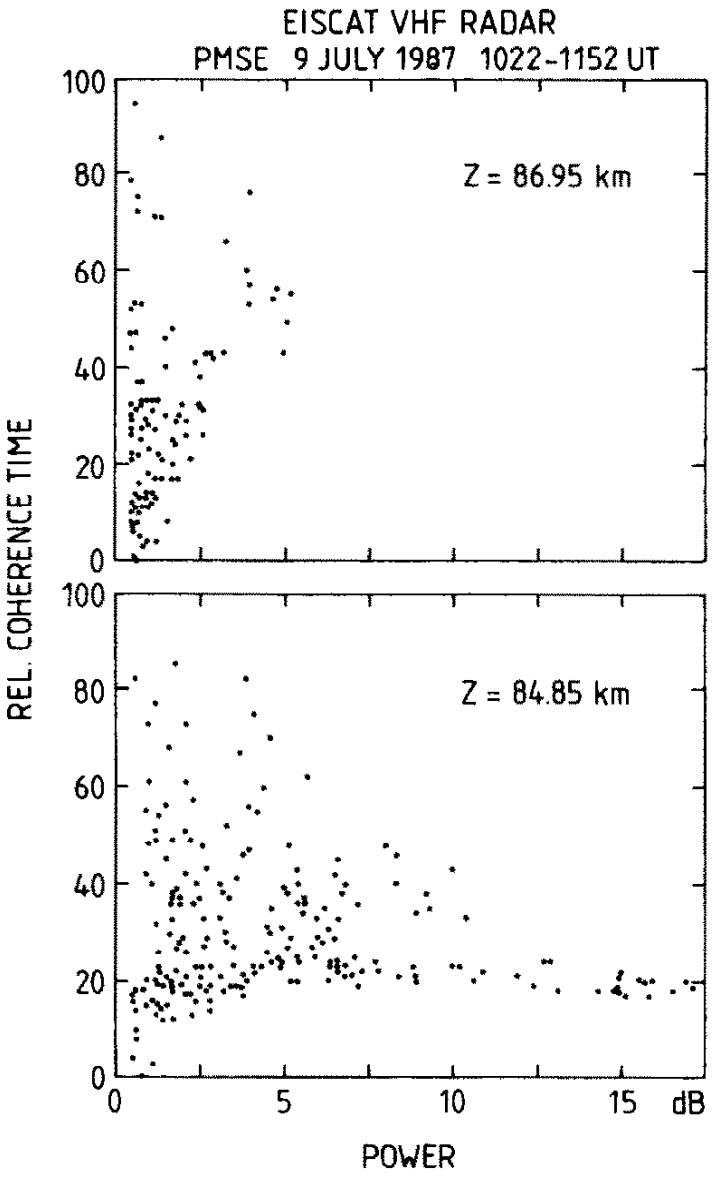


Figure 2.6: EISCAT VHF scatter plots of coherence time versus echo power. Each dot is a 30-s average. Units of coherence is $10^{-2}$ s.

### 2.1.5 Aspect Sensitivity

Another piece of evidence for the complexity of the echoing process is the dependence of the echo power on the pointing direction of the radar beam. *Czechowsky et al.* [1988] noted that the backscattered signal level at 50 MHz decreased for antenna beams pointed away from the vertical (see Fig. 2.7). If intense turbulence were responsible for the radar echoes, one would expect the scattering structure to be isotropic, and hence the scattered power should not depend on the direction of the radar beam. Because the aspect sensitivity is centered around the vertical, i.e., gravitational, axis and since the echo structures are horizontally layered, one can infer that stratification plays an important role in the formation of PMSE layers and their scattering properties.

### 2.1.6 Comparison with Rocket Measurements

There have been three major radar/rocket campaigns in the polar summer mesosphere: the structure and atmospheric turbulence environment (STATE) in 1983, the middle atmosphere cooperation/summer in northern Europe (MAC/SINE) in 1987, and the noctilucent cloud-91 (NLC-91) in 1991. Papers from the first campaign were printed in the June 20, 1988 issue of *J. Geophys. Res.*, articles from the second were published in a special issue (October/November 1990) of *J. Atmos. Terr. Phys.*, and reports from the third will be collected in future issues of *Geophys. Res. Lett.* and *J. Atmos. Terr. Phys.* Chapter 7 will also contain some first results from the NLC-91 campaign.

The first rocket probe measurements of electron density simultaneous with VHF polar radar data [*Ulwick et al.*, 1988] revealed two important clues to the PMSE puzzle: (1) The electron density was, in fact, structuring at length scales well below the viscous cutoff of the neutral gas [*Kelley and Ulwick*, 1988; *Kelley et al.*, 1990], unlike in the case of the non-summer mesosphere [*Blix*, 1988] or the equatorial mesosphere [*Røyrvik and Smith*, 1984] where the electron density fluctuations decayed rapidly beyond the viscous cutoff (see Fig. 2.8). (2) Sharp depletions or "bite-outs" were often present at the altitudes of the echo layers [*Kelley and Ulwick*, 1988; *Inhester et al.*, 1990] (see Fig. 2.9).

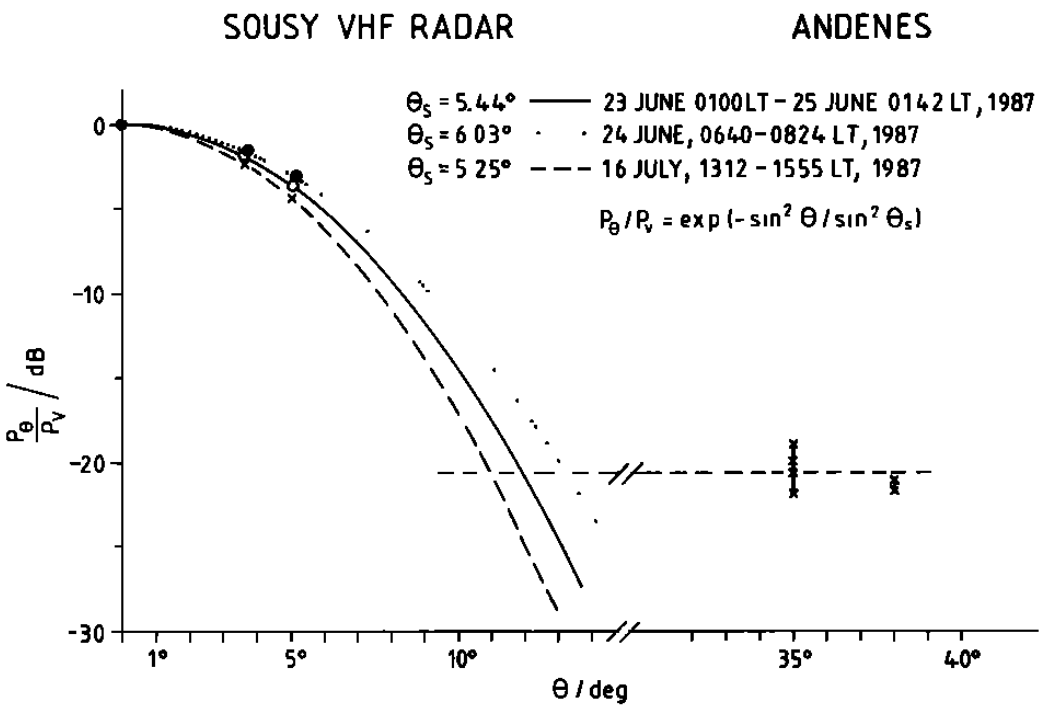


Figure 2.7: Plots of backscattered power relative to that received in the vertical beam as a function of zenith angle for three different periods.

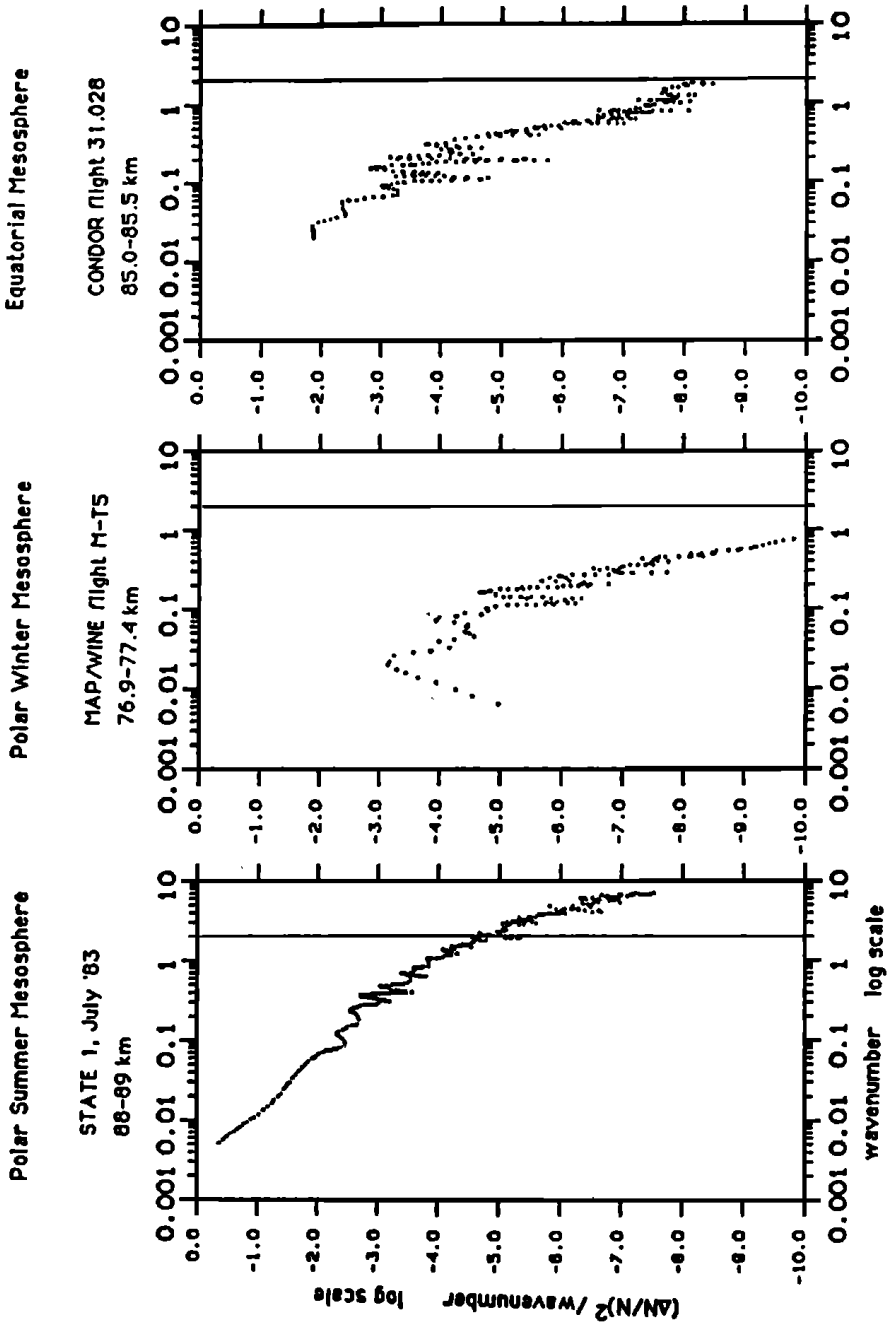


Figure 2.8: Comparison of mesospheric electron density data from (left) polar summer, (center) polar winter, and (right) equatorial rocket launches. The vertical line corresponds to the Bragg wavenumber of a 50-MHz radar.

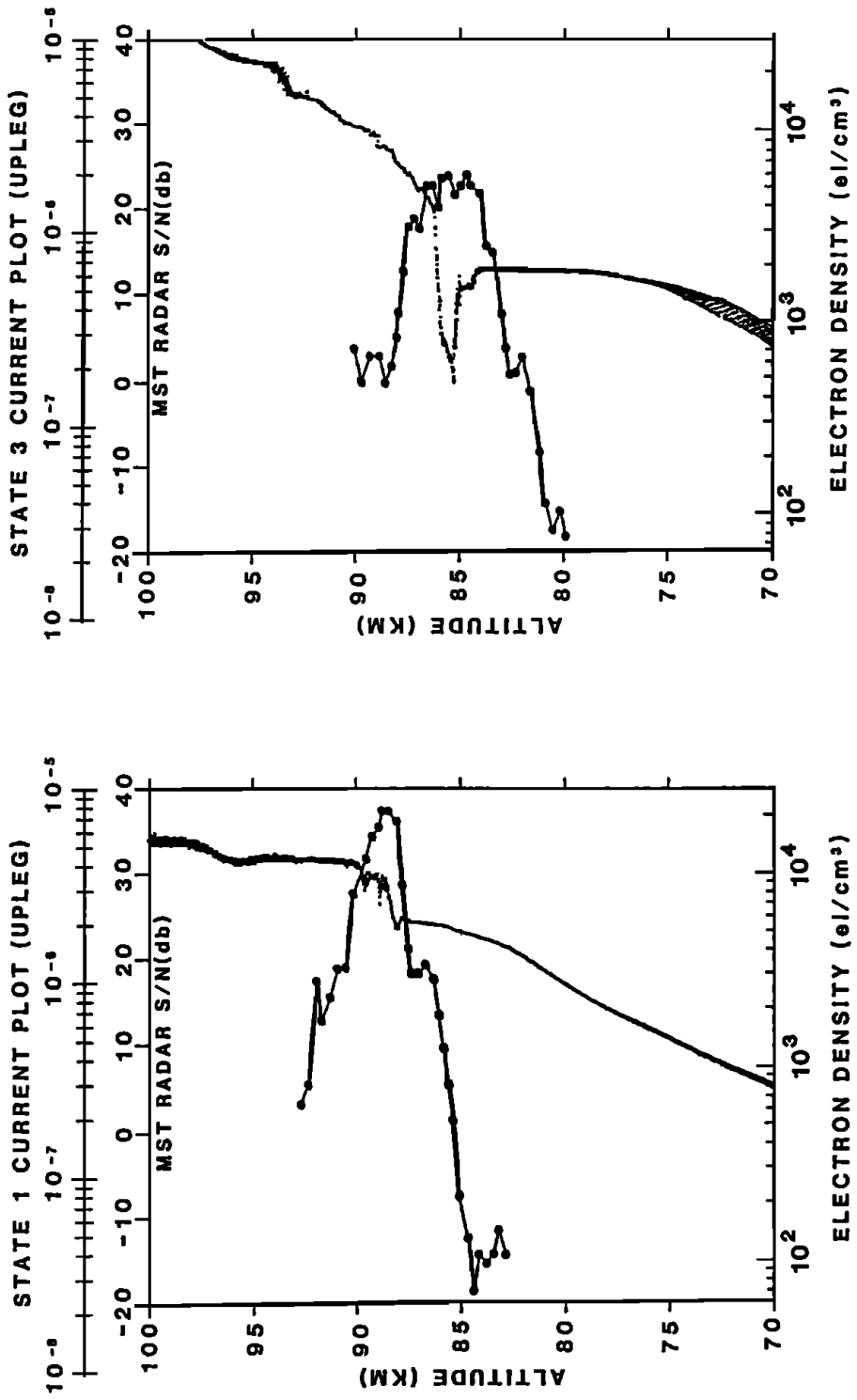


Figure 2.9: Electron density profiles for the two rocket experiments of the STATE campaign. The connected-dot profiles are the backscattered signal detected by the Poker Flat radar.

Result (1) meant that radar reflectivities calculated directly from the rocket-derived electron density fluctuation power spectra, using isotropic turbulent scatter theory, agreed reasonably well with the actual radar results [*Ulwick et al.*, 1988] (see Fig. 2.10). Thus, the suspicion was shifted from the radar backscatter theory to the assumption that the electrons were behaving as perfectly passive tracers of the neutral gas, a theory which indeed gives excellent quantitative agreement with equatorial mesosphere echo strength [*Røyrvik and Smith*, 1984]. This assumption had seemed reasonable in the past since the number of electrons are about $10^{-10}$ of the neutrals. Clearly there is some other factor that is keeping the electrons from simply mimicking the structure of the neutral gas.

Result (2) suggested that sharp gradients in the electron density were an important factor in producing the radar echo layers and may help to explain their aspect sensitivity. Once again, the mystery centers on the mechanisms that could generate and maintain such sharp "bite-outs" in the electron density. These abrupt depletions may signal the presence of a layer of aerosols that scavenge the ambient electrons.

### 2.1.7 Mean Vertical Velocity

Finally we come to one last piece of strange behavior as observed by the radars: the mean vertical velocity measured during the summer is substantially downward ($\sim$ 20–30 cm/s) [*Balsley and Riddle*, 1984; *Meek and Manson*, 1989] in opposition to the theoretical requirement that the summer polar mesosphere be flowing upward in order to cool it down to the observed temperatures that are far below the radiative equilibrium values [*Lindzen*, 1981]. Theories predict a circulation pattern in the summer of an upward velocity of $\sim$ 1 cm/s, an equatorward meridional flow, and a westward zonal mean flow [*Holton*, 1983]. The latter two conditions were observed by the radar, but the upward flow was not measured (see Fig. 2.11, from *Hall* [1991]). In fact, the winter values (which should be downward) appear to be slightly in the opposite direction to the theoretical prediction also. Shorter data sets taken by the CUPRI in northern Scandinavia have also yielded a mean downward velocity in the summer [*Hall*, 1991]. A longer CUPRI data set will be analyzed and discussed in Chapter 7.

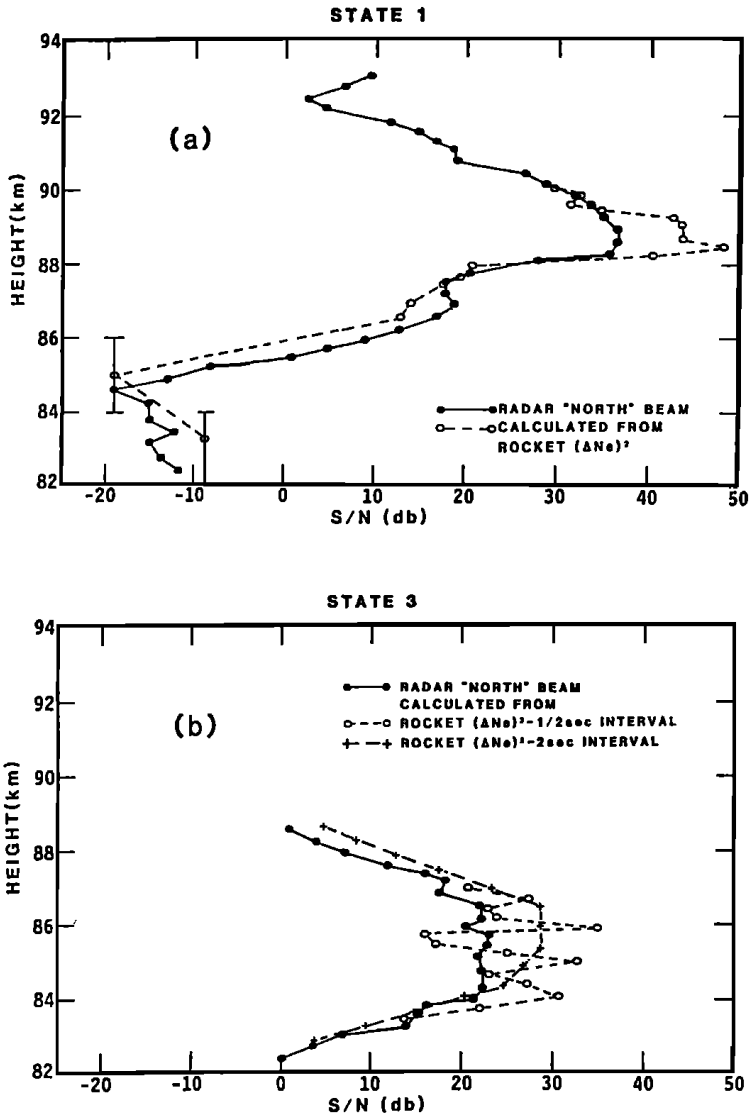


Figure 2.10: Comparison of the signal-to-noise observed by the Poker Flat radar and that calculated (using isotropic turbulent scatter theory) from the electron density fluctuation power measured by rocket probes.

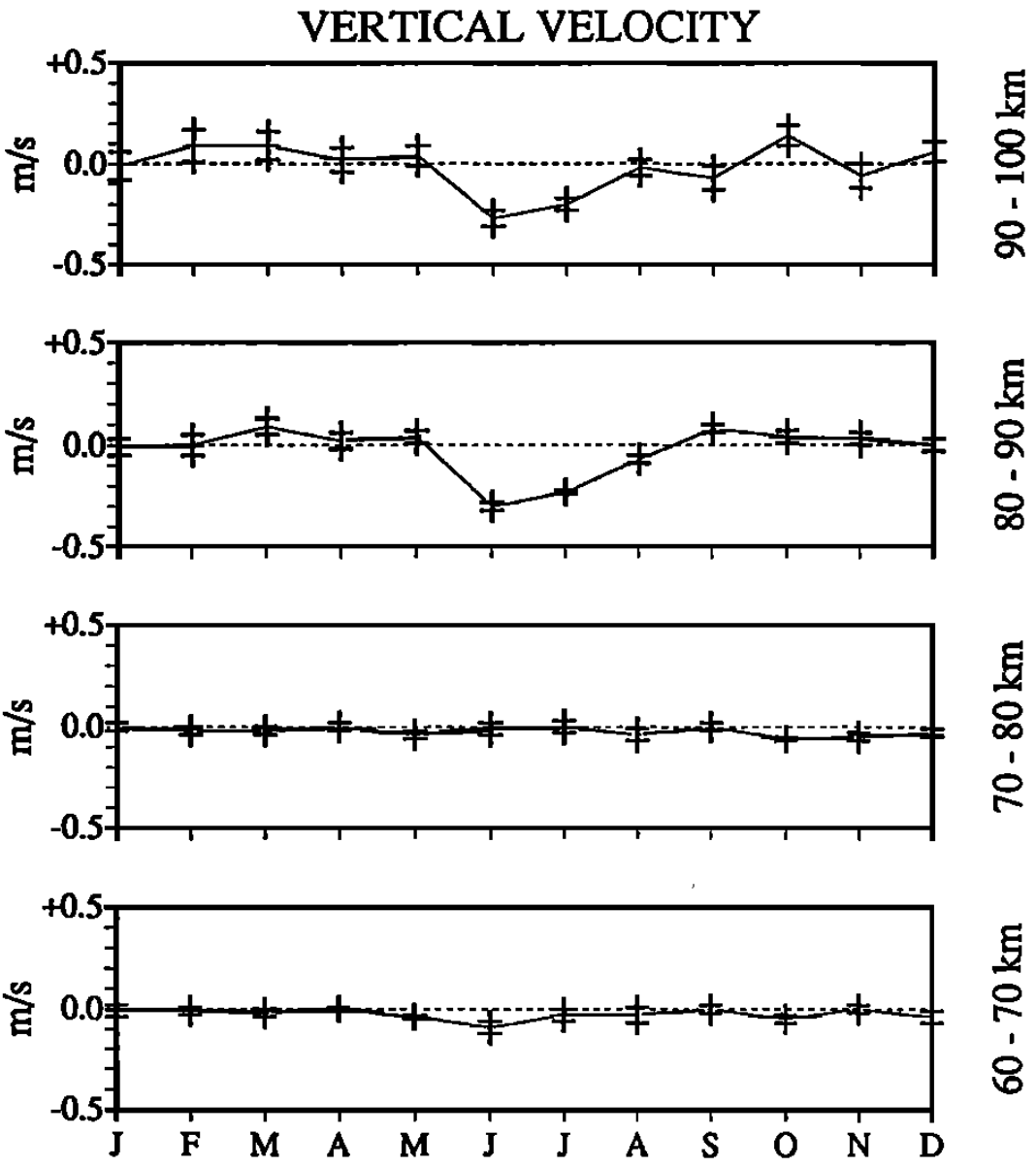


Figure 2.11: Monthly means of mesospheric vertical velocity calculated from over 4 years of Poker Flat radar data.

A second-order, compressional gravity wave effect called the Stokes drift was invoked by *Coy et al.* [1986] to reconcile the measurements with theory. However, this mechanism is not seasonally dependent and cannot account for the fact that large downward velocities are not observed in the winter as well as the summer. Moreover, *Hall et al.* [1992] showed that the Stokes drift would be about an order of magnitude smaller than the measured mean velocity for a realistic spectrum of gravity waves rather than the monochromatic wave used by *Coy et al.* [1986].

*Hall* [1991] also considered the effect of tilted scattering layers advected by horizontal winds projecting an apparent vertical velocity onto the radar Doppler measurement. He rejected this idea after failing to find evidence for a correlation between the preferred gravity wave horizontal propagation direction and the mean horizontal velocity vector in the Poker Flat data.

*Stitt and Kudeki* [1991] suggested that the distortion of waveforms in large-amplitude gravity waves can cause preferential sampling of certain phases of the velocity field. In general, velocity measurements by MST radars in the presence of waves is currently a topic of active debate. A more quantitative study needs to be conducted to evaluate whether such effects are important in the case of PMSE.

In Chapter 5 we will discuss another alternative explanation for the observed summer downward flow which ties into the theory of PMSE production which will be the topic of Chapter 4.

### 2.1.8 Summary of Observations

We list below a summary of the pertinent points from the observations.

(1) In the polar summer mesosphere, the VHF radar cross sections are enormously enhanced relative to those in other seasons and latitudes.

(2) Rocket measurements show that, in the PMSE layers, the electron density has structures well below the viscous cutoff length scale of the neutral gas.

(3) The range of occurrence of PMSE in space and time corresponds well to the cold summer mesopause. In the same region, large ions and aerosols form uniquely.

(4) Very steep gradients and "bite-outs" in the electron density are often observed in PMSE regions by rocket probes.

(5) Radar-observed mean vertical velocities in the polar summer mesosphere are

downward in opposition to theory.

(6) Semi-diurnal periodicities in PMSE strength are apparent, and specific cases have been observed in which regions of maximum echo power corresponded to an unstable phase of tidal modes and long-period gravity waves.

(7) Short-period gravity waves are often observed to be steepened, tilted, and sometimes saturated with increasing height.

(8) PMSE at 50 MHz are reported to be aspect sensitive with respect to the vertical.

(9) At VHF, the Doppler spectral widths are not positively correlated with backscattered power.

(10) The radar cross sections are highly frequency dependent, but the behaviors at 50 and 224 MHz are very similar and can most likely be explained by the same process. PMSE at 933 MHz and 1.29 GHz are much rarer and weaker, but nonetheless much stronger than reasonable extrapolations of the VHF echo strengths could account for.

Observation (2) is the direct explanation for (1); however, (2) itself is a puzzle that needs an answer. We will invoke item (3) in addressing this problem (in other words, pointing to the presence of charged aerosols as the cause for small-scale electron density structures). Furthermore, we will propose that the aerosols may also have a role in explaining (4) and (5). Items (6) and (7) suggest that neutral turbulence does exist in the summer mesosphere and affects the generation of PMSE; however, (8) and (9) imply that the turbulence, in general, is not the only or perhaps even the key element in producing PMSE. Finally, (10) hints that PMSE at VHF and UHF may be different beasts.

## 2.2 Introduction to PMSE Theories

A radio wave traveling in vacuum will keep going forever, undisturbed, barring any general relativistic effects. However, a perfect vacuum is rarely encountered in real life. In almost all cases the medium of propagation will be filled with various obstacles that disturb and scatter the wave. In the Earth's atmosphere radio waves encounter bugs, birds, rain and snow, clouds, airplanes, parachutists, ICBMs,

UFOs, meteoroids, etc., all of which can modify the propagation. The atmosphere itself can scatter radio waves when, for a variety of reasons, it has variations in the index of refraction. Radar scientists take advantage of this phenomenon to obtain information about the "target" by analyzing the scattered signal.

*Woodman and Guillén* [1974] showed that, with a sensitive and powerful enough radar, one could obtain radar echoes resulting from the index of refraction inhomogeneities in our atmosphere from virtually its entire height range. The refractive index is dependent on bound electrons in water vapor in the lower troposphere, bound electrons in dry air in the upper troposphere and stratosphere, and free electrons in the mesosphere. Variations in the refractive index are generated by the turbulence and stratification of the air, and thermal or forced fluctuations of the free electrons. Radar echoes are weakest in the stratosphere because it is dry (not much water gets transported above the tropopause "cold trap"), not ionized (most of the ionizing radiation gets absorbed above), and very stable (due to the reversed temperature gradient from the UV absorption by the ozone layer).

In the polar summer mesosphere, even though it is very dry, ice clouds can form due to the extremely cold temperatures. Thus, the first idea one might have in explaining the unusually large radar echoes from that region is that the clouds are reflecting VHF radar waves much like cumulonimbus clouds in the troposphere reflect weather radar waves. As shown next, a quick calculation reveals that this idea will not work.

The radar volume reflectivity of spherical ice aerosols with radius $r_a$ much less than the radar wavelength $\lambda_R$ (Rayleigh scattering) is given by (see, e.g., *Doviak and Zrnič* [1984])

$$\eta_{\text{Rayleigh}} = 2.1 N_a \frac{\pi^5}{{\lambda_R}^4} {r_a}^6 \tag{2.1}$$

where $N_a$ is the aerosol number density. Thus, the Rayleigh scattering increases with shorter radar wavelength and larger aerosol radius and number density. The shortest radar wavelength at which PMSE have been observed is 23 cm (1.29 GHz) [*Cho et al.*, 1992*b*] and the largest aerosols observed in the polar summer mesosphere is estimated to be around 0.1 $\mu$m with a number density of no more than $10^9$ m$^{-3}$. These numbers then yield $\eta_{\text{Rayleigh}} \approx 2 \times 10^{-28}$ m$^{-1}$.

Compare this number to the radar scatter that results only from the thermal

fluctuations of free electron density. Known as incoherent or Thomson scatter, the volume reflectivity is roughly

$$\eta_{\text{incoherent}} \approx 2\pi r_e^2 N_e \tag{2.2}$$

where $r_e = 2.82 \times 10^{-15}$ m is the classical electron radius and $N_e$ is the ambient electron number density. For a typical electron density at 85 km of $4 \times 10^9$ m$^{-3}$, we get $\eta_{\text{incoherent}} \approx 2 \times 10^{-19}$ m$^{-1}$ which is far bigger than the Rayleigh volume reflectivity and still barely detectable even by the largest radar systems in the world. Therefore, we can rule out the possibility that the radar echoes result directly from the cloud particles.

As a concise summary of typical radar volume reflectivities observed in the mesosphere, we present Table 2.1.

Table 2.1: Order of magnitude figures for radar volume reflectivities observed in the altitude region between 80 and 90 km. The non-polar-summer figure is for all three radar frequencies displayed.

| Type | Volume Reflectivity (m$^{-1}$) |
|---|---|
| 50-MHz PMSE | $\sim 10^{-12}$ |
| 224-MHz PMSE | $\sim 10^{-16}$ |
| 933-MHz PMSE | $\sim 10^{-18}$ |
| Non-polar-summer VHF | $\sim 10^{-18}$ |
| Non-polar-summer UHF | $\sim 10^{-19}$ |

Because the mesosphere is so tenuous and dry, free electrons are the dominant source of radar scatter. As far as the ionized component is concerned, the mesosphere is referred to as the ionospheric D region. The electron density fluctuations which are responsible for radar scatter can be categorized as follows: (1) the irreducible minimum resulting from the thermal energy and (2) anything above that which are created by various fluid dynamical, electrodynamical, and chemical effects. Type (1) has already been introduced in the previous paragraph and is termed incoherent (Thomson) scatter while (2) is referred to as coherent scatter. In either case, the radar waves scatter from inhomogeneities of scale corresponding to half the radar wavelength (known as the Bragg scatter condition).

In the 80–90 km height region, only incoherent scatter contributes to non-polar-

summer echoes at UHF. Because the reflectivity of incoherent scatter is not dependent on radar frequency, the reflectivity of the other cases, which rise above this level, must be due to coherent scatter. Note that PMSE is highly dependent on the radar frequency, and even the typical reflectivity at 50 MHz is many orders of magnitude above the non-polar-summer values. Obviously, PMSE are produced by coherent scatter. Whether one coherent scatter mechanism is responsible for PMSE observed at the different radar Bragg scales or multiple mechanisms operate at different scales is a question that we will be addressing in this thesis.

The existence of electron density structures can be thought of as a continuous struggle between generation and the ever-present diffusive dissipation. Fig. 2.12 summarizes this idea. Diffusion acts preferentially on shorter length scales, so in general it is harder to maintain smaller structures—they get smeared out more quickly by diffusion. Hence, the central problem of PMSE: What anomaly allows the maintenance of electron density inhomogeneities at smaller scales than are normally possible in the mesosphere? The short answer is that either (1) the generation of structures is enhanced, (2) the electron diffusivity is reduced, or possibly both. This thesis work was primarily aimed at advancing our knowledge in area (2) since there seemed to be more hope for explaining the echo strength through this process. For completeness we discuss item (1) as well.

### 2.2.1 Review of Past Theories: Enhanced Generation Mechanisms

Generation of electron density structures in the mesosphere can be due to the following mechanisms: (1) dynamics of the neutral gas, (2) chemistry, (3) photochemistry, and (4) electrodynamics. Magnetic field effects can be ignored in this altitude region because the ion-neutral and electron-neutral collision frequencies are much greater than the respective gyrofrequencies of the charged species. Also, observations show that the PMSE structures are not dependent on the geomagnetic field direction, so we have no reason to believe that magnetic effects are important to PMSE.

Early theories focused on the effects of neutral dynamics on the electrons since there are so few electrons compared to the neutral molecules; the electrons were

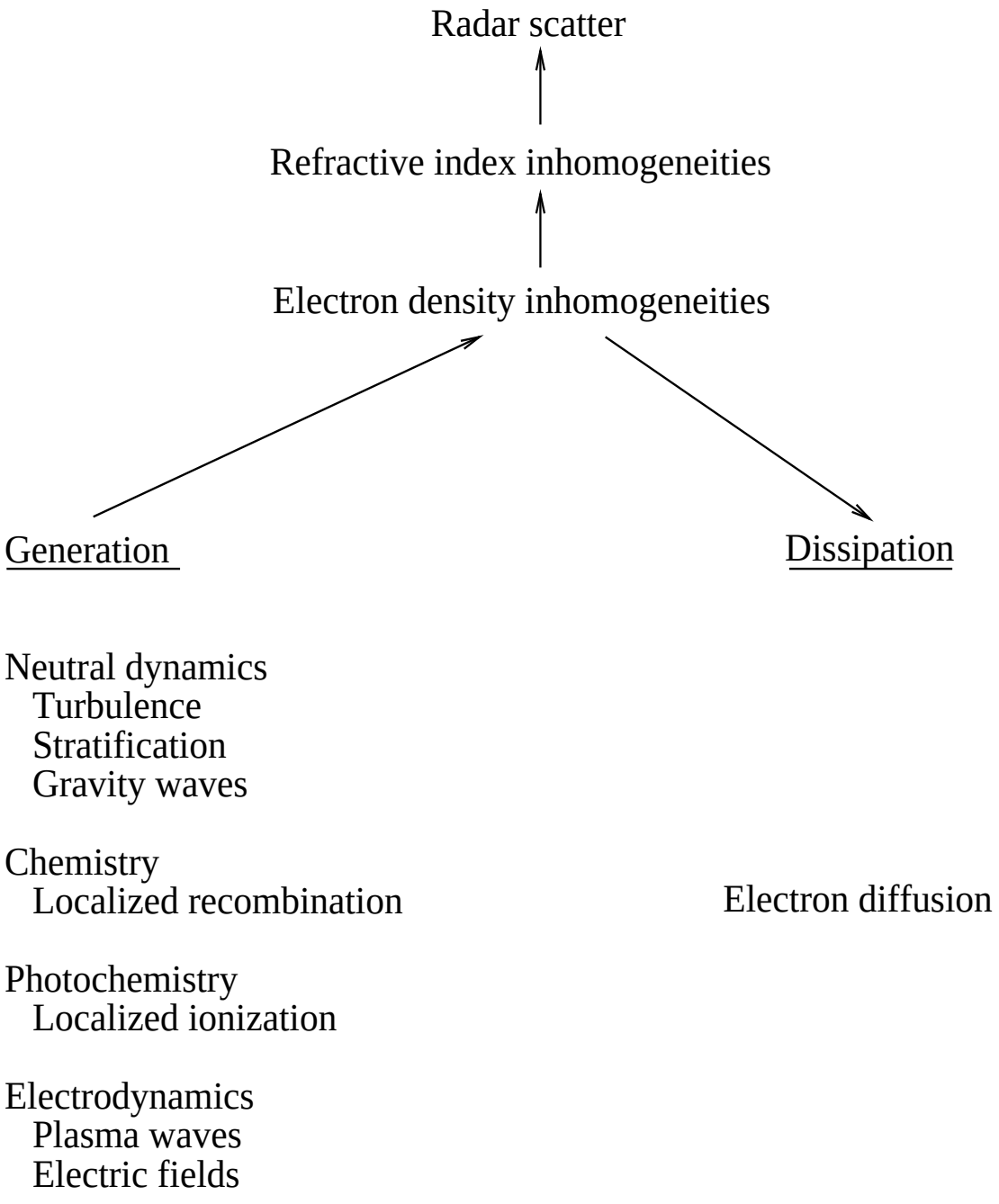


Figure 2.12: A schematic of how mesospheric coherent radar echoes are produced. Many of the inhomogeneity generation mechanisms are still speculative.

assumed to be passive tracers of the neutral gas. *Balsley et al.* [1983] attributed the generation mechanism to turbulence produced by shear instability of tidal modes and supersaturation of gravity waves was invoked by *VanZandt and Fritts* [1989] as a generation mechanism for strong turbulence. Enhanced radar backscatter was thought to be caused by regions of intense turbulence produced by regions of instability. However, it was clear that the typical turbulence intensity in the summer mesosphere was not great enough to account for the observed radar cross sections, a point that was confirmed by later measurements with the EISCAT and SOUSY radars.

There are, in fact, serious defects with a classic turbulent scatter explanation. For example, *Ulwick et al.* [1988] quoted values for the turbulent dissipation rate and electron density during the structure and atmospheric turbulence environment (STATE) rocket/radar experiments at Poker Flat nearly identical to those measured in Peru during the CONDOR rocket campaign [*Røyrvik and Smith*, 1984] but a radar cross section that was four orders of magnitude higher. Similarly, the turbulence intensities inferred from the Doppler spectral widths measured at EISCAT were much too low to produce the extremely large radar signals according to the classical theory [*Röttger and La Hoz*, 1990].

Fresnel scatter has also been proposed as a candidate for PMSE producer. Isotropic turbulence scatter and Fresnel scatter exist at different points on a spectrum scaled by the ratio of the correlation length of the scatterer along the radar beam to the correlation length transverse to the beam. If the ratio is unity, isotropic turbulence scatter results. If the ratio is zero then one gets Fresnel scatter. In between the two, one gets anisotropic turbulence scatter.

As for PMSE, the most favored scenario has been that of weak turbulence coexisting with vertically steep, horizontally coherent structures in the electron density, i.e., a combination of weak turbulent scatter and Fresnel scatter. Such a picture is supported by the following evidence: (1) billows in noctilucent clouds [*Witt*, 1962] and saturating gravity waves [*Fritts*, 1988] imply that turbulence exists near the summer mesopause, (2) radar spectral widths indicate mostly weak turbulence [*Watkins et al.*, 1988; *Röttger and La Hoz*, 1990], (3) radar aspect sensitivity shows isotropy (weak, background turbulence) at large angles and a sharp fall-off in

backscattered power with increasing zenith angle at small angles (Fresnel scatter) [*Czechowsky et al.*, 1988], and (4) simultaneous rocket/radar data often show sharp edges in the electron density profile sometimes with and sometimes without fine structure [*Ulwick et al.*, 1988].

In 1991 an important new result came to light. A rocket equipped with both a neutral density sensor and plasma probes was flown through a PMSE event exhibiting two scattering layers. The instruments showed almost no neutral turbulence in the lower layer and classic turbulence in the upper layer. Furthermore, the plasma had non-turbulent fluctuations below and turbulent fluctuations above [*Lübken et al.*, 1992]. Corresponding to these rocket observations, the CUPRI data also showed evidence of isotropic turbulent scatter in the upper region and partial reflection in the lower region [*Cho et al.*, 1993]. We will present these results in Chapter 7. Thus, at least in this particular instance, there were two distinct types of PMSE: a neutral turbulence-induced scattering in the upper region and something else in the lower region. *Kelley and Ulwick* [1988] came to a similar conclusion comparing rocket flights on two different nights of PMSE conditions.

Gravity waves can produce local minima in the vertical temperature profile where enhancement of electron recombination, water cluster formation, and nucleation of ice aerosols can take place. The direct effect of the waves on the electron density is large-scale, i.e., on the order of their vertical wavelengths, [*Sugiyama*, 1988] and not likely to cause radar scatter, but *Röttger and La Hoz* [1990] have suggested that the ice particles, while in the updraft phase of a wave, may undergo a charge separation process akin to those in tropospheric convective clouds which can develop electric fields and electron density fluctuations at short scales. In fact, there has been a rocket measurement of a localized DC electric field inside a noctilucent cloud [*Goldberg*, 1989] which is larger than the ambipolar field. As we shall see later in this section, the presence of charged aerosols is likely to be a key condition for PMSE occurrence so the gravity wave-produced local temperature minima may explain certain behaviors of PMSE such as two layers tracking each other over time.

We have thought of one more idea: the presence of dust is known to lower the threshold for shear instability onset in gases. However, the ratio of dust to air mass

density must approach an appreciable fraction of unity for this effect to become important [*Palaniswamy and Purushotham*, 1981]. For the mesopause, this critical ratio is expected to be less than $10^{-5}$ [*Havnes et al.*, 1992], so we can discard this possibility.

### 2.2.2 Introduction to the Next Two Chapters

We have now seen that the previously proposed mechanisms for the enhanced generation of electron density structures have not been very successful. However, coherent radar scatter can also be enhanced if the dissipation of the scattering structures by diffusion is reduced (see Fig. 2.12). This idea was first put forth by *Kelley et al.* [1987]. They proposed that the heavy water cluster ions that occur uniquely in the summer mesopause might effectively reduce the ambipolar diffusivity of the electrons. This was a nice heuristic argument, but the diffusion theory at that time did not appear to allow a significant reduction in diffusivity with increasing ion mass. However, it was not clear that the diffusion theory itself was valid for massive particles, an issue which led directly to work described in this thesis.

The purpose of Chapter 3 is to investigate the diffusivity of massive (or more accurately, large, since size turns out to be a dominant factor) charged particles in the mesosphere and their influence on electron diffusivity. This development represents the primary theoretical contribution to the field made in the course of this thesis work. We will then apply the results of that chapter to the radar scattering problem in Chapter 4. Other new radar scattering ideas will also be discussed in Chapter 4.

# Chapter 3

# Diffusion in the Mesosphere

As discussed in the previous chapter, radar waves are scattered in the mesosphere mainly by inhomogeneities in the free electron density. Diffusion, in turn, controls the shortness of the length scales at which electron density perturbations can exist. Therefore, electron diffusivity is a crucial element in explaining the existence of strong radar echoes at the short Bragg scales of the VHF radars. In this chapter we will develop a theory of electron diffusion in the mesosphere.

In the mesosphere, electron diffusivity is determined by the much heavier ions and charged aerosols. As a loose analogy, one can visualize a black fly buzzing around a cow as she grazes languorously across a pasture. Random winds buffet the fly, but it remains in the vicinity of the bovine due to its attraction to the feast, much like an electron that, due to an electrostatic force, tends to stick around a positively charged aerosol while being bombarded by neutral molecules. The cow, on the other hand, is pretty much impervious to the winds because of her large mass, and moves around randomly at a slow rate dictated only by her appetite for succulent grass. Now imagine herding a large number of cows (and black flies) into a small area in the middle of the pasture. The cows will spread out gradually and the flies will follow them. One can see that the diffusion of flies will be much slower in this case than if they were released on their own.

The upper mesosphere is a repository for ablated meteoroids. Furthermore, in the polar summer, the extremely cold temperatures allow large cluster ions and ice to form. Consequently the summer polar mesosphere is filled with a menagerie of particles ranging from atomic size to those with maximum radii of order 0.1 $\mu$m.

If these particles are electrically charged, then they will dominate the diffusive behavior of the electrons. In this chapter we investigate the diffusion properties of the different species in the mesosphere.

## 3.1 Ion and Aerosol Diffusion

Because molecules in a gaseous medium are spread far apart relative to their sizes, one is able to employ the methods of kinetic theory to analyze their transport behavior. Two key assumptions made in this theory is that of (1) free paths—molecules move about relatively uninfluenced by each other until making "encounters" at close range, and (2) binary collisions—these "encounters" occur only in pairs. In considering aerosols that are far bigger than molecules, one must beware that these assumptions may become invalid. If the aerosol is larger than the mean free path of the surrounding gas, then it will be bombarded almost simultaneously on all sides by molecules and it will exhibit a random walk behavior known as Brownian motion. The paradigmatic parameter that divides the free molecular (kinetic) from the continuum (Brownian) regime is the Knudsen number, defined as the ratio of the ambient mean free path to the aerosol radius. In the Earth's atmosphere the mean free path of the neutral gas increases with altitude, from less than 0.1 $\mu$m at the surface to about 1 m at 100 km. Thus the Knudsen number of all the particles in the mesosphere is much greater than one and we are justified in applying kinetic theory to our problems.

### 3.1.1 Simple Theory

First we introduce the concept of a diffusion coefficient by examining an elementary theory (see, for example, *Chapman and Cowling* [1970] for details). Consider a perfect gas such that its equation of state is

$$p = NkT \tag{3.1}$$

where $p$ is pressure, $N$ is number density, $k$ is the Boltzmann constant, and $T$ is temperature. If two such gases exist as a mixture with varying density in the $x$

direction, but with uniform pressure and temperature, then

$$\frac{\partial p}{\partial x} = kT\frac{\partial(N_1 + N_2)}{\partial x} = 0 \tag{3.2}$$

and

$$\frac{\partial N_1}{\partial x} = -\frac{\partial N_2}{\partial x} \tag{3.3}$$

The flux rate $\Phi$ of one molecular species crossing the $x = 0$ plane from the negative to the positive side for a constant $N$ is given by

$$\Phi = \int_{-\infty}^{0}\int_{-\infty}^{\infty}\int_{-\infty}^{\infty} c_x N f dc_x dc_y dc_z \tag{3.4}$$

with

$$f = \left(\frac{m}{2\pi kT}\right)^{\frac{3}{2}} e^{-\frac{m}{2kT}\left(c_x^2+c_y^2+c_z^2\right)} \tag{3.5}$$

where $f$ is the Maxwellian velocity distribution function for the molecules, the $c_i$s are the Cartesian components of the velocities, and $m$ is the molecular mass. We have clearly assumed that a Maxwellian distribution adequately describes the state of the gas. Unless strong body forces act on the molecules within the free path length to accelerate them in a preferred direction, this assumption is justified. Evaluation of (3.4) yields

$$\Phi = \frac{N\overline{c}}{4} \tag{3.6}$$

where

$$\overline{c} = \left(\frac{8kT}{\pi m}\right)^{\frac{1}{2}} \tag{3.7}$$

is the average molecular speed.

For $N$ varying in the $x$ dimension, we can perform a Taylor expansion around $x = 0$ with $\Delta x = \pm Al$, where $l = 1/4\sqrt{2}\pi N r^2$ is the mean free path, $r$ is the molecular radius, and $A$ is a constant of order unity, to get

$$\Phi|_{x=0} = \frac{\overline{c}}{4}\left(N \pm Al\frac{\partial N}{\partial x}\right) \tag{3.8}$$

where the plus sign represents flux rate from positive to negative $x$ and the minus sign represents the opposite flow. The idea behind this approximation is that

molecules that are at a distance on the order of $l$ on either side of the $x = 0$ plane and headed toward it will likely cross it. The net flux rate from negative to positive is then

$$-\frac{1}{2}Al\bar{c}\frac{\partial N}{\partial x} \tag{3.9}$$

In this approximate theory, the diffusion coefficient is defined by

$$D = \frac{1}{2}Al\bar{c} \tag{3.10}$$

Applying (3.9) to (3.3) we get

$$-\frac{1}{2}A_1 l_1 \bar{c}_1 \frac{\partial N_1}{\partial x} = \frac{1}{2}A_2 l_2 \bar{c}_2 \frac{\partial N_2}{\partial x} \tag{3.11}$$

so that the coefficient of mutual diffusion is expressed by

$$D_{12} = \frac{1}{2}A_1 l_1 \bar{c}_1 = \frac{1}{2}A_2 l_2 \bar{c}_2 \tag{3.12}$$

The foregoing analysis helps one to grasp the basic physical picture of diffusion: the flux of molecules away from an area of high number density, with the transport occurring more rapidly for longer mean free paths and faster thermal velocities. It is, however, only an approximate theory in that the flux rate was calculated for gases at rest (which does not take into account the motion introduced by the diffusive process itself), and ad hoc constants of proportionality were thrown in to simplify the results. More rigorous theories begin with the Boltzmann equation and directly evaluate the velocity distribution function using different mathematical techniques. In the next section we give the results from one such development.

### 3.1.2 Application of the Chapman-Enskog Theory

General mathematical solutions to the Boltzmann equation for simple non-uniform gases were developed independently by *Chapman* [1916] and *Enskog* [1917]. Assumptions made in this theory, in addition to the free-path and binary collision conditions mentioned above, are as follows: (1) all interactions are described by classical mechanics, i.e., quantum mechanical effects are not considered, and (2)

particles and their force fields are spherically symmetric. We present here only the results for the diffusion coefficient. For a concise exposition of the derivation, the reader is referred to *Vincenti and Kruger* [1965].

The general expression for the binary diffusion coefficient is of the form

$$D_{12}^{j} = \frac{3kT}{2N} \lim_{j\to\infty} F(j) \tag{3.13}$$

where $F$ is a converging function that depends on the particle interaction model that is used. Note also that we are assuming thermal equilibrium between the two constituents such that only one value of temperature is needed. For the mesosphere this is a reasonable assumption, even for the largest aerosols [*Grams and Fiocco*, 1977]. The approximation using $j = 1$ is quite accurate except when the masses of the two species are very different. Fortunately, however, for a quasi-Lorentzian gas where $m_1/m_2$ and $N_2/N_1$ approach zero, it has been shown that (3.13) converges immediately at $j = 1$ [*Kihara*, 1949]. This case will be relevant for aerosols and ions that are much heavier and much more sparse than the neutral gas molecules. Another special case of interest is that of Maxwellian molecules (polarization interaction) for which $F(j)$ also converges perfectly on the first term in the expansion [*Maxwell*, 1867].

The $j = 1$ term is

$$D_{12}^{1} = \frac{3kT}{16\mu_{12}(N_1 + N_2)\Omega_{12}} \tag{3.14}$$

where $\mu_{12}$ is the reduced mass given by

$$\mu_{12} = \frac{m_1 m_2}{m_1 + m_2} \tag{3.15}$$

and $\Omega_{12}$ is the Chapman-Cowling collision integral which depends on the interaction model.

Because we are interested in ions and charged aerosols in a medium of mostly neutral molecules, the interaction model that seems most apt is that of Maxwellian molecules, in which a repulsive (electric polarization) force falls off as $r^{-5}$. As noted above, in this special case the approximation (3.13) is, in fact, the exact solution.

The corresponding Chapman-Cowling integral is [*Schunk*, 1975]

$$\Omega_{an}^{M} = 2.07 \times 10^{-7} \sqrt{\frac{\pi \alpha Z_a^2 e^2}{\epsilon_0 \mu_{an}}} \tag{3.16}$$

where the subscripts have been specialized to "a" for charged aerosols and "n" for neutrals, $\alpha$ ($\mathrm{m}^{-3}$) is the neutral atom polarizability, $Z_a$ is the charge number of the aerosol, $\epsilon_0$ is the vacuum permittivity, and $e$ is the elementary charge.

However, the Maxwellian model may not be the only relevant one for our purposes. *Kelley et al.* [1987] raised the possibility that polarization forces may not be dominant for the large cluster ions found in the polar summer mesosphere. *Cho et al.* [1992*a*] showed why this might be the case. Imagine two marbles in a vacuum, one with a unit of elementary charge, the other neutral. They are headed toward each other. Will their collision be influenced by the polarization field? Hardly. Because the field force is so short range, the physical cross section of the marbles exceed that of the effective polarization cross section. For extremely small charged particles like ions, the Maxwellian model compares well with laboratory measurements [*Dalgarno et al.*, 1958]. As the particles become larger, however, we expect a transition to a more elastic-sphere-like behavior to take place. Thus we need to look at that case also.

For hard, perfectly smooth, elastic spheres, interaction occurs only when two spheres come within each other's radii, at which point they bounce off in a perfectly elastic collision. If force fields and transfer of kinetic energy to internal energy are ignored, such a model yields [*Chapman*, 1933]

$$\Omega_{an}^{H} = \sqrt{\frac{8kT}{\pi \mu_{an}}} \frac{\pi}{4} (r_a + r_n)^2 \tag{3.17}$$

where $r_a$ and $r_n$ are the aerosol and effective neutral radii.

We can now estimate the transition size where the hard sphere model takes over from the Maxwellian model by equating the values of their Chapman-Cowling integrals:

$$\Omega_{an}^{M} = \Omega_{an}^{H} \tag{3.18}$$

Solving for the critical radius, we get

$$r_{crit} = 4.55 \times 10^{-4} \left( \frac{2\alpha Z_a^2 e^2}{\epsilon_0 kT} \right)^{\frac{1}{4}} - r_n \tag{3.19}$$

For the special case of the summer polar mesopause in which we are interested, $\alpha = 1.73 \times 10^{-18}$ m$^{-3}$ (corresponding to an 80/20 mixture of $N_2$ and $O_2$), $r_n = 1.8 \times 10^{-10}$ m, and $T = 130$ K, which yield, for $|Z_a| = 1$,

$$r_{crit} = 5.2 \times 10^{-10} \text{ m} \tag{3.20}$$

For water cluster ions, which can grow to fairly large sizes, we can crudely estimate (following *Hall* [1990]) that the volume is proportional to the number of $H_2O$ molecules that accrete around the seed proton. If the water molecules pack into a hexagonal ice lattice structure, then a unit cell containing 4 molecules will have a volume of $1.3 \times 10^{-28}$ m$^3$ [*Michel*, 1978]. The effective volume occupied per water molecule will be about $3.3 \times 10^{-29}$ m$^3$. Consequently, about 20 water molecules will fill up a spherical volume with the critical radius. This is an extremely rough estimate, but it helps to shed some light on the question of applicability of the hard sphere model to highly hydrated protons, as discussed by *Kelley et al.* [1987] and *Hall* [1990]. We conclude that the Maxwellian model should be used for cluster ions with hydration number less than 20 and other singly charged particles with radii less than $r_{crit}$. For multiply charged aerosols, (3.19) will give the appropriate $r_{crit}$.

How does the hard sphere model compare with experimental measurements as the aerosols become much larger than the neutral molecules? Intuitively, it seems likely that as the aerosols become larger our assumption of no transfer of translational to internal energy will begin to break down. The larger a particle becomes the less likely it would be perfectly smooth, rigid, and elastic.

Observation of particle velocity in a steady accelerating field is one way of obtaining its diffusivity. The terminal speed is given by

$$v_{term} = D_{an} \frac{m_a}{kT} a \tag{3.21}$$

where $a$ is the acceleration constant. For $m_a \gg m_n$ and $r_a \gg r_n$ (3.21) becomes

$$v_{term} = \left(\frac{\pi}{8m_n kT}\right)^{\frac{1}{2}} \frac{\rho_a a r_a}{N_n} \tag{3.22}$$

where $\rho_a$ is the mass density of the aerosol (assumed constant). Experiments suggest that (3.22) overestimates $v_{term}$, and thus $D_{an}$, by a factor of about 1.35 for submicron aerosols [*Kasten*, 1968]. This discrepancy is greatly reduced if we incorporate a modification to the hard sphere model which assumes that neutral molecules that strike the aerosol surface end up with a Maxwellian velocity distribution which tends toward a zero mean velocity relative to the surface. The theoretical calculation simply introduces a multiplicative factor to the diffusivity [*Hidy and Brock*, 1970] so that (3.22) becomes

$$v_{term} = \zeta \left(\frac{\pi}{8m_n kT}\right)^{\frac{1}{2}} \frac{\rho_a a r_a}{N_n} \tag{3.23}$$

where

$$\zeta = \left(1 + \frac{C}{2} - \frac{C'}{2} + \frac{\pi}{8}C'\right)^{-1} \tag{3.24}$$

and $C$ and $C'$ are the tangential and normal momentum accommodation coefficients that vary from $C = C' = 0$ for specular reflection (no conversion to internal energy) to $C = C' = 1$ for perfectly diffuse scattering (zero mean relative velocity distribution). We expect $C$ and $C'$ to increase from 0 for molecular size particles to 1 for very large aerosols. As we can see, the perfectly diffuse case agrees to within 3 % of the experimental results for aerosols quoted above.

In summary, we present the expressions for the ion and aerosol diffusion coefficient. For charged particles with $r_a < r_{crit}$,

$$D_{an} = \frac{9.06 \times 10^5 kT}{N_n |Z_a| e} \sqrt{\frac{\epsilon_0}{\pi \alpha \mu_{an}}} \tag{3.25}$$

For $r_a \geq r_{crit}$,

$$D_{an} = \frac{3}{8}\zeta \sqrt{\frac{kT}{2\pi\mu_{an}}} \frac{1}{N_n (r_a + r_n)^2} \tag{3.26}$$

where $\zeta$ varies from 1 for $r_a$ on the order of $r_n$ to 0.718 in the limit $r_a \gg r_n$. We opt to use $\zeta = 0.718$ since the aerosols that we will be discussing will be mostly

much larger than the neutral molecules.

## 3.2 Electron Diffusion

As illustrated in the opening section of this chapter, the diffusion of electrons is coupled to that of the ions and charged aerosols. Because of their much smaller mass and size, the electrons want to diffuse much faster than the other charged constituents, but are held back by the subsequent space charge (ambipolar) electric field.

*Hill* [1978*b*] developed a theory for ambipolar diffusion in a multiconstituent, weakly ionized plasma that is appropriate for the mesosphere. The results were only given, however, for the specific case of electrons and singly charged positive and negative ions. We extend the theory for a plasma consisting of electrons, positive ions, and multiply charged aerosols of either sign. The derivation given below follows the work of *Hill* [1978*b*] closely.

### 3.2.1 Analytical Theory

As usual, we will make several assumptions and approximations to render the problem more tractable.

*1. Quasi-neutrality.* For diffusive length scales greater than that of the electron Debye length defined by

$$\lambda_D = 69\left(\frac{T}{N_e}\right)^{\frac{1}{2}} \text{m} \tag{3.27}$$

where $N_e$ is the electron density, the plasma maintains approximate charge neutrality. The shortest radar Bragg scale of interest to us is 11.6 cm (corresponding to 1.29 GHz) and the typical values of $T = 130$ K and $N_e = 3000$ cm$^{-3}$ for the summer mesopause yields $\lambda_D = 1.4$ cm. Thus, quasi-neutrality is a good assumption unless the electron density is extremely depleted (on the order of tens of electrons per cubic centimeter).

*2. Weak ionization.* In the mesosphere neutral molecules outnumber the charged constituents by many orders of magnitude. Therefore we can ignore the collisional interactions among the charged particles. This assumption was also made in cal-

culating the ion and aerosol diffusivities in the previous section.

*3. Equal temperatures.* Another assumption used in the previous section (shown to be reasonable by *Grams and Fiocco* [1977]) was that the temperatures of all the constituents are equal. We also assume that the temperature is constant within the diffusive length scale.

*4. No external electric, magnetic, or gravitational fields.* This is patently not true, of course. We ignore the magnetic field since frequent collisions with the abundant neutral molecules will wipe out its effect on the plasma motions. Large electric fields and gravity may, indeed, introduce anisotropies in the diffusivity; such an effect may be of interest in studying the aspect sensitivity of the radar backscatter. In this section, however, we are mainly concerned with the one-dimensional behavior of density perturbations, so we will proceed with the above assumption.

*5. Zero net current density.* Taken with quasi-neutrality this implies that there are no sources or sinks of charge. Such a condition is clearly not realistic if one were attempting to model the evolution of the plasma dynamics in its entirety. Electrons and ions are created through photo-ionization, and they are lost via recombination and attachment to aerosols. Indeed, such sources and sinks may be creating spatial inhomogeneities in the plasma density that diffusion smoothes out. However, since we are only interested in studying the diffusive behavior in this chapter, we assume the absence of such perturbation generators.

Linearization approximations will be pointed out along the way.

In the rest frame of the neutral gas, the equation of motion for the charged particles are

$$\frac{1}{N_j}\vec{\Gamma}_j = \frac{D_j}{N_j}\vec{\nabla}N_j - \frac{Z_j e D_j}{kT}\vec{E} \tag{3.28}$$

where $Z_j$ is the charge number of the species, $\vec{\Gamma}_j$ is the particle flux rate, the subscript $j$ is used to denote the species, and $\vec{E}$ is the ambipolar electric field. Note that $D_j$ means $D_{jn}$; we drop the $n$ subscript for brevity. The assumption of zero net current yields

$$\sum_j Z_j \vec{\Gamma}_j = 0 \tag{3.29}$$

Multiplying (3.28) by $Z_j N_j$ and summing over $j$ we get

$$\frac{\vec{E}}{kT}\sum_j Z_j^2 N_j D_j = \sum_j Z_j D_j \vec{\nabla} N_j + \sum_j Z_j \vec{\Gamma}_j \tag{3.30}$$

By (3.29) the last term in (3.30) is zero. Solving for the electric field yields

$$\vec{E} = \frac{\sum_j Z_j D_j \vec{\nabla} N_j}{\frac{1}{kT}\sum_j Z_j^2 N_j D_j} \tag{3.31}$$

Substituting (3.31) into (3.28) we solve for the flux rate

$$\vec{\Gamma}_j = -D_j \vec{\nabla} N_j + Z_j N_j D_j \frac{\sum_k Z_k D_k \vec{\nabla} N_k}{\sum_k Z_k^2 N_k D_k} \tag{3.32}$$

Using the quasi-neutrality condition

$$\sum_j Z_j N_j = 0 \tag{3.33}$$

and ignoring all diffusivities except for the electron since the electron diffusivity is so much larger than that of ions and aerosols, we get

$$\vec{\Gamma}_j = -D_j \vec{\nabla} N_j - Z_j N_j D_j \frac{\sum_{k\neq e} Z_k \vec{\nabla} N_k}{\sum_{k\neq e} Z_k N_k} \tag{3.34}$$

Let us now specialize to a plasma consisting of electrons, singly charged positive ions, and multiply charged aerosols of either sign, with the corresponding subscripts of $e$, $i$, and $a$. Negative ions are neglected since they are scarce in the upper mesosphere in the summer [*Björn et al.*, 1985]. Equation (3.34) becomes

$$\vec{\Gamma}_{\substack{i\\a}} = -D_{\substack{i\\a}} \left(1 + \frac{Z_{\substack{i\\a}}^2 N_{\substack{i\\a}}}{Z_i N_i + Z_a N_a}\right) \vec{\nabla} N_{\substack{i\\a}} - \frac{Z_i Z_a D_{\substack{i\\a}} N_{\substack{i\\a}}}{Z_i N_i + Z_a N_a} \vec{\nabla} N_{\substack{a\\i}} \tag{3.35}$$

Quasi-neutrality gives us

$$N_e = Z_i N_i + Z_a N_a \tag{3.36}$$

and no net current density is expressed as

$$\vec{\Gamma}_e = \vec{\Gamma}_i + \vec{\Gamma}_a \tag{3.37}$$

Note that (3.36) and (3.37) reduce the number of independent charge densities and flux rates to two each. For algebraic convenience we define the following composite quantities:

$$N_c \equiv N_i - SN_a \tag{3.38}$$

where

$$S = \frac{Z_a}{|Z_a|} \tag{3.39}$$

and

$$\vec{\Gamma}_c \equiv \vec{\Gamma}_i - \vec{\Gamma}_a \tag{3.40}$$

Using (3.36) and (3.37), and after much tedious algebra, we obtain for the composite and electron flux rates

$$\vec{\Gamma}_{\substack{c\\e}} = -\frac{\left(SZ_aD_i \pm Z_iD_a\right)\vec{\nabla}N_c}{Z_i + SZ_a} + \frac{\left[D_i\left(1+Z_i\right) \mp SD_a\left(1+Z_a\right) + S\left(D_i \pm D_a\right)Z_iZ_a\frac{N_c}{N_e}\right]\vec{\nabla}N_e}{Z_i + SZ_a} \tag{3.41}$$

Note that the upper/lower subscripts correspond to the upper/lower signs in the equation. Substituting (3.41) into the continuity equation

$$\frac{\partial N_j}{\partial t} + \vec{\nabla}\cdot\vec{\Gamma}_j = 0 \tag{3.42}$$

yields

$$\frac{\partial N_{\substack{c\\e}}}{\partial t} = \frac{\left(SZ_aD_i \pm Z_iD_a\right)\nabla^2 N_c}{Z_i + SZ_a} + \frac{\left[D_i\left(1+Z_i\right) \mp SD_a\left(1+Z_a\right) + S\left(D_i \pm D_a\right)Z_iZ_a\frac{N_c}{N_e}\right]\nabla^2 N_e}{Z_i + SZ_a} + \frac{S\left(D_i \pm D_a\right)Z_iZ_a\vec{\nabla}\frac{N_c}{N_e}\cdot\vec{\nabla}N_e}{Z_i + SZ_a} \tag{3.43}$$

We wish now to linearize (3.43) through small perturbation analysis in order to

make the problem more tractable. Let

$$N_j = N_{0j} + n_j \tag{3.44}$$

where $N_{0j}$ is a constant background density and $n_j$ is a time-varying perturbation term such that $|n_j| \ll N_{0j}$. This small perturbation assumption is valid for length scales equal to or less than the radar Bragg scales ($\leq 3$ m) in which we are interested. Rocket measurements have revealed, however, that large perturbations can exist at longer length scales in the form of electron density "bite-outs" near the summer polar mesopause [*Kelley and Ulwick*, 1988; *Inhester et al.*, 1990]. It may be of interest to study the diffusivity of these large-scale structures in order to investigate the mechanism necessary to create and maintain such sharp features.

Now let the charge neutrality condition apply to the background and perturbation quantities separately, so that

$$N_{0e} = Z_i N_{0i} + Z_a N_{0a} \tag{3.45}$$

and

$$n_e = Z_i n_i + Z_a n_a \tag{3.46}$$

Substituting (3.44) into (3.43) and dropping the nonlinear terms, we obtain

$$\frac{\partial n_{\frac{c}{e}}}{\partial t} = \frac{\left(SZ_aD_i \pm Z_iD_a\right)\nabla^2 n_c}{Z_i + SZ_a} +$$

$$\frac{\left[D_i\left(1+Z_i\right) \mp SD_a\left(1+Z_a\right) + S\left(D_i \pm D_a\right)Z_iZ_a\frac{N_{0c}}{N_{0e}}\right]\nabla^2 n_e}{Z_i + SZ_a} \tag{3.47}$$

Finally, we convert the background composite density back to a combination of the background electron and aerosol densities and rearrange terms to get

$$\frac{\partial n_{\frac{c}{e}}}{\partial t} = \frac{|Z_a|D_i \pm Z_iD_a}{Z_i + |Z_a|}\nabla^2 n_c +$$

$$\left[\frac{D_i \mp D_a}{Z_i + |Z_a|} + \left(1 - \frac{N_{0a}}{N_{0e}}Z_a\right)D_i \mp \frac{N_{0a}}{N_{0e}}|Z_a|D_a\right]\nabla^2 n_e \tag{3.48}$$

We have arrived at a set of two coupled, linear, second-order partial differential

equations that are amenable to numerical study. But before we resort to the computer let us examine a special, simple case.

If $|Z_a| = Z_i$ then the electron equation becomes decoupled from the composite equation. The electron diffusion equation becomes

$$\frac{\partial n_e}{\partial t} = \left[ \frac{D_i + D_a}{2|Z_a|} + \left(1 - \frac{N_{0a}}{N_{0e}} Z_a\right) D_i + \frac{N_{0a}}{N_{0e}} |Z_a| D_a \right] \nabla^2 n_e \tag{3.49}$$

Equation (3.49) corresponds to the case of electrons plus two species with the same magnitude of charge. For $Z_a = -1$, $Z_i = 1$, and $D_a = D_i$ it further reduces to

$$\frac{\partial n_e}{\partial t} = 2D_i \left(1 + \frac{N_{0a}}{N_{0e}}\right) \nabla^2 n_e \tag{3.50}$$

Since the ambipolar diffusion coefficient for a two-species plasma (electron and positive ion) is $2D_i$, (3.50) implies that the electron diffusivity is enhanced when negative ions are introduced into the mixture. We give a physical explanation in the next section. As an aside to our discussion, this result is of interest in the interpretation of incoherent radar backscatter spectral width which is proportional to the effective electron diffusion coefficient. Equation (3.50) means that the presence of negative ions will broaden the spectral width. This conclusion agrees with the spectral width calculations of *Fukuyama and Kofman* [1980].

### 3.2.2 Numerical Analysis

Equation (3.48) can be analyzed numerically. Our goal is to find the electron diffusivity for various parameter ranges. One way of accomplishing this task is to run simulations of the differential equations, given reasonable initial conditions, and measure the diffusive time constant from which an effective electron diffusion constant, $D_e^{\text{eff}}$, can be derived. (For details of the simulation see Appendix A.)

The problem has the free parameters $Z_i$, $Z_a$, $D_i$, $D_a$, and $N_{0a}/N_{0e}$. This is, of course, a gross simplification of the actual physical situation in which there are aerosols of many different charge state and diffusivity. The essence of the problem that we can handle is thus: a plasma with electrons, one type of positive ion, and one aerosol species in some constant charge state. Even such a simple system will

give us an insight into the effects that aerosols will have on the plasma diffusion.

First, we will take $Z_i = 1$ since the positive ions are singly charged. Next, we shall fix $D_i$ since we have some idea of the constituency of positive ions and use $D_a/D_i$ as a single parameter. Assuming (1) $m_a \gg m_n$, (2) the Maxwellian interaction model applies to the ions, and (3) the aerosols are characterized by the modified hard sphere model, we can derive an expression for this ratio

$$\frac{D_a}{D_i} = 2.97 \times 10^{-7} \sqrt{\frac{\alpha \mu_{in}}{2\epsilon_0 k T m_n}} \frac{e}{r_a^2} \tag{3.51}$$

where $\mu_{in}$ is the reduced mass of the positive ion and neutral molecule. Plugging in the summer mesopause values introduced in the previous section, $m_n = 4.8 \times 10^{-26}$ kg, and using the mass of $H^+(H_20)_5$, which from *Björn et al.* [1985] is a representative ion species at 85 km, we get

$$\frac{D_a}{D_i} = 3.1 \times 10^{-19} r_a^{-2} \tag{3.52}$$

where $r_a$ is in meters. The revised set of free parameters has become $r_a$, $Z_a$, and $N_a/N_e$, i.e., the size, the charge state, and the abundance of the aerosols.

Fig. 3.1 through Fig. 3.5 show the results of our simulations for $D_e^{\text{eff}}/D_i$ plotted versus $N_{0a}/N_{0e}$. Multiple curves represent the different values of $D_a/D_i$ that are determined by the indicated values of $r_a$. Since the usual assumption in studying the mesosphere has been to take $D_e/D_i = 2$ (the two-species ambipolar result) where $D_i$ is given by the positive ion constituent, we will give our results in terms of the ratio $D_e^{\text{eff}}/D_i$ so that it is easily compared to the base result of 2.

The results for singly negatively charged, small aerosols are displayed in Fig. 3.1. Note that when the negatively charged particles are very small (as in ions), their presence can only increase the effective diffusivity. However, as the negative aerosols become larger, a transition takes place and an increase in their abundance tends to reduce $D_e^{\text{eff}}$. This behavior is not intuitively obvious, so let us try to form a qualitative picture. First, imagine a plasma mixture with just electrons and positive ions. If we introduce a perturbed area of high density for both species, the particles in the high density region will start to diffuse outward with the electrons tending to be on the outer edge due to their higher intrinsic diffusivity. Thus the ambipolar

electric field will be set up in such a way as to rein in the electrons and to tug the positive ions outward. Now introduce negative ions of size similar to the positive ones. (We maintain overall charge neutrality by subtracting electrons.) Because they are just as large as the positive ions, the negative ions will lag behind with the positive particles in the diffusion "tug-of-war" with the electrons. Consequently, the ambipolar electric fields that the electrons experience will be "watered down" by the addition of negative charge, and thus they will diffuse more rapidly. However, if we replace the negative ions with singly charged but very large negative aerosols which diffuse even more slowly than the positive ions, then the "tug-of-war" turns into a three-way competition with the negative aerosols holding back on the inside, the electrons pulling away on the outside, and the positive ions caught in between. Therefore, the reduction in the ambipolar field felt by the electrons will be counteracted by an overall decrease in the diffusivity due to the large negative aerosols. Thus, the transition from enhancement to reduction of effective electron diffusion occurs when the aerosol "drag" starts to overcome the "freeing up" effect of the diminished ambipolar electric field. Fig. 3.1 indicates that, in our particular case, this transition occurs when the aerosol radius becomes larger than $\sim 1.1$ nm.

Fig. 3.2 through Fig. 3.5 correspond respectively to the aerosol charge $Z_a = -100$, -10, 10, 100. As one would expect, the curves start from $D_e^{\text{eff}}/D_i = 2$, as in Fig. 3.1. As the fraction of aerosols are increased, $D_e^{\text{eff}}/D_i$ approaches $D_a/D_i$. Notice that the curves in Fig. 3.2 are virtually indistinguishable from those in Fig. 3.3. This is also true for Fig. 3.4 and Fig. 3.5. Since the $x$ axes differ by a factor of 10, it seems that the important scaling factor is not $N_a/N_e$ but $|Z_a|N_a/N_e$. This makes sense physically; it means that the important factor is how much charge of the plasma is tied up in aerosols. For the larger aerosols of our interest the transition from ion to aerosol domination occurs sharply around $|Z_a|N_a/N_e = 1.2$ (for $Z_a$ negative) and 0.6 (for $Z_a$ positive), in other words, when somewhat more than half of the charge is tied up in aerosols. Also, it appears that positively charged aerosols are somewhat more efficient than negatively charged ones at slowing down diffusion. This observation fits the hand-waving argument given above concerning the competition between the aerosol "drag" and reduction of the ambipolar field—positive aerosols do not reduce the ambipolar field so they ought to be more effective

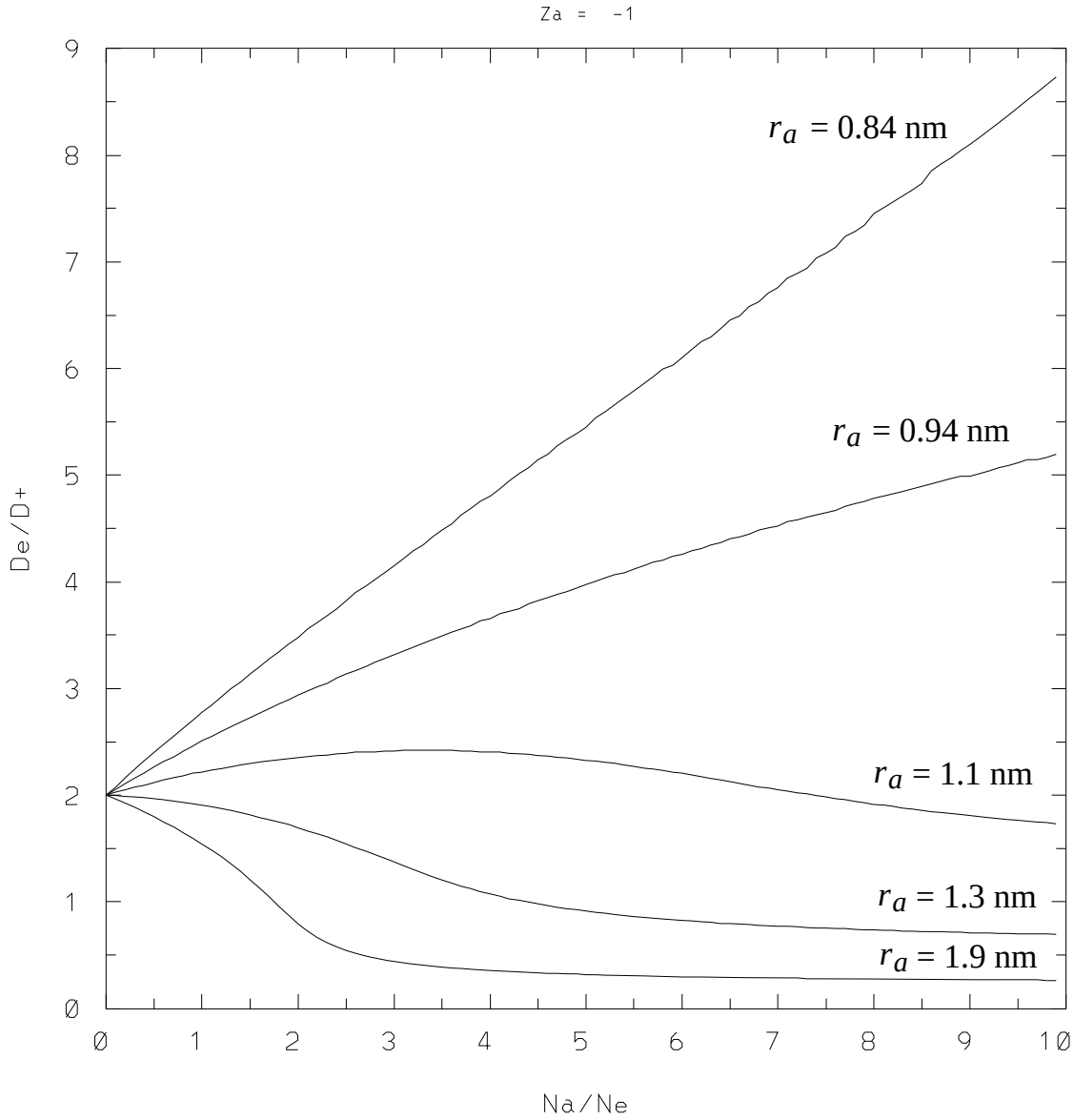


Figure 3.1: Plot of effective electron diffusivity versus aerosol number density for positive ions with $Z_i = 1$ and negative ions or small aerosols with $Z_a = -1$. Electron diffusivity is normalized with respect to the positive ion diffusivity, and the aerosol number density is normalized with respect to the electron number density.

in retarding the overall diffusion.

We have shown in this chapter that the presence of charged aerosols can have a significant effect on the diffusion of electrons in the mesosphere. In the next chapter we will show how this aerosol-controlled electron diffusivity can dramatically affect mesospheric coherent radar scatter.

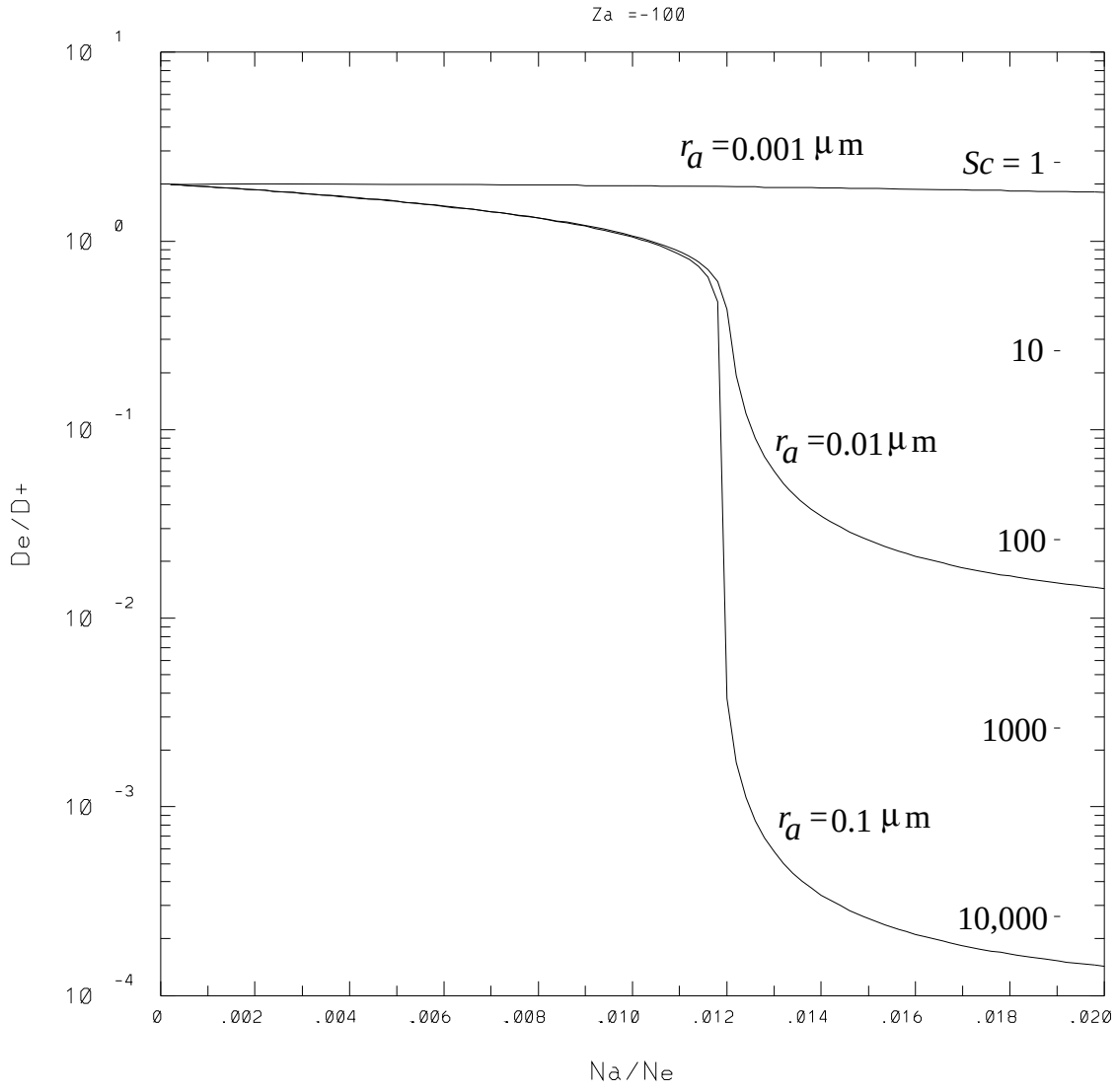


Figure 3.2: Plot of effective electron diffusivity versus aerosol number density for positive ions with $Z_i = 1$ and various size aerosols with $Z_a = -100$. Electron diffusivity is normalized with respect to the positive ion diffusivity, and the aerosol number density is normalized with respect to the electron number density. The Schmidt numbers indicated on the right side of the figure will be defined and referred to in Chapter 4.

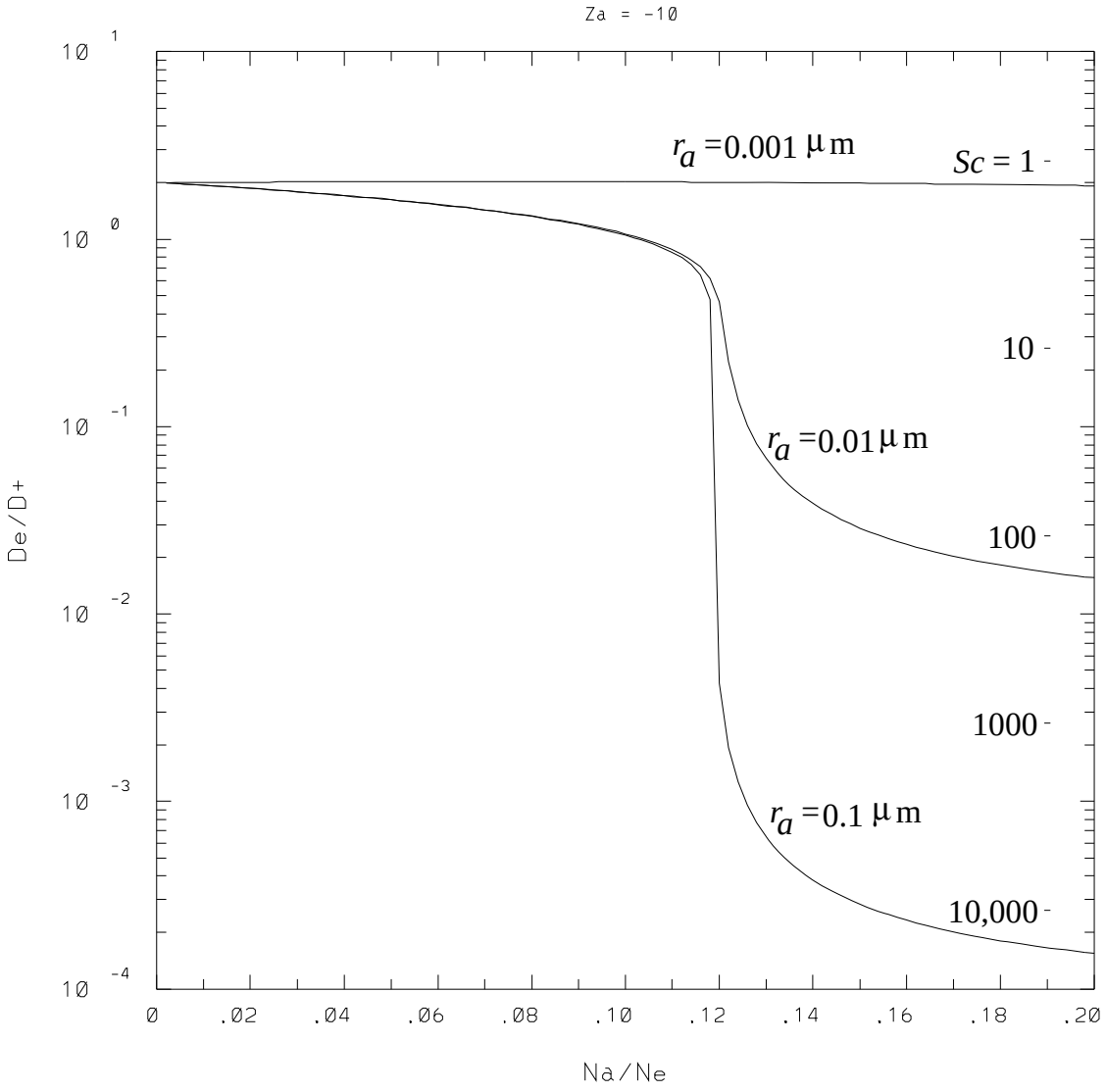


Figure 3.3: Same as Figure 3.2 except $Z_a = -10$.

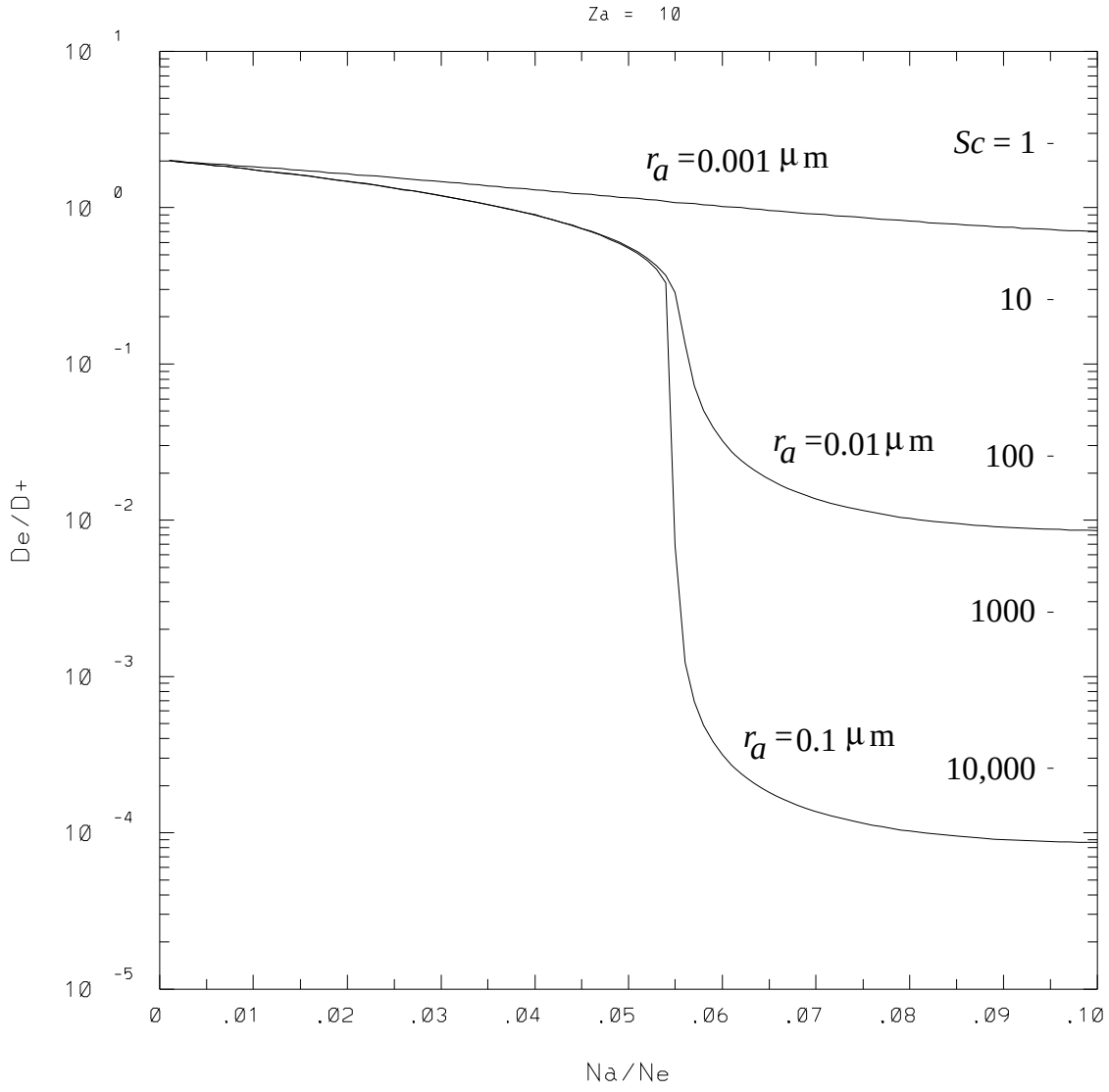


Figure 3.4: Same as Figure 3.2 except $Z_a = 10$.

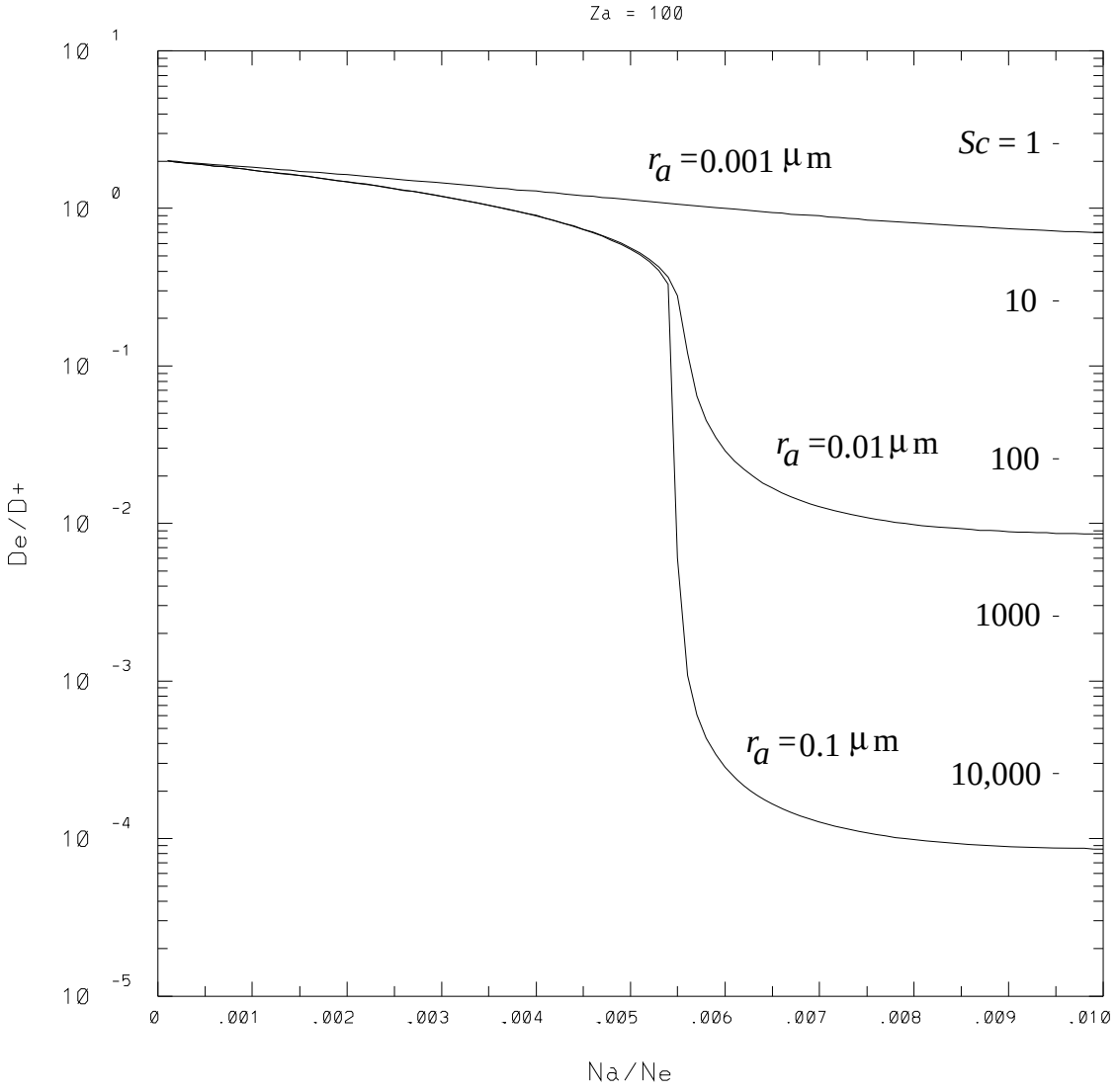


Figure 3.5: Same as Figure 3.2 except $Z_a = 100$.

# Chapter 4

# Theories of Radar Scattering in the Polar Summer Mesosphere

As discussed in Chapter 2, radar scattering in the mesosphere results from inhomogeneities in the electron density. The scattered power is enhanced if the generation rate of such fluctuations is increased or if the dissipation of the scattering structures is reduced. The former alternative has been explored previously by other researchers without much success. In this thesis work we have primarily developed the latter alternative. In Chapter 3, we showed that charged aerosols can significantly reduce the electron diffusivity. We are now ready to apply this result to the radar scatter theories.

First we investigate the effects of reduced electron diffusivity on isotropic turbulence scatter theory since well-tested theories describing the behavior of passive scalars mixed by turbulence have been developed since the original work by *Batchelor* [1959].

## 4.1 Reduced Diffusion Effects on Isotropic Turbulence Scatter

Turbulence theory is a fairly murky field that suffers from a fundamental closure problem in its set of fluid dynamics equations. For our purposes, the classic theory of *Kolmogorov* [1941] which was based on a heuristic argument and simple

dimensional considerations is adequate in introducing the extension of the ideas to the turbulent advection of scalar quantities. We refer the reader to *Tennekes and Lumley* [1972] for a fuller development of this and other turbulence theories.

As we will be dealing with the energy density spectrum in wavenumber space, we will proceed to define what we mean by it. (In the following development the units for all energy quantities will be implicitly per unit mass.) First, define the spatial correlation tensor for velocity fluctuations as

$$R_{ij}(\vec{x}) = \langle u_i(\vec{x_0}, t) u_j(\vec{x_0} + \vec{x}, t) \rangle \tag{4.1}$$

Note that $R_{ij}$ is independent of $\vec{x_0}$ and $t$ provided that the turbulence is homogeneous and stationary. The Fourier transform of (4.1) yields the spectral tensor

$$\Phi_{ij}(\vec{k}) = \frac{1}{(2\pi)^3} \int_{-\infty}^{\infty} R_{ij}(\vec{x}) e^{-i\vec{k}\cdot\vec{x}} d\vec{x} \tag{4.2}$$

where the kinetic energy for a certain wave vector is given by the trace of $\Phi_{ij}$. Normalization is such that the integral of $\Phi_{ij}$ over the entire $k$-space gives the velocity variance $< u^2 >$. If isotropy is assumed, one can integrate the trace over a spherical shell of radius $k$ to get a velocity fluctuation energy density spectrum that is most commonly used in turbulence literature

$$E(k) = \oint_{\text{surface}} \Phi_{ii}(\vec{k}) dS \tag{4.3}$$

The theoretical form of the function $E(k)$ in a highly turbulent medium was predicted by *Kolmogorov* [1941] and has been proven to be remarkably accurate in the description of turbulence in the atmosphere and many other fluid media. The basic scenario is thus: (1) energy from large-scale mean flows and waves are converted to three-dimensional turbulent eddies via instabilities, (2) vortex stretching mechanisms transfer the eddy kinetic energies to smaller eddies until (3) the eddies become so small that molecular viscosity begins to destroy them. The key postulate is that, in the scale range between the large-scale energy input and the small-scale energy dissipation, there exists a range where the kinetic energy spectrum depends

only on the energy dissipation rate

$$\epsilon = -\frac{\partial}{\partial t}\left(\frac{1}{2}\left\langle u^2\right\rangle\right) = \nu\left\langle(\nabla u)^2\right\rangle \tag{4.4}$$

where $<u^2>$ is the total velocity variance, and the wavenumber $k$. Then, simply on dimensional grounds, the energy spectrum in the so-called inertial subrange must be given by the form

$$E(k) = C_0\epsilon^{\frac{2}{3}}k^{-\frac{5}{3}} \tag{4.5}$$

where $C_0 \approx 1.5$ [*Tennekes and Lumley*, 1972] is a constant. The existence of an inertial subrange in the atmosphere depends on the relationship between the Kolmogorov microscale

$$l_K = \nu^{\frac{3}{4}}\epsilon^{-\frac{1}{4}} \tag{4.6}$$

and the Lumley-Shur buoyancy scale [*Shur*, 1962; *Lumley*, 1964]

$$l_{LS} = {\omega_B}^{-\frac{3}{2}}\epsilon^{\frac{1}{2}} \tag{4.7}$$

is a constant and $\omega_B$ is the Brunt-Väisälä frequency defined by

$${\omega_B}^2 = \frac{g}{T}\left(\frac{\partial T}{\partial z} + \frac{g}{c_p}\right) \tag{4.8}$$

where $c_p$ is the specific heat of air at constant pressure. The actual breakpoints occur at $C_K l_K$ and $C_{LS} l_{LS}$ where the constants are found empirically to be $C_K \approx 12.8$ [*Hill and Clifford*, 1978], and $C_{LS} \approx 10.1$ [*Weinstock*, 1978]. At scales larger than $C_{LS} l_{LS}$ a fraction of the turbulent kinetic energy will be lost to the potential energy of stratification, and thus the energy spectrum becomes dependent not only on $\epsilon$ and $k$ but also on buoyancy parameters (see, e.g., *Weinstock* [1978]). The result is that there is a much steeper fall off of the energy spectrum in the buoyancy subrange with a wavenumber dependence of $k^{-3}$. Thus, a $k^{-5/3}$ inertial subrange can only exist for $C_{LS} l_{LS} > C_K l_K$. In the Earth's atmosphere this condition is roughly satisfied up to $\sim$ 100 km, so a turbulent inertial subrange can exist in the mesosphere. At lengths shorter than the inner scale, viscosity damps out the velocity fluctuations and the energy spectrum falls off exponentially with $k$ [*Corrsin*,

1964]. (A note on the relationship between $k$ and turbulence length scales $l$s: in most turbulence literature $k = 1/l$ is assumed and this is the convention we will follow. Others occasionally use $k = 2\pi/l$, e.g., *Hocking* [1985], so one must be careful. For other lengths such as wavelength and physical size, the $2\pi$ factor will kept.)

These ideas of universal spectral forms can be extended to the spectrum of a passive scalar additive mixed by turbulence fairly straightforwardly provided we assume adiabatic fluid motion and conservation of the additive such that the additive follows the fluid parcel affected only by diffusion. For the additive of our interest, electron density, the above assumptions are valid as long as the time scales of recombination and ionization are slow relative to the lifetime of the turbulent eddies. For now we will take the assumptions to be valid; we will consider them more carefully later.

Analogous to (4.4) we can define the variance dissipation rate of the additive $\xi$ to be

$$\chi_\xi = D_\xi \left\langle (\nabla \xi)^2 \right\rangle \tag{4.9}$$

Because the scale at which viscosity begins to destroy the velocity fluctuations may be different from the scale at which diffusivity of the additive, $D_\xi$, starts to dampen the scalar fluctuations, $E_\xi(k)$ at high wavenumbers will in general have a more complex form than $E(k)$. Thus, a key ratio is the Schmidt number defined as

$$Sc = \frac{\nu}{D_\xi} \tag{4.10}$$

and two additional length scales become important: the Obukhov-Corrsin scale [*Obukhov*, 1949; *Corrsin*, 1951]

$$l_{OC} = {D_\xi}^{\frac{3}{4}} \epsilon^{-\frac{1}{4}} \tag{4.11}$$

and the Batchelor scale [*Batchelor*, 1959]

$$l_B = \nu^{\frac{1}{4}} {D_\xi}^{\frac{1}{2}} \epsilon^{-\frac{1}{4}} \tag{4.12}$$

For $Sc \ll 1$ we get two subranges in the scalar energy spectrum delineated by

$l_{OC}$: the inertial-convective subrange with a $k^{-5/3}$ slope where the additive follows the inertial subrange turbulence of the fluid, and the inertial-diffusive subrange where the scalar fluctuations are damped out by diffusion even though the fluid is maintaining turbulent eddies. For $Sc \gg 1$ two subranges appear divided by $l_B$ in addition to the inertial-convective subrange: the viscous-convective subrange with a $k^{-1}$ dependence where the scalar fluctuations are not yet affected by diffusion but the fluid velocity fluctuations have been dissipated by viscosity, and the viscous-diffusive subrange where the additive inhomogeneities are finally smeared out by diffusion. Fig. 4.1 illustrates the various wavenumber subranges described above. From a dimensional point of view the scalar spectrum can be expressed as

$$E_\xi(k) = C_\xi \chi_\xi \epsilon^{-\frac{1}{3}} k^{-\frac{5}{3}} f(k l_K, Sc) \tag{4.13}$$

where $f$ is a non-dimensional function. (As an aside, we would like to add a cautionary note to the calculation of the viscosity in the cold summer mesopause. The temperatures there may get so cold that commonly used expressions such as Sutherland's formula and empirically determined temperature power laws which are employed to calculate viscosity, can become invalid. For example, the viscosity formula used by *Banks and Kockarts* [1973] for molecular oxygen, while accurate to within 5 % of measured values down to 200 K, overestimates laboratory values [*Johnston and McCloskey*, 1940] by 16 % at 130 K.)

Herein lay the crux of the original difficulty with classical turbulence scatter theory as applied to PMSE: at the PMSE altitudes the inner scale is in the tens of meters, much longer than the radar Bragg lengths. Because it has been assumed that $Sc \sim 1$ (which is valid for the non-summer or non-polar mesopause [*Hill and Bowhill*, 1976; *Røyrvik and Smith*, 1984]) the radars should not have significant structures from which to scatter since they would have been dissipated by viscosity. However, if for some reason the electron diffusivity is drastically reduced, then $Sc$ would become much greater than one and a viscous-convective subrange would appear; as a result structures in the electron density would be maintained to smaller lengths, i.e., the VHF radar Bragg scales [*Kelley et al.*, 1987]. We have already established in Chapter 2 that the presence of charged aerosols will greatly reduce the diffusivity of the electrons. Thus, the formation of aerosols in the uniquely cold

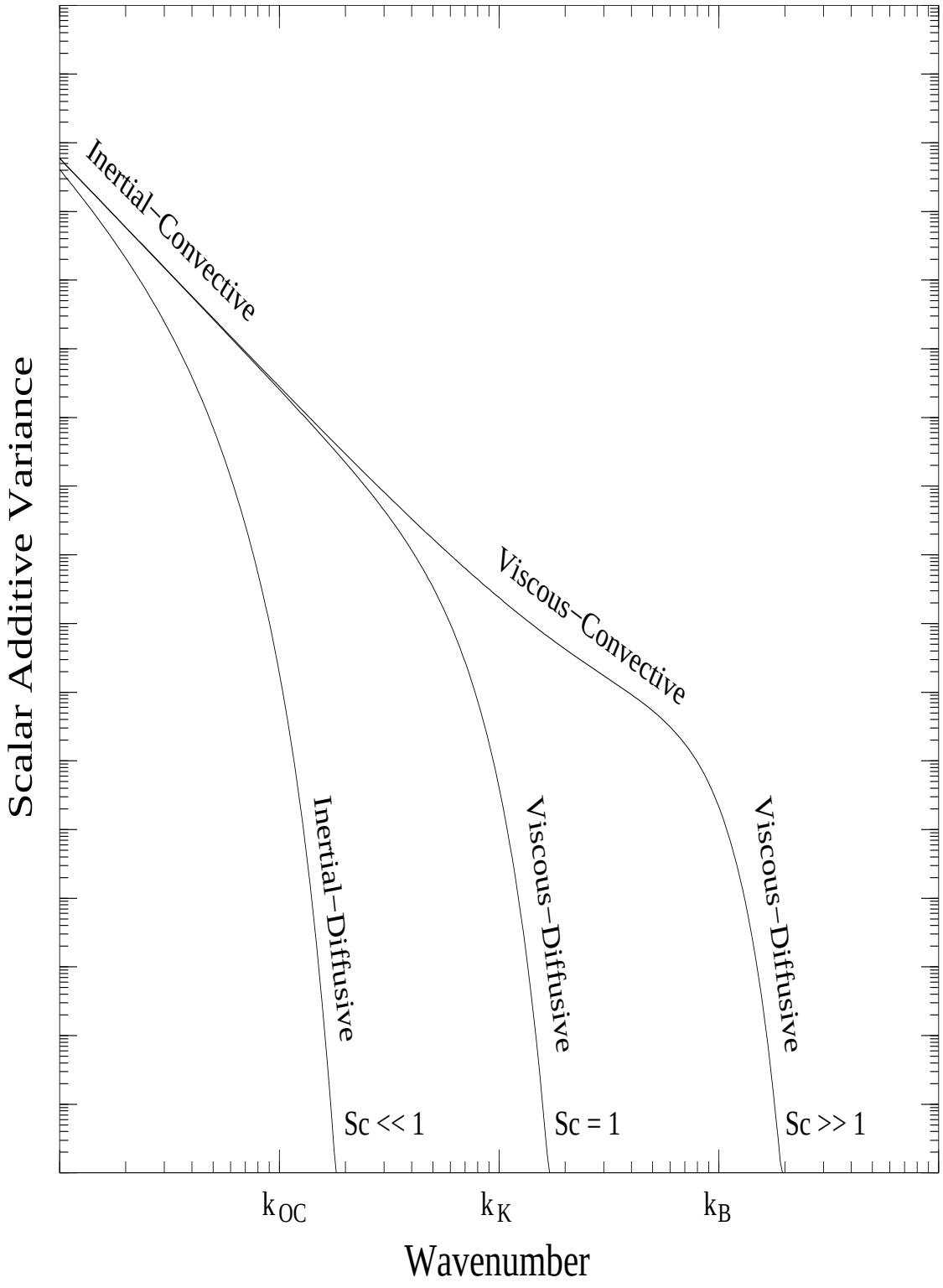


Figure 4.1: A schematic plot showing the theoretical fluctuation energy spectra, $\Phi_\xi$ for a scalar additive mixed by isotropic turbulence.

summer mesopause can enhance radar scattering in the VHF range (and maybe even in the UHF range).

In order to perform a more quantitative analysis we now develop a model of how the radio refractive index, via the electron density, is mixed by turbulence (see, e.g., *Tatarskii* [1971]). The goal is to express the dissipation rate of fluctuations in the refractive index, $\chi_n$, in terms of the electron density, $n_e$.

Because the mesosphere is part of the D region of the ionosphere, its refractive index is dominated by free electrons and is given by

$$n = \left(1 - \frac{f_e^2}{f^2}\right)^{\frac{1}{2}} \tag{4.14}$$

where

$$f_e = \frac{e}{2\pi}\left(\frac{n_e}{\epsilon_0 m_e}\right)^{\frac{1}{2}} \tag{4.15}$$

is the plasma frequency. Even for a large value of $n_e = 10^{10}$ m$^{-3}$, $f_e = 900$ kHz, so (4.14) can be approximated by

$$n \approx 1 - \frac{f_e^2}{2f^2} \tag{4.16}$$

Thus, we see that perturbations in $n$ are linearly dependent on perturbations in $n_e$.

Although it seems reasonable to assume that the ratio of electron density to the neutral density would remain constant during the turbulent advection process, we should scrutinize this assumption before blithely proceeding any further.

Charge in a turbulent eddy may be considered to be conserved if the time scales of the charge sources and sinks are longer than the lifetime of the eddy. Roughly, an electron density eddy of size $L$ will have a diffusive decay time of

$$\tau_{\text{diff}} = \frac{L}{2\pi}^2 \frac{1}{D_e} \tag{4.17}$$

where $D_e$ is the effective electron diffusivity (see, e.g., *Hall* [1991]). We know from Chapter 2 that $D_e$ is dependent on the size of charged aerosols if any are present. If none are present, a typical value for the summer mesopause is about $D_e \approx 1$ m$^2$s$^{-1}$. This yields $\tau_{\text{diff}} \approx 0.2$ s for $L = 3$ m (Bragg scale for a 50-MHz

radar) and $\tau_{\text{diff}} \approx 0.3$ ms for $L = 12$ cm (1.29-GHz radar). Aerosols of radius on the order of 0.01 $\mu$m that are numerous and charged enough to dominate the electron diffusion will lower $D_e$ by a factor of about 100. So the eddy lifetimes will also increase by two orders of magnitude to $\tau_{\text{diff}} \approx 20$ s (50 MHz) and 0.03 s (1.29 GHz).

The primary source of electrons is photo-ionization which has a diurnal variation in its rate but no short-period fluctuations. Precipitation of highly energetic particles can produce electrons within $\tau_{\text{diff}}$ but does not occur very often, so we can ignore it for the typical case. Therefore, the sources of electrons do not pose a difficulty in the assumption of a constant mixing ratio of electron to neutral density.

PMSE occur in a region where the electron density rapidly increases with height, known as the D region ledge. This sharp change in the $N_e$ profile is mostly attibutable to the formation of water cluster ions, $H^+(H_2O)_n$, in the cold region of the mesopause. These ions have much faster recombination times than $NO^+$ which is the predominant ion species above the ledge. The recombination rate for the cluster ions is $\alpha_{\text{cluster}} \approx 10^{-11}$ m$^3$s$^{-1}$ [*Leu et al.*, 1973]. So the recombination time scale, $1/\alpha N_e$, for $N_e = 10^9$ m$^{-3}$ is about 100 s.

For neutral aerosols the rate of electron capture per unit electron concentration is [*Natanson*, 1960]

$$\alpha_{ae} = \pi r_a^2 \left(\frac{8kT}{\pi m_e}\right)^{\frac{1}{2}} \left[1 + \left(\frac{e^2}{8\epsilon_0 kT r_a}\right)^{\frac{1}{2}}\right] \tag{4.18}$$

For $r_a = 0.01$ $\mu$m, $\alpha_{ae} = 10^{-10}$ m$^3$s$^{-1}$. The corresponding electron capture time scale, $1/\alpha_{ae} N_e$, for $N_e = 10^9$ m$^{-3}$ is about 10 s, which is actually less than $\tau_{\text{diff}}$ at 3 m. Thus, we see that in the presence of aerosols the constant mixing ratio assumption may break down for 50-MHz radars. In all other cases the assumption remains valid.

Does this mean that the following development of turbulent radar scatter should be disregarded for the low VHF regime? We argue that any "action" that affects the electron concentration within an eddy lifetime would be an additional source of inhomogeneity and radar scatter. Thus, if the reality deviates somewhat from the model, it will be in the direction of higher radar reflectivity. Since we are attempting

to show that reduced electron diffusivity due to charged aerosols enhances radar scatter, the deviation works in our favor.

We can now go back to (4.9) to derive an expression for $\chi_n$, the dissipation rate of refractive index variance. First, let us point out that the "$\nabla$"s can be replaced by "$d/dz$"s because the vertical gradients are much larger than the horizontal gradients in a stratified medium. Next, we reformulate $\chi_n$ in terms of mean quantities since that is what we will have as inputs to the model:

$$\chi_n = D_n \left\langle \left( \frac{dn}{dz} \right)^2 \right\rangle = K_n \left( \frac{d \langle n \rangle}{dz} \right)^2 \tag{4.19}$$

where $K_n$ is the vertical turbulent diffusion coefficient for $n$. Such an equivalence is justified given our turbulence model which assumes no source or sink in the intermediate range between the energy input scales and the dissipation scales. *Weinstock* [1978] has calculated

$$K \approx 0.81 \frac{\epsilon}{\omega_B^2} \tag{4.20}$$

for turbulent diffusion of momentum. In the atmosphere, the ratio of turbulent diffusivity of momentum to turbulent diffusivity of a passive scalar is about unity, so $K_{n_e} = K_n = K$.

Now, express $n$ in terms of $n_e$

$$\frac{dn}{dz} = \frac{\partial n}{\partial n_e} \left( \frac{dn_e}{dz} \right)_p \tag{4.21}$$

and combine (4.16) and (4.15) to obtain

$$\frac{\partial n}{\partial n_e} = \frac{e^2 \lambda_R^2}{8\pi^2 \epsilon_0 m_e c^2} = \frac{r_e \lambda_R^2}{2\pi} \tag{4.22}$$

where $r_e$ is the classical electron radius, $\lambda_R$ is the radar wavelength, and $c$ is the speed of light. Note that $(dn_e/dz)_p$ in (4.21) is the potential refractive index gradient since we are assuming that the electron density follows the adiabatic motion of the air parcel. *Hocking* [1985] has derived the following expression for the potential

refractive index gradient

$$\left(\frac{dn_e}{dz}\right)_p = \frac{dn_e}{dz} - \frac{\omega_B^2 n_e}{g} - \frac{n_e}{H} \tag{4.23}$$

where $H = RT/g$ is the scale height and $R$ is the gas constant for air.

Finally, putting together (4.19) to (4.23), we have

$$\chi_n = \frac{0.81}{4\pi^2}\epsilon\omega_B^{-2} r_e^2 \lambda_R^4 \left(\frac{dN_e}{dz} - \frac{\omega_B^2 N_e}{g} - \frac{N_e}{H}\right)^2 \tag{4.24}$$

and we can plug (4.24) into (4.13) to get $E_n(k)$.

The total radar cross section per unit volume, also known as the volume reflectivity, is [*Booker*, 1956]

$$\eta_{\text{turb}}(k) = 8\pi^2 k^4 \Phi_n(k) \tag{4.25}$$

where

$$\Phi_n(k) = \frac{1}{4\pi k^2} E_n(k) \tag{4.26}$$

is the full three-dimensional refractive index variance spectrum that is the scalar equivalent of $\Phi_{ij}(k)$.

Putting $\lambda_R = 4\pi/k$ into (4.24), such that $k$ equals the radar Bragg wavenumber, and using (4.13), (4.25), and (4.26), we get

$$\eta_{\text{turb}}(k) = 104 C_n \pi^3 r_e^2 \omega_B^{-2} \epsilon^{\frac{2}{3}} N_e^2 k^{-\frac{11}{3}} \left(\frac{1}{N_e}\frac{dN_e}{dz} - \frac{\omega_B^2}{g} - \frac{1}{H}\right)^2 f(k, \epsilon, \nu, D_e) \tag{4.27}$$

where $C_n$ is an empirical constant that has been measured to be anywhere between 0.52 [*Grant et al.*, 1968] and 1.93 [*Gibson et al.*, 1970]. *Hill* [1978*a*] recommends the use of values between 0.68 and 0.83. We will assume a medium value of $C_n = 0.76$.

For the function $f$ which determines where the scalar variance spectrum breaks between the various possible subranges, we will adopt the model developed by *Hill and Bowhill* [1976]:

$$\begin{aligned} f \;=\; & (\beta k)^{\frac{1}{3}} \{2\cosh\left[C_1 \ln\left(\beta k\right)\right]\}^{\frac{1}{3C_1}} \\ & \exp\left\{-2C_n Sc^{-1} \varrho^{\frac{4}{3}} \left[\frac{3}{4}\left(\beta\frac{k_{LS}}{C_{LS}}\right)^{\frac{4}{3}} + \int_{\beta\frac{k_{LS}}{C_{LS}}}^{\beta k} e^{\frac{5x}{3}} \left[2\cosh\left(C_1 x\right)\right]^{\frac{1}{3C_1}} dx\right]\right\} \end{aligned} \tag{4.28}$$

where $\beta = \epsilon^{-1/4}\nu^{3/4}\varrho^{-1}$, $C_1 \approx 2.5$ [*Grant et al.*, 1968], $k_{LS} = 2\pi/l_{LS}$, and $\varrho \approx 0.15$ [*Gibson and Schwartz*, 1963]. Equation (4.28) is valid for arbitrary values of $Sc$ and is easy to calculate numerically. However, it is sensitive to changes in $C_n$ which, unfortunately, is not precisely known. One must keep this in mind when contemplating the accuracy of this model. Also, note that the universal spectral model breaks down if $\epsilon$ is so small that inertial subrange disappears altogether; this happens when $l_K$ approaches $l_{LS}$. For our summer mesopause parameters, turbulence theory becomes invalid for $\epsilon < 0.4$ mW/kg.

We are now ready to show how reduced electron diffusivity affects isotropic turbulence radar scatter in more quantitative terms. Fig. 4.2 through Fig. 4.5 display plots of $\eta_{\text{turb}}$ versus $k$ for various values of $N_e$, $(1/N_e)(dN_e/dz) = 1/H_e$, $\epsilon$, and $Sc$. Although this model is only valid for turbulence scatter, it gives us an idea of how each of the four parameters (electron density, vertical electron density gradient, turbulence intensity, and Schmidt number—all suspects in the search for PMSE generators) influences the radar reflectivity.

In general, an increase in $N_e$ or a decrease in $H_e$ shifts the level of the entire $\eta_{\text{turb}}$ curve upward, a larger $Sc$ pushes the tail of $\eta_{\text{turb}}$ to higher wavenumbers, and $\epsilon$ tends to do both. As we are in the business of examining the effect of reduced electron diffusivity on radar scatter, let us highlight the importance of $Sc$. Note that in all four plots, Fig. 4.2 to Fig. 4.5, $\eta_{\text{turb}}$ never rises above the incoherent scatter level for $Sc = 1$, even at 46.9 MHz. However, the Jicamarca 50-MHz radar does detect coherent echoes in the equatorial mesopause region with reflectivities that agree with those calculated from in situ measurements of electron density fluctuations using a similar isotropic turbulence scatter model [*Røyrvik and Smith*, 1984], so either there must be extremely strong turbulence there or the exponential fall-off of the *Hill and Bowhill* [1976] model is too rapid. Note the tremendous leverage that the Schmidt number has in extending coherent scatter to higher radar frequencies. Therefore, for isotropic turbulence scatter, raising $Sc$ is the only way to generate PMSE while keeping the other parameters within reasonable bounds. For moderate values of $N_e$, $H_e$, and $\epsilon$, $Sc \sim 100$ can produce typical PMSE reflectivities for the VHF radars. Harking back to the results of Chapter 2, this would require the presence of charged aerosols with $r_a \sim 0.01$ $\mu$m. Later in this chapter we will

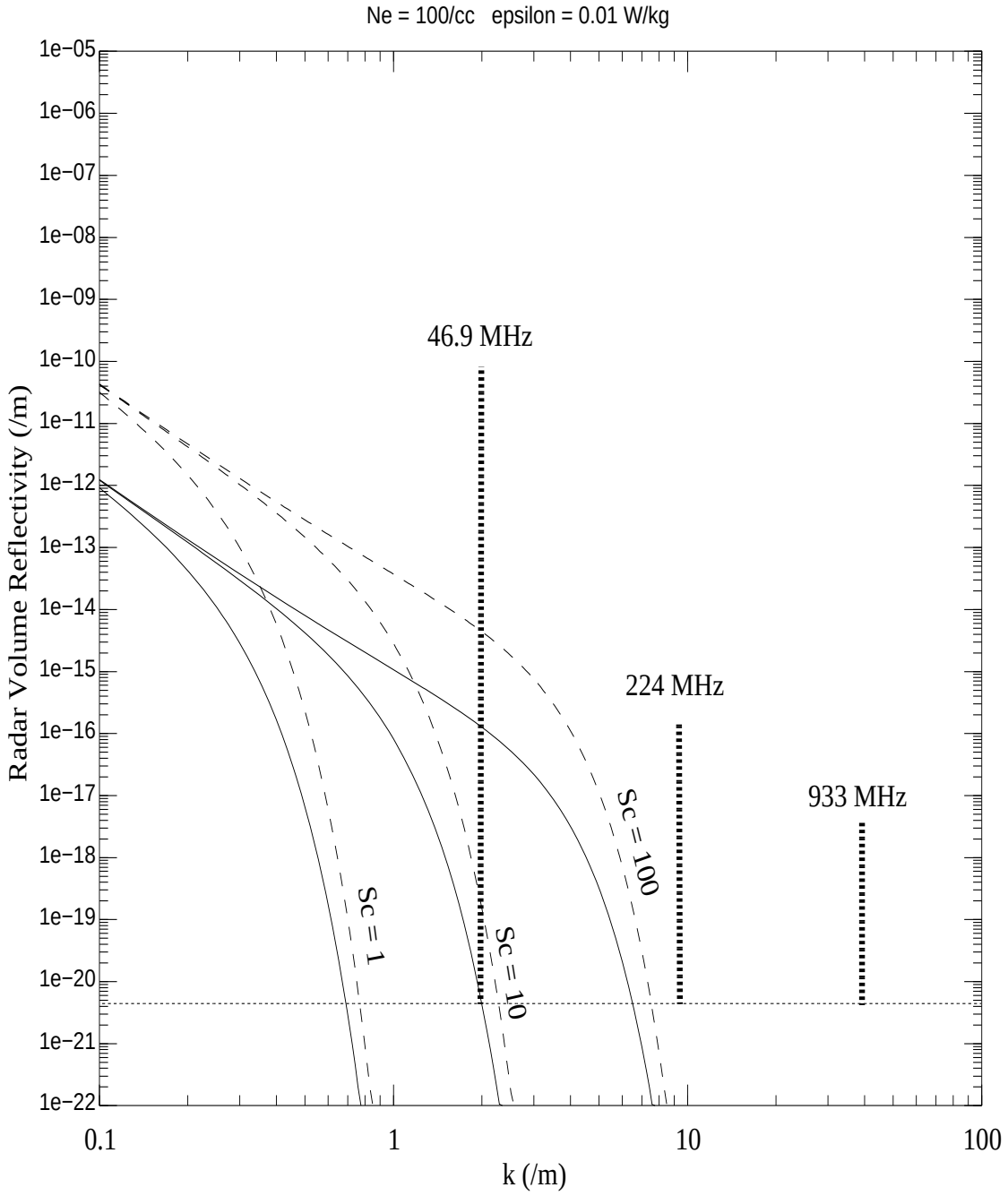


Figure 4.2: Radar volume reflectivity, $\eta_{\mathrm{turb}}$, versus the Bragg wavenumber plotted for different values of $Sc$ and local electron density scale height, $H_e = N_e(dN_e/dz)^{-1}$ (the reciprocal of the normalized electron density gradient). The solid lines correspond to $H_e = 10$ km and the dashed lines correspond to $H_e = 1$ km. Values for the other parameters are $N_e = 10^8$ m$^{-3}$ and $\epsilon = 0.01$ W/kg. For reference, the level of classical incoherent scatter, i.e., the irreducible minimum signal, is plotted (dotted horizontal line) for the given $N_e$. Also the range of reflectivities observed by the 46.9-MHz CUPRI, the 224-MHz EISCAT, and the 933-MHz EISCAT radars from Tromsø, Norway are displayed (vertical bars).

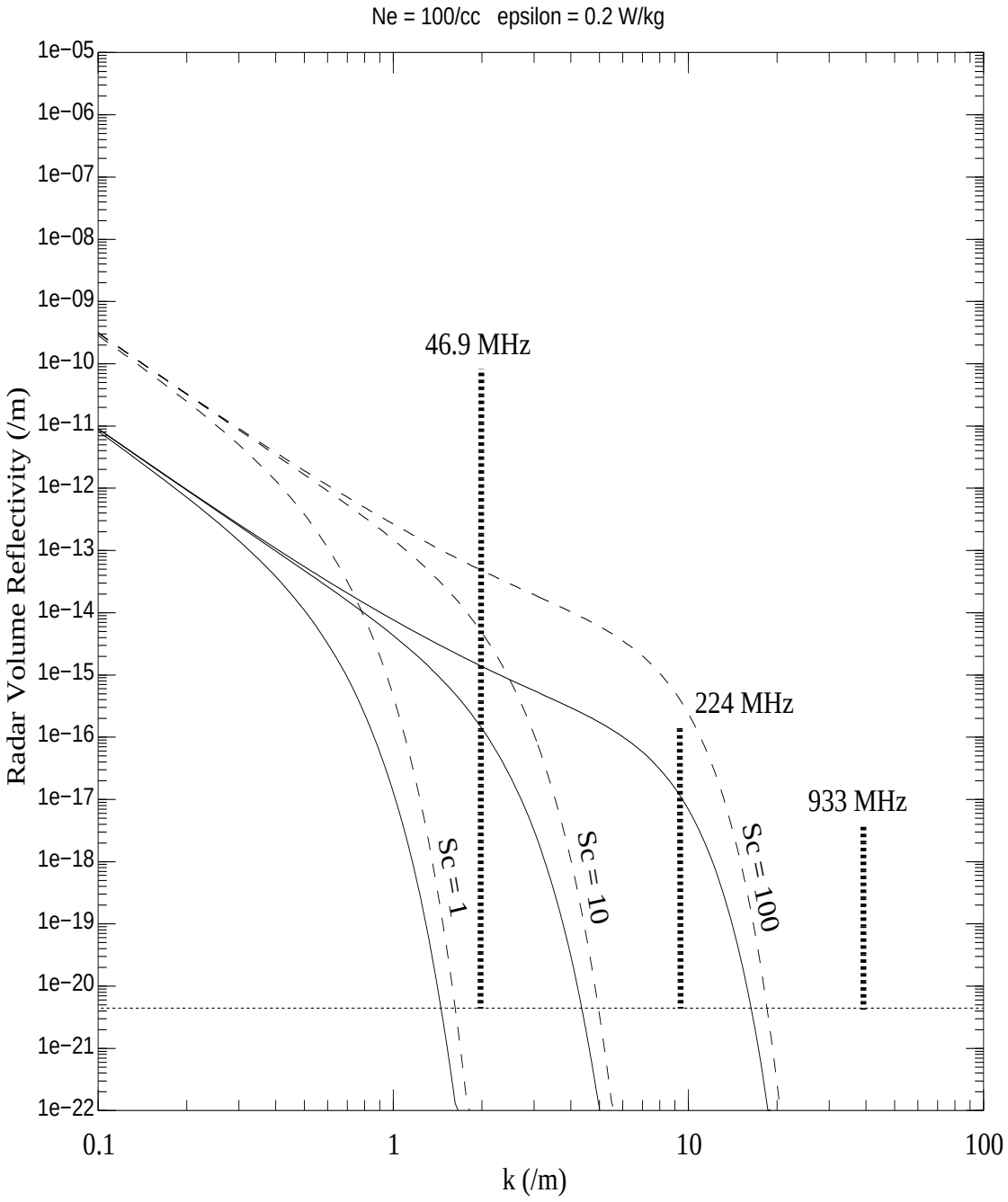


Figure 4.3: Same as Figure 4.2 with $\epsilon = 0.2$ W/kg.

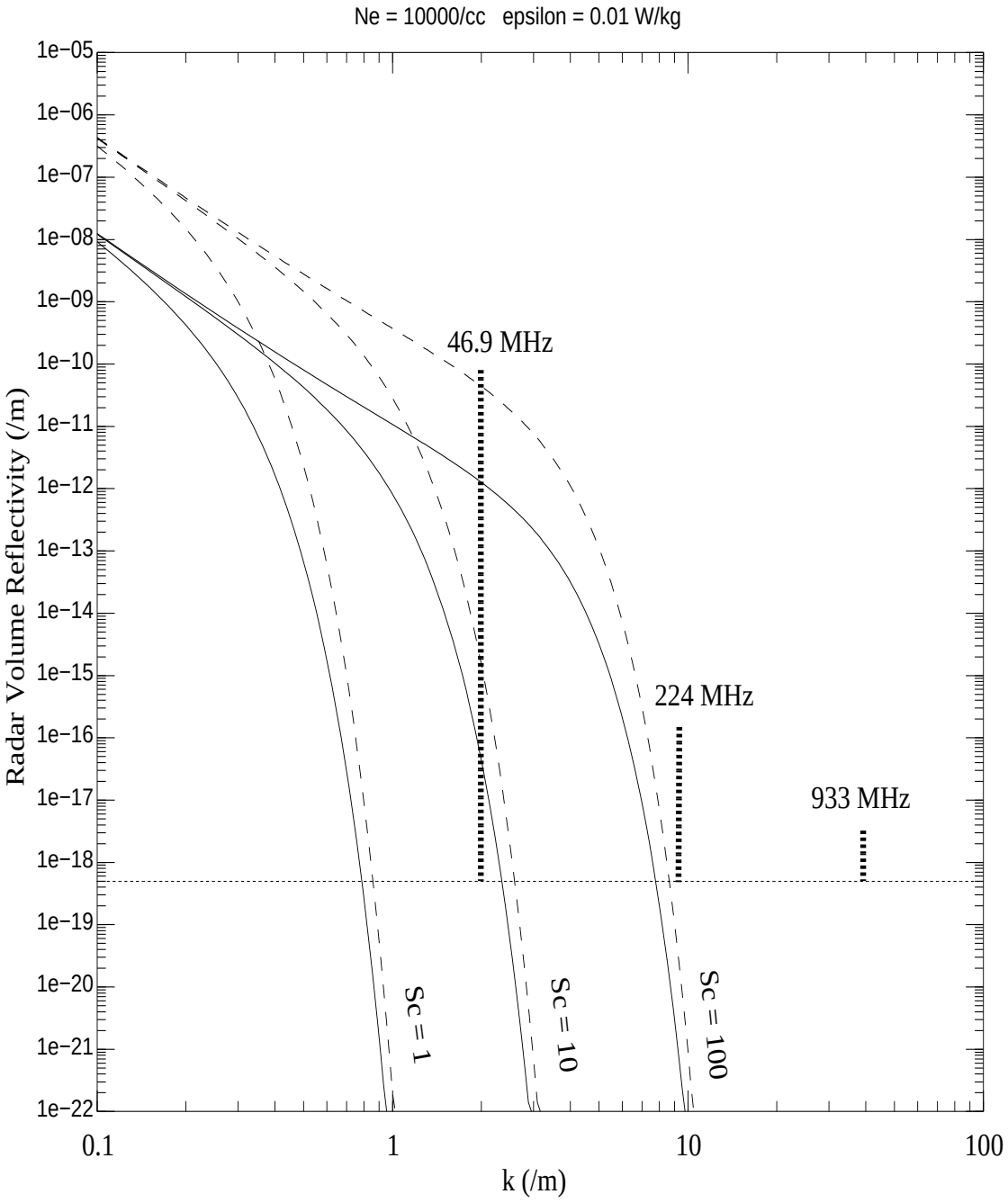


Figure 4.4: Same as Figure 4.2 with $N_e = 10^{10}$ m$^{-3}$.

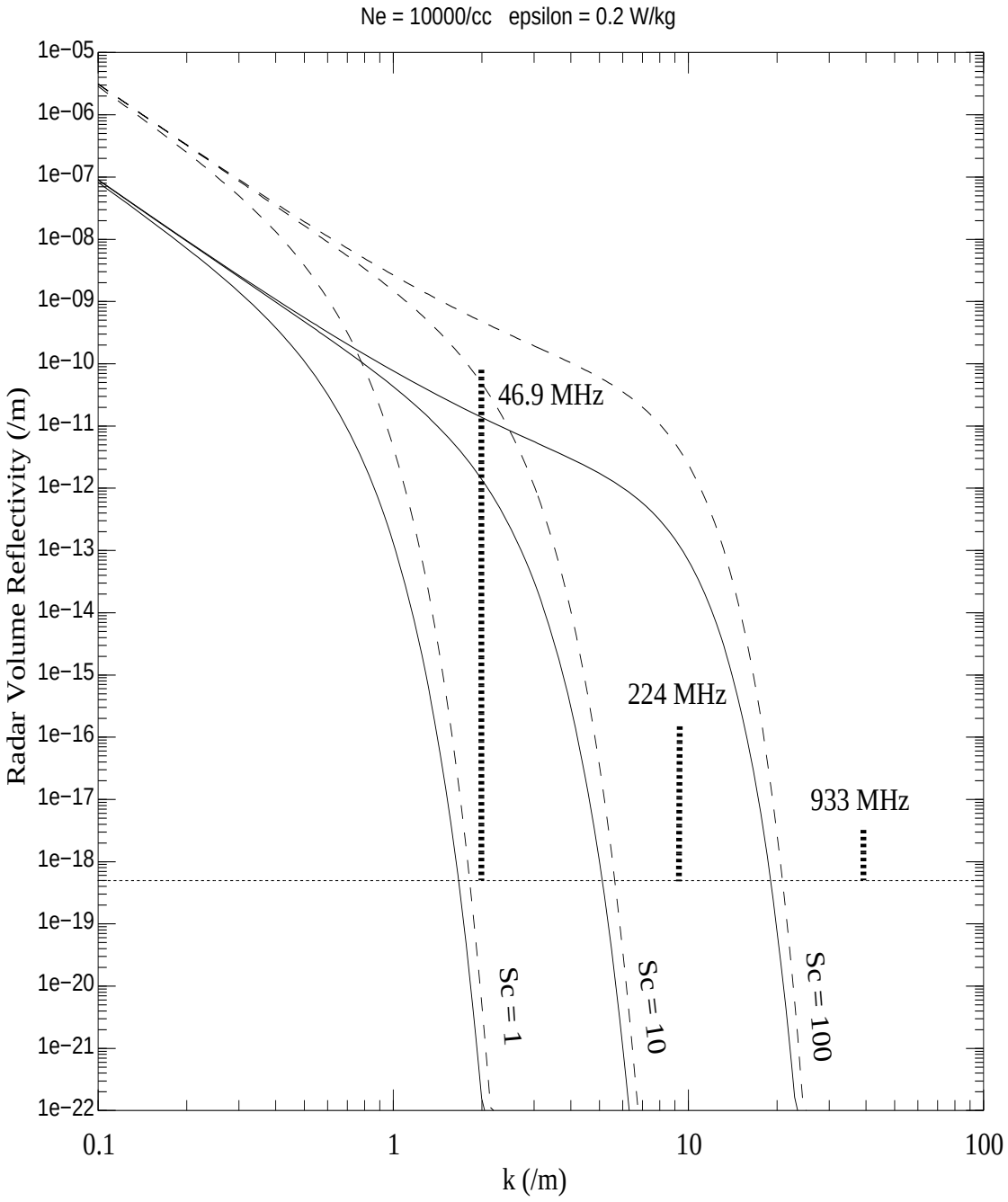


Figure 4.5: Same as Figure 4.2 with $N_e = 10^{10}$ m$^{-3}$ and $\epsilon = 0.2$ W/kg.

address the issue of plausible aerosol size, number density, and charge state.

PMSE at 933 MHz requires either $Sc \sim 5000$, requiring charged aerosols with $r_a \sim 0.07$ $\mu$m, or a combination of extremely high $N_e$ and $\epsilon$ with $Sc \sim 100$. In either case, it is expected that the right condition for enhanced radar scatter would be met less frequently than that for the VHF radars, and this is indeed the case. In both published reports of UHF PMSE, a dramatic increase in the ambient electron density due to the precipitation of highly energetic particles preceded the PMSE events [*Röttger et al.*, 1990*b*; *Cho et al.*, 1992*b*]. Thus, whatever the exact mechanisms, it seems that a high electron density level or another byproduct of particle precipitation such as aerosol charging is necessary for UHF PMSE.

An alternative scattering mechanism (which is also dependent on the presence of charged aerosols) has been proposed by *Havnes et al.* [1990] and we will discuss it in the section on dressed aerosol scatter.

## 4.2 Fossil Turbulence

Imagine going down to the bottom of Taughannock Falls and releasing a tank of nontoxic tracer dye where the pool is still turbulent (see Fig. 4.6). Now run downstream to the flat section where the flow is laminar and wait for the initial release to reach you. Trickle in the dye again and note that it describes a fairly straight line. The original tracer, however, retains a turbulent look as it is carried past you by the current.

What has happened, of course, is that the turbulence-like spatial structures in the scalar additive (the dye) mixed by turbulence has survived beyond the decay of turbulence itself. The term "fossil turbulence" was coined by *Woods* [1969] to describe this phenomenon and "hydropaleontology" has been playfully tossed around as the word to describe its study. Note that fossil turbulence is not turbulence, just as fossil trilobytes are not trilobytes—just their imprints. However, unlike fossil trilobytes, fossil turbulence is not frozen in time; it begins with kinetic energies on the order of the original turbulence and decays with time. (Models of fossil turbulence using frozen initial conditions are called "zombie turbulence." [*Gerz and Yamazaki*, 1990]) Most of the subject has revolved around oceanic observations of

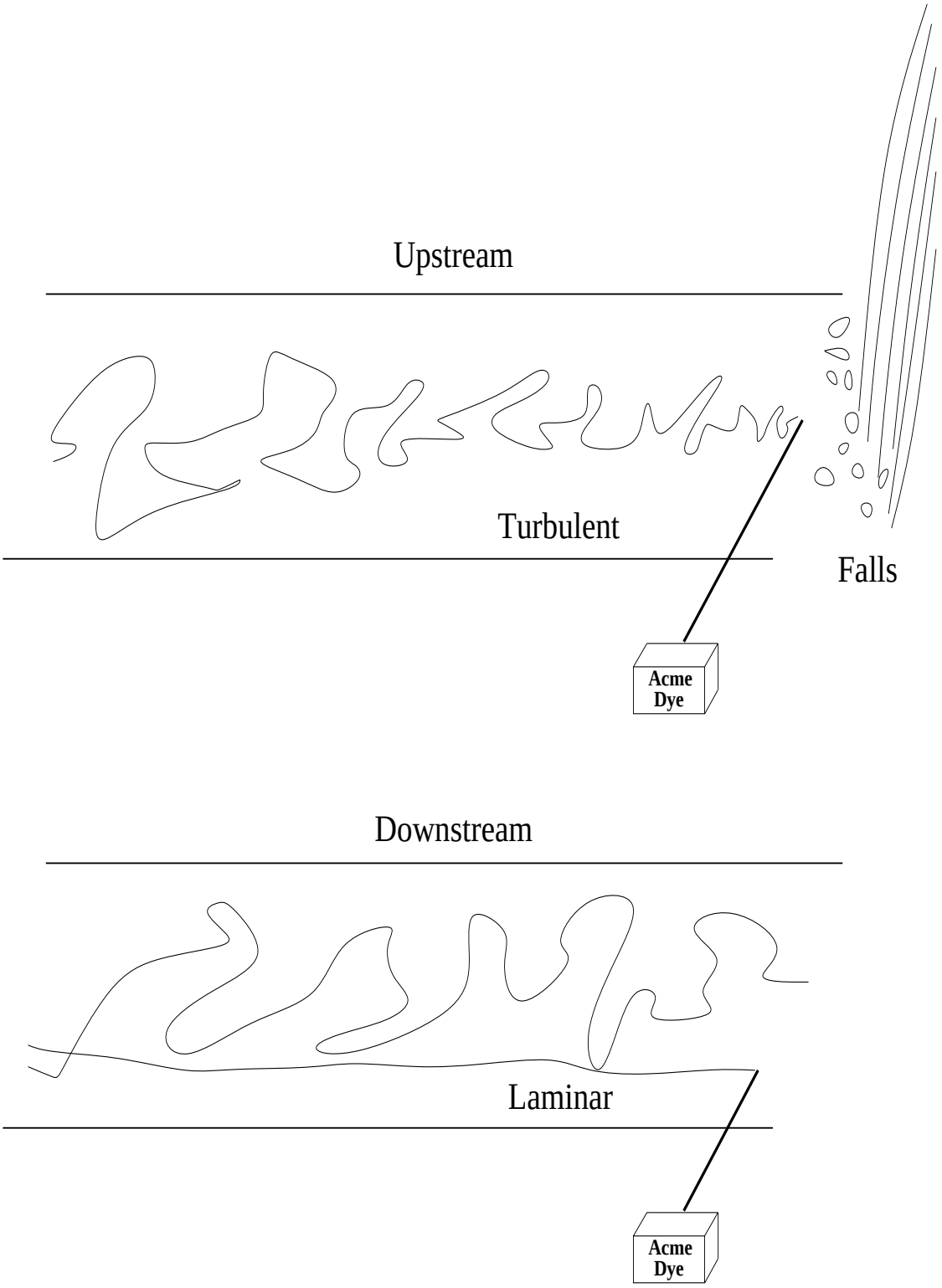


Figure 4.6: Schematic of dye release *gedanken* experiment at Taughannock Falls.

temperature fluctuations. (The reader is referred to *Gibson* [1991] for a review.)

The following scenario unfolds after the source of kinetic energy is removed from the turbulent mixing of a high Schmidt number scalar (see Fig. 4.7). Begin with a turbulent patch of length scale $L_p$ imbedded in a nonturbulent, stably stratified region with an ambient vertical gradient in the scalar. With no energy input, the velocity fluctuation spectrum starts to decay and the inertial subrange shrinks as the inner scale moves to longer lengths. The size of the patch grows due to the entrainment of ambient fluid. The Batchelor scale of the scalar variance spectrum also shifts to larger scales, but the level of the spectrum rises because the difference in the scalar quantity between fluid entrained at the top and bottom increases as the patch grows.

Fossilization sets in as $L_p$ grows to $l_{LS}$, the buoyancy scale. (In fossil turbulence literature, the buoyancy scale is often referred to as the Ozmidov scale.) At this point, the inertial forces become approximately equal to the buoyancy forces. Complete fossilization is deemed to be reached when the viscous dissipation rate subsides to $\epsilon = 24.5\nu\omega_B^2$ [*Stillinger et al.*, 1983] and the Batchelor scale has reached the fossil Batchelor scale $l_{BF} = D^{1/2}\omega_B^{-1/2}$ [*Gibson*, 1986]. The actual breakpoints occur at $C_B l_B$ and $C_B l_{BF}$ where $C_B \approx 4$ [*Gibson*, 1982].

There is some controversy over whether the persistence time of fossil scalar turbulence depends on the scalar molecular diffusivity. The models of *Benilov* [1988] say "yes." *Gibson* [1986] also answered in the affirmative, but later reversed himself [*Gibson*, 1991], stating that the persistence time should be independent of diffusivity because the microstructure dissipation scales adjust to the fossil Batchelor scale and length scales determined by the local strain rates. Gibson [1980] gives a scalar fossil "decay time" of

$$\tau_F = \epsilon_0^{\frac{1}{3}} \nu^{-\frac{1}{3}} \omega_B^{-\frac{5}{3}} \tag{4.29}$$

where $\epsilon_0$ is the energy dissipation rate at the onset of fossilization which lies between the $\epsilon$ of the original turbulence and $\epsilon_F = 24.5\nu\omega_B^2$ which occurs at complete fossilization. ($\epsilon_F \approx 8$ mW/kg for the summer mesopause.) The time $\tau_F$ can be taken as the minimum persistence time for fossil scalar turbulence with $Sc > 1$, since the fossil should last longer if it is dependent on the scalar molecular diffusivity. Turbulence dissipation energy $\epsilon_0 \approx 10$ mW/kg translates to $\tau_F \approx 3$ minutes.

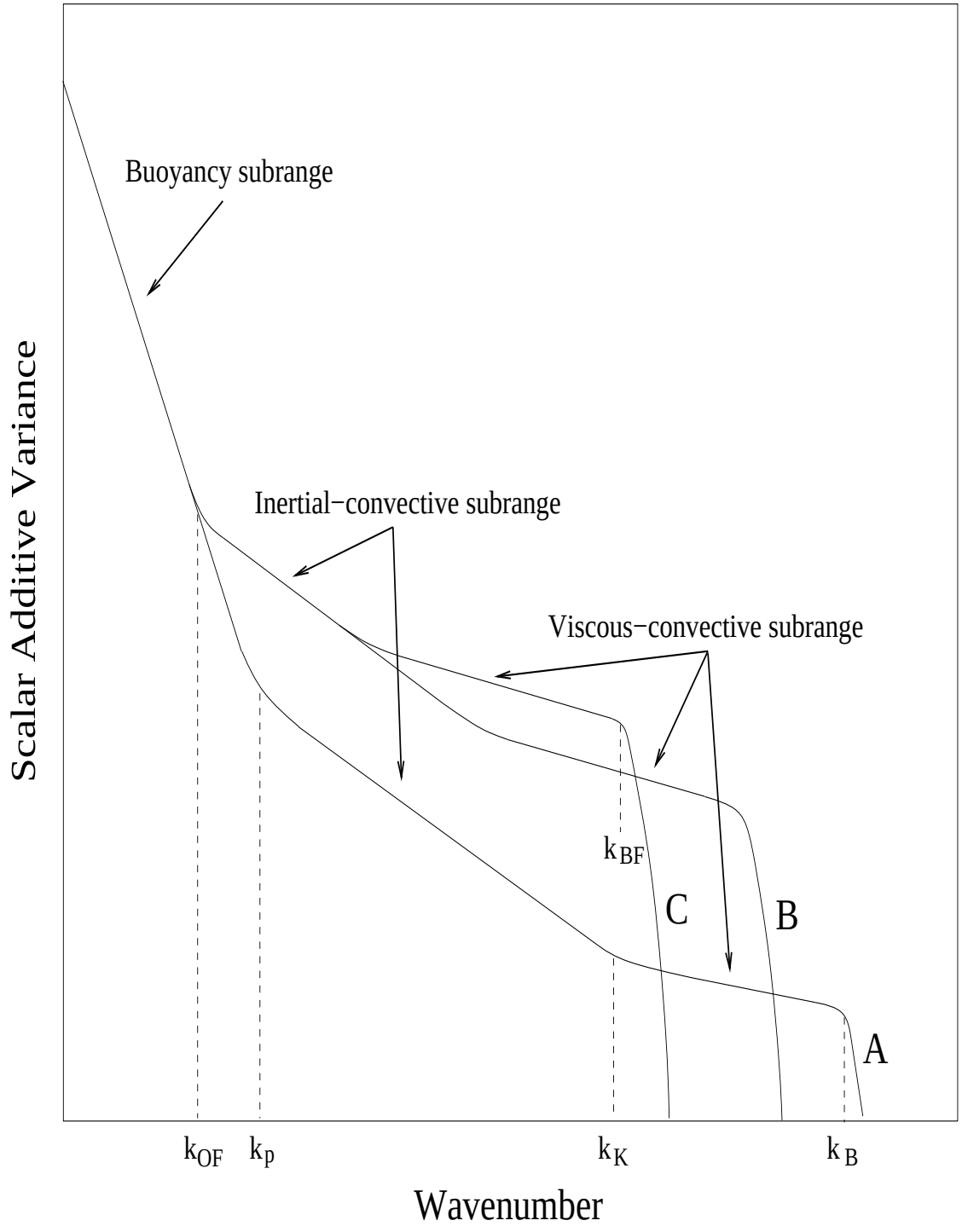


Figure 4.7: A schematic of scalar fluctuation spectra versus wavenumber for progressive stages of turbulence fossilization. A: Active turbulence. B: Fossilization commences. C: Fossilization completed. The wave number $k_{OF} = \epsilon^{-1/2}\omega_B^{3/2}$ is the reciprocal of the fossil Ozmidov scale.

How relevant is fossil turbulence to mesospheric radar scatter? Two possible effects come to mind. First, it can "mask" the intermittent nature of the neutral turbulence in the radar backscatter data. That is, the radar will continue to detect electron density inhomogeneities even though the neutral turbulence may have dropped out momentarily. Completely fossilized electron density turbulence would present large reflectivities for a 50-MHz radar only if the electron Schmidt number is at least 100, because the cutoff length is $C_B l_{BF} \approx 3$ m for $Sc = 100$. The fossil will then last for a few minutes (on the order of $\tau_F$ or more). This is one way to explain the report of a PMSE layer through which rocket probes revealed electron density inhomogeneities but no neutral density fluctuations [*Lübken et al.*, 1992].

Secondly, charged aerosols falling through a thin layer of turbulence will fossilize after descending to a region of calmness and will still create electron density inhomogeneities that scatter radar waves. However, the terminal velocity of an ice sphere of radius 0.07 $\mu$m, using (3.23), is about 0.2 m/s; thus, in 3 minutes the aerosol will fall only 40 m. Since this distance is well within the range resolution of all radars involved, this particular effect is not likely to be detected if it does occur.

## 4.3 Reduced Diffusion Effects on Fresnel Scatter

The two previous subsections explored the effect of reduced electron diffusivity on isotropic turbulence radar scatter. We developed the theory in fair detail because, besides the fact that PMSE exhibit some characteristics that point toward a turbulent scattering mechanism (morphology that correspond to unstable wave and tide phases, saturated velocity amplitudes), the theory is a nice pedagogical tool—it can be used as a black box that takes as its inputs standard parameters such as $N_e$, $H_e$, $\epsilon$, and $Sc$ and out pops the radar reflectivity for any frequency. However, as we noted before, turbulence, even if it is the main driving force behind PMSE, is probably not isotropic most of the time as evidenced by the aspect sensitivity of PMSE backscatter [*Czechowsky et al.*, 1988]. It may be that PMSE result from abrupt steps in the vertical electron density profile that are horizontally coherent

over a Fresnel zone defined to be

$$R_F = \sqrt{\frac{\lambda_R}{2} r} \tag{4.30}$$

where $r$ is the distance to the scatterer. For $r = 85$ km, $R_F$ ranges from 500 m at 46.9 MHz to 100 m at 1.29 GHz. Rocket-measured electron density bite-outs co-located with PMSE layers hint at such a picture. The reflectivity calculation for these Fresnel reflections requires the knowledge of the electron density profile and the results are very sensitive to its shape [*Woodman and Chu*, 1989]. No generalized black box approach is possible which can yield quantifiable insight into the mechanism. Therefore, we will only discuss the conceptual aspects of reduced diffusivity effects on Fresnel reflection. Attempts at deriving radar reflectivity from one-dimensional rocket electron density profiles are currently being performed (C. Alcala and U.-P. Hoppe, private communications).

The principal idea remains the same: radar scatter requires the presence of a Bragg-scale perturbation in the electron density. Something creates the perturbation and diffusion destroys it. The key ratio is the time scale of creation to that of destruction—it needs to be less than one for the density perturbation to grow over time.

The diffusive decay time of an electron density perturbation of size $L$ is given by (4.17). We have already considered various sources and sinks of free electrons in the subsection on isotropic turbulence which may generate density perturbations. The conclusion was that scavenging of electrons by aerosols was the only mechanism which could work faster than diffusion. (Of course, we cannot completely rule out the sparsely explored effects of electrodynamics or some hitherto undiscovered fluid dynamics forcing; for the purposes of this discussion we will stick to what we do know.) Thus, for the maintenance of an electron density perturbation

$$\tau_{\text{diff}} > \frac{1}{\alpha_{ae} N_e} \tag{4.31}$$

where $\tau_{\text{diff}}$ is given by (4.17) and $\alpha_{ae}$ is given by (4.18). A rough estimate of the dependence of $D_e$ on aerosol size is given by (3.26). Then assuming $r_a \gg r_n$,

$m_a \gg m_n$, and $r_a \ll e^2/(8\epsilon_0 kT) = 0.2$ $\mu$m, we arrive at the condition

$$r_a > \left[ \frac{3\pi\zeta}{4L^2 e N_n N_e} \left( \frac{2\epsilon_0 kT m_e}{m_n} \right)^{\frac{1}{2}} \right]^{\frac{2}{7}} \tag{4.32}$$

Taking $N_n = 2 \times 10^{20}$ m$^{-3}$ and $N_e = 10^9$ m$^{-3}$ we get $r_a > 3$ nm for $L = 3.2$ m (46.9 MHz) and $r_a > 0.03$ $\mu$m for $L = 12$ cm (1.29 GHz). Thus, we see that the presence of reasonably sized aerosols makes the maintenance of electron density steps on the order of the radar Bragg scales plausible.

Recently a new scheme for producing Fresnel scatter that relies on the interaction of charged aerosols with the ambient air flow was proposed by *Havnes et al.* [1992]. Assuming the existence of neutral gas vortices imbedded in a field of falling aerosols yields "holes" inside the vortices into which the aerosols cannot penetrate. A sharp gradient in the aerosol density (and correspondingly the electron density) develops at the edge of each vortex. The gradients are maintained against dissipation because the aerosols diffuse slowly. Radar waves then scatter from the resulting steep electron density gradients at the top and bottom sides of the vortex. *Havnes et al.* [1992] were able to produce reasonable values of reflectivity for VHF radars. However, some questionable assumptions were used in the calculations such that one must be wary of the final results. First of all, the existence of neutral vortices with diameters on the order of 2–4 m is a tenuous proposition since the viscous cut-off scale for velocity fluctuations in the mesosphere is in the tens of meters. Secondly, the use of an aerosol size spectrum that extends well above 0.1 $\mu$m assumes a noctilucent cloud condition; it is not likely that such large particles are present most of the time. Finally, in the calculation of the radar reflectivity, the physical cross section of the vortex is used, whereas the radar backscatter is likely to come only from very small sections of each vortex wall due to their high curvatures. Also this radar scatter generation mechanism relies on the existence of high wind shear to create the vortices, but as mentioned earlier *Czechowsky et al.* [1989] have shown that regions of maximum wind shear do not always correlate with enhanced radar backscatter.

In summary, charged aerosols contribute positively in two ways to the generation of Fresnel scatter: (1) they allow electron density perturbations to last longer by

retarding the diffusivity of electrons and (2) they generate electron density inhomogeneities by scavenging electrons (and possibly by the "empty vortex" mechanism proposed by *Havnes et al.* [1992]).

## 4.4 Dressed Aerosol Scatter

So far, the presence of charged aerosols has proved to be critical in the theoretical justification of radar echoes as powerful as those of PMSE. Perhaps it will not be a surprise to the reader that there is yet another way in which charged aerosols can enhance radar scattering.

Picture an aerosol with charge number $Z_a$ in a plasma. ($Z_a$ can be positive or negative.) Statistically there will be a spherical "cloud" of charge $-Z_a$ around the aerosol due to the average surplus or debit of free electrons. This shielding sphere will have a scale length given by the plasma Debye length

$$\lambda_D = \left( \sum_\alpha \frac{N_\alpha Z_\alpha^2 e^2}{\epsilon_0 k T_\alpha} \right)^{-\frac{1}{2}} \tag{4.33}$$

where $\alpha$ refers to each of the plasma particle species.

Now send a radar wave through this "dressed" aerosol. If $Z_a = 1$ then the scattered power will be exactly that of incoherent scatter. However, if the aerosol is multiply charged, and provided that the radar Bragg scale is much longer than the plasma Debye length, the electron "cloud" around the aerosol will respond in phase to the wave and will thus increase the scattered amplitude by $|Z_a|$ and the power by $Z_a^2$. Since there was a decrease in the number of free electrons involved by $|Z_a|$, the per electron enhancement of scattered power over incoherent scatter is proportional to $|Z_a|$.

The above scenario ignores the existence of other aerosols in the near vicinity. If another charged aerosol was placed closer to the original one than the plasma Debye shielding length, then their mutual interaction will tend to cancel the enhancement. Therefore, two conditions need to be met for substantial enhancement of radar scatter above incoherent scatter to take place: (1) $\lambda_R/2 > 2\pi\lambda_D$ and (2) $N_a^{-1/3} \gg \lambda_D$.

Before we go on, a note should be made about the terminology of this type of wave scattering. Historically, it was first discussed in the context of plasma waves in dusty plasma and was called "transition scattering" [*Tsytovich et al.*, 1989]. It was then extended to the case of electromagnetic wave scatter [*Bingham et al.*, 1991] and was proposed as a mechanism for PMSE by *Havnes et al.* [1990]. *Hagfors* [1992] and *La Hoz* [1992] developed a parallel theory using the Debye-Huckel "dressed particle" approach which was one of the bases for the development of incoherent scatter theory. Because of this intimate relationship to incoherent (Thomson) scatter, *Cho et al.* [1992*b*] referred to it as "enhanced Thomson scatter." However, by whatever name it is called, it should still be categorized as a form of coherent scatter by definition. We shall refer to it as "dressed aerosol scatter" in this thesis as a compromise between brevity and descriptiveness.

Assuming for the moment that the $\lambda_R/2 > 2\pi\lambda_D$ condition is met, the radar volume reflectivity of dressed aerosol scatter is [*Hagfors*, 1992]

$$\eta_{\text{dressed}} = \frac{4\pi r_e^2 {Z_a}^2 N_a}{\left(2 + \varpi^2 - Z_a \frac{N_a}{N_e}\right)^2} \tag{4.34}$$

for $N_a^{-1/3} \gg \lambda_D$ and

$$\eta_{\text{dressed}} = \frac{4\pi r_e^2 {Z_a}^2 N_a}{\left(2 + \varpi^2 - Z_a \frac{N_a}{N_e}\right)\left(2 + \varpi^2 - Z_a \frac{N_a}{N_e} + {Z_a}^2 \frac{N_a}{N_e}\right)} \tag{4.35}$$

for $N_a^{-1/3} \ll \lambda_D$, where $\varpi = 4\pi\lambda_{De}/\lambda_R$ and $\lambda_{De}$ is the electron Debye length. Note that this does not allow for a realistically smooth transition in the regime where $N_a^{-1/3} \sim \lambda_D$. Thus, it is expected to be accurate only when sufficiently distanced from the transition zone.

Comparing $\eta_{\text{dressed}}$ to the reflectivity for incoherent scatter [*Dougherty and Farley*, 1963]

$$\eta_{\text{incoherent}} = 4\pi \frac{1 + \varpi^2}{2 + \varpi^2} r_e^2 N_e \tag{4.36}$$

we find that, as expected, large enhancements over incoherent scatter reflectivity are only possible with (4.34) where the spacing between aerosols is greater than the plasma Debye length.

Now we need to make some estimates of the plasma Debye length. If thermal equilibrium and a three-component plasma consisting of electrons, positive ions, and aerosols are assumed then we get

$$\lambda_D = 69\left(\frac{T}{N_e + N_i + Z_a^2 N_a}\right)^{-\frac{1}{2}} \tag{4.37}$$

With the charge neutrality condition $N_e = N_i + Z_a N_a$ (4.37) becomes

$$\lambda_D = 69\left[\frac{T}{2N_e + Z_a N_a\,(Z_a - 1)}\right]^{-\frac{1}{2}} \tag{4.38}$$

To compare $\lambda_D$ to the radar Bragg scales, let us take the worst case scenario where $Z_a = 1$. Then for our usual $T = 130$ K we need about $N_e = 8 \times 10^8$ m$^{-3}$ to satisfy criterion (1) for the smallest Bragg scale of 12 cm (1.29 GHz) that we are considering. The electron density in the summer mesopause usually surpasses this level.

Comparing $\lambda_D$ to the aerosol spacing $N_a^{-1/3}$ is not so straightforward since $\lambda_D$ is a function of $N_a$. A useful alternative is to calculate the minimum aerosol charge required for a given aerosol abundance to fulfill $N_a^{-1/3} \gg \lambda_D$. Fig. 4.8 maps out the regimes for which (4.34) or (4.35) are valid. Equation (4.34) applies in the regions above the curves where significant signal enhancement over incoherent scatter can occur. We note that *Hagfors* [1992] uses $\lambda_{Da}$, the aerosol Debye length, instead of the plasma Debye length as the characteristic length scale of the dressed aerosol. This choice omits the dependency of the critical aerosol charge number on electrons and ions, and Fig. 4.8 correspondingly reduces to one curve, $|Z_a| = 69T^{1/2}N_a^{-1/6}$, wiping out an entire area of possible enhancement in the low-$|Z_a|$, low-$N_a$ regime. This is a significant difference. We assert that the Debye length of the entire plasma mixture rather than just the aerosols must be considered since the fall-off of the aerosol electric potential depends on all the charged constituents. *La Hoz* [1992] is in agreement with our interpretation, but he does not make the point explicitly.

What might be the role of dressed aerosol scatter in PMSE? As one can see from (4.34) and (4.35), the dependence of $\eta_{\text{dressed}}$ on radar frequency is negligible. But we know that PMSE depend sharply on radar frequency (see Fig. 4.2, *Hoppe et al.*

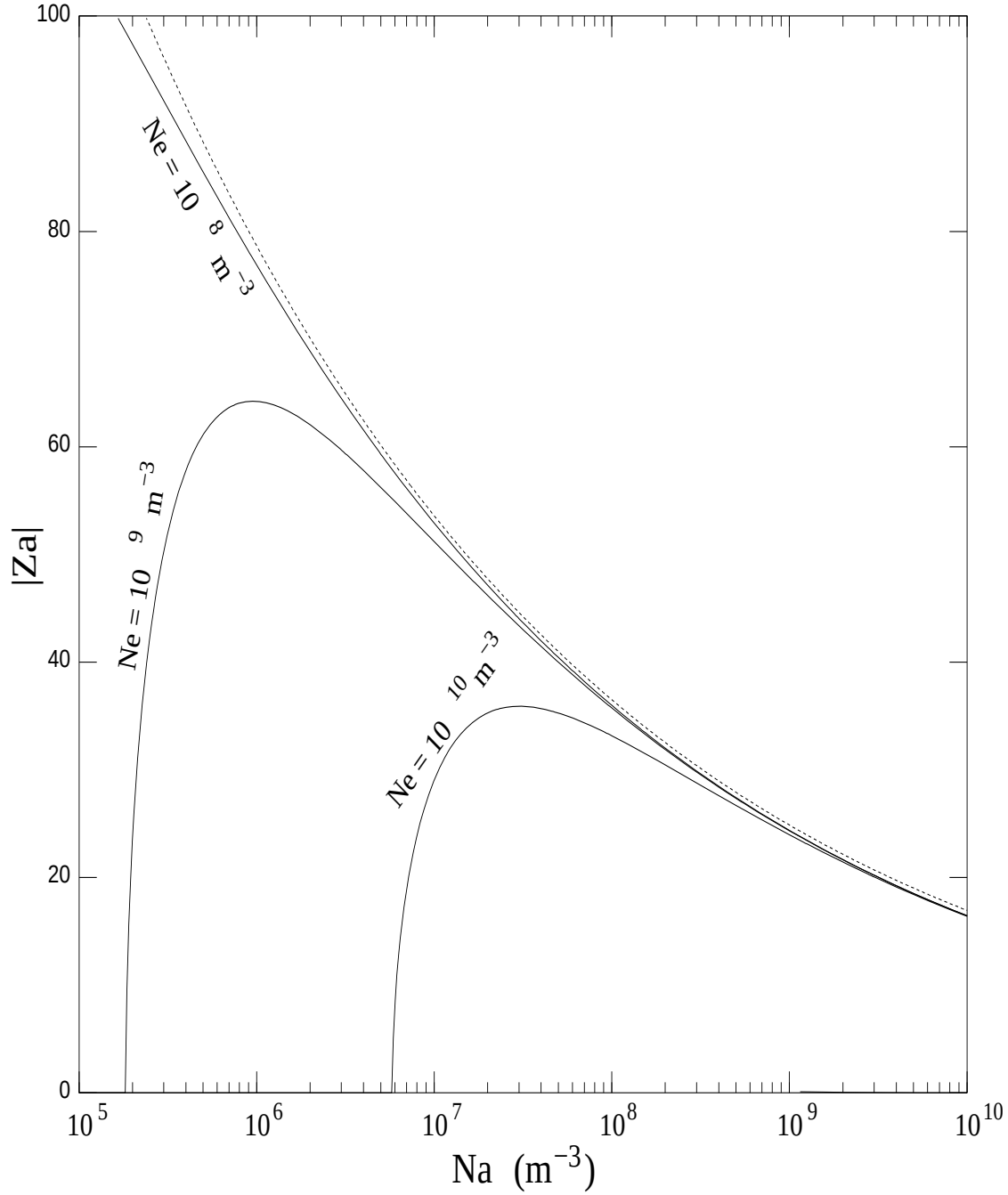


Figure 4.8: Plots of minimum aerosol charge number required for dressed aerosol scatter versus aerosol number density. The regions above the solid curves for the different electron abundances are the regimes where the enhanced scattering can take place. The dotted line represents the case where only the aerosol Debye length is taken into account.

[1990], and *Röttger et al.* [1990*b*]). Therefore, we must immediately rule out the possibility that dressed aerosol scatter is responsible for all PMSE, in disagreement with *Havnes et al.* [1990].

As we have seen in previous sections, coherent scatter due to the raised Schmidt number effect does a good job of accounting for both the absolute reflectivities and their dependence on radar frequency except, perhaps, at the highest frequencies. Under typical conditions, dressed aerosol scatter will be overwhelmed by the Schmidt number effect at VHF. It is in the UHF regime where dressed aerosol scatter could contribute to PMSE.

Let us take a concrete example. During the one published PMSE event that was observed by the EISCAT 933-MHz radar, the ambient electron density was estimated to be $N_e = 4 \times 10^9$ m$^{-3}$ which corresponds to $\eta_{\text{incoherent}} = 2 \times 10^{-19}$ m$^{-1}$. The PMSE layer had a reflectivity of $\eta = 2 \times 10^{-18}$ m$^{-1}$, so (sticking with one significant figure) dressed aerosol scatter needs to provide $\eta_{\text{dressed}} = 2 \times 10^{-18}$ m$^{-1}$. We can solve (4.34) to obtain the $Z_a$ needed for a given $N_a$.

$$Z_a = \frac{2 + \varpi^2}{\frac{4\pi r_e^2 N_a}{\eta_{\text{dressed}}} - \frac{N_a^2}{N_e^2}} \left[ -\frac{N_a}{N_e} \pm \left( \frac{4\pi r_e^2 N_a}{\eta_{\text{dressed}}} \right)^{\frac{1}{2}} \right] \tag{4.39}$$

The result of (4.39) is plotted in Fig. 4.9 for positive aerosol charge and parameters for the 933-MHz PMSE event. (The magnitudes are slightly higher for negative aerosol charge, but of the same order.) Also shown in the same figure are the regime where the raised Schmidt number effect is expected to dominate and the region where mutual interactions between aerosols tend to nullify the dressed aerosol scattering enhancement. Note that the minimum charge per aerosol needed is $Z_a = 40$ at $N_a = 4 \times 10^7$ m$^{-3}$.

Dressed aerosol scatter differs from incoherent scatter in another important way. Because the Doppler spectral width is inversely proportional to the time taken by the aerosol to diffuse $\lambda_R/4\pi$, where $\lambda_R$ is the radar wavelength, the width should be much narrower than that for the ion-controlled incoherent scatter. Indeed, the spectra of the PMSE observed by the EISCAT 933-MHz radar were much narrower than the usual incoherent scatter spectra [*Röttger et al.*, 1990*b*].

*Fukuyama and Kofman* [1980] calculated the full-width-half-maximum incoher-

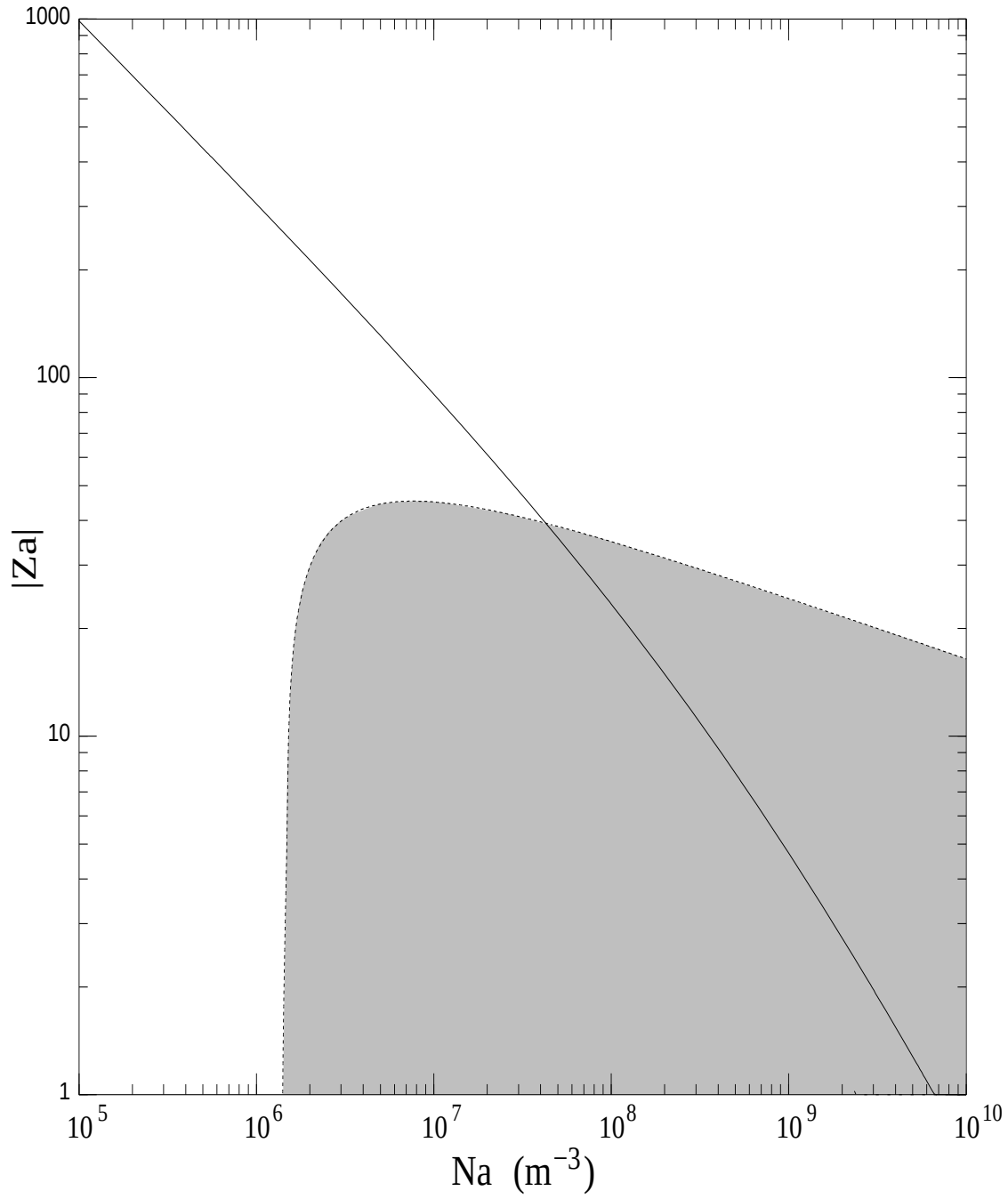


Figure 4.9: Aerosol charge necessary to explain the PMSE event observed by the EISCAT 933-MHz radar (solid line). The area under the dotted line (shaded) is where mutual interactions between aerosols nullify the dressed scattering effect.

ent scatter spectral width to be

$$\Delta f_{\text{incoherent}} = \frac{16\pi}{\lambda_R^2} \frac{2+\varpi^2}{1+\varpi^2} \frac{kT}{m_i \nu_{in}} \tag{4.40}$$

where $\nu_{in}$ is the ion-neutral collision frequency. Since $kT/m_i\nu_{in}$ is the diffusion coefficient for ions, we can naively generalize (4.40) to

$$\Delta f_{\text{dressed}} = \frac{16\pi}{\lambda_R^2} \frac{2+\varpi^2}{1+\varpi^2} D_a \tag{4.41}$$

for dressed aerosol scatter, where $D_a$ is given by (3.25) or (3.26). Monodisperse aerosols are assumed. Equation (4.41) is strictly valid only for the case of a two-species plasma, i.e., electrons and positively charged aerosols, and is not valid for $\varpi^2 \gg 1$, i.e., if $\lambda_R/4\pi$ is much less than the radius of the electron cloud shielding the aerosol. Fig. 4.10 shows the variation of the spectral width with aerosol radius for polar summer mesopause parameters.

Realistically, the electrons will enshroud aerosols and ions of various size such that the resulting spectrum would be a sort of superposition of spectra produced by the entire range, so that the spectral information would be smeared out. If, however, the electrons are divided between the positive ions and one fairly well defined size of aerosol, one should be able to see the contributions from each in the spectra: the aerosol portion should be much narrower. This is analogous to the technique used in extracting ion composition information from conventional incoherent scatter data (e.g., *Farley et al.* [1967]). As one moves into a region where dressed aerosol scattering becomes important, one would expect to see a narrow spectral peak starting to poke out of the normal, broad, incoherent scatter spectrum. If the aerosols are completely dominant, then the broad component should disappear altogether. If the vertical resolution of the radar is good enough, one may even observe the narrowing of the aerosol component with descending height corresponding to an increase in size due to sedimentation. However, one would not expect to see the extremely narrow spectra using a typical D region incoherent scatter radar mode, since such a great number of time lags need to be measured. For example, the EISCAT 933-MHz data clearly show a narrowing of the spectral width in the PMSE height bin, but due to the applied radar program

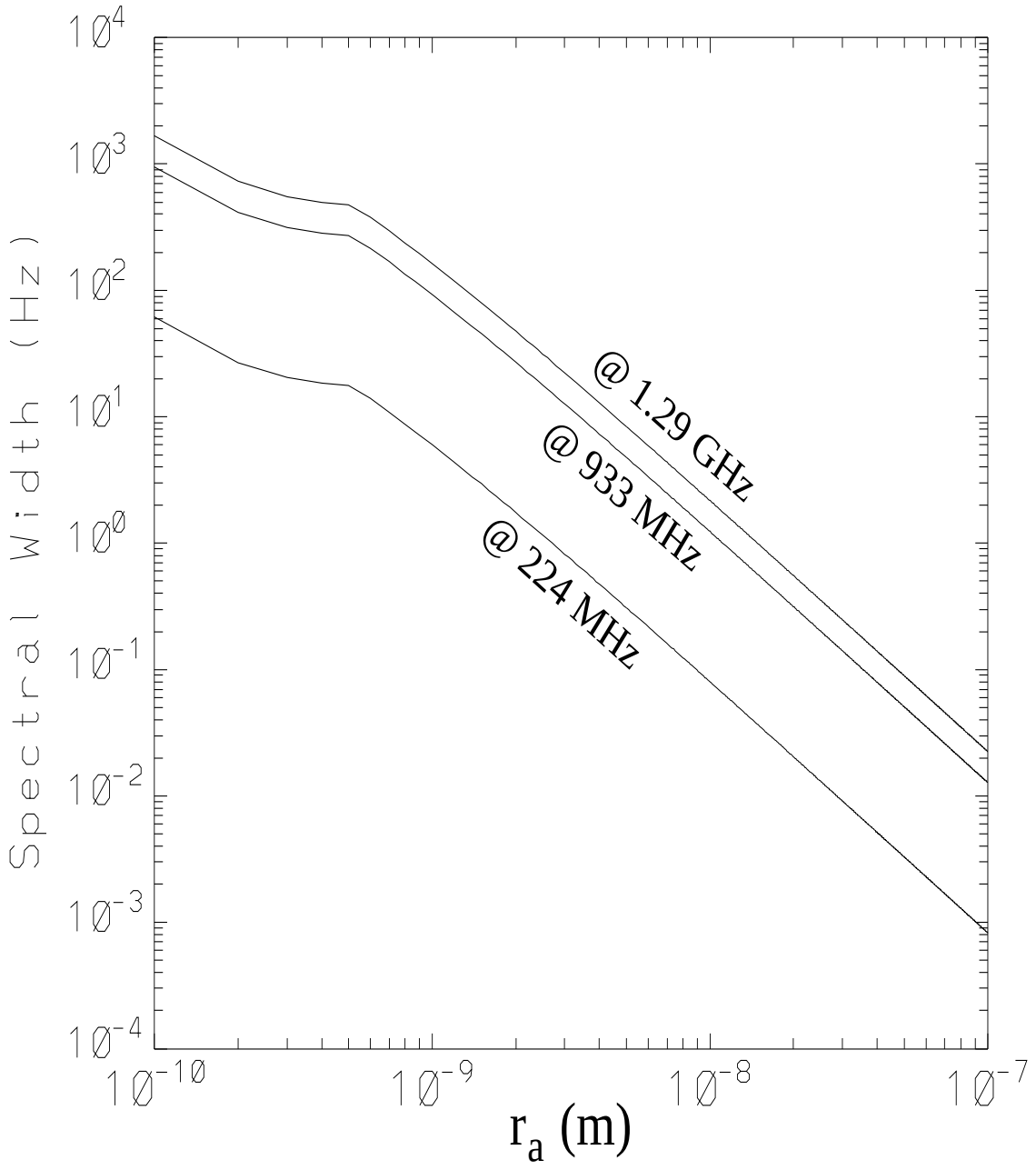


Figure 4.10: Doppler spectral width versus aerosol radius for dressed aerosol scatter at selected radar frequencies. The bump near $r_a = 5 \times 10^{-10}$ represents the transition from the polarization to the hard sphere collision model.

it was not possible to resolve widths less than 20.4 Hz [*Röttger et al.*, 1990*b*]. We are currently planning a high Doppler resolution experiment using the Sondrestrom radar.

## 4.5 Discussion

All the promising mechanisms for PMSE production that we have explored in this chapter depend crucially on the presence of aerosols. In one important sense, this is encouraging since the dependence would explain the fundamental climatology of PMSE, i.e., their appearance only in the polar summer and only in the region of the mesopause; ice aerosols of radii greater than a few nanometers can only grow in the cold temperatures that occur precisely within those seasonal and altitudinal constraints. However, we have so far estimated values of aerosol charge, number density, and size that could account for the PMSE reflectivities without evaluating the plausibility of the numbers with respect to real aerosols in the summer mesopause. Now we need to examine the observational and modeling data for these particles to see whether the previously discussed theories of PMSE are really appropriate.

In the next chapter, we will examine the characteristics of the aerosols that exist in the summer mesopause. We will explore the size, mass and number densities, composition, and most importantly, the charge state of the aerosols. At the end of the chapter, we will discuss the PMSE theories that best fit the observations and the types of charged aerosols that are most likely to exist in the summer mesopause.

# Chapter 5

# The Characteristics of Aerosols in the Summer Mesopause

Aerosols in the summer mesosphere can be divided into two categories: meteoric dust and ice particles. The former, along with ions, are thought to serve as nucleation sites for the latter. Let us now examine them separately.

## 5.1 Meteoric Dust

First, the terminology: an interplanetary particle entering the atmosphere is a meteoroid; the optical and radio wave scattering phenomena that the interaction of the meteoroid with the atmosphere produces is a meteor; if a remnant of the original meteoroid survives intact through the atmosphere, it is called a meteorite.

Most of the incoming meteoric material ablates between 80 and 100 km. The meteoric smoke particles (MSP) left in the wake of vaporization quickly recondense and begin to coagulate into dust. Unfortunately, observational data for these dust particles is extremely sparse. Only very recently have there been any reports of in situ measurements of MSP [*Schulte and Arnold*, 1992]. Thus, we must rely on the modeling efforts of *Hunten et al.* [1980] for quantitative results. The following is a brief summary of their work.

Assuming a reasonable mass influx rate and velocity distribution, the altitude distribution of dust peaks at 84 km, with a fairly rapid cutoff above 90 km and a slow decay below 80 km. The peak concentration depends greatly on the size of

the initial smoke particle. *Hunten et al.* [1980] recommends an initial radius of 0.2 nm, which yields a peak dust density of about $6 \times 10^{10}$ m$^{-3}$, which is equal to or greater than the ambient plasma density. If an initial smoke particle radius of 1 nm is assumed (which is what *Turco et al.* [1982] does in their NLC model), the peak dust concentration becomes $2 \times 10^{9}$ m$^{-3}$, which is still comparable to a typical plasma density.

Dust growth by coagulation is expected to be a minor factor in the mesopause region, thus the size distribution peaks near the initial smoke particle size. The concentration drops off rapidly with radius, e.g., by four orders of magnitude between radius 0.2 nm and 2 nm for an initial smoke particle radius of 0.2 nm.

Dust composition is uncertain, but is likely to be a mixture of meteoric metals and atmospheric elements. Oxidation of atoms such as Fe and Si are likely to occur before recondensation, thus forming compounds such as $SiO_2$ and FeO. The sodium layers observed around 90 km are also believed to be the result of ablating meteoroids.

In short, the meteoric dust is a substrate of very small, nanometer size aerosols, with a concentration on the order of the ambient electron density. Due to their small size they are thought to be optically undetectable. Because their existence is not limited to the summer, they cannot be the direct and only cause of PMSE. They are, however, important as nucleation cores for the growth of ice particles.

## 5.2 Ice Particles

Because of the extremely cold temperatures in the summer mesopause, water vapor can condense into ice even though the air is very dry. Hydrated protons are the smallest examples of this phenomenon and they (and meteoric dust), in turn, become seeds around which more water molecules will cluster. The ice aerosols then grow through coalescence. If the conditions are right to sustain an extended growth period, then the particles become large enough to be optically visible as NLCs.

Because of the difficulty of detecting the smaller aerosols, and due to the historical fascination with NLCs, most of the existing ground-based and rocket-borne observational data were taken in the presence of visible NLCs. Therefore, the

statistics are bound to be skewed toward conditions in which very large particles are present. For example, the average measured height of the cloud layer at 83 km only gives the lower boundary of the ice particle distribution since the largest particles are expected to be at the bottom of the distribution due to sedimentation. Thus, we have no measurement of how far the ice particle layer extends upward. The same thing can be said for the size distribution. Furthermore, ambiguities exist in all the different types of observational methods used to extract information about the state of the ice aerosols; indeed, to this day, it has not been conclusively proven that NLCs are composed of ice. Therefore, once again, we must rely heavily on the prediction of models. Below, we describe selected results of a model by *Jensen and Thomas* [1991].

For a temperature profile that is at a constant 128 K between 87 and 92 km and linearly increasing above and below, the model predicts a rather broad height distribution of ice crystals which peaks around 86 km at a density of $1 \times 10^8$ m$^{-3}$. If a narrower mesopause is assumed between 86 and 88 km, then a correspondingly narrower layer of ice crystals results with a higher peak concentration of about $1 \times 10^9$ m$^{-3}$. The model also predicts a significant depletion in the dust concentration since they were used up by the formation of the ice aerosols. Average density values inferred from observations range from $1 \times 10^6$ m$^{-3}$ [*Rössler*, 1972] to $1 \times 10^{11}$ m$^{-3}$ [*Thomas and McKay*, 1985].

The size distribution predicted by the model generally shifts to larger radii with decreasing height. At 86 km the peak in the size distribution is at a radius of 0.01 $\mu$m, while at 83 km it is around 0.03 $\mu$m. Measurements taken by rockets that flew through visible NLC layers yielded peaks at radii 0.01 $\mu$m [*Tozer and Beeson*, 1974] and 0.06 $\mu$m [*Farlow et al.*, 1970]. In regards to the upper limit of aerosol size, experimentalists tend to fall in either of two schools of thought: the "Western" which sees the upper limit to be at most 0.13 $\mu$m and probably half that, and the "Eastern" which believes in a much higher limit on the order of 0.7 $\mu$m (see discussion in *Gadsden and Schröder* [1989]).

The composition of NLC particles is believed to consist mostly of pure ice with some meteoric dust imbedded as nucleation cores. *Havnes et al.* [1990] also raised the possibility that smoke from ablating meteoroids might condense directly onto

the surface of the ice crystals, thus changing their photoelectric properties.

## 5.3 Aerosol Charge States

Because the aerosols exist within a plasma, they will inevitably become electrically charged. The amount of average charge will be determined by the equilibrium of all currents to the aerosol. The currents result from collisions with electrons and ions, photoemission, and secondary electron emission if the colliding electrons are highly energetic.

Assuming a plasma consisting of electrons, positive ions, and aerosols, and assuming a negligible relative velocity between the aerosols and the other charged components, the currents due to primary electrons and ions are [*Spitzer*, 1978]

$$J_e = -\pi r_a^2 N_e e \left(\frac{8kT}{\pi m_e}\right)^{\frac{1}{2}} e^{\frac{e\phi_a}{kT}} \tag{5.1}$$

$$J_i = \pi r_a^2 N_i e \left(\frac{8kT}{\pi m_i}\right)^{\frac{1}{2}} \left(1 - \frac{e\phi_a}{kT}\right) \tag{5.2}$$

for $\phi_a < 0$ and

$$J_e = -\pi r_a^2 N_e e \left(\frac{8kT}{\pi m_e}\right)^{\frac{1}{2}} \left(1 + \frac{e\phi_a}{kT}\right) \tag{5.3}$$

$$J_i = \pi r_a^2 N_i e \left(\frac{8kT}{\pi m_i}\right)^{\frac{1}{2}} e^{\frac{e\phi_a}{kT}} \tag{5.4}$$

for $\phi_a > 0$, where $\phi_a$ is the aerosol surface potential.

If the aerosols are assumed to be composed of pure ice, then their photoelectric work function is likely to be about 8.7 eV (the value for amorphous ice) [*Baron et al.*, 1978]. Because, under solar quiet conditions, the solar spectrum reaching the mesopause largely cuts off at 6.7 eV [*Allen*, 1964], the photoemission current can be neglected. Secondary electron emission can also be ignored.

An equilibrium condition is reached when $\sum_\alpha J_\alpha = 0$, which yields

$$1 - \frac{e\phi_a}{kT} = \frac{N_e}{N_i}\left(\frac{m_i}{m_e}\right)^{\frac{1}{2}} e^{\frac{e\phi_a}{kT}} \tag{5.5}$$

Assuming $N_e = N_i$ and using the mass of $H^+(H_2O)_5 = 1.5 \times 10^{-25}$ kg for the ion mass [*Björn et al.*, 1985], we get $\phi_a = -49$ mV. The charge number is given by

$$Z_a = \frac{C\phi_a}{e} \tag{5.6}$$

where the capacitance $C$ of a spherical aerosol in plasma is given by [*Whipple et al.*, 1985]

$$C = 4\pi\epsilon_0 r_a e^{-\frac{r_a}{\lambda_D}} \tag{5.7}$$

for $\lambda_D \ll N_a^{-1/3}$, i.e., if the aerosols fall outside of each other's Debye sphere. So the aerosol charge is given by

$$Z_a = \frac{4\pi\epsilon_0 r_a e^{-\frac{r_a}{\lambda_D}} \phi_a}{e} \tag{5.8}$$

Strictly speaking, $\lambda_D$ is not independent of $Z_a$ so (5.8) is not as simple as it appears. However, since $r_a \ll \lambda_D$, we can neglect the Debye shielding term. Subsequently we arrive at

$$Z_a = -3.4 \times 10^7 r_a \tag{5.9}$$

A more sophisticated calculation using polydisperse ice crystals and charge distribution yielded a similar dependence, $Z_a = -4.1 \times 10^7 r_a$, for radii greater than about 10 nm [*Jensen and Thomas*, 1991]. For smaller ice particles, the charge was shown to be constant at $Z_a = -1$. This makes sense physically since the charge comes in quantized packets (electrons) and the electron thermal speed is much greater than that of an ion; thus, on the average, the aerosol will be in the $Z_a = -1$ state more often that in the uncharged state.

The moral of this story is that pure ice aerosols will be charged to a low negative value that increases in magnitude with radius. The charge value is limited by the electron temperature, and even for a large particle of radius 0.1 $\mu$m, $Z_a$ will only be about -3 to -5.

It may, however, be possible for the aerosols to be charged positively if their photoelectric work function is reduced or the energy spectrum of incoming radiation and particles is enhanced. The former condition could happen if the ice is sufficiently contaminated by meteoric metals and the latter condition occurs, for

example, during geomagnetic storms or polar cap absorption events.

The current due to photoemission is [*Havnes et al.*, 1990]

$$J_\nu = \pi r_a^2 \Lambda \gamma F_\nu e \tag{5.10}$$

where $\gamma$ is the photoemission efficiency which is about 1 for metals and 0.1 for dielectrics [*Goertz*, 1989],

$$\begin{aligned} \Lambda &= 3 \times 10^4 \pi r_a^3 \qquad r_a \leq 3 \times 10^{-7} \text{ m} \\ \Lambda &= \pi r_a^2 \qquad r_a > 3 \times 10^{-7} \text{ m} \end{aligned} \tag{5.11}$$

is the effective cross section factor for absorption (for ice), and $F_\nu$ is the flux rate per unit incident area of photons. For a solar spectrum with a cutoff at 6.7 eV [*Havnes et al.*, 1992],

$$F_\nu = \left\{ 2.6 \times 10^{23} e^{-\frac{\phi_a + \phi_w}{\phi_w}} - 5.2 \times 10^{16} \right\} H\left(6.7 - \phi_a\,[\text{eV}] - \phi_w\,[\text{eV}]\right) \tag{5.12}$$

where $H$ is the Heaviside step function. For positively charged aerosols the $J_i$ will be negligible and the current equilibrium condition becomes $J_e + J_\nu = 0$ which yields

$$N_e \left( \frac{8kT}{\pi m_e} \right)^{\frac{1}{2}} \left( 1 + \frac{e\phi_a}{kT} \right) = \Lambda \gamma F_\nu(\phi_a) \tag{5.13}$$

Assuming $\gamma = 0.1$, $N_e = 10^9$ m$^{-3}$, and $\phi_w = 2.3$ eV (the value for Na), we numerically solve (5.13) for $\phi_a$ and substitute into (5.8) to get

$$\begin{aligned} Z_a &= 3 \qquad r_a = 0.001\ \mu\text{m} \\ Z_a &= 29 \qquad r_a = 0.01\ \mu\text{m} \\ Z_a &= 290 \qquad r_a = 0.1\ \mu\text{m} \end{aligned} \tag{5.14}$$

Thus we see that if the aerosol work function is low, significant positive charging is possible for large aerosols. (Note that in the above calculation we had assumed $\lambda_D \ll N_a^{-1/3}$. If this condition is not met, i.e., if the aerosol potentials are affected by each other's presence, then the equilibrium charge state will be somewhat lower

[*Goertz and Ip*, 1984].)

Precipitation of energetic electrons might also charge the aerosols positively through secondary electron emission. For the sake of simplicity let us assume a monoenergetic flux of electrons. The current to a positively charged aerosol due to secondary electron emission is then given by [*Meyer-Vernet*, 1982]

$$J_{\rm sec} = \pi r_a^2 e \delta F_s e^{-\frac{e\phi_a}{kT_s}} \left(1 + \frac{e\phi_a}{kT_s}\right) \tag{5.15}$$

where

$$\delta(E) = 7.4\delta_m \frac{E}{E_m} e^{-2\sqrt{\frac{E}{E_m}}} \tag{5.16}$$

is the electron yield function, $F_s$ is the flux per unit area per unit time of the primary electrons, and $T_s$ is the thermal energy of the emitted electrons. Note that the electron yield peaks at $E = E_m$. Unfortunately, the parameters of the electron yield function are not known for ice. We will use typical values which are known for other dielectrics: $\delta_m \approx 10$ and $E_m \approx 2$ keV. $kT_s$ is typically $\sim 3$ eV [*Bruining*, 1954].

Ignoring the photoelectric and ion currents, we get $J_e + J_{\rm sec} = 0$. Assume $N_e = 10^{10}$ m$^{-3}$, $T = 130$ K, and $E = 40$ keV, which is about the minimum energy necessary for an electron to penetrate below $\sim 90$ km altitude. Then plugging in all the values, we have

$$7 \times 10^{14} \left(1 + 89\phi_a\right) = 0.2 e^{-0.3\phi_a} \left(1 + 0.3\phi_a\right) F_s \tag{5.17}$$

Thus, we see that in order for secondary electron emission to even begin to charge an ice aerosol positively, the flux of primary electrons must be on the order of $F_s \sim 10^{15}$ m$^{-2}$s$^{-1}$. However, even for a fairly strong precipitation event such a large flux is not likely to be realized. *Larsen et al.* [1976], for example, show a differential flux of precipitating electrons during a $-4$ $K_p$-index event of $2 \times 10^7$ m$^{-2}$s$^{-1}$ per keV at 30 keV. Therefore, aerosol charging due to secondary electron emission appears to be negligible.

The ultimate upper bound for the amount of charge that an aerosol can sustain is dictated by the electrostatic fragmentation criterion, i.e., the point at which the

electrostatic stress exceeds the tensile strength of the material. For a sphere with a homogeneously charged surface, the critical electric field strength is [*Böhnhardt*, 1986]

$$E_c = \sqrt{\frac{2\sigma}{\epsilon_a}}, \tag{5.18}$$

where $\epsilon_a$ is the aerosol permittivity and $\sigma$ is its tensile strength. Theory predicts $\epsilon_a$ proportional to $T^{-1}$ and experiment gives $\epsilon_a \approx\ 2.2 \times 10^{-7}\ T^{-1}$ for pure ice [*Auty and Cole*, 1952]. Thus for $T = 130$ K, $\epsilon_a \approx 1.5 \times 10^{-9}$ F/m. The corresponding critical charge number is

$$|Z_c| = \frac{4\pi r_a^2}{e}\sqrt{2\epsilon_a\sigma} \tag{5.19}$$

*Michel* [1978] gives the tensile strength of polycrystalline ice to be

$$\sigma_{\text{ice}} = 7.94 \times 10^3 \sqrt{\frac{1 - 9 \times 10^{-4}(T - 273)}{2r_a}}\ \text{N/m}^2 \tag{5.20}$$

which yields

$$|Z_c| = 3.3 \times 10^{17} r_a^{\frac{3}{2}} \tag{5.21}$$

for our parameters. For $r_a = 0.01$ $\mu$m, $|Z_c| = 3 \times 10^5$. This is probably an overestimate because the tensile strength is likely to be lower than the model value. But it does appear that electrostatic fragmentation is not a serious limiting factor on aerosol charge.

Keep in mind that the above calculations of aerosol charging are extremely uncertain given the dearth of data concerning the composition and characteristics of the particles. There is also no direct observational data with which to make comparisons. However it does provide a basis for a discussion of the appropriateness of the PMSE theories discussed earlier which are critically dependent on the state of the charged aerosols.

## 5.4 Discussion

First, let us take the case of the VHF PMSE apart from the observations made with UHF radars, because simultaneous observations with the 46.9-MHz CUPRI and the 224-MHz EISCAT radar have shown a remarkable similarity in their morphologies

[*Hall*, 1991] (also see Chapter 7). From the few measurements we have with the 933 and 1290-MHz radars, it appears that UHF PMSE are much more rare. We cannot rule out the possibility of one mechanism creating PMSE at all frequencies, but we have already seen that the geophysical and charged aerosol requirements for enhanced echoes at UHF are much more restrictive than for the VHF echoes.

### 5.4.1 VHF PMSE

To generate PMSE-class echoes at 50 and 224 MHz, we need aerosols with $r_a \sim 0.01$ $\mu$m and for the total aerosol to electron charge ratio $|Z_a|N_a/N_e$ to be at least $\sim 1.2$ for negatively charged aerosols and at least $\sim 0.6$ for positively charged aerosols. (These numbers are taken from the discussion of Schmidt number enhanced turbulent scatter; for a simple look at Fresnel scatter, (4.32) yields the requirement $r_a > 7$ nm, which is less stringent.) These requirements can be met by assuming either (1) low charge, high concentration or (2) high charge, low concentration aerosols. Also, because negative charging is restricted to low values, the condition of positive charge must be added to case (2).

The question of which condition is more likely hinges on the extent to which photoemission contributes to aerosol charge. If photoelectric charging of aerosols is a vital necessity for PMSE production, then one would expect to observe a distinct diurnal trend in echo characteristics tied to the solar zenith angle variation. Such a dependence is not observed. Therefore, we conclude that, for typical VHF PMSE, aerosols with low negative charge and high number density are responsible. For example, $Z_a = -1$ and $N_a = 4 \times 10^9$ m$^{-3}$ would be reasonable figures that would fulfill the PMSE requirements.

Of course, the real situation must be more complex since aerosols of many different sizes must exist simultaneously at any given time. Because photoelectric charging is more effective for larger particles, it may be that only the very large aerosols (which are normally much fewer than the smaller ones) are positively charged. Such a charge distribution could explain the rocket data of *Inhester et al.* [1990] in which the DC Langmuir probe data showed a consistently lower value for electron density in the PMSE region than the RF capacitance probe. *Havnes et al.* [1990] suggested that an apparent reduction in the electron density could result

from the inability of the Langmuir probe (essentially a positively biased ram) to deflect massive, positively charged aerosols. Then, instead of $N_e$ the probe would measure a current proportional to $N_e - Z_a N_a = N_i$, where $N_i$ is the density of positive ions. Also, M. C. Kelley has recently suggested that secondary emission from the probe due to aerosol impact coould explain these data.

Another peculiar feature of numerous rocket data are "bite-outs" in the electron density profile that often occur at the heights of PMSE layers. The most promising explanation for these electron depletion regions is the scavenging of electrons by aerosols. Model results of *Reid* [1990] show that, due to the cap on available water vapor, small and numerous ice particles ($r_a \sim 0.01$ $\mu$m, $Z_a \sim -1$, and $N_a \sim 10^9$ m$^{-3}$) are needed to create the observed bite-outs. We see that his results are very much compatible with the aerosol parameters required for Schmidt number enhanced PMSE. Also, as we have noted before, the aerosol scavenging have time scales short enough relative to the reduced electron diffusivity created by the same aerosols such that Fresnel scatter becomes a real possibility.

There are some predictions we can now make concerning the relationship of PMSE to NLCs. Because we have arrived at the conclusion that VHF PMSE rely on the presence of small, numerous aerosols, we would expect the average height of PMSE to be higher than that of NLCs, which require the presence of larger particles for optical detection. We do have fairly good statistics to confirm that this is indeed true. The average altitude of PMSE is about 86 km [*Ecklund and Balsley*, 1981; *Czechowsky et al.*, 1989] (also see Chapter 7) and the average height of NLCs is about 83 km [*Gadsden and Schröder*, 1989]. We can go one step further. Assuming a restriction on the water vapor content in a given volume of air, an abundance of large ice crystals would mean a lack of smaller aerosols (both ice and dust) to satisfy the conservation of water. Therefore, it is unlikely for a VHF PMSE layer and a NLC layer to coexist in the same space. Co-location of PMSE and NLC is made even more difficult by the fact that the ambient electron density begins to fall off sharply in the 80 to 83 km range. The only exception would be if the NLC particles are contaminated enough by metals to become substantially charged by photoemission. And even this is difficult since NLCs can only be observed from the ground after the sun has dipped below the horizon. Both *Taylor et al.* [1989] and

S. Kirkwood (private communication) report no correlation between NLC sightings and PMSE occurrence. *Jensen et al.* [1988] reported a low correlation between satellite observations of polar mesospheric clouds and 50-MHz PMSE, which may be attributed to the higher sensitivity of the ultraviolet spectrometer to smaller particles compared with optical observations. In Chapter 7 we will show the first height comparison of simultaneously observed PMSE and NLC and discuss the implications of the data to our theory.

There is, however, one piece of evidence that seems to point toward PMSE dependence on large aerosols. Here begins the story.

The mean vertical velocity measured by radars during the summer is substantially downward ($\sim$ 20–30 cm/s) [*Balsley and Riddle*, 1984]. This result is in opposition to the theoretical requirement that the summer polar mesosphere be flowing upward in order to cool it down to the observed temperatures that are far below the radiative equilibrium values [*Lindzen*, 1981]. Theories predict a circulation pattern in the summer of an upward velocity of $\sim$ 1 cm/s, an equatorward meridional flow, and a westward zonal mean flow. The latter two conditions were observed by radar, but the upward flow was not measured. In fact, the winter values (which should be downward) also appear to be slightly in the opposite direction to the theoretical prediction. Shorter data sets taken by the CUPRI in northern Scandinavia have also yielded a mean downward velocity in the summer (see Chapter 7 and *Hall* [1991]).

A second-order, compressional gravity wave effect called the Stokes drift was invoked by *Coy et al.* [1986] to reconcile the measurements with theory. However, this mechanism is not seasonally dependent and cannot account for the fact that large downward velocities are not observed in the winter as well as the summer. Moreover, *Hall et al.* [1992] showed that the Stokes drift would be about an order of magnitude smaller than the measured mean velocity for a realistic spectrum of gravity waves rather than the monochromatic wave used by *Coy et al.* [1986].

*Hall* [1991] also considered the effect of tilted scattering layers advected by horizontal winds projecting an apparent vertical velocity onto the radar Doppler measurement. He rejected this idea after failing to find evidence for a correlation between the preferred gravity wave horizontal propagation direction and the mean

horizontal velocity vector in the Poker Flat data.

After rejecting a number of other effects as well, *Hall et al.* [1992] proposed that the radars have been measuring the fall velocity of charged ice aerosols that may also be the key to the generation of PMSE. This mechanism has the advantage of turning off during the non-summer seasons when the temperature gets too warm for the particles to form, thus matching the observed seasonal behavior. However, it is not clear whether this idea could explain the mean downward flow observed by the Saskatoon MF radar [*Meek and Manson*, 1989] which, at the longer Bragg scale, may or may not be affected by the charged aerosols.

The bottom line is that in order to have a fall velocity of 30 cm to match the Poker Flat data, the ice aerosols must be of size $r_a = 0.1$ $\mu$m. They can be somewhat smaller if the ice is substantially contaminated by higher density metallic substances. The extended presence of such large aerosols is hard to support since they would be optically detectable and we know that visible clouds do not exist most of the time (a 10 % rate of occurrence is estimated by *Thomas and Olivero* [1989]).

### 5.4.2 UHF PMSE

There have been only two published reports of PMSE observed by UHF radars [*Röttger et al.*, 1990*b*; *Cho et al.*, 1992*b*] and a third case which, in retrospect, appears to be an instance of UHF PMSE [*Collis et al.*, 1988]. In all three cases the PMSE event was preceded by dramatic changes in the electron density profile due to the precipitation of energetic electrons. We considered the possibility that secondary electron emission due to the suprathermal electrons may have charged ice aerosols positively, but concluded that the flux of precipitating electrons necessary was unrealistically large. The increase in ambient electron density due to precipitating particles certainly enlarges the regime in which dressed aerosol scatter is possible (see Fig. 4.8); this may be the reason why we have so far only observed UHF PMSE during time of increased electron density. However, we still need a substantial amount of charge per aerosol which can only be accomplished (according to current theory) via photoelectric charging of metal-contaminated aerosols. We do not yet have enough experimental data to confirm or reject such a hypothesis.

Assuming, for now, that highly charged aerosols are possible, we estimated that $Z_a \sim 40$ for $N_a \sim 4 \times 10^7$ m$^{-3}$ was required for dressed aerosol scatter to explain the 933-MHz PMSE event.

We cannot completely rule out the possibility of the enhanced Schmidt number effect on turbulent scatter extending down to UHF frequencies. However, it would take a combination of high electron density ($\sim 10^{10}$ m$^{-3}$), intense turbulence ($\sim$ 0.2 W/kg), large aerosols ($\sim 0.07$ $\mu$m), and probably fairly highly charged aerosols for the effect to rise above the incoherent scatter level.

Even Fresnel scatter cannot be written off completely (see Section 4.3), but intuitively it would seem extremely unlikely that an electron density perturbation on the order of 12 cm would be likely to be maintained horizontally coherently across a Fresnel zone.

# Chapter 6

# Sondrestrom 1.29-GHz Radar Data

The intense 3-m echoes originally observed by the Poker Flat radar in 1979 were quite an unexpected result [*Ecklund and Balsley*, 1981]. Then the prediction by *Kelley et al.* [1987] that similar radar backscatter should be detectable at 67 cm was confirmed by *Hoppe et al.* [1988]. But the extension of the PMSE regime proceeded further down the length scale to 16 cm with the report by *Röttger et al.* [1990*b*].

Theoretically, it was getting more and more difficult to explain the enhancement of radar echoes at shorter and shorter length scales with the same mechanism. The effectiveness both of the two proposed scatter types, Fresnel and turbulent mixing, drop off sharply with decreasing scale size. Then *Havnes et al.* [1990] proposed an alternate PMSE mechanism which invoked the idea that a "cloud" of charge surrounding a multiply charged aerosol will respond to radio waves in phase such that the scattered power will be greater than that of classic incoherent scatter from the same number of electrons. Contrary to *Havnes et al.* [1990], *Cho et al.* [1992*a*] pointed out that this mechanism was only plausible for the higher frequency radars and not for VHF since the PMSE cross sections are extremely frequency dependent, whereas this theory predicts an essentially constant cross section with respect to frequency. Thus, if this mechanism was responsible for the 16-cm PMSE, then it should also work at shorter scales as long as the scattering length is above the Debye length cutoff. Therefore, in light of these conflicting theories, it was a natural step

to search for PMSE with the Sondrestrom 1.29-GHz (12-cm) radar.

## 6.1 Experimental Set-Up

The Sondrestrom radar is situated at geographic 67° N which is similar in latitude to the other radars which have observed PMSE. (The European incoherent scatter (EISCAT) radars are at 69° N (as was the Cornell University portable radar interferometer (CUPRI)), the Poker Flat radar was at 65° N, and the mobile sounding system (SOUSY) radar was at 69° N.) The peak transmission power is 4 MW, the effective antenna aperture is 403 $m^2$, antenna gain is 49.9 dB, and system noise temperature is 110 K. Other details of the radar are given by *Kelly* [1983].

A new mode was created for mesospheric observations, since the usual modes used by the Sondrestrom radar were designed for high-altitude incoherent scatter measurements. We used a Barker-coded single pulse designed for fine height resolution while maintaining a high signal-to-noise ratio (SNR). A 13-baud code with 4-$\mu$s bauds was employed, which resulted in a 600-m resolution. The primary drawback with the single pulse scheme was the lack of auto-correlation function (ACF) data, thus precluding knowledge of Doppler spectra. A Barker-coded multipulse scheme was also tried in order to gain spectral data at the expense of SNR, but the spectral resolution of 1.6 kHz was too coarse to get any meaningful information from the mesosphere. Integration times of 10- and 30-s were used on-line at different times.

## 6.2 Observations

Under our operating modes, electron density levels in the mesosphere were such that it was difficult to get a radar return below $\sim$ 90 km without an enhancement caused by a particle precipitation event. Although geomagnetic activity was low during the periods of observation, one such event did occur on July 14, 1990, starting at 10:00 am local time. The local riometer indicated an absorption event, and the digisonde traces vanished at this time as well, providing further evidence and implying that particle precipitation penetrated at least as low as the upper D region.

The first three panels in Fig. 6.1 show 5-minute averaged electron density profiles obtained during this active period. The dotted line is an average from a quiet day. In the first three panels, particle precipitation increased the electron density in the upper mesosphere thus making the region below 90 km "visible" to the radar. The electron density at 90 km, for example, is roughly an order of magnitude above the extrapolated quiet day curve. This enhancement is a necessary condition for PMSE detection since they occur almost exclusively below 90 km. The peak in the signal near 88 km is shaded and often persists from one 5-minute integration to the next. The narrow layer of enhanced radar scatter shown in Fig. 6.1*a* and Fig. 6.1*b* is difficult to explain with known mechanisms of electron production or gathering mechanisms. On the other hand the data are quite reminiscent of the narrow peak in 933-MHz echo strength reported by *Röttger et al.* [1990*b*] which was coexistent with a strong, classic PMSE echo at 50 MHz. Fig. 6.1*d* shows an example late in the event when the layer was no longer present and the electron density was returning to normal solar induced levels.

To systematically search for these peaks we took the ratio of the electron density to a 2-hour mean value taken at the same time during a geomagnetically quiet day. (Data below 85.8 km were not included because the rms fractional errors became too large.) Then a color-scale plot was made using a 5-minute running average of the signal advanced every minute. Fig. 6.2 shows the result, along with the riometer absorption curve for reference. The color-scale plot is in good agreement with the riometer curve, i.e., vertical streaks of enhanced SNR (roughly proportional to the electron density) correspond to absorption peaks in the riometer graph. During such events the SNR is above that of the quiet day curve throughout the height range plotted. There also appears to be a persistent thin layer of enhanced backscatter beginning at time near 10:05 at about 88 km, which then descends quickly at first and then more slowly at an average rate of approximately 0.3 m/s. This type of behavior is consistent with past observations of PMSE [*Balsley et al.*, 1983; *Czechowsky et al.*, 1989; *Röttger et al.*, 1990*b*] and could be related to the horizontal advection of a tilted layer or from the falling of scatter-enhancing particles as suggested by *Hall et al.* [1992]. Unfortunately, Murphy's Law prevailed and the electrical power generator failed during the period of largest absorption

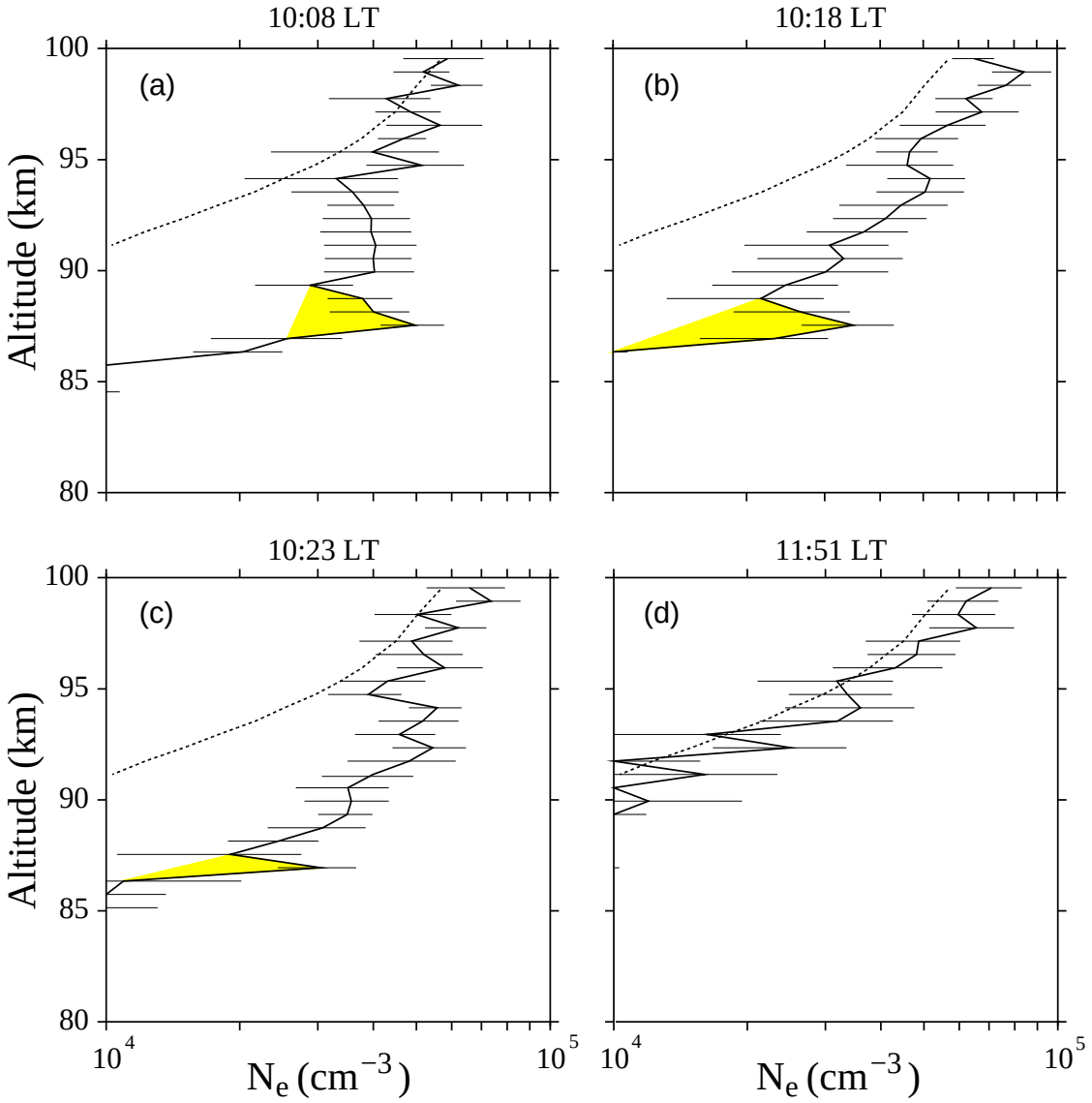


Figure 6.1: Examples of range-corrected signal-to-noise ratio plotted vs. height for July 14, 1990. The abscissa is calibrated for incoherent scatter such that the values give a reasonable estimate of the electron density. The solid line is a 5-minute average, while the dotted line is a 2-hour mean taken on a geomagnetically quiet day. The altitude resolution is 600 m. The first three frames show profiles during a period of electron precipitation, such that the region below 90 km is observable. Note the persistence of a peak at $\sim$ 88 km. The last frame is from a much later time when the ambient electron density level had gone back down.

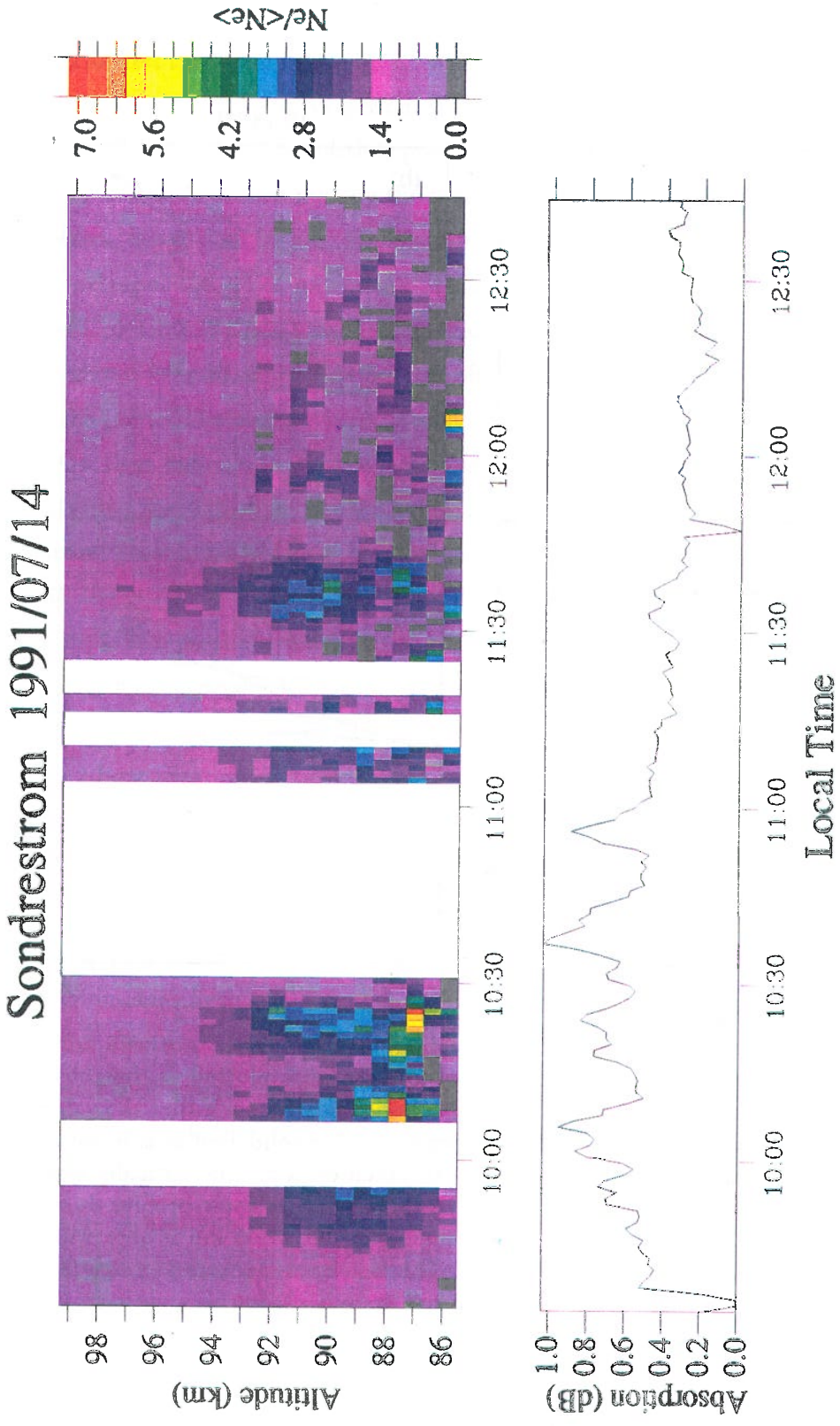


Figure 6.2: The ratio of the 5-minute moving-average range-corrected SNR to the quiet-day 2-hour mean is plotted vs. height and time. The 24-MHz riometer absorption curve is plotted at the bottom on the same time axis. Higher values correspond to larger absorption.

between 10:30 and 11:00. The other time gaps in Fig. 6.2 are due to the changing of parameters in the radar modes.

## 6.3 Discussion

What could be causing such a thin scattering layer to form? First consider the possibility of a sporadic E formation. Periodic wind shears in a gravity wave can create, through drag and magnetic forces on the plasma, regions of increased plasma density which are transported downward with the phase propagation of the wave [*Whitehead*, 1961]. This mechanism, however, operates only down to altitudes where the magnetic field effect on the ions are dominant over that of collisions with the neutral gas. The relevant parameter is $\kappa_i$, the ratio of the ion gyrofrequency to the ion-neutral collision frequency, which must be a significant fraction of unity. At 90 km in the polar summer $\kappa_i \sim 2 \times 10^{-3}$, so this mechanism cannot explain the existence of a layer at these heights.

*Sugiyama* [1988] considered the effect of gravity waves on electron density through changes in chemical reaction rates. This approach can only produce layers with thickness on the order of the vertical wavelength of the wave itself ($\sim$ 5–15 km), thus it is not a candidate for producing the layer in question.

Since we observe the layer during periods of electron precipitation, one might ask whether it is simply a result of an unusual spectral distribution in the energy of precipitating electrons. However, to produce a narrow layer below 90 km requires a physically implausible energy distribution as shown by *Collis and Kirkwood* [1990]. Moreover, the layer that they were trying to reproduce was more than 10 km wide; we are interested in something that is on the order of 600 m, which is even harder to produce. Also, such a narrow layer of electrons would tend to diffuse away rapidly unless there was an accompanying stratus of positively charged macroscopic particles that inhibited the motion through an anomalously low diffusion coefficient.

Finally we examine the possibility that the layer might be a manifestation of PMSE. Two distinct mechanisms have been proposed so far for the generation of PMSE: (1) enhanced Schmidt number turbulence scattering and (2) dressed aerosol scatter.

The highest radar volume reflectivity, $\eta$, recorded during the event reported here was $\approx 2.5 \times 10^{-18}$ m$^{-1}$. For reference the ambient electron density extrapolated from nearby heights above and below the layer was $N_e \approx 2.7 \times 10^{10}$ m$^{-3}$. (The largest PMSE $\eta$ observed at 933 MHz is $\approx 4 \times 10^{-18}$ m$^{-1}$ with $N_e \approx 8 \times 10^9$ m$^{-3}$ [*Röttger et al.*, 1990*b*].) Since we do not have a measure for the turbulent energy dissipation rate $\epsilon$, it is difficult to compare the observed $\eta$ with that derived from turbulent scattering theory. Using $\epsilon = 0.1$ W/kg [*Watkins et al.*, 1988] in the turbulence scatter model we developed in Chapter 4, we find that $Sc \sim 5000$ is required to yield the observed $\eta$. In turn, this requires the presence of charged aerosols with radii of at least 0.07$\mu$m such that their total charge accounts for at least 60 % of the plasma charge (see Chapter 3). Such large aerosols can only be noctilucent cloud particles which are usually found at a lower height ($\sim$ 83 km [*Gadsden and Schröder*, 1989]), although they have been detected as high as 89 km [*Witt et al.*, 1976]. Another difficulty with such large particles is that they must be limited in number. The largest observationally inferred number density $N_a$ for cloud aerosols of radius 0.07$\mu$m is $1.5 \times 10^8$ m$^{-3}$ [*Thomas*, 1984]. Since $N_e$ was $\approx 2.7 \times 10^{10}$ m$^{-3}$, this would require an average charge of at least $Z \approx 100$. Such high values are implausible for pure ice particles whose charging is expected to be dominated by collection of electrons; photoemission has little influence due to the high work function for ice. Model calculations by *Jensen and Thomas* [1991] yield an average value of $Z \approx$ -5 for particles of radius 0.1 $\mu$m. However, *Havnes et al.* [1990] have pointed out that the cloud particles may be a mixture of ice and metallic substances from meteor ablation which could significantly lower the work function, thus leading to high positive charges.

The alternative explanation is to invoke the dressed aerosol scatter mechanism proposed by *Havnes et al.* [1990]. To compare with our data, first we check the Debye length criterion. The plasma Debye length is given by (4.33). But since we do not know the aerosol parameters we can instead calculate the electron Debye length, $\lambda_{De}$, which will give the upper bound on the plasma Debye length. Near the observed layer we calculate $\lambda_{De} \approx 6$ mm (using $N_e = 2 \times 10^{10}$ m$^{-3}$ and $T = 130$ K) which is much smaller than the radar Bragg scale of 12 cm, so the Debye length criterion is met. Recall from Chapter 4 that the other criterion that

must be met for enhanced dressed aerosol scatter to take place is for the plasma Debye length to be much less than the aerosol spacing. Fig. 6.3 shows the combinations of $Z_a$ and $N_a$ that fulfill the enhanced scattering criterion and produce the amount of radar reflectivity that explains the Sondrestrom observations. We see that $Z_a = 30$ and $N_a = 7 \times 10^7$ m$^{-3}$ can produce the observed peak reflectivity. These values are much more reasonable than those required for the enhanced Schmidt number turbulent scatter mechanism. In other words, unlike the turbulence case, the backscattered power is not dependent on the aerosol size; therefore, particles smaller than noctilucent cloud droplets can be responsible, which raises the ceiling on available number density. This, in turn, is more consistent with the observed height of the layer, because larger particles are expected to reside at lower altitudes due to sedimentation.

The apparent descent of the layer with time is a common PMSE feature. It could be a real vertical motion of the scatterers, a horizontal advection of a tilted layer, or both. The estimate of $\sim 0.3$ m/s downward velocity happens to match the long-term, radar-observed mean velocity in the summer mesopause region, which is in disagreement with the generally accepted theory [*Holton*, 1983] that predicts an upward motion. *Hall et al.* [1992] proposed that the radars have measured the fall speed of the charged aerosols which are responsible for PMSE. Thus, it is possible that the apparent descent of our layer is the manifestation of falling aerosols. Such a conclusion is problematic given the short period of observation. Furthermore, a fall speed of $\sim 0.3$ m/s would imply a particle radius of $\sim 0.1\mu$m, and one would not expect such big aerosols to reside at 88 km.

## 6.4 Summary

Observation of the polar summer mesosphere with the Sondrestrom 1.29-GHz radar revealed a narrow peak in the backscattered power profiles. It is most likely due to the presence of a thin layer of charged aerosols which induces dressed aerosol scatter, i.e, a form of PMSE. We estimated that for $N_a = 10^8$ m$^{-3}$, the average charge state of the aerosols must be $\approx 30$ to produce the enhancement.

However, this scenario would be more convincing if we had obtained Doppler

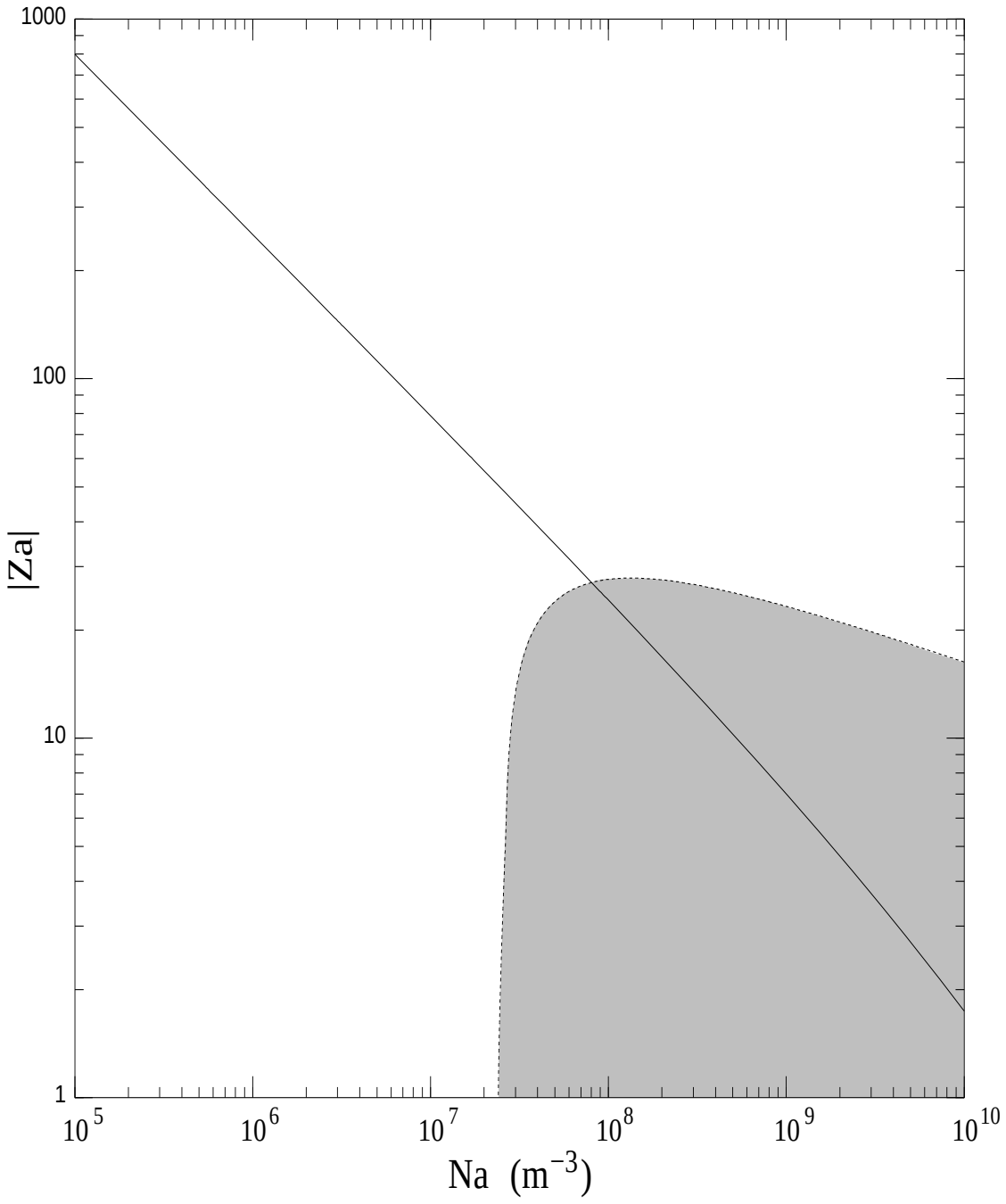


Figure 6.3: Aerosol charge necessary to explain the PMSE event observed by the Sondrestrom 1.29-GHz radar (solid line). The area under the dotted line (shaded) is where mutual interactions between aerosols nullify the dressed scattering effect.

spectral data showing the characteristic narrow spectra as calculated in Section 4.4, or simultaneous 50-MHz echoes showing an obvious PMSE. (*Röttger et al.* [1990*b*] have shown that the PMSE observed by the EISCAT UHF radar had spectral widths much too narrow for incoherent scatter.) The spectral resolution of the radar mode, which was wider than the normal incoherent scatter spectral width for these heights, prevented us from making this comparison. Also, a higher SNR would make reliable measurements possible down to 80 km without the help of precipitation events. Therefore, the development of new radar modes with these points in mind is suggested as future work.

# Chapter 7

# Observations with the 46.9-MHz CUPRI

The Cornell University portable radar interferometer (CUPRI) was incubated at Zeman Laboratory just outside the university campus in Ithaca, New York. By aiming its antenna beam far northward, it was able to make the first interferometer observations of auroral plasma irregularities [*Providakes et al.*, 1983]. Its truly portable status was attained with the acquisition of a 1984 Winnebago 27RH in which to house the system. Thus was CUPRI born with six tires for legs and a robust Chevy 454-cubic-inch four-barrel aspirated V8 for a heart. In 1991, a smaller sibling was released to the world with the body of a used U-Haul truck.

CUPRI ('Bago version) resided in northern Scandinavia between 1987 and 1992. It was first configured to study PMSE during the summer of 1988 in Tromsø, Norway where it operated in the shadow of the huge EISCAT VHF radar antenna. Even though its operators worried that a system as small as CUPRI would not be able to detect echoes in the mesosphere, the distinctive peak in the oscilloscope trace soon dispelled those fears. CUPRI successfully recorded PMSE data and the Cornell and EISCAT groups jointly published a paper comparing their respective data [*Röttger et al.*, 1990*b*]. The results were also included in a dissertation by *Hall* [1991].

During the summer of 1991, we operated the CUPRI in two campaigns. The first experiment, dubbed PMSE-91, was conducted in Tromsø at the EISCAT radar site from July 8 to 18. The primary objective was to simultaneously record PMSE

data at three different frequencies, an experiment that had not been done before. The two EISCAT radars were operated for 6 hours per day, while we tried to keep the CUPRI running as much as possible. We refer the reader to Appendix B for a description of the CUPRI system and the configuration used for these campaigns.

We then moved the CUPRI to Esrange, Sweden to participate in the rocket and radar campaign called NLC-91. The relocation (including the take-down and set-up of the antenna arrays) was accomplished within three days by two graduate students, despite an unscheduled detour through Narvik due to a dead battery. CUPRI recorded data between July 21 and August 10 with fairly good continuity despite unexpected adversities such as a severe electrical storm that wreaked costly havoc on the Esrange facilities and fuses in the transmitter that kept blowing for no good reason. (For further stories, we refer the reader to C. Miller.)

After the completion of the NLC-91 campaign, we shipped CUPRI back to the U.S. It is currently being rejuvenated and refurbished in the comforting confines of Zeman Lab.

The primary purpose of the PMSE-91 campaign was to compare the data from the radars operating at three different frequencies. Unfortunately, we have not yet been able to obtain the EISCAT radar data from the PMSE-91 campaign. Thus, we will only present the data from the NLC-91 campaign in this thesis.

As explained in Chapter 1 the mesosphere can only be sampled in situ by rockets. The NLC-91 campaign was a coordinated effort to fly many different probes through a NLC layer and a PMSE event while ground-based radars made simultaneous observations. Twenty-one rockets were launched from Esrange where the CUPRI was located, and ten more were launched from Heiss Island, Russia. The EISCAT VHF radar also made observations from Tromsø which is approximately 200 km north of Esrange.

The main objective of the campaign was to obtain information about the chemical and physical nature of NLCs and their relationship to PMSE. The strategy was to launch one sequence of rockets through an NLC event with or without the presence of PMSE and to launch another sequence into a strong PMSE event with or without the presence of NLCs. The real-time displays from CUPRI were used as the primary signifier of PMSE conditions, while ground-based and aircraft-borne

watchers approximately 500 km south of Esrange signaled the presence or absence of NLCs over the rocket range.

As it turned out, both sequences of rockets were launched into their desired criteria. The sequences were named Salvo A (NLC and PMSE), and Salvo B (PMSE only). Furthermore, a third mini-sequence was launched into an extremely strong PMSE event and, at less than 100 K, the lowest temperature ever recorded in our atmosphere [*Schmidlin*, 1992]. This sequence was named Salvo C. Salvo B occurred first (August 1), then Salvo C (August 5), then finally, after despairing that the NLC season might be over, Salvo A was launched into simultaneously occurring NLC and PMSE on the night of August 9–10. CUPRI made observations during all three salvos, while the EISCAT VHF radar was on-line for Salvos B and C only. (The EISCAT UHF radar made measurements briefly during Salvo B at the cost of "crowbarring" the VHF system.)

In Fig. 7.1 through Fig. 7.3 we present the CUPRI data during the periods of Salvos A, B, and C. The times of the rocket launches are marked by letters and are listed in Table 7.1.

In the following sections we will present selected results in which CUPRI was involved. First, we will show the first height comparisons made between a simultaneously occurring NLC and PMSE (Salvo A). We will discuss the implications of this result for our PMSE theories discussed in previous chapters. Second, we will investigate the aspect sensitivity of the radar backscatter during Salvos B and C. Third, we will look at some of the dynamics as revealed by Doppler spectrograms with high time resolution and discuss their implications for the radar scattering mechanisms. Finally, we will examine the long-term statistics compiled during the NLC-91 campaign.

## 7.1 Simultaneous Height Comparisons of NLC and PMSE

The observation of NLCs from below is possible only when the background sky becomes dark enough but with the sun still shining on the mesopause from below the horizon. Because at high latitudes the sun never sets during the height of summer,

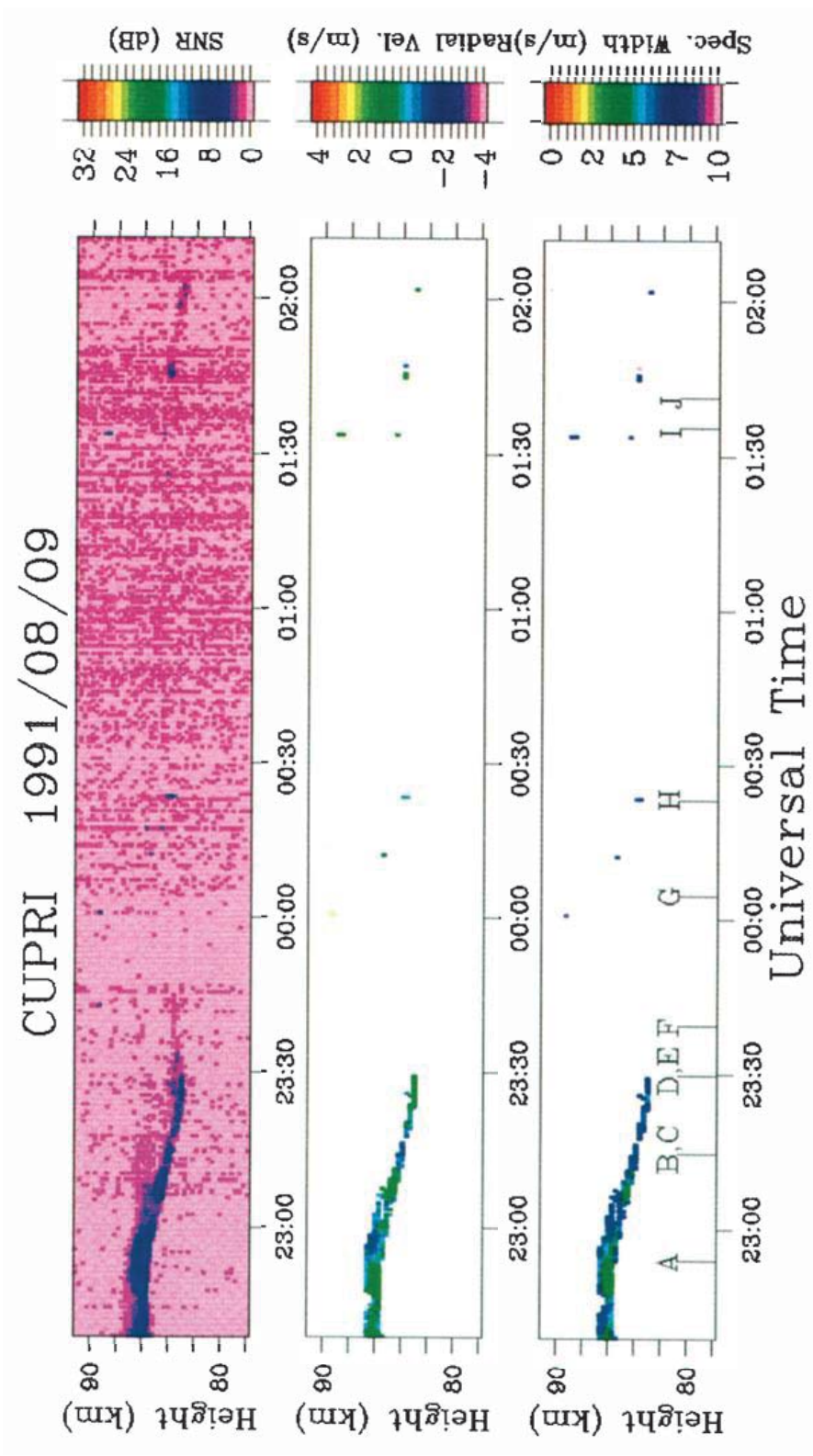


Figure 7.1: CUPRI data during the Salvo A launch sequence. The top panel displays the post-processing signal-to-noise ratio versus altitude and time. The middle panel shows the radial velocity (positive is upward and negative is downward). The Doppler spectral width is displayed in the bottom panel.

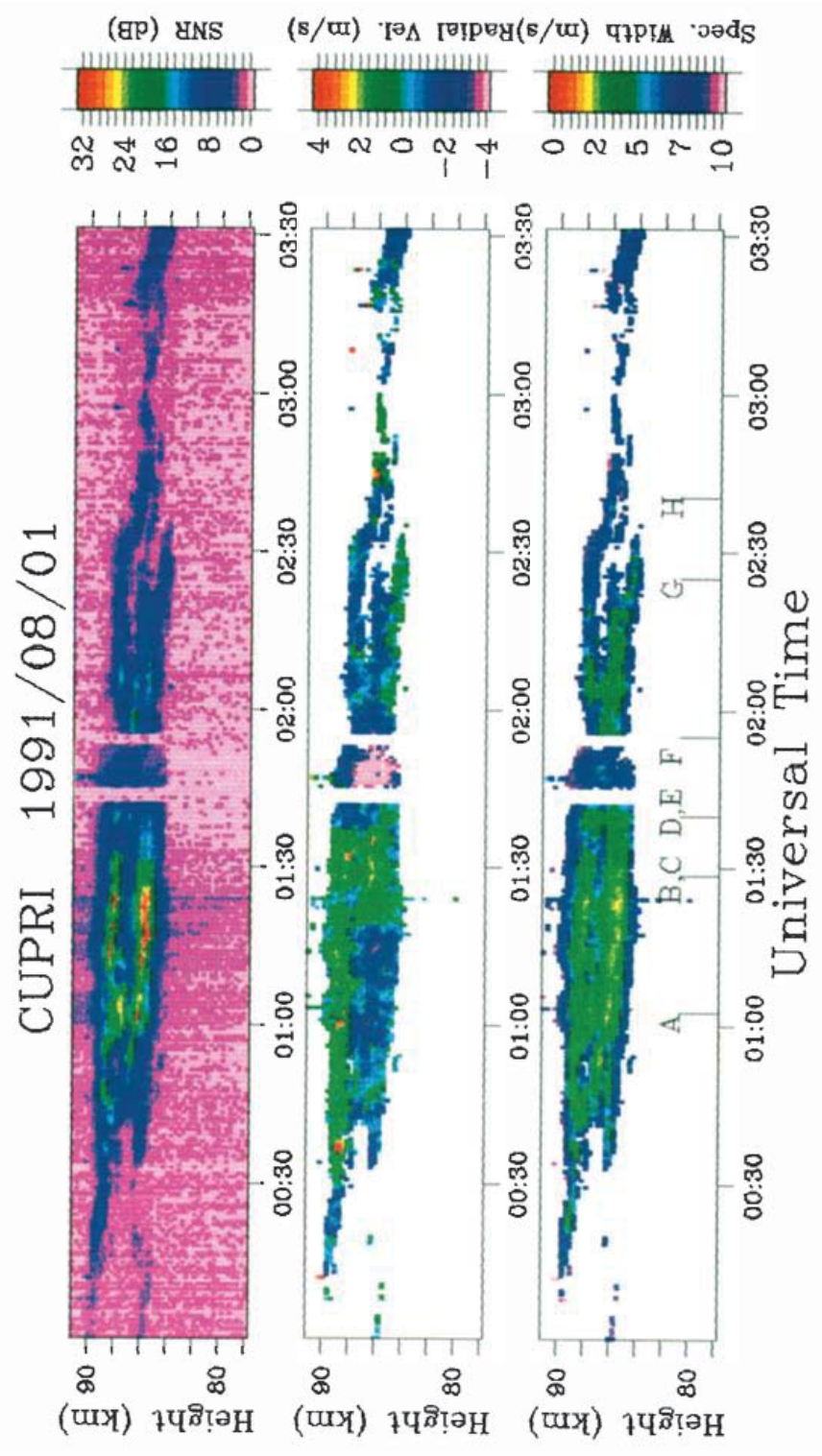


Figure 7.2: Same as Figure 7.1 but for Salvo B. The antenna beam was shifted to 8° N during 1:45–1:52.

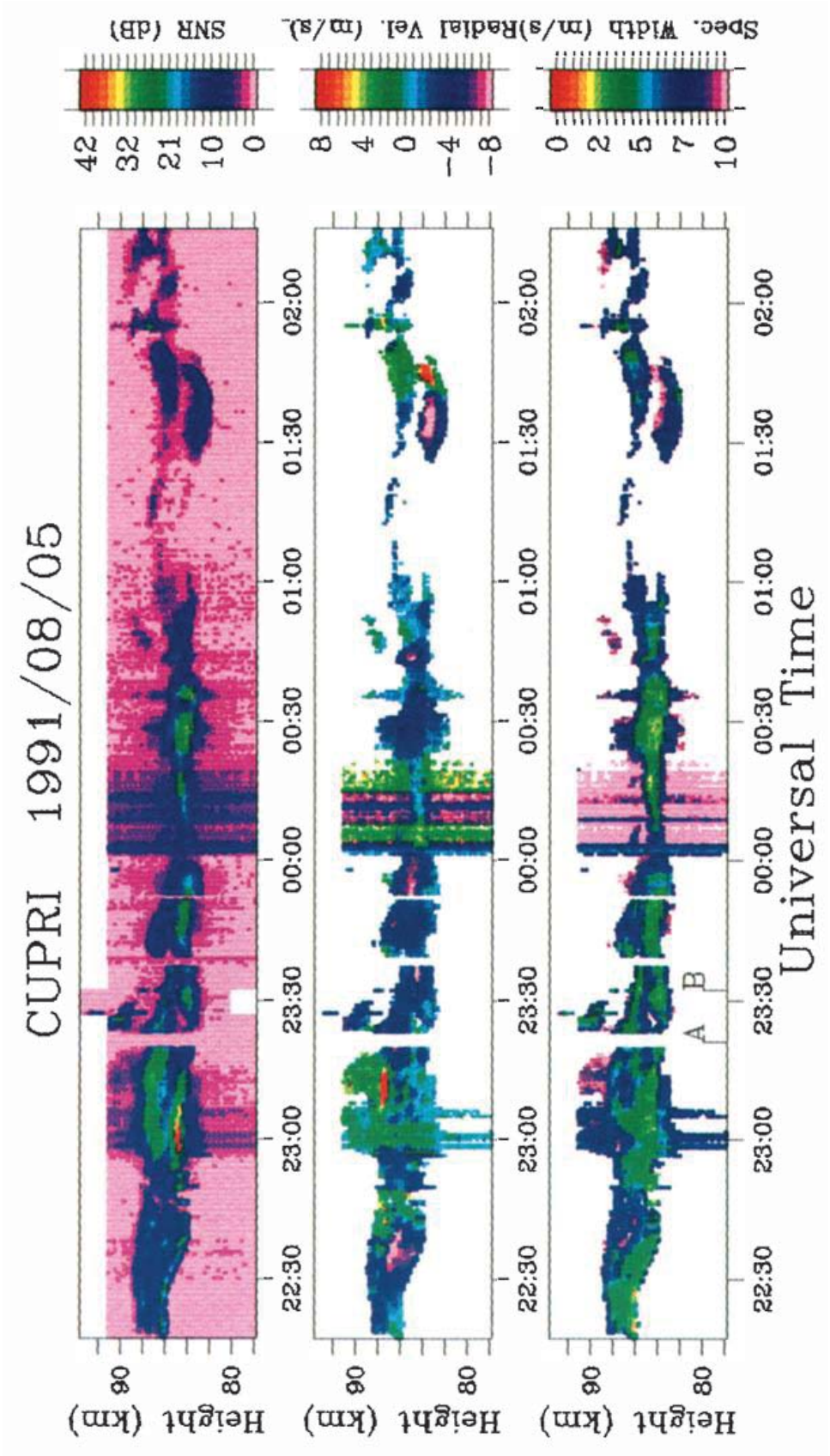


Figure 7.3: Same as Figure 7.1 but for Salvo C. The antenna beam was shifted to 8° N during 23:23–23:37 and 23:53–0:02.

Table 7.1: Rocket launch times corresponding to the labeled times in the CUPRI figures.

| Salvo | Label | Name | Launch Time (UT) | Date |
|---|---|---|---|---|
| A | A | Viper 6 | 22:53:00 | 1991-08-09 |
| | B | Turbo A | 23:15:00 | 1991-08-09 |
| | C | DECIMALS A | 23:15:15 | 1991-08-09 |
| | D | MISTI A | 23:30:00 | 1991-08-09 |
| | E | EFIELD A | 23:30:20 | 1991-08-09 |
| | F | PEP A | 23:40:00 | 1991-08-09 |
| | G | Viper 7 | 00:06:00 | 1991-08-10 |
| | H | Viper Chaff 2 | 00:24:00 | 1991-08-10 |
| | I | DECIMALS B | 01:37:00 | 1991-08-10 |
| | J | Viper 8 | 01:42:00 | 1991-08-10 |
| B | A | Viper 1 | 01:03:00 | 1991-08-01 |
| | B | MISTI B | 01:28:00 | 1991-08-01 |
| | C | EFIELD B | 01:28:20 | 1991-08-01 |
| | D | PEP B | 01:39:00 | 1991-08-01 |
| | E | Turbo B | 01:40:00 | 1991-08-01 |
| | F | Viper 2 | 01:54:00 | 1991-08-01 |
| | G | Viper Chaff 1 | 02:24:00 | 1991-08-01 |
| | H | Viper 3 | 02:39:00 | 1991-08-01 |
| C | A | MISTI C | 23:21:00 | 1991-08-05 |
| | B | Viper 4 | 23:32:00 | 1991-08-05 |

there is a well defined period of days near the beginning and end of summer in which this viewing condition can be met. The difficulty in trying to observe NLCs and PMSE simultaneously is that the strength of mesospheric radar echoes depend, in general, on the ambient electron density which, in turn, is largely produced by solar ionization in the absence of energetic particle precipitation. Sunlight which reaches the mesosphere after having traveled a long way through the atmosphere may be too weak to produce enough ionization with which to "illuminate" the Bragg scattering structures. This was the problem facing the NLC-91 campaign after the two salvos dedicated strictly to PMSE had been launched.

Then on the evening of August 9, an NLC display developed some distance away from Esrange. By 22:30 UT the aircraft observer had confirmed that the cloud cover had moved in above the rocket range. At this time, CUPRI was also detecting PMSE and the campaign scientists made the decision to proceed with Salvo A. As the rockets were launched, the PMSE layer began to fade (see Fig. 7.1). By 23:45 UT it had disappeared altogether. Visual confirmation of NLC above Esrange continued until 0:30 UT, August 10, when the contrast of the clouds against the brightening sky became too low. A PMSE layer resurfaced briefly between 1:44 and 2:05 UT.

### 7.1.1 Instrumentation

Three of the rocket payloads in Salvo A contained instruments capable of sensing NLC particles: DECIMALS-A and DECIMALS-B, each of which carried a scattered light intensity profile sensor (SLIPS) [*Wilhelm and Witt*, 1989] and a particle and aerosol trap (PAT) [*Wälchli et al.*, 1992], and PEP-A, which had a SLIPS on board.

The SLIPS is a diode photometer with a 6° full-width circular field of view pointed 30° upward from the plane perpendicular to the rocket's vertical axis. As the rocket approaches the cloud layer from below, the SLIPS measures the sum of the Rayleigh scatter from the atmosphere, the Mie scatter from the cloud aerosols, and the background starlight. Thus, the SLIPS signal should decrease sharply as it passes through the cloud layer and the magnitude of the intensity difference should correspond to the light scattered by the cloud. Because the Mie scattering drops dramatically with decreasing scatterer size, the SLIPS cannot detect small aerosols

even though the scattered light intensity also depends on the number density which is likely to be greater for smaller particles.

The PAT measures an electrical current created by the impact of photons, electrons, ions, and aerosols on its gold surface. It registers a significant increase in current as it passes through an NLC layer because massive particles produce secondary electron upon impact. The current due to secondary emission increases with particle concentration and energy. The threshold energy above which secondary emission takes place is 4.8 eV, the workfunction for gold. For a rocket traveling at 800 m/s, an air molecule with mass 30 amu will collide with the PAT at an energy of 0.1 eV, so it will not produce any current in the sensor. At the same velocity, it would require a particle of at least 1400 amu to overcome the 4.8 eV barrier. If the particle were spherical and composed of ice, the equivalent radius would be 0.9 nm. However, it has not been experimentally verified that particles with energies above 4.8 eV do, in fact, produce measurable signals. The threshold energy of the real-life system is likely to be much higher (U. Wälchli, private communication). Therefore, as with the SLIPS, the PAT is "blind" to aerosols below a certain unknown size.

### 7.1.2 Observations

The SLIPS and PAT data from DECIMALS-A are displayed side by side with the simultaneous CUPRI SNR profiles in Fig. 7.4. The rocket sensors indicate an NLC layer between 82.5 and 83.5 km altitude on the upleg and between 83 and 84 km on the downleg. Because of the high noise level encountered in the SLIPS data, extra numerical filtering had to be applied which precluded the conversion of the data to volume emission rate. Note that the SLIPS sensor detect particle layers below the heights at which the PAT data show layers. This is not a surprising result given the difference in sensitivity of the two instruments to particle size. The radar backscatter data has a peak distinctively above the NLC layers measured by the rocket instruments.

The SLIPS data from PEP-A and the CUPRI SNR profiles from the corresponding time period are shown in Fig. 7.5. For this data set, the noise level was low enough such that the SLIPS current could be height differentiated to obtain

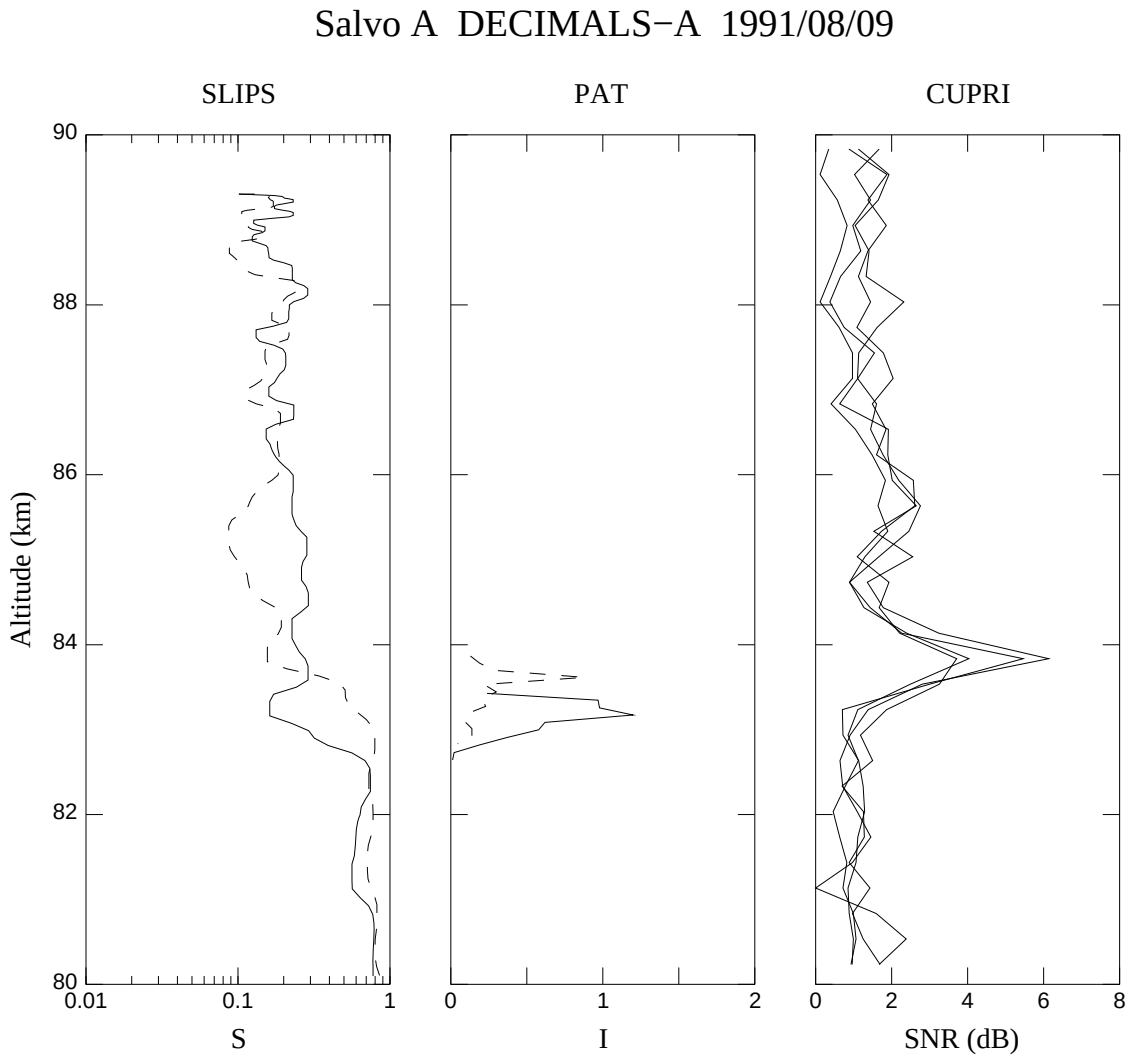


Figure 7.4: Left: Signal strength from the SLIPS (in arbitrary units). Center: Current output from the PAT (in arbitrary units). Solid lines are for the upleg and dashed lines correspond to the downleg. Right: Successive 34-s profiles of CUPRI SNR from 23:15:07 to 23:16:49 UT.

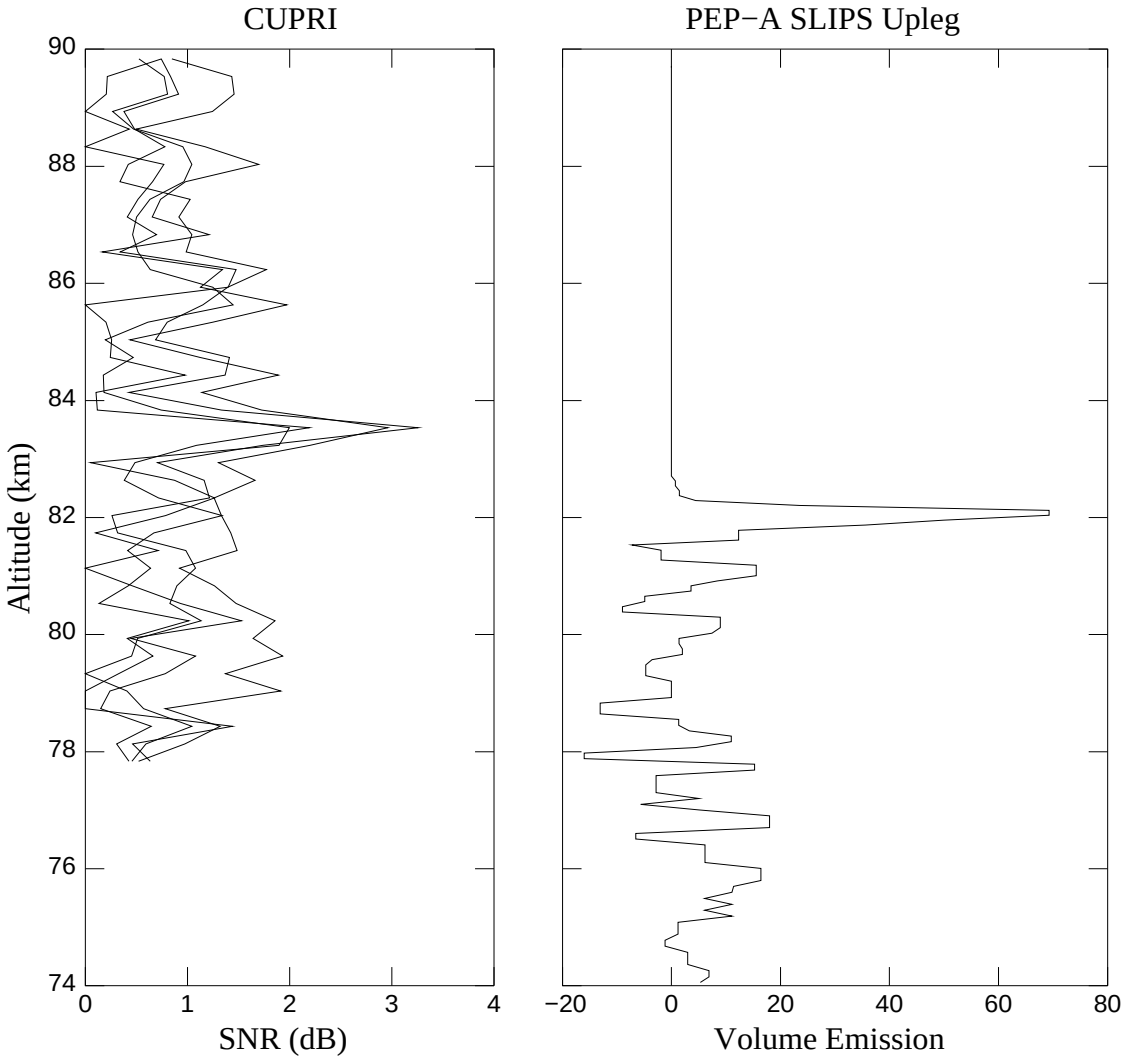


Figure 7.5: The SLIPS data for the upleg flight of PEP-A is shown in the left panel (the units are arbitrary). Successive 34-s profiles of CUPRI SNR from 23:40:26 to 23:42:07 UT are displayed in the right panel.

the volume emission rate as displayed in the figure. However, a reduced sensitivity problem with the instrument precluded the determination of the upper edge of the cloud layer. The local maximum in the profile at 82.5 km and the drop to zero volume emission rate above are not a physical result. Only the upleg data for the PEP-A payload is available since the downleg was dedicated to the Gerdien condenser measurement accomplished via a parachute descent which swung wildly through the cloud layer. Note that, again, the PMSE signals appeared to come from above the NLC layer.

The SLIPS and PAT data from the DECIMALS-B flight are displayed in Fig. 7.6 along with the profiles of the PMSE layer detected a short time after the rocket flight. By the time this payload was launched visual confirmation of NLC was not possible due to the brightening sky. But the rocket sensors clearly revealed the continued presence of NLC. About 7 min after DECIMALS-B was launched, a PMSE layer re-emerged in the radar volume, again above the NLC layer heights.

### 7.1.3 Discussion

Although in all three cases presented above of the comparison of NLC vs. PMSE heights it appears that the PMSE layer was somewhat above the cloud layer, there are several factors which make it difficult to reach such a conclusion with certainty.

First, there are uncertainties in the altitudes of both the rocket and radar data. For the rockets, the uncertainty is estimated to be about $\pm 200$ m. The altitude data for the CUPRI was calculated using the approach given in Appendix B and we believe that the uncertainty is within the range resolution of 300 m. So we have about a $\pm 500$ m uncertainty altogether.

Second, the radar volume was not co-located with the trajectories of the rockets as they flew through the mesopause region. The radar beam was pointed straight up with a full-width-half-maximum of $5^\circ$ implying a volume with about 7 km in horizontal extent at 83 km altitude. The rockets were launched to the NNE with trajectories that carried them about 20 km downrange at 83 km altitude on the upleg and about 40 km downrange on the downleg at the same height. Such spatial separations would not pose a problem if the NLC and PMSE layers were horizontally flat and vertically stationary with respect to time, but clearly this was not the case.

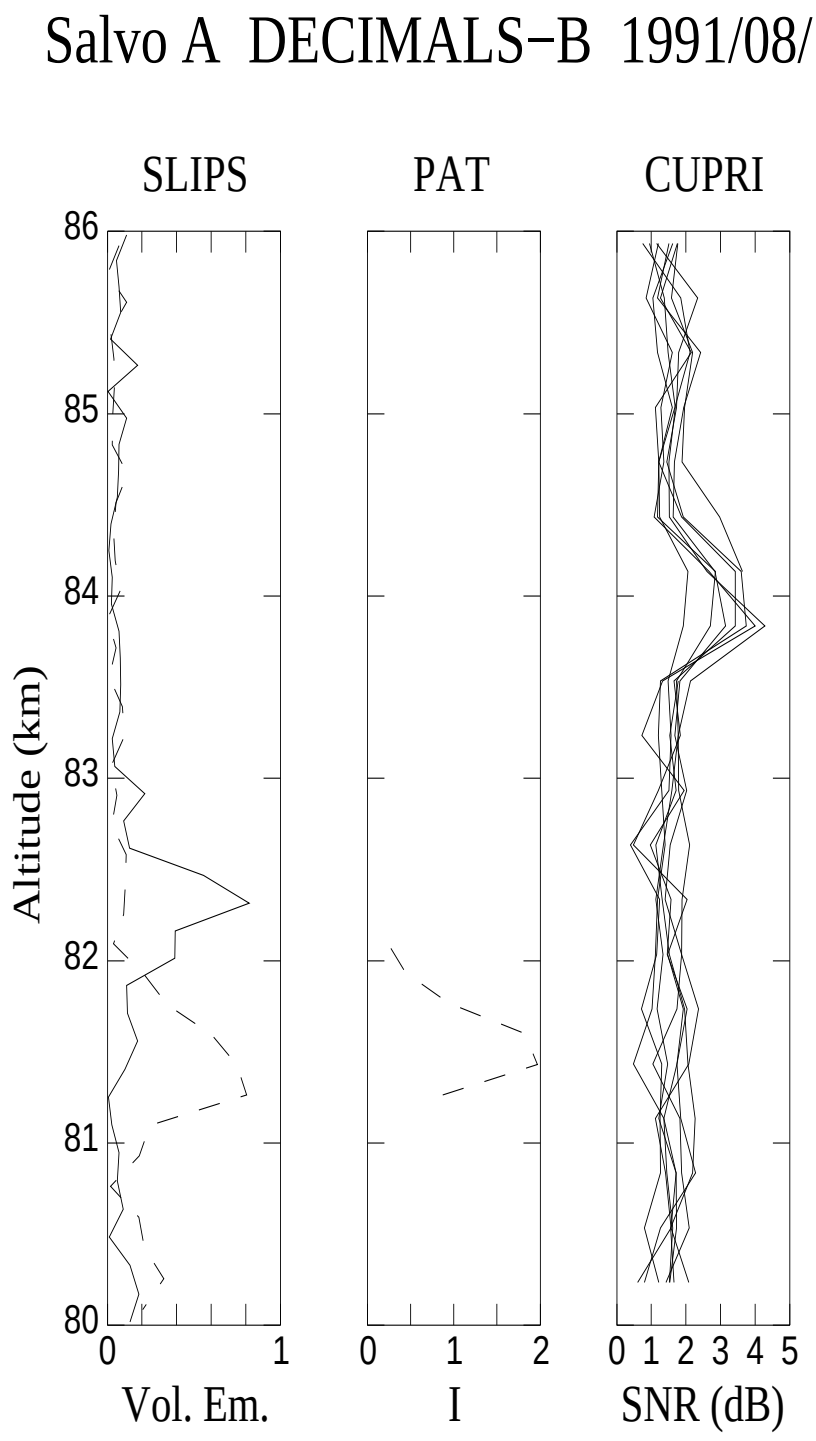


Figure 7.6: Left: SLIPS data converted to volume emissivity (arbitrary units). Center: PAT current (arbitrary units). Solid lines correspond to upleg and dashed lines indicate downleg data. Right: Successive 34-s profiles of CUPRI SNR from 1:44:09 to 1:48:05 UT. There was no PMSE detected at 1:37:00 UT.

The DECIMALS-A data indicate a higher NLC layer for the downleg compared to the upleg, implying a cloud layer which was tilted up by about 1° in the NNE direction. The later DECIMALS-B data show a reverse inclination: the NLC layer is tilted down by about 3° in the NNE direction. This is not at all surprising since NLCs are often wave-like in response to the passage of gravity waves. In fact, photographs taken by the airborne observer show such wave structures in the NLCs that occurred above the rocket range on this night. The PMSE layer during both the DECIMALS-A and B flights appeared to be descending at approximately 2 m/s. Because the mean Doppler velocity of the PMSE layer between, say, 23:00 and 23:20 UT was about 0.2 m/s downward, the apparent descent of the layer must have been mostly due to the horizontal advection of a tilted layer. Wind measurements taken by the falling sphere Viper 6 launched at 22:53 UT indicate that the horizontal wind at 83 km was blowing from the ENE at about 50 m/s, which would imply a 2° downward tilt of the PMSE layer in the ENE direction during the time of the DECIMALS-A flight.

Finally, the extreme dependence of both the SLIPS and PAT sensors on the size of the aerosols means that there was an unknown quantity of "dark matter," i.e., small particles, that went undetected by the probes. If sedimentation brings the larger, visible ice particles down to lower altitudes than the smaller, invisible ones, we would expect the "dark matter" to reside somewhat above the detected NLC layer.

To help put the data from all three rockets in perspective with respect to the CUPRI data, we have plotted the altitude of peak CUPRI SNR with respect to time in Fig. 7.7. The height of the center of NLC layer measured by the rockets is also plotted. This height corresponds to the peak in the PAT data where available, and to the sharp transition in the SLIPS data otherwise.

What can we conclude from this experiment given the inherent uncertainties in measurement? From Fig. 7.7 we see that the observed PMSE layer was consistently above $\sim 83$ km while three of the five rocket measurements showed the NLC layer to be below 83 km. Although exact height differences cannot be determined from the results of this experiment, it seems safe to conclude that the NLC particles which were *detectable by the sensors used* existed somewhat below the PMSE layer.

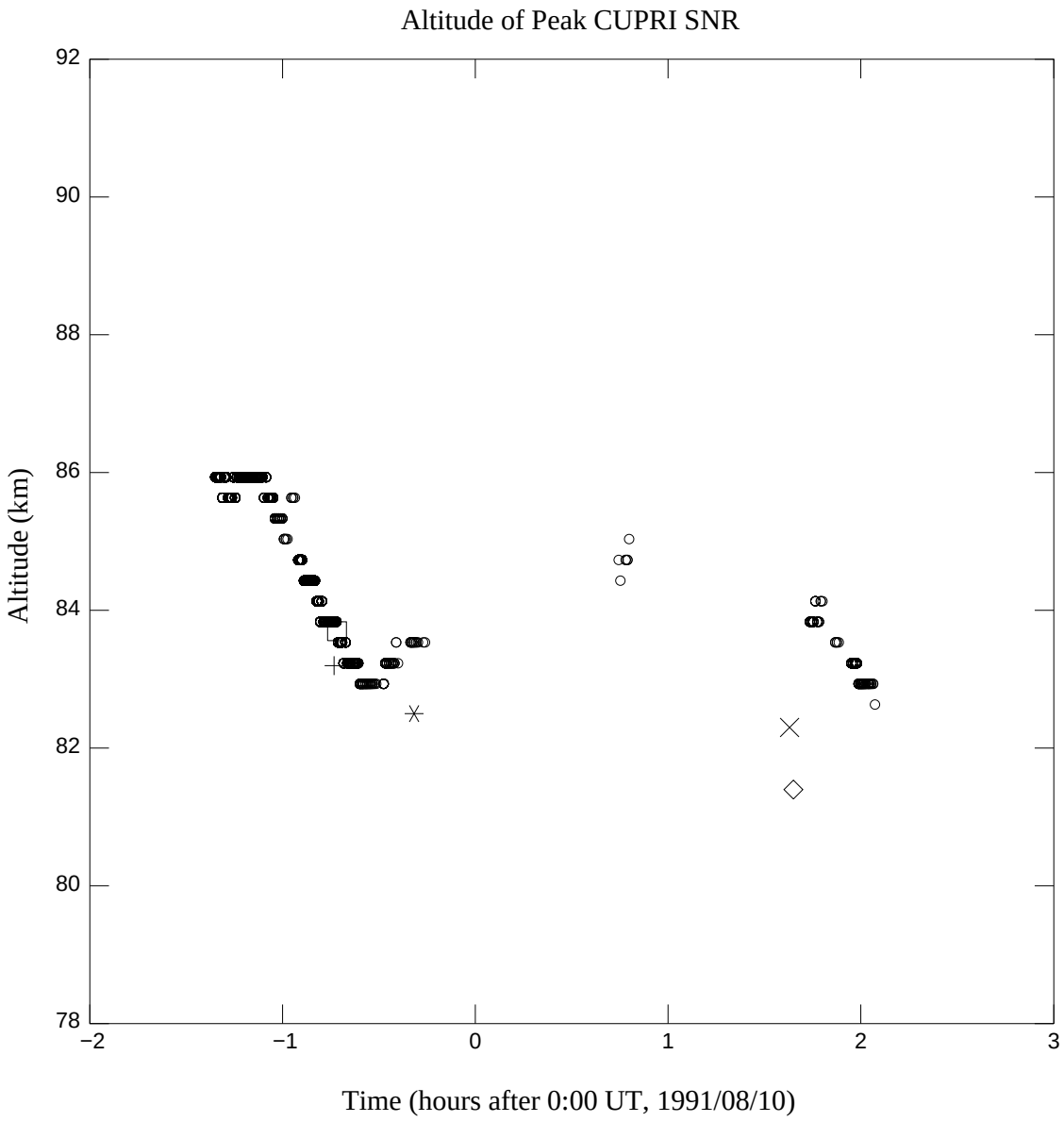


Figure 7.7: The altitude of peak SNR from the CUPRI data plotted with the height of NLC measured on the DECIMALS-A upleg (+), the DECIMALS-B downleg (square), the PEP-A upleg (asterisk), the DECIMALS-B upleg (X), and the DECIMALS-B downleg (diamond). A small circle is plotted whenever three consecutive peaks in the CUPRI data remained within one altitude bin of each other.

This result agrees with the prediction we made at the end of Chapter 5, i.e., PMSE are more likely to result from charged aerosols smaller than those which compose NLCs, thus the radar echoes are more likely to occur above any visible cloud layer. However, due to the lack of rocket instrument sensitivity to these small particles we are not able to say whether or not they existed at the PMSE altitudes.

## 7.2 Aspect Sensitivity Measurements During Salvos B and C

During Salvos B and C, we shifted the radar beam 8° off zenith by inserting phasing cables in the antenna feed network (see Appendix B). We hoped to gain information about the aspect sensitivity of the particular PMSE event by swinging the antenna beam back and forth. Because it was necessary to shut down the transmitter during the beam shifting operation, thereby losing some data, we performed the maneuver only once during Salvo B and twice during Salvo C.

The effect of swinging the antenna beam off vertical during Salvo B is shown in Fig. 7.8. If the radar scattering were perfectly isotropic and homogeneous, the SNR observed at 8° off zenith should be lower than the value observed straight up by about 1 dB due to the decrease in antenna gain and increase in range. Taking this factor into account, the upper region (87–88 km) shows no sign of aspect sensitivity, while the lower region (85–86 km) indicates a drop of about 5 dB in the radar reflectivity at 8° off vertical. Such a figure is comparable or slightly less aspect sensitive than the observations reported by *Czechowsky et al.* [1988].

The data suggests that isotropic turbulence scatter was operating in the upper region, while some type of Fresnel scatter was dominant in the lower region. This conclusion happens to agree very well with the Turbo B data which showed that the plasma was being advected by neutral air turbulence in the upper region, while the lower region contained "spiky" plasma fluctuations without the presence of neutral gas turbulence [*Lübken et al.*, 1992].

A serious caveat must be kept in mind, however. Because the beam swinging shifts the radar volume horizontally by 12 km, the actual scatterers observed during that time may have been significantly different from what would have been observed

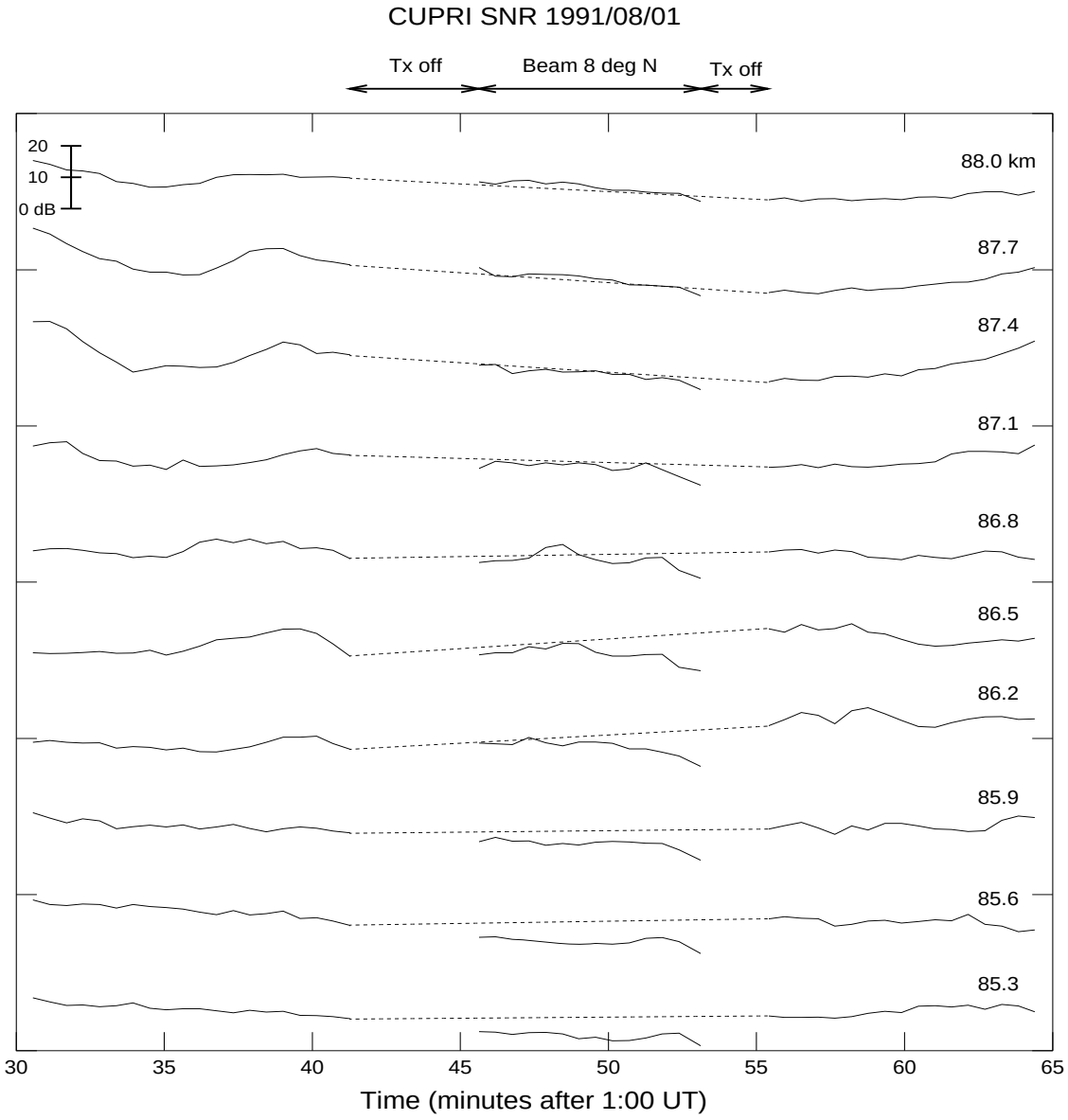


Figure 7.8: CUPRI SNR values are plotted for the height range where PMSE existed during Salvo B. The horizontally dashed lines simply connect the SNR value last observed before beam swinging to the first value recorded after shifting back to vertical.

in the original volume. Are PMSE structures horizontally similar over 12 km? This is a question that we cannot answer at this time. However, we can derive some encouragement from the fairly continuous appearance of the data across the beam swinging period—there is no obvious indication that the action in the two radar volumes were drastically different (also see the RTI plot in Fig. 7.2). Besides, the radar volume itself is 7.5 km wide at 86 km so the space of no overlap between the two positions is really only 4.5 km.

A similar plot for the Salvo C period is displayed in Fig. 7.9. As can be seen, the PMSE event here was much more dynamic. Because the signal levels were changing quite rapidly, we can surmise that horizontally very patchy scattering structures were being advected through the radar volume. In this case, it is more difficult to draw any conclusion about the aspect sensitivity of the radar scatter. The best way of making the aspect sensitivity measurement, of course, is to employ a well-calibrated multi-static system such that a common radar volume can be examined from different angles simultaneously.

## 7.3 Observations of Mesospheric Dynamics

As alluded to in Chapters 1 and 2, the interactions between the mean flow and various classes of atmospheric waves play a vital role in the dynamics of the mesosphere. Gravity waves which transfer energy and momentum from the lower atmosphere to the mesosphere are especially important in determining the large-scale circulation patterns and the temperature structure. However, ground-based remote sensing of summer mesospheric dynamics is typically difficult—too bright for lidars and not enough reflectivity for radars except for the largest ones in the world. Fortunately, the uniquely large radar cross sections of PMSE enable even a relatively small and inexpensive radar like the CUPRI to make observations during a large percentage of the time near the summer mesopause.

The plots of SNR, radial velocity, and Doppler spectral width that we showed earlier in this chapter provided a quick insight into the dynamics. However, since they were produced by integrating over the Doppler spectra, interesting features that were apparent in the full spectrum may have been smoothed out. Also the total integration time of 34 s might have smeared out fine temporal (or spatial,

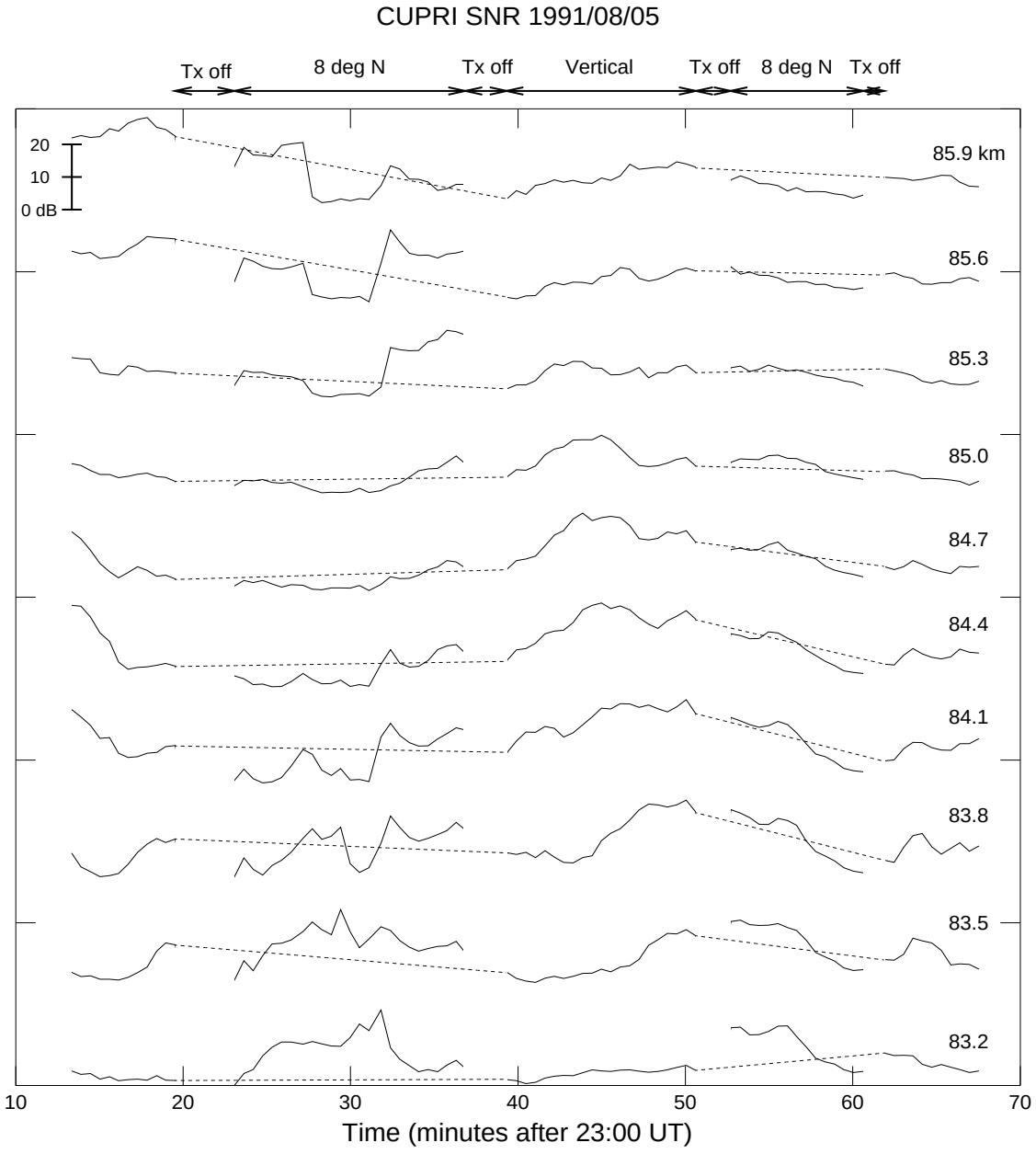


Figure 7.9: Same as the previous figure but for Salvo C.

since structures are advected through the radar volume) variations.

In Fig. 7.10 we display high time-resolution Doppler spectrograms from the period of the main rocket sequence in Salvo B. A range of consecutive height bins were selected such that most of the PMSE region was covered. What immediately strikes the eye is the presence of velocity structures that look like diagonal hatching in the lowest two windows between 1:30 and 1:40, and in the top panel between 1:10 and 1:20. The velocity appears to increase linearly until reaching a limit, abruptly drops back to the initial value, then repeats again. Moreover, there is an overlap period where the new cycle begins before the previous one had ended. In Fig. 7.10, the example at the higher altitude has a shorter period and a steeper slope.

Two different explanations for this type of Doppler spectral discontinuity have been proposed by *Röttger et al.* [1990*a*]. The first one requires the horizontal advection through the radar beam of a partially reflecting sheet which has an upward bump in its shape. Due to the finite width of the radar beam, a bump in the reflecting structure will produce more than one reflection point causing interference and a superposition of different Doppler shifts. The model computations of *Röttger et al.* [1990*a*] resulted in a sawtooth-like structure in the Doppler spectrogram for a narrow-beam radar (like the EISCAT VHF radar) and a diagonal hatching structure very similar to the ones seen in Fig. 7.10 for a wide-beam radar (like the CUPRI).

We can roughly estimate the size of a bump required to produce the observed data. The magnitude of the horizontal wind at 86 km was about 60 m/s at 1:54 UT (F. Schmidlin, private communication). The time spanned by the three-striped structure (corresponding to one bump width plus the beam width) at 86.2 km is about 4 minutes. The beamwidth at 86 km is 7.5 km. Therefore, the width of the bump is approximately $(60 \text{ m/s})(240 \text{ s}) - 7.5 \text{ km} = 7 \text{ km}$. The height of the bump would be more than 300 m since the velocity signature also appears in the next altitude gate up. The same estimation procedure used on the three-striped structure at 87.7 km yields (the horizontal wind at 88 km at 1:03 UT was about 40 m/s) a bump width of approximately 4 km. Note that in our estimations we have used values of horizontal wind that were measured by rocket-launched falling spheres released at the indicated times. Given the time and space differences between the

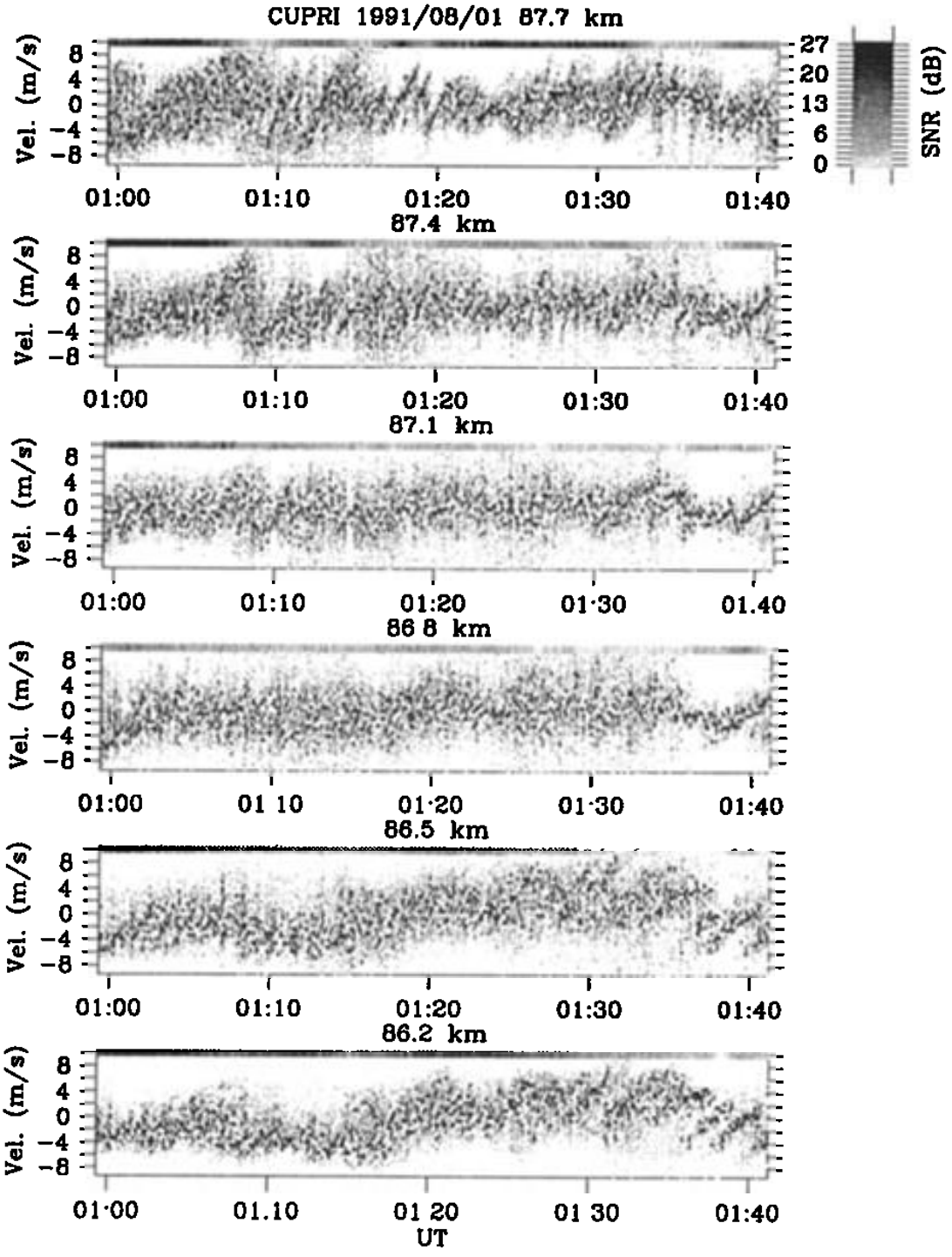


Figure 7.10: CUPRI Doppler spectrograms for a selected range of heights. Each time strip is self-normalized and the corresponding SNR is given by a grey-scale bar at the top of each panel (the scale is given at top right). The time resolution is 5.6 s. Only ±9 m/s of the Nyquist range of ±18 m/s is shown in this figure. Positive velocity is upward, negative is downward.

wind measurements and the Doppler spectral events, there is no assurance that the wind values are really appropriate.

The second model capable of producing a discontinuity in the Doppler spectrogram is the distortion of a scattering layer by steepening and tilting gravity waves. The amplitudes of gravity waves in the mesosphere can become so large that nonlinear effects begin to distort the waveforms. Wave-wave interactions can also seriously affect the wave shapes. For example, a model calculation by *Weinstock* [1986] shows that the gravity wave perturbation velocity can grow into a sawtooth waveform before being limited by saturation. Then the diagonal hatching structures we observe may be explained by such a sawtooth wave.

The two models are similar in that both require a physical distortion of the scattering medium. The fundamental difference between them is thus: the first model requires a strictly partial reflection mechanism but is not dependent on the exact shape of the distortion, while the second one is independent of the radar scattering mechanism but requires a certain waveform.

There is, in fact, a third alternative which can explain the observed linear structures in the spectrograms. Any localized scattering patch advected across the radar beam will produce a linear progression in the Doppler spectra since it will appear to be approaching as it enters the beam and receding as it exits on the other side. For evenly spaced and overlapping hatching structures to result in the spectrogram, the patches must be evenly spaced and more than one must be in the beam simultaneously. Also, the patches are not likely to be caused by strong turbulence since there is no known mechanism for creating such small, localized regions of turbulence. It is more likely that the localized patches were due to some type of partial reflecting structure, e.g., the sharp electron density gradients produced by the interaction of charged aerosols with neutral gas vortices proposed by *Havnes et al.* [1992].

For the structures observed in Fig. 7.10 the first or third model seems to apply for the following reasons. First, the period between the diagonal lines is less than the Brunt-Väisälä period which is typically about 7 minutes in the mesosphere, so gravity waves (which have periods greater than the Brunt-Väisälä period) can not be responsible for the velocity structures. Second, the structures correspond

to some of the narrowest spectra seen in Fig. 7.10, pointing to a partial reflection mechanism when they were present. (Note that such an observation would not have been possible in a "second moment" plot, since the overlapping hatching structure would have smoothed out the true spectral widths.) Finally, we see no obvious evidence of a steepening wave field leading to the velocity discontinuities.

The second model, however, is more appropriate in other instances such as the spectacular example of gravity wave steepening and tilting shown in Fig. 7.11. The most obvious discontinuity occurs shortly after 22:50 at 88.3 km. We can clearly see the growth and progressive distortion of the wave with height. Also, the lack of spectral broadening accompanying the wave growth suggests that not much turbulence was produced in this height region. The wave may finally have broken at 88.6 km directly above the spectral discontinuity where some spectral broadening is discernible.

One can see the advection of the scattering layer due to the wave motion in Fig. 7.12. Note the burst of power around 23:45 when the waveform appears to be breaking. This may be indication that intense turbulence was produced at that point, thus enhancing the radar backscatter. The oscillation in the vertical velocity clearly indicate the presence of a gravity wave. The phase fronts appear to be only slightly tilted from the vertical implying a mostly horizontally propagating wave. This is consistent with the fact that the period, on the order of 10 minutes, is only slightly larger than the Brunt-Väisälä period, since the dispersion relation of a gravity wave is approximately

$$\omega^2 = \omega_B^2 \frac{k^2}{k^2 + m^2} \tag{7.1}$$

where $\omega_B$ is the Brunt-Väisälä frequency, $k$ is the horizontal wavenumber, and $m$ is the vertical wavenumber.

### 7.3.1 A Note on Doppler Spectra Broadening

We have so far talked loosely about the width of the Doppler spectrum being proportional to the turbulence intensity. There are, in fact, other spectral broadening factors that must be considered. For a wide-beam radar like the CUPRI, the beam-

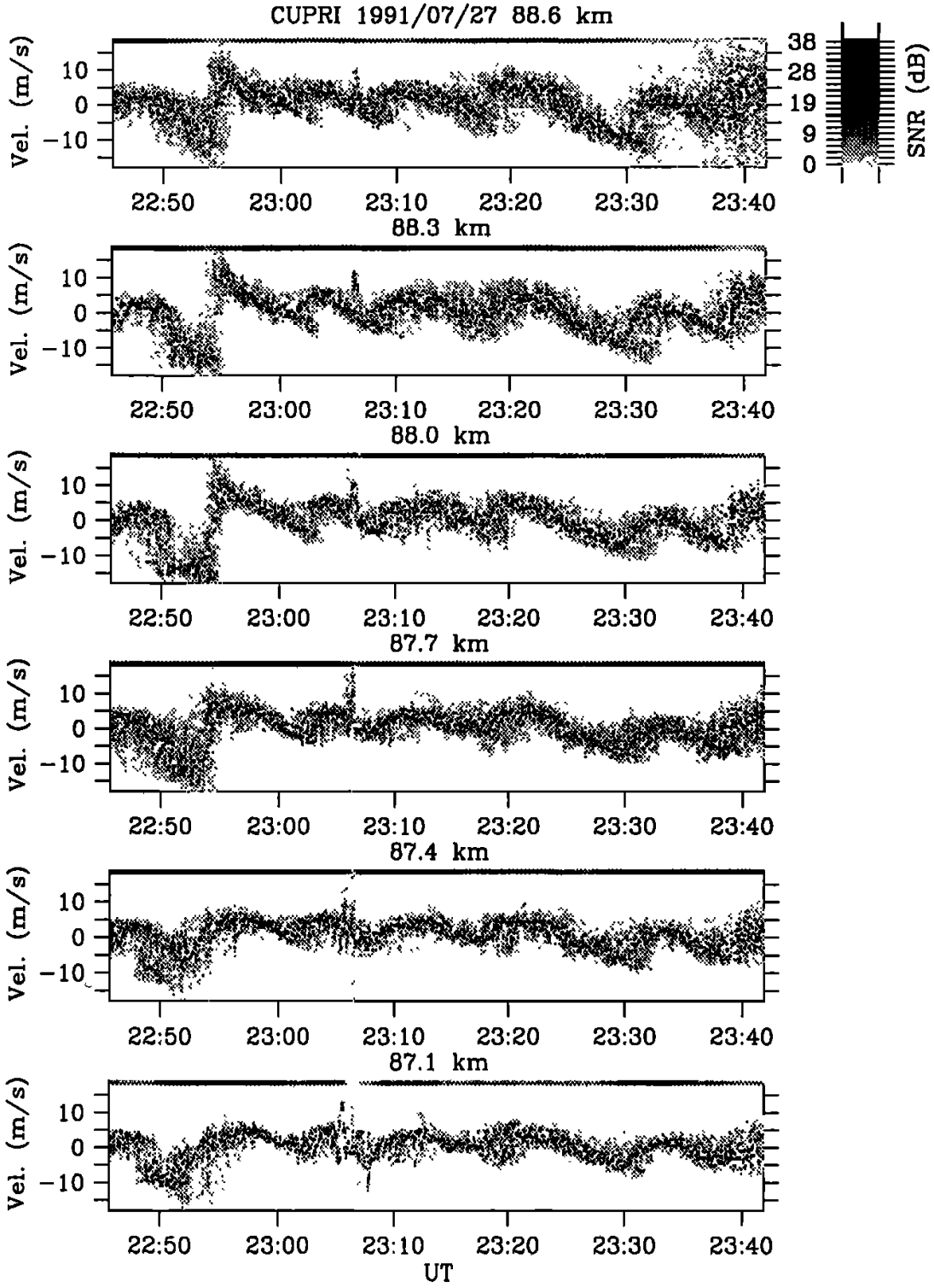


Figure 7.11: Same as the previous figure but for a different day. Also in this case the entire Nyquist range is displayed.

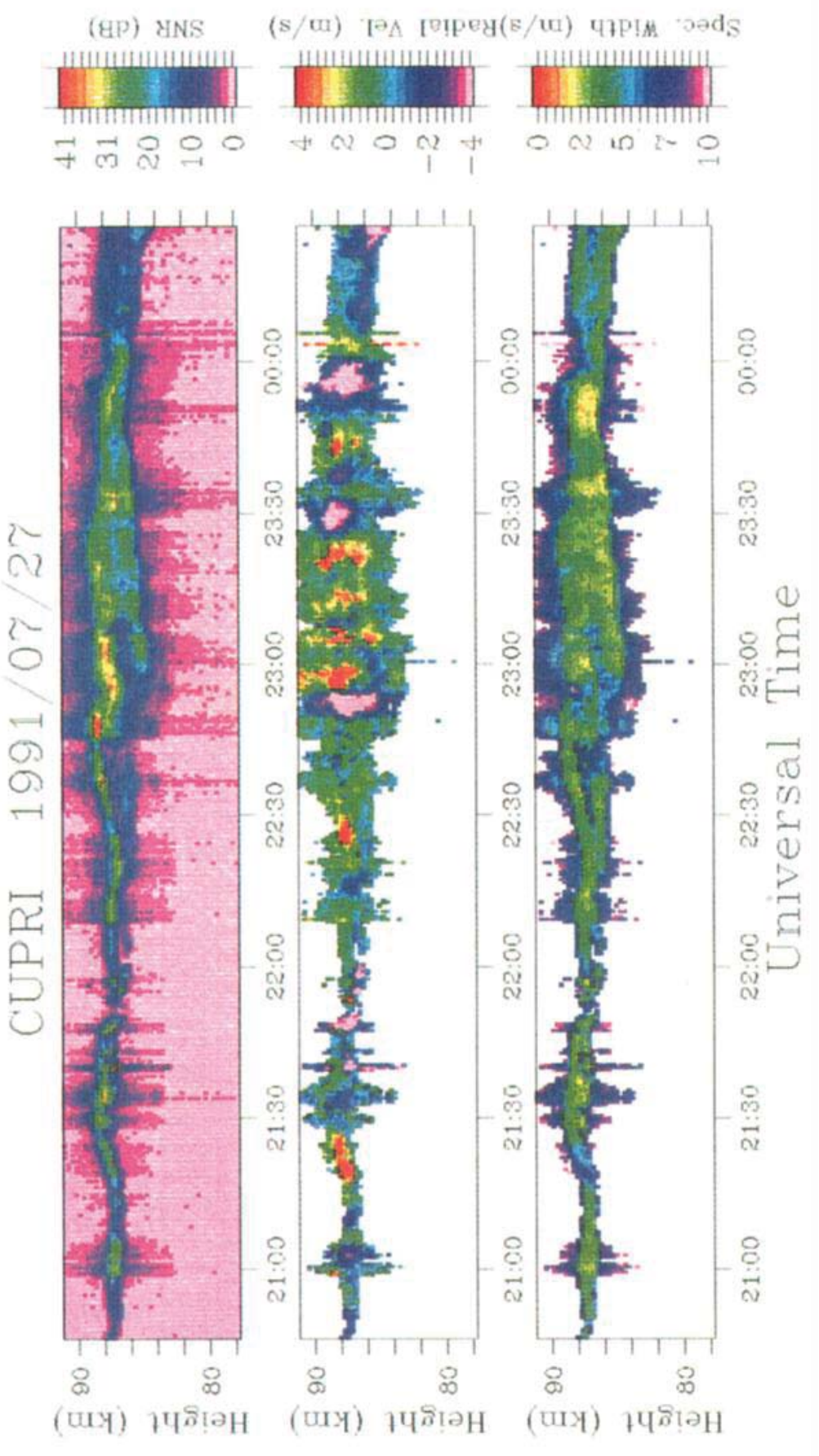


Figure 7.12: Same as Figure 7.1 but on a day with no rocket launches.

broadening effect becomes very important.

Due to the finite width of a radar beam, even a turbulent scattering layer moving purely transversally to it will impart radial components of Doppler shift except in the vertical plane at the center of the radar volume. At one edge of the beam the layer will appear to be approaching the receiver and at the opposite edge the layer will seem to be receding from the receiver. The result is a spread in the Doppler spectrum. Quantitatively, the half-power, half-width of the beam broadening effect is [*Hocking*, 1985]

$$\Delta v_{bb} = |u|\theta_{\frac{1}{2}} \tag{7.2}$$

where $|u|$ is the magnitude of the transverse wind and $\theta_{\frac{1}{2}}$ is the half-power, half-width of the radar beam. For the CUPRI, $\theta_{\frac{1}{2}} \approx 0.04$ rad. Thus, for a typical mesospheric horizontal wind of, say, 80 m/s, the beam broadening contribution to the Doppler velocity spectrum would be $\Delta v \approx 3$ m/s. The turbulence broadening factor is approximately [*Hocking*, 1985]

$$\Delta v_{turb} = 1.6\epsilon^{\frac{1}{2}}\omega_B^{-\frac{1}{2}} \tag{7.3}$$

So for an 80 m/s horizontal wind and $\omega_B$ of 0.02 rad/s, $\epsilon$ would have to be greater than about 0.07 W/kg for turbulence broadening to dominate over beam broadening. Since 0.07 W/kg is a fairly large value for $\epsilon$ in the mesosphere, we must conclude that, for the CUPRI, beam broadening typically dominates turbulence broadening of the Doppler spectra.

Let us take a specific example from Salvo B. The neutral density fluctuations measured by Turbo B yielded $\epsilon \approx 0.08$ W/kg in the upper region of PMSE [*Lübken et al.*, 1992]. The CUPRI observed a Doppler half-width of about 3 m/s at 87.7 km at 1:40 (see Fig. 7.10). The falling sphere released at 1:54 yielded a horizontal wind speed of 56 m/s at 88 km. The radar-deduced turbulence energy dissipation rate is

$$\epsilon = 0.4\omega_B \left[(\Delta v_{obs})^2 - |u|^2 \theta_{\frac{1}{2}}^2\right] \tag{7.4}$$

Then, for $\omega_B = 0.035$ rad/s calculated from the falling sphere measurement, we get $\epsilon = 0.04$ W/kg. Given the distance between the radar volume and the Turbo trajectory, and the time delay until the falling sphere measurement, this result for

$\epsilon$ compares quite reasonably with the rocket-derived value of 0.08 W/kg.

We can also calculate the Schmidt number necessary to produce the observed echo strength by using the enhanced isotropic turbulence scatter theory of Chapter 4. At 88 km during the time of the Turbo-B flight, the radar volume reflectivity measured was $\eta = 5 \times 10^{-14}$ m$^{-1}$ (see Appendix B for how $\eta$ was derived from SNR). From the capacitive probe data of MISTI-B, we estimate $N_e = 10^{10}$ m$^{-3}$ and $H_e = 1$ km at 88 km (J. Ulwick, private communication). Plugging these values and $\epsilon = 0.04$ W/kg into the model we developed in Chapter 4 yields $Sc = 7$. We note that *Lübken et al.* [1992] estimate $Sc \sim 3$ for their ion density fluctuation spectrum. Looking back to Chapter 3, we see that aerosols of radius $\sim 0.003\mu$m are required for $Sc = 7$.

Turbo, however, measured almost no turbulence in the lower PMSE region around 86 km. From Fig. 7.10 we see that this was exactly the region in which the diagonal hatching structure appeared in the Doppler spectrum, with a corresponding decrease in the spectral width. If the model of the distorted partially reflecting layer advected across the radar beam is correct, then the rocket observation of no neutral gas turbulence in this region matches the radar spectral data quite nicely.

## 7.4 Long-Term Statistics

Over the course of the NLC-91 campaign CUPRI recorded 264 hours of mesospheric data. During this period PMSE, defined as a radar echo with a post-processing SNR greater than 4 dB, were observed for a total of 140 hours giving an average occurrence rate of 53 %. Comparisons with other ground-based instruments show a statistically significant correlation with the PMSE occurrence on the EISCAT VHF radar which was located about 200 km away, but no statistically significant correlation with energetic particle precipitation or geomagnetic activity (S. Kirkwood, private communication).

We have also compiled statistics for the SNR and vertical velocity with respect to altitude and local time of day. Fig. 7.13 displays the means versus altitude. The rate of PMSE occurrence peaks at 86 km, which is consistent with the statistics compiled from the Poker Flat [*Ecklund and Balsley*, 1981] and the SOUSY radar

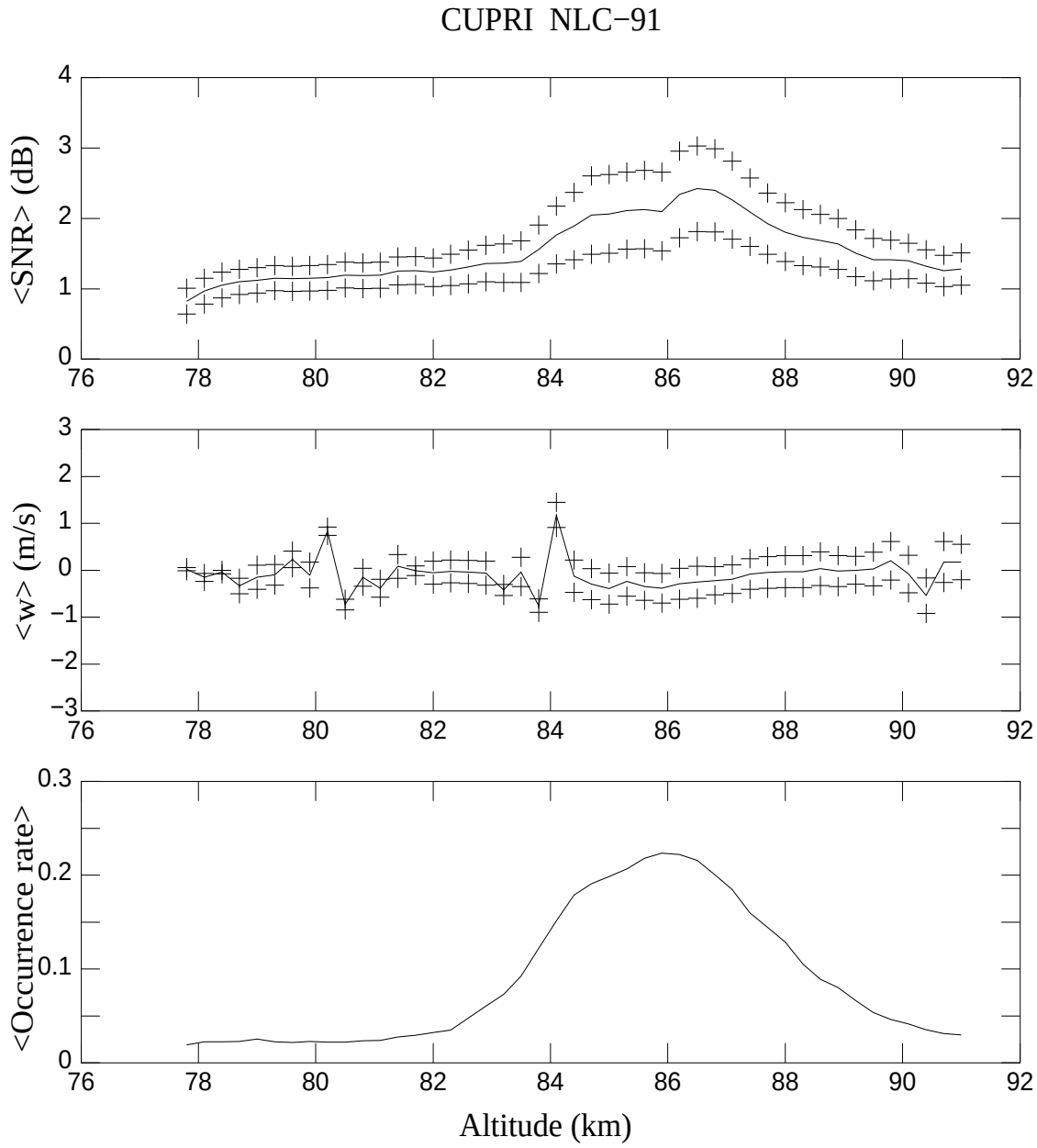


Figure 7.13: Top panel: Mean radar SNR vs. altitude; average was taken over all data, not only when PMSE was present. Middle panel: Mean vertical velocity vs. altitude; data was included only when the SNR was above 4 dB. Bottom panel: Mean rate of PMSE occurrence vs. altitude. The + symbols indicate the statistical uncertainty in the mean which is the standard deviation divided by the square root of the number of samples.

data [*Czechowsky et al.*, 1989]. The SNR peaks at a slightly higher altitude, which is probably due to the rapidly increasing ambient electron density with height. The vertical velocity is fairly constant with height as one might expect from continuity and has a small downward component as observed by other radars [*Balsley and Riddle*, 1984; *Meek and Manson*, 1989].

The means versus local hour of day are shown in Fig. 7.14. The averages were taken over all altitudes. Note that the SNR has a diurnal periodicity, whereas the occurrence rate appears to have an 8-hour period. To have an occurrence of PMSE, only the minimum conditions necessary for echo production need to be met. Enhancements in the SNR are caused by an increase beyond the minimum criteria in one or more of the factors contributing to PMSE production. According to the theory we have developed in this thesis, the most crucial condition for PMSE occurrence is the presence of charged aerosols which, in turn, require low temperatures. Thus, the fluctuation in the occurrence rate may have been due to the temperature modulation of a hypothetical 8-hour wave which was prominent during the NLC-91 period. The diurnal periodicity in the mean SNR may have been caused by a variation in turbulence production due to tidal shear instabilities. The general diurnal trend in the vertical velocity may also be attributable to tides. However, the peak in the downward velocity at local noon is very difficult to explain.

The overall mean vertical velocity averaged over both time and altitude was $-2.8 \pm 2.0$ cm/s. The intermediate means were weighted according to their calculated statistical uncertainty. This is comparable to the $\sim -7$ cm/s monthly mean value for August at 80–90 km compiled from the 1979–1983 Poker Flat data base [*Hall et al.*, 1992]. If the velocity values shown in Fig. 7.14 are averaged without weighting them according to the uncertainties, then we get an overall mean of $-24$ cm/s. This value may be more meaningful since effects of preferential sampling with respect to hour of day is cancelled. These observed downward flows in the upper mesosphere contradict the theoretical requirement that the mean flow be upward on the order of 1 cm/s in order to cool down the mesopause to the observed low temperatures.

Serious questions were thus raised regarding what velocity the radars were actually measuring. *Balsley and Riddle* [1984] eliminated the possibility that the

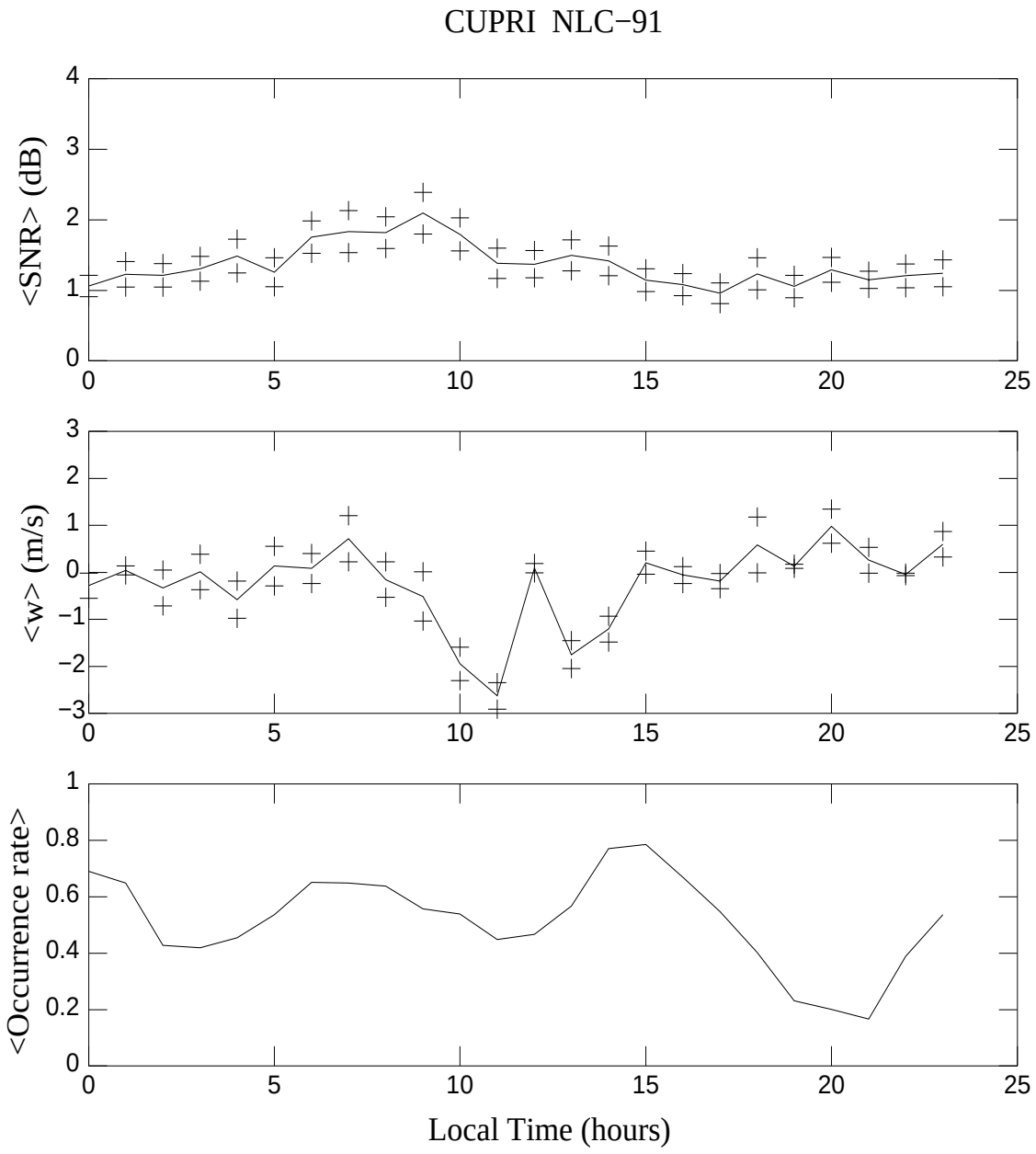


Figure 7.14: Same as the previous figure except the means are plotted with respect to local hour of day instead of altitude. The values were averaged over all altitudes.

vertical velocity observations were skewed by a slightly tilted antenna beam or a bending of the beam by refractive index variations. *Coy et al.* [1986] proposed that the Stokes drift, a second-order compressional gravity wave effect, could explain the discrepancy between theory and observation. In other words, they were contending that the radars had been measuring the Eulerian velocity which differed from the true Lagrangian motion of the air. However, *Hall et al.* [1992] showed that the Stokes drift would be limited to producing a difference in the two velocities of less than 4 cm/s, which was much too small to explain the observed 20–30 cm/s downward flows in June and July. Also, there is no reason to believe that the Stokes drift only occurs during the summer.

*Hall* [1991] carefully examined other possible sources of contamination in the Poker Flat vertical velocity data. He found no evidence that effective beam tilting due to the advection of slanted scattering layers had introduced a bias in a downward direction. He also ruled out the possibility that preferential sampling due to a correlation between PMSE occurrence and velocity direction had altered the mean data.

If our theory of PMSE generation due to the presence of charged aerosols is correct, then it also provides us with a source of radar-observed downward velocity. If, for example, the radio waves were scattering directly from the "aerosol-bound" electrons, the radar would measure a downward Doppler velocity corresponding to the aerosol terminal velocity. After falling to a warmer region, they would evaporate, and the upward motion of the aerosol constituents would not be detected by the radar. In this way the background fluid motion can be in the opposite direction of the radar Doppler velocity. However, this is not exactly our situation since the radar actually scatters coherently from inhomogeneities in the electron distribution which must follow the charged aerosols. Intuitively, it seems reasonable that even though the pattern of aerosols and electrons encounter a changing dynamic input as they descend through the neutral gas, they should retain at least a partial correlation from height to height in their spatial structure, especially at scales in the viscous-convective subrange where the charged particle dynamics is effectively decoupled from the immediate behavior of the neutrals. This aerosol explanation of the apparent downward flow also has the advantage that it naturally

shuts off during the non-summer months, which matches the seasonal behavior of the observations.

We can calculate the terminal velocity of an aerosol from (3.23). For summer mesopausal parameters we get 2 cm/s for $r_a = 0.01\mu$m and 20 cm/s for $r_a = 0.1\mu$m (the velocity is linearly proportional to the particle radius). Therefore, we still find it difficult to explain the $\sim -30$ cm/s June values in the Poker Flat data. In addition, it is not clear whether the 2.78-MHz Saskatoon radar, which also measures downward mean velocities in the mesosphere, would be affected since the radar scatter at such a large Bragg scale is not dependent on the presence of aerosols.

# Chapter 8

# Summary and Suggestions for Future Research

If the reader has immediately skipped to this final chapter after only reading the abstract, biographical sketch, and acknowledgments, then he/she would not be aware that we have made every effort to keep this thesis succinct and generally pleasant to read. We have "eschewed obfuscation" as much as possible and have resisted the natural urge to grandstand on tangential subjects far away from the heart of the dissertation topic. Thus, staying within the estabished *modus operandi* we move right along...

## 8.1 Summary

As the title had promised, the work contained in this thesis was about PMSE and can be conceptually divided into two parts: theory and observation.

First, we introduced the simple idea (which until now had not been articulated clearly) that the enhancement of coherent radar scatter must be due to the increase in the generation rate of electron density inhomogeneities and/or the reduction in the dissipation rate of such structures. We noted that previously proposed theories to explain the enormous enhancement of radar scatter leading to PMSE dealt with the former option—an increase in the driving forces—and were not very successful.

These past failures prompted us to explore the possibility of an anomalously low electron diffusivity in the summer mesopause. *Kelley et al.* [1987] had already

suggested that the presence of heavy hydrated ions, unique to the low temperatures of the polar summer mesosphere, might slow down the diffusion of electrons through the creation of ambipolar electric fields. Our kinetic theory results showed that what matters is the size and not the mass. The ions, which are dominated by polarization interactions, were not large enough to reduce the ambipolar diffusivity significantly. On the other hand, we showed that electrically charged aerosols could dramatically reduce the effective electron diffusivity.

We then examined the effect of reduced electron diffusivity on radar scatter due to isotropic turbulence. We were able to account for the observed signal strengths of PMSE with this theory using realistic parameters. We also showed that reduced electron diffusivity was necessary to maintain partial reflection structures.

*Havnes et al.* [1990] had previously contended that PMSE could result from the enhanced radar scatter from "Debye spheres" which form around charged aerosols in a plasma. After studying this idea we concluded that it was only applicable to PMSE observed by UHF radars. The enhancement above the background incoherent scatter due to this dressed aerosol scattering cannot be very large and the resulting Doppler spectral width should be very narrow: these characteristics match the observations.

Because these theories depend crucially on the nature of the aerosols, we examined their possible composition, size, abundance, and charge state. We concluded that the most plausible type of aerosols which would produce PMSE observed by VHF radars were a large number of small, sub-visible ice particles with a low negative charge. On the other hand, PMSE observed by UHF radars are more readily explained by dressed aerosol scatter from a small number of highly positively charged aerosols.

We began the observational half of the thesis by presenting data taken by the Sondrestrom 1.29-GHz radar. Under geomagnetically quiet conditions it appeared that the signal-to-noise ratio would be too low in the mesosphere to make any meaningful measurements. However, we were fortunate enough to catch a precipitation event during which an enhanced scattering layer emerged at around 87 km. We believe this event was the first PMSE ever observed at a radar frequency above one gigahertz. We showed that dressed aerosol scattering could reasonably explain

the observation.

We then presented selected CUPRI and rocket data from the NLC-91 campaign. The first simultaneous height comparison between noctilucent clouds and PMSE showed that the radar scattering region was near or slightly above the visible cloud layer. This result supported our earlier proposition that PMSE result from small, sub-visible ice aerosols which tend to reside above the large, visible NLC particles.

We inferred from aspect sensitivity measurements and Doppler spectrograms that there are two distinct types of PMSE: enhanced turbulence scatter and partial reflection. This CUPRI result agreed well with the simultaneous rocket measurements of neutral and plasma density fluctuations made by *Lübken et al.* [1992].

Also we showed one clear example of nonlinear gravity wave steepening, tilting, and finally breaking, which appeared to be very similar to theoretical model calculations.

Finally we compiled long-term statistics of PMSE during the NLC-91 campaign. The results were comparable to the data from the Poker Flat and SOUSY radars, including the downward direction of the mean vertical velocity which contradicts the theoretical requirement that the summer mesopause have a mean upward motion in order to cool down the mesopause to the observed low temperatures. If our theory of charged aerosol-induced radar scatter is correct, then the apparent downward motion can be attributed to the fall speed of the aerosols.

## 8.2 Suggestions for Future Research

In this thesis we have formulated a theory of PMSE generation which depends on the presence of charged aerosols. The observations that we made have added some credence to the theory, but were not sufficient to prove it correct. In general, we are at a stage where we could come up with any number of theories which cannot be proven or disproven with the available data. Clearly, it is time to concentrate on obtaining more definitive experimental data.

First, we should obtain PMSE data at three different frequencies from a common radar volume in order to compare the frequency dependence with that predicted by theory. We have presumably performed such an experiment during PMSE-91,

but so far we have not been able to exchange data sets with EISCAT, so this task will be left to future students of PMSE. Alternatively, one radar with multiple frequency capability (such as the frequency agile radar (FAR) developed by SRI) could be used. Second, we need to get a statistically better data set on aspect sensitivity. The EISCAT VHF radar configured in the split-beam mode can make such an observation. Third, an incoherent scatter radar should be run with high spectral, time, and space resolution in order to detect extremely narrow Doppler spectra that are expected to result from reduced electron diffusivity. Fourth, a VHF radar should be set up in Antarctica to see if PMSE exist in the southern hemisphere. Presumably they are there as we have no reason to believe otherwise. However, there may be interesting differences between PMSE borealis and australis. Satellite observations of polar mesospheric clouds, which are believed to be basically the same phenomenon as the ground-observed NLCs, indicate brighter clouds in the north than in the south [*Olivero and Thomas*, 1986], which implies a warmer or drier mesopause in the south.

A note concerning global change: NLC observations are absent from the historical record before 1885 and systematic observations in the last two decades have revealed an increase in their frequency of occurrence [*Gadsden*, 1990]. If the long-term increase in cloud formation is real, it is probably due to (1) an increase in the water vapor or (2) a decrease in the temperature. *Thomas et al.* [1989] opted for (1) and argued that the anthropogenic increase in methane gas (the oxidation of which in the stratosphere is an important source of water in the middle atmosphere) was responsible for the cloud increase. *Gadsden* [1990] noted that (2) was just as likely. We point out, however, that *Roble and Dickinson* [1989] have predicted a cooling of the mesopause with an increase in carbon dioxide and methane using their global upper atmosphere model. Therefore, it is very likely that anthropogenic effects on both (1) and (2) are working together to increase the cloudiness in the summer mesopause. Assuming that this is indeed the case, then PMSE could also be useful as an indicator of global change. According to our theory, PMSE are dependent on the presence of charged ice aerosols which are in turn sensitive to the temperature and the water mixing ratio. Therefore, changes in those parameters should be observable as changes in the radar echo characteristics such as the intensity, length

and frequency of occurrence, average altitude, and latitudinal distribution. Currently, there are no VHF radars in the polar region operating on a continual basis, but fortunately the high strength of PMSE allows relatively small and inexpensive radars to study them. It would be much easier to get long-term statistics from radar measurements than from optical NLC observations. We highly recommend that such a system be put into operation.

One of the great unknowns in the PMSE puzzle is the compositions, sizes, numbers, shapes, orientations, and charge states of the aerosols. Optical methods such as spectrophotometry and polarimetry have given us some information regarding the larger particles, and rocket-borne mass spectrometers have been successful in measuring ion compositions. However, we know very little about the intermediate size regime including meteoric dust and embryonic ice cloud particles, and the charge states of the aerosols are virtually unknown. Collection of aerosols by rockets has been attempted several times but without very conclusive results (see *Gadsden and Schröder* [1989]). More clever in situ experiments need to be devised in order to further our understanding of these particles. For example, a more sensitive version of the PAT sensor used during NLC-91 is currently being developed (U. Wälchli, private communication). Laboratory results have also been very sparse as the summer mesopause is an especially complex region to imitate. More effort needs to be expended in this direction.

The dependence of PMSE on temperature is also a relationship that needs to be explored. Was it coincidence that the second strongest PMSE event during NLC-91 occurred right before a falling sphere experiment measured the lowest atmospheric temperature ever recorded [*Schmidlin*, 1992]? If PMSE is really dependent on the presence of ice particles, then one would expect there to be a correlation between PMSE and temperatures low enough for ice crystals to nucleate and grow. A whole series of falling spheres should be launched while a radar observes PMSE.

Electric field measurements should also be made inside a PMSE layer. A rocket-borne double probe has measured a vertical dc electric field across an NLC layer on the order of several mV/m *Goldberg* [1989]. During the NLC-91 campaign, an electric field mill on the DECIMALS-B rocket showed short-period fluctuations of mV/m through the NLC and a V/m vertical E-field in the PMSE region

[*Zadorozhny et al.*, 1993]. This was an intriguing result, but the field mill as a rocket-borne instrument to measure electric fields has many potential problems (pun intended). In fact, the measurements of apparent V/m electric fields in the mesosphere have long been controversial [*Kelley et al.*, 1983]. Even so, the field mill did detect something very interesting in the PMSE region and we need to determine what parameter the instrument really measured.

# Appendix A

# Numerical Analysis of the Diffusion Equations

The one-dimensional versions of the diffusion equations for a weakly ionized three-component plasma derived in Chapter 3 were solved by applying the Dufort-Frankel method (see, e.g., *Ames* [1977]). Converting (3.48) into difference equations we get

$$f_i^{n+1} = f_i^{n-1} + 2r\eta_1\left(f_{i+1}^n - f_i^{n-1} + f_{i-1}^n\right) + 2r\eta_2\left(g_{i+1}^n - g_i^{n-1} + g_{i-1}^n\right) - 2r\eta_1 f_i^{n+1} - 2r\eta_2 g_i^{n+1} \tag{A.1}$$

$$g_i^{n+1} = g_i^{n-1} + 2r\eta_3\left(f_{i+1}^n - f_i^{n-1} + f_{i-1}^n\right) + 2r\eta_4\left(g_{i+1}^n - g_i^{n-1} + g_{i-1}^n\right) - 2r\eta_3 f_i^{n+1} - 2r\eta_4 g_i^{n+1} \tag{A.2}$$

where $f$ and $g$ correspond to $n_c$ and $n_e$, the superscripts are the time indexes, the subscripts are the space indexes, $r = \Delta t/\Delta x^2$, and

$$\eta_1 = \frac{|Z_a|D_i + Z_i D_a}{Z_i + |Z_a|} \tag{A.3}$$

$$\eta_2 = \frac{D_i - D_a}{Z_i + |Z_a|} + \left(1 - \frac{N_{0a}}{N_{0e}}Z_a\right)D_i - \frac{N_{0a}}{N_{0e}}|Z_a|D_a \tag{A.4}$$

$$\eta_3 = \frac{|Z_a|D_i - Z_i D_a}{Z_i + |Z_a|} \tag{A.5}$$

$$\eta_2 = \frac{D_i + D_a}{Z_i + |Z_a|} + \left(1 - \frac{N_{0a}}{N_{0e}}Z_a\right)D_i + \frac{N_{0a}}{N_{0e}}|Z_a|D_a \tag{A.6}$$

Solving for $f_i^{n+1}$ and $g_i^{n+1}$ we obtain

$$f_i^{n+1} = \left[(1+2r\eta_1)(1+2r\eta_4) - 4r^2\eta_2\eta_3\right]^{-1} \{(1+2r\eta_4) f_i^{n-1} - 2r\eta_2 g_i^{n-1} +$$

$$2r\left[2r(\eta_1\eta_4 - \eta_2\eta_3) + \eta_1\right]\left(f_{i+1}^n - f_i^{n-1} + f_{i-1}^n\right) + 2r\eta_2\left(g_{i+1}^n - g_i^{n-1} + g_{i-1}^n\right)\} \quad \text{(A.7)}$$

$$g_i^{n+1} = \left[(1+2r\eta_1)(1+2r\eta_4) - 4r^2\eta_2\eta_3\right]^{-1} \{(1+2r\eta_1) g_i^{n-1} - 2r\eta_3 f_i^{n-1} +$$

$$2r\left[2r(\eta_1\eta_4 - \eta_2\eta_3) + \eta_4\right]\left(g_{i+1}^n - g_i^{n-1} + g_{i-1}^n\right) + 2r\eta_3\left(f_{i+1}^n - f_i^{n-1} + f_{i-1}^n\right)\} \quad \text{(A.8)}$$

(A.7) and (A.8) are in a form amenable to iterative computation.

Our aim was to solve the above equations with a sinusoidal perturbation with wavenumber $\kappa$ as the initial condition and measure the exponential decay time constant $\tau$ in order to calculate the effective electron diffusion coefficient, $D_e^{\text{eff}} = 1/\tau\kappa^2$. We chose the initial perturbation amplitudes by enforcing the charge neutrality condition of (3.46) and keeping the ratios of the perturbations equal to the ratios of the background values. The following equation expresses the initial condition used:

$$n_c(0) = \frac{1 - (Z_a \pm Z_i)\frac{N_{0a}}{N_{0e}}}{Z_i} n_e(0) \quad \text{(A.9)}$$

where the plus sign corresponds to positively charged aerosols and the minus sign to negatively charged ones.

The numerical method used was stable for all the parameters that we applied to it. However, since the object was to measure the $e$-folding decay time of the perturbations, setting the time steps too large resulted in inaccurate results. Setting the time steps too small, on the other hand, caused the program to run for many hours. The problem was that the equations contained two distinct modes of diffusion which could be separated by many orders of magnitude. For different ratios of the constituents the diffusion speed would be drastically different, thus requiring different size time steps. $\Delta t = 0.5$ was usually a good value to use. Applying too few gridpoints had an adverse effect on the accuracy also. Once again it was a competition between accuracy and computation time. $NX = 50$ seemed to be a good compromise.

# Appendix B

# The CUPRI System

## B.1 System Description

The Cornell University portable radar interferometer (CUPRI) is a ground-based observational tool small enough to be packed entirely in a Winnebago motor home. Originally designed to take interferometric measurements from auroral plasma irregularities [*Providakes et al.*, 1983], it has been continuously evolving and it has been used to observe the mesosphere since 1988. In 1991, a very similar system ("CUPRI—The Sequel") was developed and housed in a used U-Haul truck.

In Fig. B.1 we show a block diagram of the Winnebago CUPRI which was operated in northern Scandinavia during the summer of 1991. The basic configuration of the system had not changed, so we refer the reader to earlier descriptions of the system [*Providakes*, 1985; *Sahr*, 1990; *Hall*, 1991]. The most crucial changes that we made for this edition were the replacement of the old analog-to-digital converters (ADC) with new, faster (10 MHz) ones which allowed for a much finer range resolution, the addition of a dual Exabyte tape drive capable of writing much more data per tape (up to 2.2 GB) than before, and the incorporation of a phase encoder for the transmitter pulse which allowed us to use pulse compression schemes for improved SNR. During the NLC-91 campaign, we also set up a printer, driven via a modem link, at the remote rocket launch control center. Table B.1 gives the specifications and parameters used during the summer of 1991.

A schematic of the antenna arrays is shown in Fig. B.2. The main antenna array used for transmission and reception was composed of 16 rows of coaxial colinears

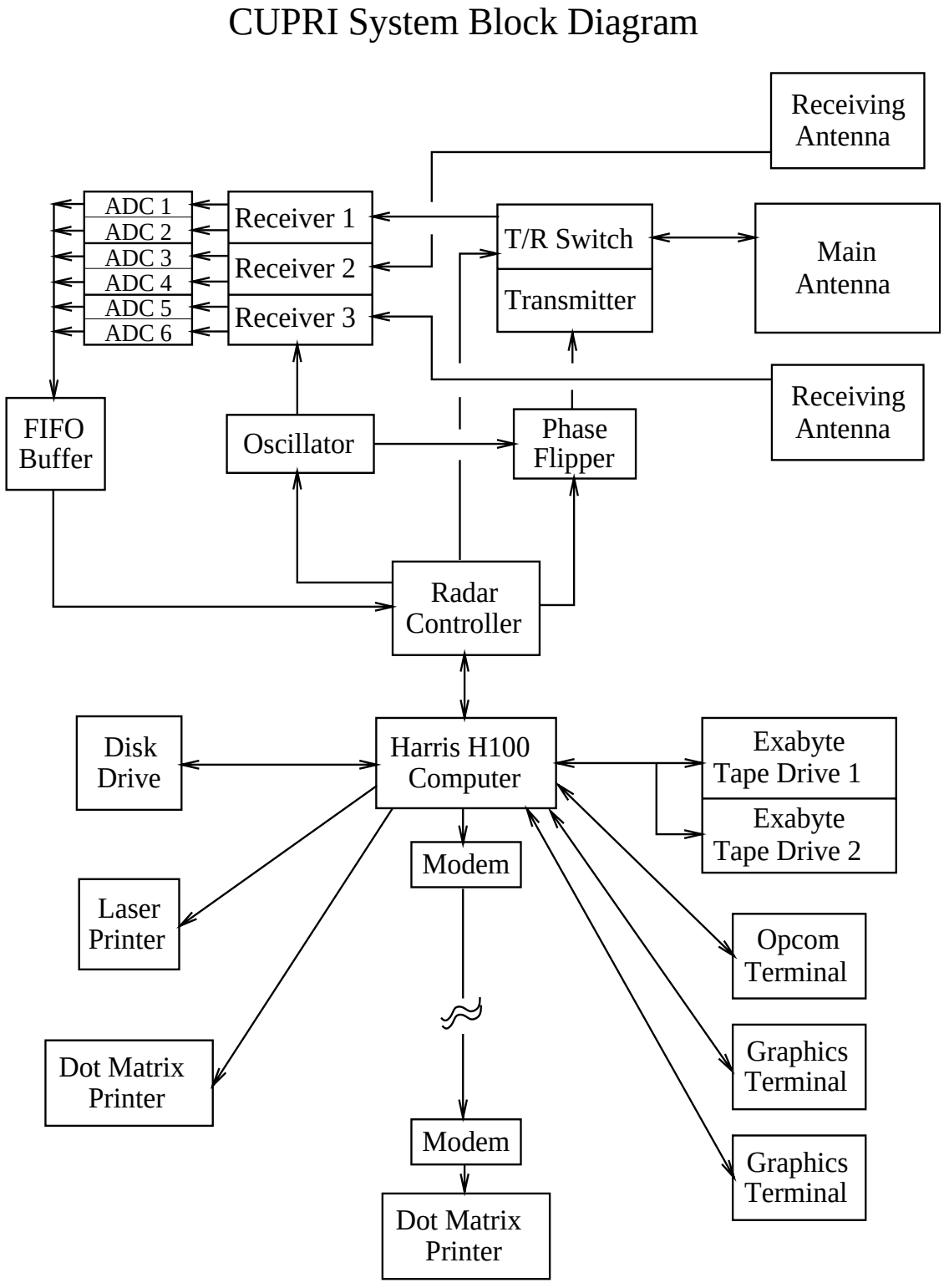


Figure B.1: A block diagram of the Winnebago CUPRI as implemented during the summer of 1991.

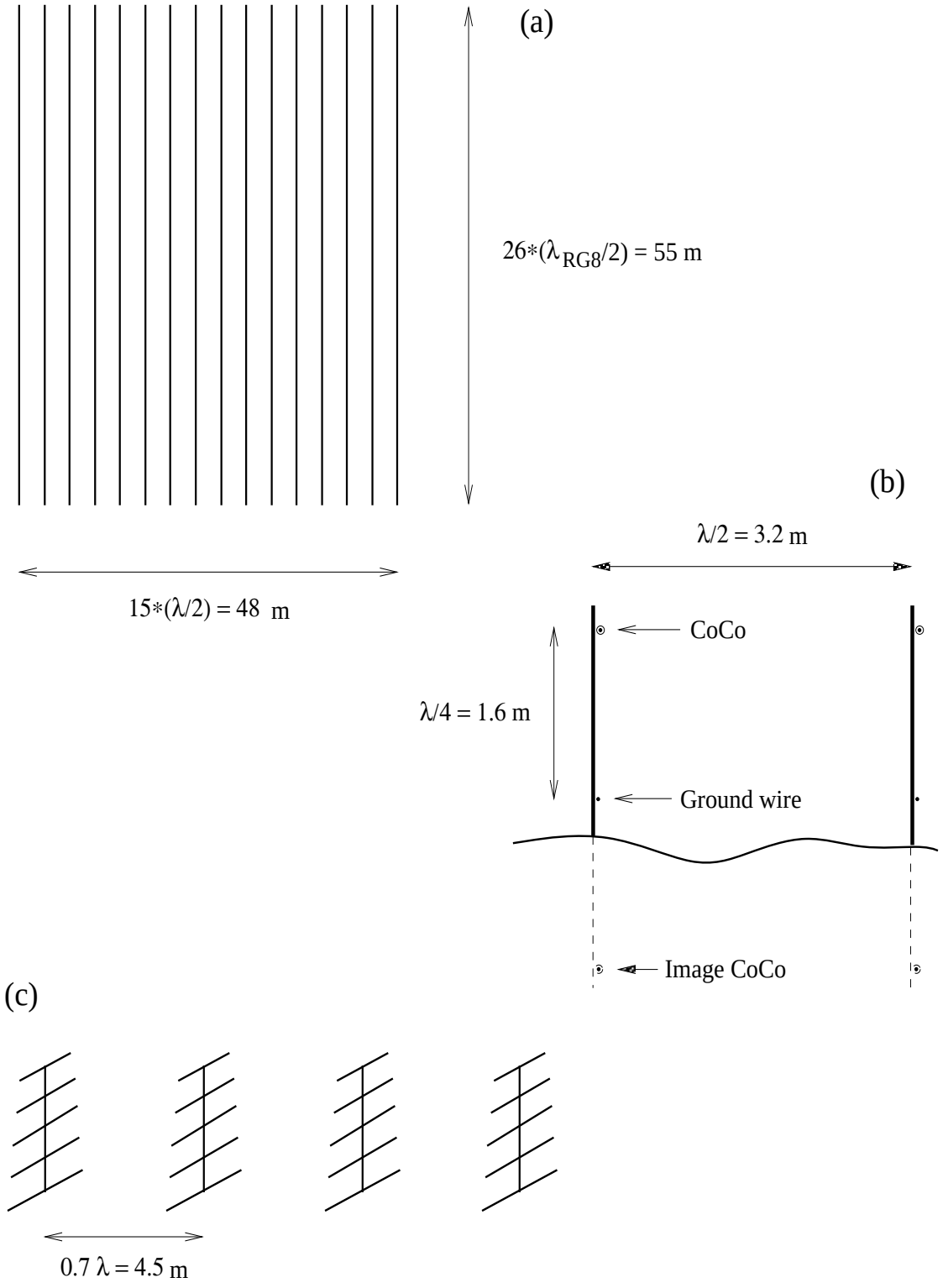


Figure B.2: Schematics of (a) the main antenna array, (b) a close-up side view of the main array, and (c) the Yagi receiving array.

Table B.1: CUPRI system specifications and parameters used during the PMSE-91 and NLC-91 campaigns.

| | |
|---|---|
| Transmitter frequency: | 46.9 MHz |
| Transmitter peak power: | 50 kW |
| Transmitter pulse lengths: | 1.5–32 $\mu$s |
| Main antenna (Tx and Rx): | 16 CoCos |
| Beamwidth: | 5° FWHM |
| Interferometer antennas (Rx): | 2 arrays of 4 (5-element) Yagis |
| Receiver bandwidth: | 1 MHz |
| ADC: | 8 bits, 10 MHz |
| 8mm tape drives (2): | 2.2 GBytes, 256 kByte/s |

(CoCos) [*Balsley and Ecklund*, 1972], each one of which was a string of 26 half-wave dipoles laid end-to-end. (Because the relative permittivity of the RG8 coaxial cable was 2.26, the physical length of the half-wave dipole was $3.2/\sqrt{2.26} = 2.1$ m.) The CoCos were spaced a half wavelength (3.2 m) apart to get a peak in the antenna gain straight up and a null on the horizon. A copper reflecting wire was placed a quarter wavelength below each CoCo to take maximum advantage of the constructive contribution from the image CoCo. Also, to shift the beam by 8° off-zenith in order to obtain aspect sensitivity data, phasing cables of lengths 1.2, 2.4, and 3.6 m could be inserted manually into the feed network (see Fig. B.3). With the phasing elements in place, the beam pointed 8° off zenith in the direction perpendicular to the CoCo polarization. The theoretical beam pattern can be calculated straightforwardly from the principle of array pattern multiplication (see, e.g., *Collin* [1985]) and is given by

$$G = \left[\sin\left(kd_v \cos\theta\right)\right]^2 \times \tag{B.1}$$

$$\left\{ \frac{\cos\left(\frac{\pi}{2}\sin\theta\right)}{\cos\theta} \frac{\sin\left(\frac{m}{2}kd_c\sin\theta\right)}{\sin\left(\frac{1}{2}kd_c\sin\theta\right)} \frac{\sin\left(\frac{n}{2}kd_h\cos\theta\sin\phi\right)}{\sin\left(\frac{1}{2}kd_h\cos\theta\sin\phi\right)} \frac{\sin\left[\frac{N}{2}kD_h\left(\cos\theta\sin\phi-\delta\right)\right]}{\sin\left[\frac{1}{2}kD_h\left(\cos\theta\sin\phi-\delta\right)\right]} \right\}^2$$

where $\theta$ and $\phi$ are the zenith angles parallel and perpendicular to the CoCo polarization, $m$ is the number of half-wave dipoles in each CoCo, $n$ is the number of CoCos phased together, $N$ is the number of groups of $n$ CoCos, $k$ is the radar

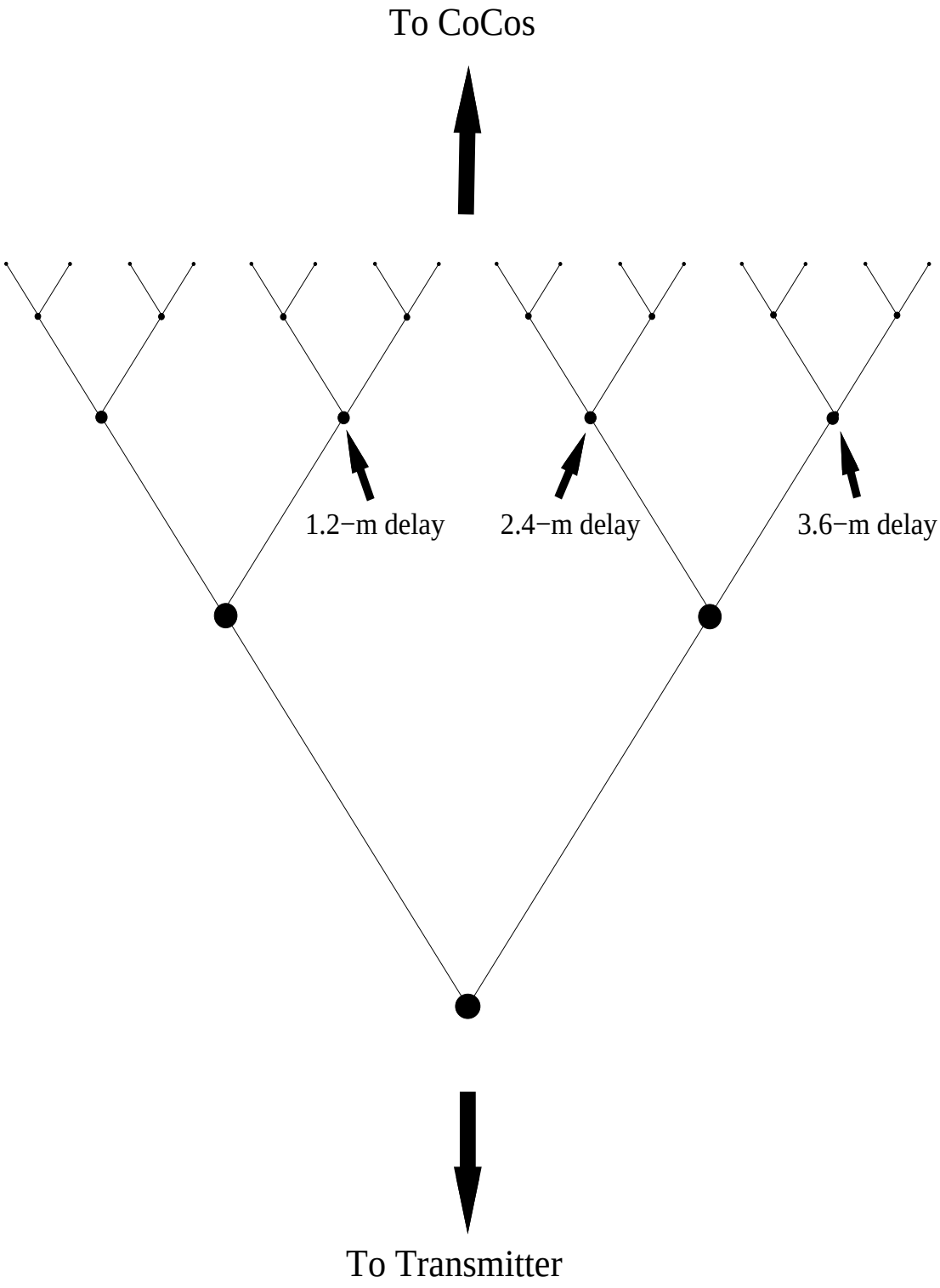


Figure B.3: Schematic of main antenna feed network. With the phasing elements inserted at the indicated points, the beam shifted 8° in the direction of increasing delay.

wavenumber, $d_c$ is the physical length of an RG8 half-wave dipole, $d_h$ is the spacing between CoCos, $D_h$ is the spacing between the groups of CoCos phased together, $d_v$ is the distance between the CoCo and the reflecting wire, and $\delta$ is a measure of the phase difference between the $N$ groups of $n$ CoCos. (B.1) is normalized such that the peak gain for $\delta = 0$ is unity.

Substituting in the parameters of the CUPRI antenna, we get

$$G = \left[\sin\left(\frac{\pi}{2}\cos\theta\right)\right]^2 \times \left\{\frac{\cos\left(\frac{\pi}{2}\sin\theta\right)}{\cos\theta}\frac{\sin\left(\frac{26}{3}\pi\sin\theta\right)}{\sin\left(\frac{1}{3}\pi\sin\theta\right)}\frac{\sin\left(2\pi\cos\theta\sin\phi\right)}{\sin\left(\frac{\pi}{2}\cos\theta\sin\phi\right)}\frac{\sin\left[8\pi\left(\cos\theta\sin\phi-\delta\right)\right]}{\sin\left[2\pi\left(\cos\theta\sin\phi-\delta\right)\right]}\right\}^2 \quad \text{(B.2)}$$

The resulting pattern for $\delta = 0$ is displayed in Fig. B.4. The full-width-half-maximum is about 5° and the strongest sidelobe is about 15 dB below the peak. Fig. B.5 shows the theoretical main antenna beam pattern with the phasing cables inserted into the feed network ($\delta = 0.14$). The beam has shifted 8° off zenith. Calculations show that the peak gain drops by about 1 dB and the beamwidth widens slightly compared to the vertically pointed beam.

Four Yagi-Uda antennas were used in each of the two receiving-only arrays used to form the interferometry baselines (see Fig. B.2). The five-element Yagis were spaced a 0.7 wavelength apart for maximum gain in the vertical direction (W. Swartz, private communication).

The layout of the antenna arrays is shown in Fig. B.6. Because the poles planted for the main array were not lined up very well, the actual disposition of the CoCos was not nearly so linear as pictured. The antenna field layout at the Esrange site is displayed in Fig. B.7. Here, the CoCos were very straight.

## B.2 Modes of Operation

While at Tromsø, we operated the CUPRI in three different modes. The parameters for the modes are listed in Table B.2. Because raw data was dumped directly to tape for recording, the interpulse period (IPP) was determined by setting it at the shortest value possible with which the tape drive could keep up. For PMSE observations at Esrange, we only operated the CUPRI in mode (2) for maximum

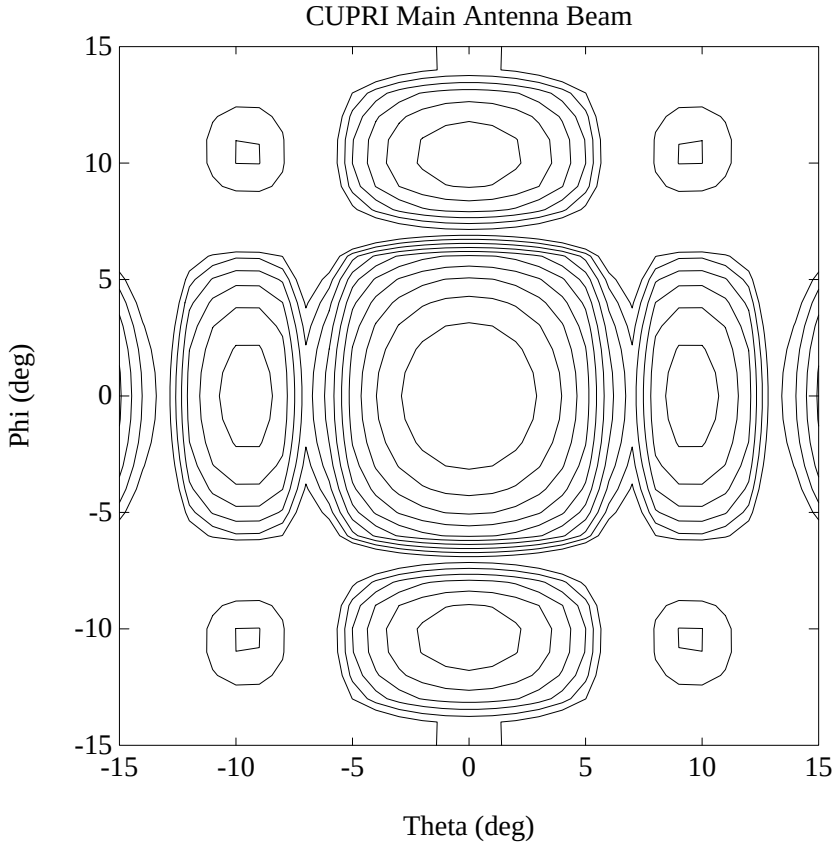


Figure B.4: The theoretical beam pattern of the CUPRI main antenna array for in-phase excitation of all CoCos. The peak is normalized to 0 dB and the contour interval is -3 dB. The minimum contour line plotted corresponds to -30 dB.

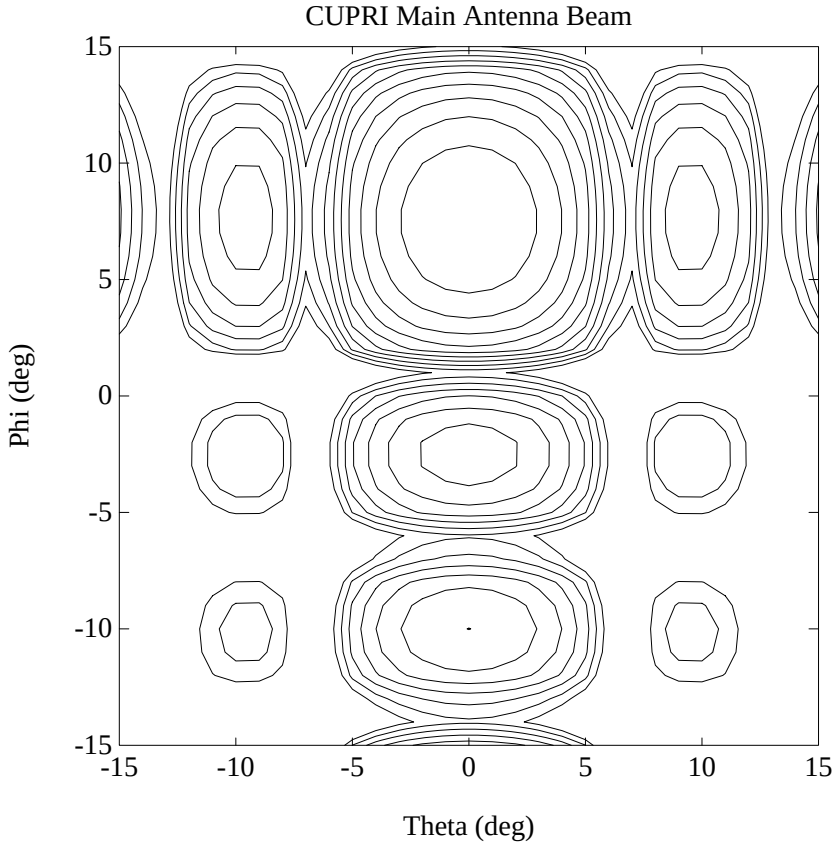


Figure B.5: The theoretical beam pattern of the CUPRI main antenna array with the phasing elements in place. The peak is normalized to 0 dB and the contour interval is -3 dB. The minimum contour line plotted corresponds to -30 dB.

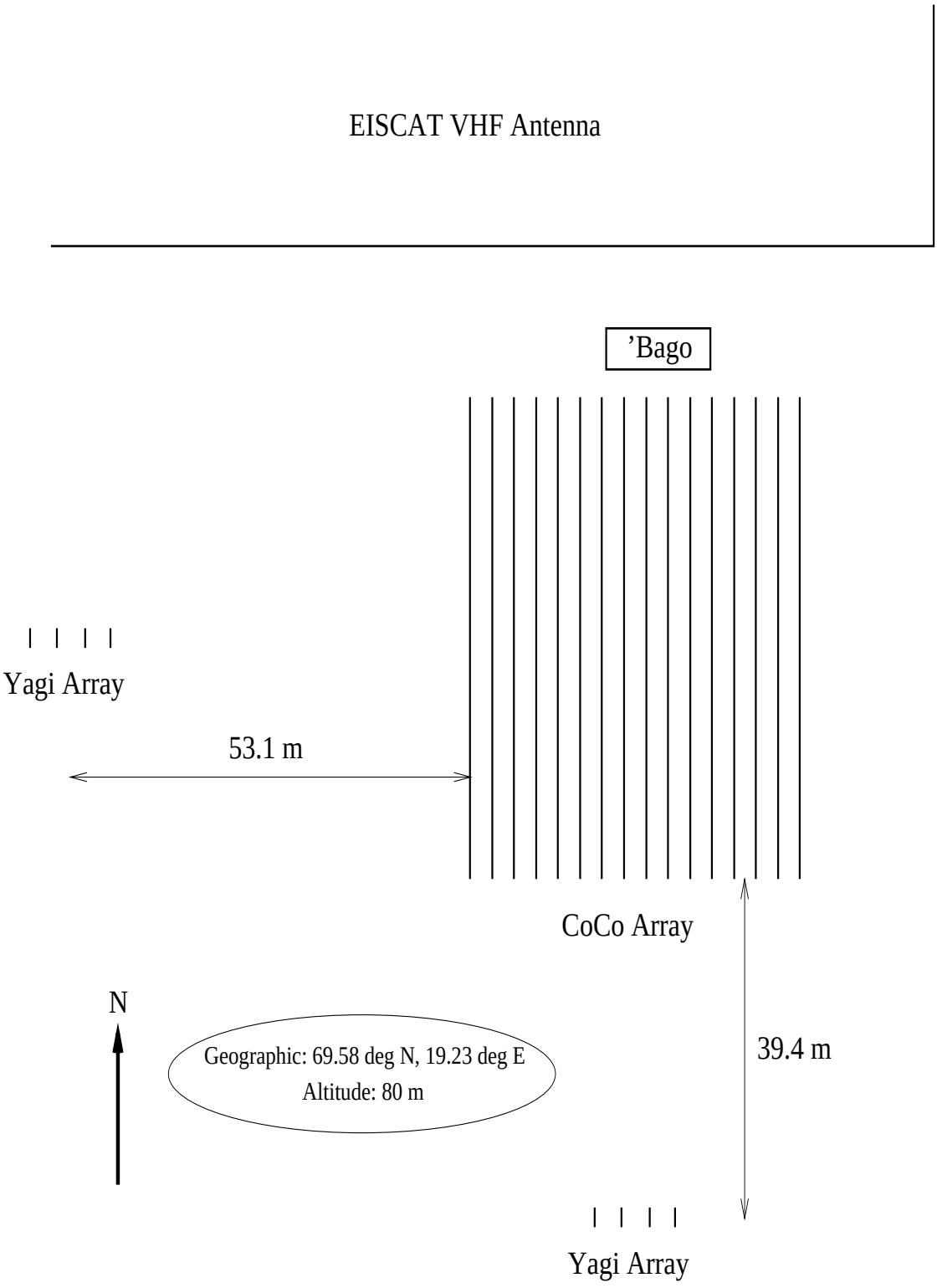


Figure B.6: The layout of the CUPRI antenna field in Tromsø, Norway.

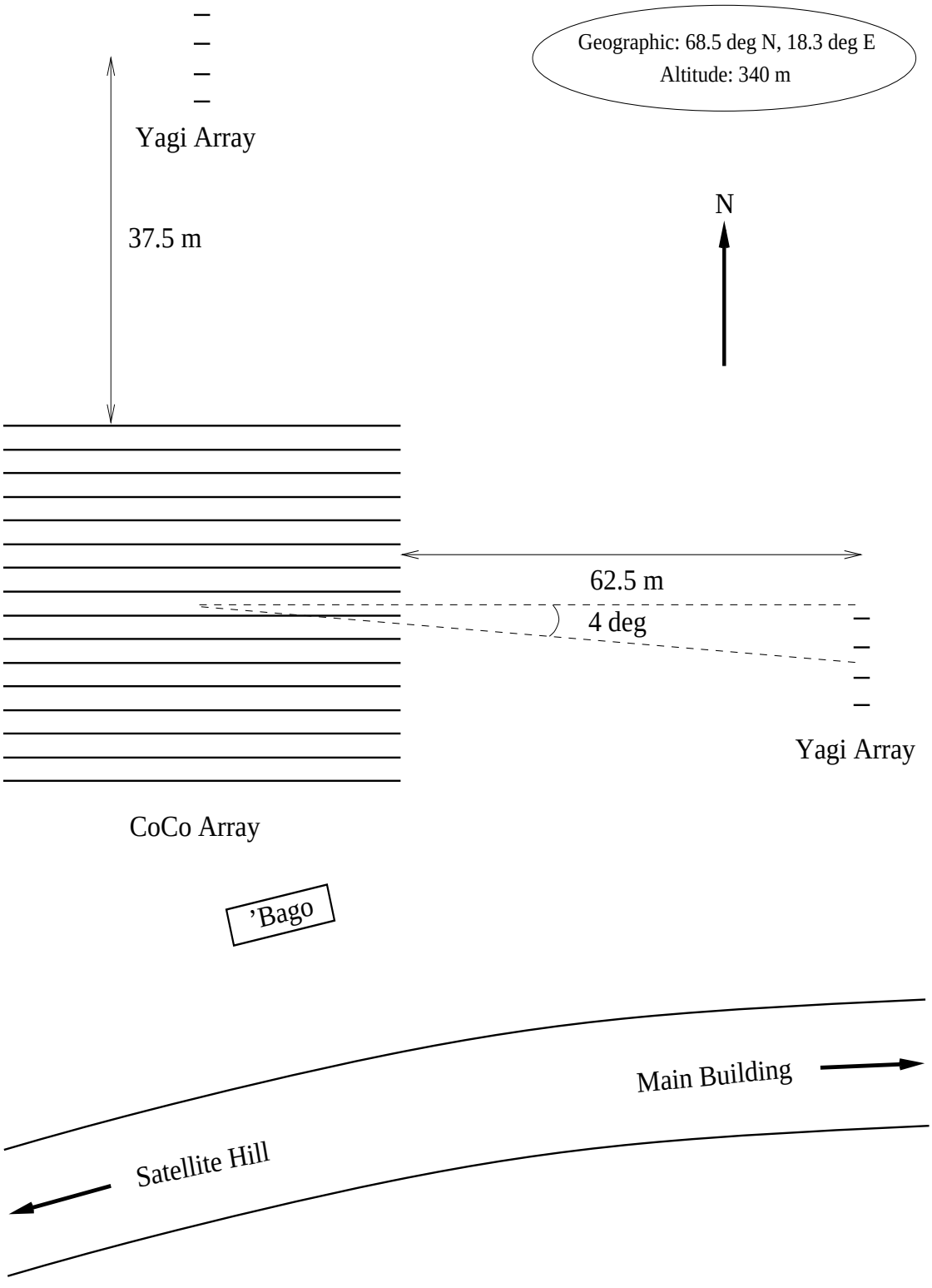


Figure B.7: The layout of the CUPRI antenna field in Esrange, Sweden.

Table B.2: Modes of operation used during the PMSE-91 campaign.

| Mode | Pulse Coding | IPP | Range Resolution | Range Sampled |
|---|---|---|---|---|
| (1) | None | 2.8 ms | 300 m | 78–94 km |
| (2) | 16-baud complementary | 4.0 ms | 300 m | 78–91 km |
| (3) | 16-baud complementary | 6.0 ms | 225 m | 78–92 km |

signal detection capability. (We also used CUPRI in tropospheric and stratospheric modes to test the mettle of the system as a MST radar. We succeeded in receiving echoes up to the tropopause.)

The complementary code used was actually a complementary code sequence transmitted over 4 IPPs as $AB\overline{AB}$. The phase flipping sequence of $AB$ is given in Table B.3. The theoretical SNR enhancement is linearly proportional to the

Table B.3: Phase sequence of the 16-baud complementary code pair.

| | |
|---|---|
| $A$ | $+-++-+---+-++-+++$ |
| $B$ | $+-++-+---+--+--+--$ |

baud length, hence it is a factor of 16 in this case. The $\overline{AB}$ sequence provides an extra measure of DC cancellation if the individual bauds are not well balanced. In general, complementary codes of length $2^n$ bauds are produced by the recursive relation

$$A_n = A_{n-1}B_{n-1} \tag{B.3}$$

and

$$B_n = A_{n-1}\overline{B_{n-1}} \tag{B.4}$$

where $A_0B_0$ can be any combination of $+$ and $-$.

## B.3 Data Processing

For the purposes of this dissertation, only data received by the main antenna was analyzed. (The interferometry data provided by the other two receivers is currently

being processed by C. Alcala.)

The general data processing scheme was as follows. First, we decoded the raw data digitally if the data had been encoded. Second, we coherently integrated the data $N_c$ times. Although coherently integrating before decoding would have been faster, this scheme allowed an arbitrary $N_c$ to be used, whereas $N_c$ would have been restricted to a multiple of 4 (the number of IPPs used for one cycle of the code) in the other case. Third, we FFTed $N_f$ points and squared the data to get the power spectra. Fourth, we estimated the noise level from the noise gates sampled far above the data raster and subtracted it from the power. Finally, we incoherently averaged the spectra $N_i$ times. The resulting theoretical SNR enhancement is given by

$$N_{\mathrm{SNR}} = N_b N_c \sqrt{N_i} \tag{B.5}$$

where $N_b$ is the number of bauds in the complementary code. The final time resolution is then

$$\delta t = (\mathrm{IPP})\, N_c N_f N_i \tag{B.6}$$

The Doppler frequency resolution is given by

$$\delta f = \frac{1}{(\mathrm{IPP})\, N_c N_f} \tag{B.7}$$

and the Nyquist frequency range is

$$\Delta f = \frac{1}{(\mathrm{IPP})\, N_c} \tag{B.8}$$

The corresponding velocity values are given by the relation

$$v = \frac{\lambda_R}{2} f \tag{B.9}$$

where $\lambda_R$ is the radar wavelength and $f$ is the Doppler frequency shift. Table B.4 lists the data processing parameters and the subsequent time resolution $\delta t$, velocity resolution $\delta v$, Nyquist velocity range $\Delta v$, and SNR enhancement $N_{\mathrm{SNR}}$.

Table B.4: Data processing parameters used for the different data acquisition modes and the resulting specifications.

| Mode | $N_c$ | $N_f$ | $N_i$ | $\delta t$ (s) | $\delta v$ (m/s) | $\Delta v$ (m/s) | $N_{\mathrm{SNR}}$ |
|---|---|---|---|---|---|---|---|
| (1) | 32 | 64 | 10 | 57 | 0.56 | 36 | 100 |
| (2) | 22 | 64 | 6 | 34 | 0.57 | 36 | 860 |
| (3) | 22 | 64 | 6 | 51 | 0.38 | 24 | 860 |

The height from which the radar waves are backscattered is given by

$$h = h_0 + \frac{c\tau}{2}\cos\theta \tag{B.10}$$

where $h_0$ is the altitude of the radar site (80 m for Tromsø and 340 m for Esrange), $\theta$ is the zenith pointing angle of the radar beam, and

$$\tau = \tau_{SD} - \tau_{TD} - \tau_{FD} - \frac{\mathrm{PW}}{2} + \frac{\frac{1}{\mathrm{BW}}}{2} \tag{B.11}$$

where $\tau_{SD}$ is the nominal sample delay which is the time elapsed between the command sent by the radar controller to begin transmission and when the received sample was digitized, $\tau_{TD} = 2\mu$s is the delay before the transmitter actually begins transmission, $\tau_{FD} = 0.87\mu$s is the two-way delay due to the antenna feed network, and the last two terms are the pulsewidth and receiver bandwidth factors needed to center the height within the radar volume. (PW is pulsewidth for an uncoded pulse, baud width for a coded pulse. BW = 1 MHz for both campaigns.)

The radar volume reflectivity can be calculated from the radar equation

$$P_r = \frac{P_t A_e^2 \alpha^2 V \eta}{4\pi\lambda_R^2 r^4} \tag{B.12}$$

where $P_r$ is the received power, $P_t$ is the transmitted power, $A_e = 2640$ m$^2$ is the effective antenna area, $\alpha = 0.5$ is the one-way system efficiency factor, $V$ is the radar volume, $\eta$ is the volume reflectivity, and $r$ is the range. Substituting in

$$V = \frac{\pi}{4} r^2 {\theta_{BW}}^2 \Delta r \tag{B.13}$$

where $\theta_{BW} = 0.87$ rad is the beamwidth and $\Delta r$ is the range resolution, into (B.12) and solving for $\eta$ yields

$$\eta = \frac{16\lambda_R^2 r^2 P_r}{P_t A_e^2 \alpha^2 \theta^2 \Delta r} \tag{B.14}$$

Since $P_r = kT_nB(\text{SNR})$ where $T_n$ is $B = 1$ MHz is the receiver bandwidth, and including the SNR enhancement factor given by (B.5), we get

$$\eta = \frac{16\lambda_R^2 r^2 kT_nB(\text{SNR}_{\text{final}})}{P_t A_e^2 \alpha^2 {\theta_{BW}}^2 \Delta r N_{\text{SNR}}} \tag{B.15}$$

Because the background cosmic noise temperature is expected to be much greater than the system temperature, we can use $T_n = 5000$ K as a good estimate of noise temperature.

# References


Allen, C. W., *Astrophysical Quantities*, The Athlone Press, London, 1964.

Ames, W. F., *Numerical Methods for Partial Differential Equations*, Academic Press, New York, 1977.

Andrews, D. G., J. R. Holton, and C. B. Leovy, *Middle Atmosphere Dynamics*, volume 40 of *International Geophysics Series*. Academic Press, Orlando, 1987.

Auty, R. P., and R. H. Cole, Dielectric properties of ice and $D_2O$, *J. Chem. Phys.*, *20*, 1309, 1952.

Backhouse, T. W., The luminous cirrus cloud of June and July, *Meteorol. Mag.*, *20*, 133, 1885.

Balsley, B. B., and W. L. Ecklund, A portable coaxial colinear antenna, *IEEE Trans. Antennas Propagat.*, *20*, 513, 1972.

Balsley, B. B., W. L. Ecklund, and D. C. Fritts, VHF echoes from the high-latitude mesosphere and lower thermosphere: Observations and interpretations, *J. Atmos. Sci.*, *40*, 2451, 1983.

Balsley, B. B., and A. C. Riddle, Monthly mean values of the mesospheric wind field over Poker Flat, Alaska, *J. Atmos. Sci.*, *41*, 2368, 1984.

Banks, P. M., and G. Kockarts, *Aeronomy*, Academic Press, New York, 1973.

Baron, B., D. Hoover, and F. Williams, Vacuum ultraviolet photoelectric emission from amorphous ice, *J. Chem. Phys.*, *68*, 1997, 1978.

Batchelor, G. K., Small-scale variation of convected quantities like temperature in a turbulent fluid, part 1, *J. Fluid Mech.*, *5*, 113, 1959.

Benilov, A. Y., Fossil turbulence in the ocean pycnocline, *Izv. Atmos. Oceanic Phys.*, *24*, 406, 1988.

Bingham, R., U. de Angelis, V. N. Tsytovich, and O. Havnes, Electromagnetic

wave scattering in dusty plasmas, *Phys. Fluids B*, *3*, 811, 1991.

Björn, L. G., E. Kopp, U. Herrmann, P. Eberhardt, P. H. G. Dickinson, D. J. Mackinnon, F. Arnold, G. Witt, A. Lundin, and D. B. Jenkins, Heavy ionospheric ions in the formation process of noctilucent clouds, *J. Geophys. Res.*, *90*, 7985, 1985.

Blix, T. A., In situ studies of turbulence in the middle atmosphere by means of electrostatic ion probes, *NDRE/PUBL-88/1002*, Norwegian Defense Research Establishment, Kjeller, Norway, 1988.

Böhnhardt, H., The charge of fluffy dust grains of silicate and carbon near P/Halley and P/Giacobini-Zinner, *Proc. 20th ESLAB Symp. Halley's Comet*, *ESA SP-250*, pp. 207–213, 1986.

Booker, H. G., A theory of scattering by non-isotropic irregularities with applications to radar reflections from the aurora, *J. Atmos. Terr. Phys.*, *8*, 204, 1956.

Bruining, H., *Physics and Applications of Secondary Electron Emission*, Pergamon Press, London, 1954.

Chapman, S., On the law of distribution of velocities, and on the theory of viscosity and thermal conduction, in a non-uniform simple monatomic gas, *Phil. Trans. R. Soc.*, *A216*, 115, 1916.

Chapman, S., On the convergence of the infinite determinants in the Lorentz case, *J. Lond. Math. Soc.*, *8*, 266, 1933.

Chapman, S., and T. G. Cowling, *The Mathematical Theory of Non-Uniform Gases*, Cambridge University Press, New York, 1970.

Cho, J. Y. N., T. M. Hall, and M. C. Kelley, On the role of charged aerosols in polar mesosphere summer echoes, *J. Geophys. Res.*, *97*, 875, 1992*a*.

Cho, J. Y. N., M. C. Kelley, and C. J. Heinselman, Enhancement of Thomson scatter by charged aerosols in the polar mesosphere: Measurements with a 1.29-GHz radar, *Geophys. Res. Lett.*, *19*, 1097, 1992*b*.

Cho, J. Y. N., W. E. Swartz, and C. A. Miller, CUPRI observations of PMSE during Salvo B of NLC-92: Evidence of both partial reflection and turbulent scatter, *Geophys. Res. Lett.*, 1993, (submitted).

Collin, R. E., *Antennas and Radiowave Propagation*, McGraw Hill, New York, 1985.

Collis, P. N., and S. Kirkwood, Discrete layers of D-region ionisation in the high-latitude ionosphere, *Adv. Space Res.*, *10*, 41, 1990.

Collis, P. N., T. Turunen, and E. Turunen, Evidence of heavy positive ions at the summer arctic mesopause from the EISCAT UHF incoherent scatter radar, *Geophys. Res. Lett.*, *15*, 2, 1988.

Corrsin, S., On the spectrum of isotropic temperature fluctuations in isotropic turbulence, *J. Applied Phys.*, *22*, 469, 1951.

Corrsin, S., Further generalizations of Onsager's cascade model for turbulent spectra, *Phys. Fluids*, *7*, 1156, 1964.

Coy, L., D. C. Fritts, and J. Weinstock, The Stokes drift due to vertically propagating internal gravity waves in a compressible atmosphere, *J. Atmos. Sci.*, *43*, 2636, 1986.

Czechowsky, P., I. M. Reid, and R. Rüster, VHF radar measurements of the aspect sensitivity of the summer polar mesopause echoes over Andenes (69°N, 16°E), Norway, *Geophys. Res. Lett.*, *15*, 1259, 1988.

Czechowsky, P., I. M. Reid, R. Rüster, and G. Schmidt, VHF radar echoes observed in the summer and winter polar mesosphere over Andøya, Norway, *J. Geophys. Res.*, *94*, 5199, 1989.

Dalgarno, A., M. R. C. McDowell, and A. Williams, The mobilities of ions in unlike gases, *Phil. Trans. R. Soc.*, *250*, 413, 1958.

Donahue, T. M., B. Guenther, and J. E. Blamont, Noctilucent clouds in daytime circumpolar particulate layers near the summer mesopause, *J. Atmos. Sci.*, *30*, 515, 1972.

Dougherty, J. P., and D. T. Farley, A theory of incoherent scattering of radio waves by a plasma, 3, Scattering in a partly ionized gas, *J. Geophys. Res.*, *68*, 5473, 1963.

Doviak, R. J., and D. S. Zrnič, *Doppler Radar and Weather Observations*, Academic Press, San Diego, 1984.

Ecklund, W. L., and B. B. Balsley, Long-term observations of the Arctic mesosphere with the MST radar at Poker Flat, Alaska, *J. Geophys. Res.*, *86*, 7775, 1981.

Enskog, D., *The Kinetic Theory of Phenomena in Fairly Rare Gases.* PhD thesis,

Uppsala University, Uppsala, Sweden, 1917.

Farley, D. T., J. P. McClure, D. L. Sterling, and J. L. Green, Temperature and composition of the equatorial ionosphere, *J. Geophys. Res.*, *72*, 5837, 1967.

Farlow, N. H., G. V. Ferry, and M. B. Blanchard, Examination of surfaces exposed to a noctilucent cloud, *J. Geophys. Res.*, *75*, 6736, 1970.

Fogle, B., Noctilucent clouds, *UAG Rep. 177*, Univ. Alaska, Fairbanks, 1966.

Franke, S. J., J. Röttger, C. LaHoz, and C. H. Liu, Frequency domain interferometry of polar mesosphere summer echoes with the EISCAT VHF radar: A case study, *Radio Sci.*, *27*, 417, 1992.

Fraser, G. J., and U. Khan, Semidiurnal variations in the time scale of irregularities near the Antarctic mesopause, *Radio Sci.*, *25*, 997, 1990.

Fritts, D. C., Observational evidence of a saturated gravity wave spectrum in the troposphere and lower stratosphere, *J. Atmos. Sci.*, *45*, 1741, 1988.

Fukuyama, K., and W. Kofman, Incoherent scattering of an electromagnetic wave in the mesosphere: A theoretical consideration, *J. Geomagn. Geoelectr.*, *32*, 67, 1980.

Gadsden, M., Observations of the colour and polarization on noctilucent clouds, *Ann. Geophys.*, *31*, 507, 1975.

Gadsden, M., Noctilucent clouds, *Space Sci. Rev.*, *33*, 279, 1982.

Gadsden, M., Observations of noctilucent clouds from NW-Europe, *Ann. Geophys.*, *3*, 119, 1985.

Gadsden, M., A secular change in noctilucent cloud occurrence, *J. Atmos. Terr. Phys.*, *52*, 247, 1990.

Gadsden, M., and W. Schröder, *Noctilucent Clouds*, Springer-Verlag, Berlin, 1989.

Gardner, F. F., and J. L. Pawsey, Study of the ionospheric D-region using partial reflections, *J. Atmos. Terr. Phys.*, *3*, 321, 1953.

Gerz, T., and H. Yamazaki, 1990. Mixing during the final stage of decay of turbulence in stratified flow. In *Ninth Symposium on Turbulence and Diffusion*. American Meteorological Society.

Gibson, C. H., 1980. *Marine Turbulence*, chapter Fossil temperature, salinity, and vorticity turbulence in the ocean, pages 221–257. Elsevier, Amsterdam.

Gibson, C. H., On the scaling of vertical temperature gradient spectra, *J. Geophys. Res.*, *87*, 8031, 1982.

Gibson, C. H., Internal waves, fossil turbulence, and composite ocean microstructure spectra, *J. Fluid Mech.*, *168*, 89, 1986.

Gibson, C. H., Laboratory, numerical, and oceanic fossil turbulence in rotating and stratified flows, *J. Geophys. Res.*, *96*, 12,549, 1991.

Gibson, C. H., and W. H. Schwartz, The universal equilibrium spectra of turbulent velocity and scalar fields, *J. Fluid Mech.*, *16*, 365, 1963.

Gibson, C. H., G. R. Stegen, and R. B. Williams, Statistics of the fine structure of turbulent velocity and temperature fields measured at high Reynolds number, *J. Fluid Mech.*, *41*, 153, 1970.

Goertz, C. K., Dusty plasmas in the solar system, *Rev. Geophys.*, *27*, 271, 1989.

Goertz, C. K., and W.-H. Ip, Limitation of electrostatic charging of dust particles in a plasma, *Geophys. Res. Lett.*, *11*, 349, 1984.

Goldberg, R. A., Electrodynamics of the high-latitude mesosphere, *J. Geophys. Res.*, *94*, 14,661, 1989.

Gore, A., *Earth in the Balance: Ecology and the Human Spirit*, Houghton Mifflin, Boston, 1992.

Grams, G., and G. Fiocco, Equilibrium temperatures of spherical ice particles in the upper atmosphere and implications for noctilucent cloud formation, *J. Geophys. Res.*, *82*, 961, 1977.

Grant, H. L., B. A. Hughes, W. M. Vogel, and A. Moilliet, The spectrum of temperature fluctuations in turbulent flow, *J. Fluid Mech.*, *34*, 423, 1968.

Hagfors, T., Note on the scattering of electromagnetic waves from charged dust particles in a plasma, *J. Atmos. Terr. Phys.*, *54*, 333, 1992.

Hall, C., Modification of the energy-wavenumber spectrum for heavy proton hydrates as tracers for isotropic turbulence at the summer mesopause, *J. Geophys. Res.*, *95*, 5549, 1990.

Hall, T. M., *Radar Observations and Dynamics of the Polar Summer Mesosphere*. PhD thesis, Cornell Univ., Ithaca, N.Y., 1991.

Hall, T. M., J. Y. N. Cho, M. C. Kelley, and W. K. Hocking, A re-evaluation of the

Stokes drift in the polar summer mesosphere, *J. Geophys. Res.*, *97*, 887, 1992.

Havnes, O., U. de Angelis, R. Bingham, C. K. Goertz, G. E. Morfill, and V. Tsytovich, On the role of dust in the summer mesopause, *J. Atmos. Terr. Phys.*, *52*, 637, 1990.

Havnes, O., F. Melandsø, C. La Hoz, T. K. Aslaksen, and T. Hartquist, Charged dust in the Earth's mesopause; effects on radar backscatter, *Phys. Scr.*, *45*, 535, 1992.

Hidy, G. M., and J. R. Brock, *The Dynamics of Aerocolloidal Systems*, Pergamon Press, New York, 1970.

Hill, R. J., Models of the scalar spectrum for turbulent advection, *J. Fluid Mech.*, *88*, 541, 1978*a*.

Hill, R. J., Nonneutral and quasi-neutral diffusion of weakly ionized multiconstituent plasma, *J. Geophys. Res.*, *83*, 989, 1978*b*.

Hill, R. J., and S. A. Bowhill, Small-scale fluctuations in D region ionization due to hydrodynamic turbulence, *Aeron. Rep. 75*, Aeron. Lab., Univ. of Ill., Urbana, 1976.

Hill, R. J., and S. F. Clifford, Modified spectrum of atmospheric temperature fluctuations and its application to optical propagation, *J. Opt. Soc. Am.*, *68*, 892, 1978.

Hocking, W. K., Measurement of turbulent energy dissipation rates in the middle atmosphere by radar techniques: A review, *Radio Sci.*, *20*, 1403, 1985.

Holton, J. R., The influence of gravity wave breaking on the general circulation of the middle atmosphere, *J. Atmos. Sci.*, *40*, 2497, 1983.

Hoppe, U.-P., D. C. Fritts, I. M. Reid, P. Czechowsky, C. M. Hall, and T. L. Hansen, Multiple-frequency studies of the high-latitude summer mesopause: Implications for scattering processes, *J. Atmos. Terr. Phys.*, *52*, 907, 1990.

Hoppe, U.-P., C. Hall, and J. Röttger, First observations of summer polar mesospheric backscatter with a 224-MHz radar, *Geophys. Res. Lett.*, *15*, 28, 1988.

Houghton, J. T., *The Physics of Atmospheres*, Cambridge U. Press, Cambridge, 1986.

Hunten, D. M., R. P. Turco, and O. B. Toon, Smoke and dust particles of meteoric

origin in the mesosphere and stratosphere, *J. Atmos. Sci.*, *37*, 1342, 1980.

Inhester, B., J. C. Ulwick, J. Y. N. Cho, M. C. Kelley, and G. Schmidt, Consistency of rocket and radar electron density observations: Implication about the anisotropy of mesospheric turbulence, *J. Atmos. Terr. Phys.*, *52*, 855, 1990.

Jensen, E. J., and G. E. Thomas, Charging of mesospheric particles: Implications for electron density and particle coagulation, *J. Geophys. Res.*, *96*, 18,603, 1991.

Jensen, E. J., G. E. Thomas, and B. B. Balsley, On the statistical correlation between polar mesospheric cloud occurrence and enhanced mesospheric radar echoes, *Geophys. Res. Lett.*, *15*, 315, 1988.

Jesse, O., Die Beobachtungen der leuchtenden Nachtwolken, *Meteorol. Z.*, *4*, 179, 1887*a*.

Jesse, O., Die Höhe der leuchtenden (silbernen) Wolken, *Meteorol. Z.*, *4*, 424, 1887*b*.

Johnston, H. L., and K. E. McCloskey, Measurements of viscosity for some common gases, *J. Phys. Chem.*, *44*, 1038, 1940.

Kasten, F., Falling speed of aerosol particles, *J. Appl. Meteor.*, *7*, 944, 1968.

Kelley, M. C., D. T. Farley, and J. Röttger, The effect of cluster ions on anomalous VHF backscatter from the summer polar mesosphere, *Geophys. Res. Lett.*, *14*, 1031, 1987.

Kelley, M. C., C. L. Siefring, and R. F. Pfaff, Jr., Large middle atmospheric electric fields, fact or fiction?, *Geophys. Res. Lett.*, *10*, 733, 1983.

Kelley, M. C., and J. C. Ulwick, Large- and small-scale organization of electrons in the high-latitude mesosphere: Implications of the STATE data, *J. Geophys. Res.*, *93*, 7001, 1988.

Kelley, M. C., J. C. Ulwick, J. Röttger, B. Inhester, T. Hall, and T. Blix, Intense turbulence in the polar mesosphere: Rocket and radar measurements, *J. Atmos. Terr. Phys.*, *52*, 875, 1990.

Kelly, J. D., Sondrestrom radar—initial results, *Geophys. Res. Lett.*, *10*, 1112, 1983.

Kihara, T., *Imperfect Gases*, Asakusa Books, Tokyo, 1949.

Kolmogorov, A. N., The local structure of turbulence in viscous fluids for very high Reynolds numbers, *Dokl. Akad. Nauk SSSR*, *30*, 301, 1941.

La Hoz, C., Radar scattering from dusty plasmas, *Phys. Scr.*, *45*, 529, 1992.

Larsen, T. R., J. B. Reagan, W. L. Imhof, L. E. Montbriand, and J. S. Belrose, A coordinated study of energetic electron precipitation and D region electron concentrations over Ottawa during disturbed conditions, *J. Geophys. Res.*, *81*, 2200, 1976.

Leu, M. T., M. A. Biondi, and R. Johnsen, Measurements of the recombination of electrons with $H_3O^+ \cdot (H_2O)_n$-series ions, *Phys. Rev. A*, *7*, 292, 1973.

Lindzen, R. S., Turbulence and stress owing to gravity wave and tidal breakdown, *J. Geophys. Res.*, *86*, 9707, 1981.

Lübken, F.-J., G. Lehmacher, T. A. Blix, U.-P. Hoppe, E. V. Thrane, J. Y. N. Cho, and W. E. Swartz, First in situ observations of neutral and plasma density fluctuations in the presence of PMSE, *Geophys. Res. Lett.*, 1992, (submitted).

Luhmann, J. G., R. M. Johnson, M. J. Baron, B. B. Balsley, and A. C. Riddle, Observations of the high-latitude ionosphere with the Poker Flat MST radar: Analyses using simultaneous Chatanika radar measurements, *J. Geophys. Res.*, *88*, 10,239, 1983.

Lumley, J. L., The spectrum of nearly inertial turbulence in a stably stratified fluid, *J. Atmos. Sci.*, *21*, 99, 1964.

Maxwell, J. C., On the dynamical theory of gases, *Phil. Trans. R. Soc.*, *157*, 49, 1867.

Meek, C. E., and A. H. Manson, Vertical motions in the upper middle atmosphere from the Saskatoon (52° N, 107° W) M. F. radar, *J. Atmos. Sci.*, *46*, 849, 1989.

Meyer-Vernet, N., "Flip-flop" of electric potential of dust grains in space, *Astron. Astrophys.*, *105*, 98, 1982.

Michel, B., *Ice Mechanics*, University of Laval Press, Quebec, 1978.

Natanson, G. L., On the theory of the charging of amicroscopic aerosol particles as a result of capture of gas ions, *Sov. Phys. Tech. Phys.*, *5*, 538, 1960.

Obukhov, A. M., Structure of the temperature field in turbulent flows, *Izvestiya Akademii Nauk SSSR, Geogr. Geophys. Ser.*, *13*, 58, 1949.

Olivero, J. J., and G. E. Thomas, Climatology of polar mesospheric clouds, *J. Atmos. Sci.*, *43*, 1263, 1986.

Palaniswamy, V. I., and C. M. Purushotham, Stability of shear flow of stratified

fluids with fine dust, *Phys. Fluids*, *24*, 1224, 1981.

Providakes, J. F., *Radar Interferometer Observations and Theory of Plasma Irregularities in the Auroral Ionosphere*. PhD thesis, Cornell U., Ithaca, N.Y., 1985.

Providakes, J. F., W. E. Swartz, D. T. Farley, and B. G. Fejer, First VHF auroral interferometer observations, *Geophys. Res. Lett.*, *10*, 401, 1983.

Reid, G. C., Ice particles and electron "bite-outs" at the summer polar mesopause, *J. Geophys. Res.*, *95*, 13,891, 1990.

Reid, I. M., P. Czechowsky, R. Rüster, and G. Schmidt, First VHF radar measurements of mesopause summer echoes at mid-latitudes, *Geophys. Res. Lett.*, *16*, 135, 1989.

Roble, R. G., and R. E. Dickinson, How will changes in carbon dioxide and methane modify the mean structure of the mesosphere and thermosphere?, *Geophys. Res. Lett.*, *16*, 1441, 1989.

Rössler, F., Aerosol layers in the atmosphere, *Space Res.*, *12*, 423, 1972.

Röttger, J., and C. La Hoz, Characteristics of polar mesosphere summer echoes (PMSE) observed with the EISCAT 224-MHz radar and possible explanations of their origin, *J. Atmos. Terr. Phys.*, *52*, 893, 1990.

Röttger, J., C. La Hoz, S. J. Franke, and C. H. Liu, Steepening of reflectivity structures detected in high-resolution Doppler spectra of polar mesosphere summer echoes (PMSE) observed with the EISCAT 224-MHz radar, *J. Atmos. Terr. Phys.*, *52*, 939, 1990*a*.

Röttger, J., C. La Hoz, M. C. Kelley, U.-P. Hoppe, and C. Hall, The structure and dynamics of polar mesosphere summer echoes observed with the EISCAT 224-MHz radar, *Geophys. Res. Lett.*, *15*, 1353, 1988.

Röttger, J., M. T. Rietveld, C. La Hoz, T. Hall, M. C. Kelley, and W. E. Swartz, Polar mesosphere summer echoes observed with the EISCAT 933-MHz radar and the CUPRI 46.9-MHz radar, their similarity to 224-MHz radar echoes and their relation to turbulence and electron density profiles, *Radio Sci.*, *25*, 671, 1990*b*.

Røyrvik, O., and L. G. Smith, Comparison of mesospheric VHF radar echoes and rocket probe electron concentration measurements, *J. Geophys. Res.*, *89*, 9014,

1984.

Sahr, J. D., *Observations and Theory of the Radar Aurora*. PhD thesis, Cornell U., Ithaca, N.Y., 1990.

Schlegel, K., A. Brekke, and A. Haug, Some characteristics of the quiet polar D-region and mesosphere obtained with the partial reflection method, *J. Atmos. Terr. Phys.*, *40*, 205, 1978.

Schmidlin, F. J., First observation of mesopause temperatures lower than 100 K, *Geophys. Res. Lett.*, *19*, 1643, 1992.

Schröder, W., Krakatoa 1885, *Geowiss. in unserer Zeit*, *1*, 155, 1985.

Schulte, P., and F. Arnold, Detection of upper atmospheric negatively charged microclusters by a rocket-borne mass spectrometer, *Geophys. Res. Lett.*, *19*, 2297, 1992.

Schunk, R. W., Transport equations for aeronomy, *Planet. Space Sci.*, *23*, 437, 1975.

Shur, G. N., Eksperimental'nyye issledovaniya energeticheskogo spektra atmosfernoy turbulentnosti, *Trudy Tsentral Aero. Obs.*, *43*, 79, 1962.

Spitzer, L., *Physical Processes in the Interstellar Medium*, John Wiley, New York, 1978.

Stillinger, D. C., K. N. Helland, and C. W. Van Atta, Experiments on the transition of homogeneous turbulence to internal waves in a stratified fluid, *J. Fluid Mech.*, *131*, 91, 1983.

Stitt, G. R., and E. Kudeki, Interferometric cross-spectral studies of mesospheric scattering layers, *Radio Sci.*, *26*, 783, 1991.

Stroud, W. G., W. Nordberg, W. R. Bandeen, F. L. Bartman, and P. Titus, Rocket-grenade observation of atmospheric heating in the Arctic, *J. Geophys. Res.*, *64*, 1342, 1959.

Sugiyama, T., Response of electrons to a gravity wave in the upper mesosphere, *J. Geophys. Res.*, *93*, 11,083, 1988.

Tatarskii, V. I., *The Effects of the Turbulent Atmosphere on Wave Propagation*, Israel Program for Scientific Translations, Jerusalem, 1971.

Taylor, M. J., A. P. van Eyken, H. Rishbeth, G. Witt, N. Witt, and M. A. Clilverd, Simultaneous observations of noctilucent clouds and polar mesospheric radar

echoes: Evidence for non-correlation, *Planet. Space Sci.*, *37*, 1013, 1989.

Tennekes, H., and J. L. Lumley, *A First Course in Turbulence*, MIT Press, Cambridge, 1972.

Thomas, G. E., Solar Mesospheric Explorer measurements of polar mesospheric clouds (noctilucent clouds), *J. Atmos. Terr. Phys.*, *46*, 819, 1984.

Thomas, G. E., and C. P. McKay, On the mean particle size and water content of polar mesosphere clouds, *Planet. Space Sci.*, *33*, 1209, 1985.

Thomas, G. E., and J. J. Olivero, Climatology of polar mesospheric clouds, 2, Further analysis of Solar Mesospheric Explorer data, *J. Geophys. Res.*, *94*, 14,673, 1989.

Thomas, G. E., J. J. Olivero, E. J. Jensen, W. Schröder, and O. B. Toon, Relation between increasing methane and the presence of ice clouds at the mesopause, *Nature*, *338*, 490, 1989.

Thomas, L., I. Astin, and I. T. Prichard, The characteristics of VHF echoes from the summer mesopause region at mid-latitudes, *J. Atmos. Terr. Phys.*, *54*, 969, 1992.

Tozer, W. F., and D. E. Beeson, Optical model of noctilucent clouds based on polarimetric measurements from two sounding rocket campaigns, *J. Geophys. Res.*, *79*, 5607, 1974.

Tsytovich, V. N., U. de Angelis, and R. Bingham, Nonlinear transition scattering of waves on charged dust particles in a plasma, *J. Plasma Phys.*, *42*, 429, 1989.

Turco, R. P., O. B. Toon, R. C. Whitten, R. G. Keesee, and D. Hollenbach, Noctilucent clouds: Simulation studies of their genesis, properties and global influences, *Planet. Space Sci.*, *30*, 1147, 1982.

Ulwick, J. C., K. D. Baker, M. C. Kelley, B. B. Balsley, and W. L. Ecklund, Comparison of simultaneous MST radar and electron density probe measurements during STATE, *J. Geophys. Res.*, *93*, 6989, 1988.

van Eyken, A. P., C. Hall, and P. J. S. Williams, A determination of the orientation of Polar Mesosphere Summer Echo layers using the EISCAT as a dual beam radar, *Radio Sci.*, *26*, 395, 1991.

VanZandt, T. E., and D. C. Fritts, A theory of enhanced saturation of the gravity

wave spectrum due to increases in atmospheric stability, *Pure Applied Geophys.*, *131*, 399, 1989.

Vincenti, W. G., and C. Kruger, *Introduction to Physical Gas Dynamics*, Krieger, Malabar, 1965.

Vlaskov, V. A., E. B. Vasilev, T. N. Semjashkina, and E. Turunen, A study of PMSE using the partial reflection techniques, *J. Atmos. Terr. Phys.*, 1992, (submitted).

von Zahn, U., and W. Meyer, Mesopause temperatures in polar summer, *J. Geophys. Res.*, *94*, 14,647, 1989.

Wälchli, U., J. Stegman, G. Witt, J. Y. N. Cho, C. A. Miller, M. C. Kelley, and W. E. Swartz, NLC and PMSE observations by the CUPRI radar and by optical electrical instruments on the night of the 9/10 August during the NLC-91 campaign, *Adv. Space Res.*, 1992, (submitted).

Wälchli, U., J. Stegman, G. Witt, J. Y. N. Cho, C. A. Miller, M. C. Kelley, and W. E. Swartz, First height comparisons of noctilucent clouds and simultaneous PMSE, *Geophys. Res. Lett.*, 1993, (submitted).

Watkins, B. J., C. R. Philbrick, and B. B. Balsley, Turbulence energy dissipation rates and inner scale sizes from rocket and radar data, *J. Geophys. Res.*, *93*, 7009, 1988.

Wegener, A., Die Erforschung der obersten Atmosphärenschichten, *Gerlands Beitr. Geophys.*, *11*, 102, 1912.

Weinstock, J., On the theory of turbulence in the buoyancy subrange of stably stratified flows, *J. Atmos. Sci.*, *35*, 634, 1978.

Weinstock, J., Finite amplitude gravity waves: Harmonics, advective steepening and saturation, *J. Atmos. Sci.*, *43*, 688, 1986.

Whipple, E. C., T. G. Northrop, and D. A. Mendis, The electrostatics of a dusty plasma, *J. Geophys. Res.*, *90*, 7405, 1985.

Whitehead, J. D., The formation of sporadic E layer in the temperate zones, *J. Atmos. Terr. Phys.*, *20*, 49, 1961.

Wilhelm, N., and G. Witt, 1989. The SLIPS: A scattered light intensity profile sensor for rocket borne investigations of noctilucent clouds. In *Collection of Works of the International Workshop of Noctilucent Clouds*. International Association

of Meteorology and Atmospheric Physics, Tallinn, Estonia.

Williams, P. J. S., A. P. van Eyken, C. Hall, and J. Röttger, Modulations in the polar mesosphere summer echoes and associated gravity waves, *Geophys. Res. Lett.*, *16*, 1437, 1989.

Witt, G., Height, structure, and displacements of noctilucent clouds, *Tellus*, *14*, 1, 1962.

Witt, G., J. E. Dye, and N. Wilhelm, Rocket-borne measurements of scattered sunlight in the mesosphere, *J. Atmos. Terr. Phys.*, *38*, 223, 1976.

Woodman, R. F., and Y. Chu, Aspect sensitivity measurements of VHF backscatter made with the Chung-Li radar: Plausible mechanisms, *Radio Sci.*, *24*, 113, 1989.

Woodman, R. F., and A. Guillén, Radar observations of winds and turbulence in the stratosphere and mesosphere, *J. Atmos. Sci.*, *31*, 493, 1974.

Woods, J. D., Fossil turbulence, *Radio Sci.*, *4*, 1365, 1969.

Zadorozhny, A. M., A. A. Tyutin, G. Witt, N. Wilhelm, U. Wälchli, J. Y. N. Cho, and W. E. Swartz, Electric field measurement in the vicinity of noctilucent clouds and PMSE, *Geophys. Res. Lett.*, 1993, (submitted).